The Thresholds and Mechanisms of Tissue Injury by Focused Ultrasound

Julianna Simon

A dissertation

submitted in partial fulfillment of the

requirements for the degree of

Doctor of Philosophy

University of Washington

2013

Reading Committee:

Lawrence Crum, Co-Chair

Michael Bailey, Co-Chair

Oleg Sapozhnikov

Program Authorized to Offer Degree:

Bioengineering

University of Washington

Abstract

The Thresholds and Mechanisms of Tissue Injury by Focused Ultrasound

Julianna Simon

Co-Chairs of the Supervisory Committee:
Dr. Lawrence A. Crum
Dr. Michael R. Bailey
Department of Bioengineering

Therapeutic ultrasound is used in clinics around the world to treat ailments such as uterine fibroids, kidney stones, and plantar fasciitis. While many of the therapeutic effects of ultrasound are elicited by hyperthermia, bubbles can also interact with tissue to produce beneficial effects. For example, bubbles are used in boiling histotripsy to de-bulk tissue and are used in shock wave lithotripsy to break kidney stones. However, the same bubbles that break the kidney stones also damage the kidney, which is why bubble damage is a concern in every ultrasound application including fetal imaging. Whether the aim is to emulsify a tumor or image a fetus, understanding the thresholds and mechanisms of tissue injury by bubbles in an ultrasound field is important for all ultrasound applications and was the goal of this dissertation.

One specific application of therapeutic ultrasound, known as boiling histotripsy, uses shock wave heating to explosively expand a millimeter-size boiling bubble at the transducer focus and fractionate bulk tissue. Yet it was unclear how the millimeter-size boiling or vapor bubble broke down the tissue into its submicron components. In this dissertation, we experimentally tested the hypothesis that ultrasonic atomization, or the

emission of fine droplets from an acoustically excited liquid film, is the mechanism by which the millimeter-size boiling bubble in boiling histotripsy fractionates tissue into its submicron components. Using high speed photography, we showed that tissue can behave as a liquid such that a miniature acoustic fountain forms and atomization occurs within a millimeter-size cavity that approximates the boiling or vapor bubble produced by boiling histotripsy. The end result of tissue atomization was a hole in the tissue surface. After showing that tissue can be eroded by atomization, a series of experiments were conducted to determine the tissue properties that influence atomization. The results indicated that highly collagenous tissues such as the liver capsule were difficult to atomize; however it was also shown that surface wetting could be used to enhance atomization by changing the focus of the inverted and reflected ultrasound wave. Finally, the role of bubbles in tissue atomization was investigated using a high static pressure chamber, where it was determined that bubbles are necessary for tissue fractionation. While the investigation into the mechanism of boiling histotripsy was the primary focus of this dissertation, we also established thermal and mechanical injury thresholds for renal tissue injury. This work was driven by the need to determine the safety of a specific therapeutic ultrasound application - renal stone repositioning by ultrasonic propulsion – for FDA approval to begin clinical trials. The end result of this dissertation was an increased understanding of how and at what levels bubbles in an ultrasound field can damage tissue, which is important for developing safe and reliable therapies.

TABLE OF CONTENTS

LIST OF FIGURES

Figure Number Page

List of Tables

Table Number Page

ACKNOWLEDGEMENTS

I would like to thank all of the people who helped and supported me in my PhD studies. First of all, I would like to thank my supervisory committee: Drs. Lawrence Crum, Michael Bailey, Oleg Sapozhnikov, Matthew O'Donnell, and Susan Herring for all of their time and support. In particular, I would like to thank Dr. Crum for his guidance and wisdom in lab and in life and Dr. Bailey for his unending enthusiasm and his support and direction in the wide variety of projects I pursued. I would also like to thank Drs. Oleg Sapozhnikov and Vera Khokhlova for proposing the acoustic fountain mechanism of fractionation and for always being willing to listen to my ideas and suggest alternatives. Thanks to Dr. Yak-Nam Wang for her expertise and patience in teaching me histology and for her help in designing and implementing the tissue wetness and preservation studies. Furthermore, I would like to thank Frank (Rusty) Starr for generously training me to perform *in vivo* animal studies in pigs and in mice. I would also like to thank Brian MacConaghy for designing and building a safe high static pressure chamber. Further thanks go to Drs. Tanya Khokhlova, Wayne Kreider, and Adam Maxwell for always being willing to answer questions or help with an experiment. Even more thanks goes to some of our collaborators in other departments or in other Universities: Drs. Denny Liggitt, Ziyue Li, Andrew Evan, and James McAteer. I would also like to thank all of the wonderful students and staff at the Center for Industrial and Medical Ultrasound (CIMU) – you have been fantastic to work with and I am looking forward to another two years as a postdoc on the Rolling Stones project. Last but not least, I would like to thank my family, friends, and my horse, Tiny, who have unconditionally supported me and kept me sane throughout this journey to a PhD. Without you, I could not have succeeded.

CHAPTER 1

Introduction

1.1. Motivation

The field of therapeutic ultrasound has been in development since 1917, when, during the development of sonar, Langevin first observed fish death [1]. In 1938, therapeutic ultrasound was first considered for use on humans when Ziess began to study the effects of ultrasound on the eye [2]. Now, therapeutic ultrasound is used in clinics and physical therapy centers around the world to treat a wide array of diseases ranging from prostate cancer to kidney stones to plantar fasciitis. The main advantage to using ultrasound as a therapeutic is that it can produce clinical effects on tissues deep inside the body without damaging the intervening tissue. Additionally, ultrasound has the advantage of being a real-time imaging modality that is relatively inexpensive and can be extremely portable. These traits make ultrasound especially useful for space travel, battlefield care, and in developing countries.

The most well-known use of ultrasound is for fetal imaging; however, new and widespread therapies are in various stages of development. While many of the therapeutic effects of ultrasound are elicited by some degree of hyperthermia (mild or extreme), other therapies utilize bubbles, a so-called mechanical effect of ultrasound, to interact with the tissues. Bubbles can be used to enhance drug delivery through the formation of transient pores in the cell membrane [2]–[4]; can aid in the breaking of kidney stones in shock wave lithotripsy (SWL) [5]–[7]; and can be used to emulsify cancerous tumors or other unwanted tissues in cavitation cloud and boiling histotripsies [8]–[11]. However, the same bubbles that aid in breaking kidney stones can also cause significant damage to the kidney, which is why bubble damage is a concern in every ultrasound application, including fetal imaging [12]. Because of this, all clinical machines must display the Mechanical Index, an indicator of the likelihood of cavitation

[13], [14]. The lack of information as far as how bubbles interact and cause damage to tissue has made it difficult for the FDA to establish safety guidelines for therapeutic ultrasound, thus creating an additional barrier for researchers to overcome when transitioning a device from developmental stages to the clinic. Whether the aim is to emulsify tumors or image a fetus, identifying the levels at which ultrasound causes damage to tissues in addition to understanding how bubbles in an ultrasound field can damage tissue is important for all ultrasound applications and is the goal of the research presented here.

1.2. Background

1.2.1 Therapeutic Ultrasound

Therapeutic ultrasound, or the use of ultrasound for purposes other than imaging or diagnostics, acts on cells and tissues by thermal and mechanical mechanisms. Ultrasound-enhanced drug delivery uses these mechanisms to cause bio-effects that can improve targeting and delivery of chemotherapeutic agents [3], [15]. Physical therapists use therapeutic ultrasound to reduce pain and promote soft tissue healing, although there is still debate as to whether the bioeffects of ultrasound are beneficial [16]. Therapeutic ultrasound has also been used to treat glaucoma and tumors in the eye [17] and has been used for applications such as tissue fractionation, renal stone fragmentation, tissue cauterization, and wound healing acceleration [2], [18], [19]. One of the greatest advantages of therapeutic

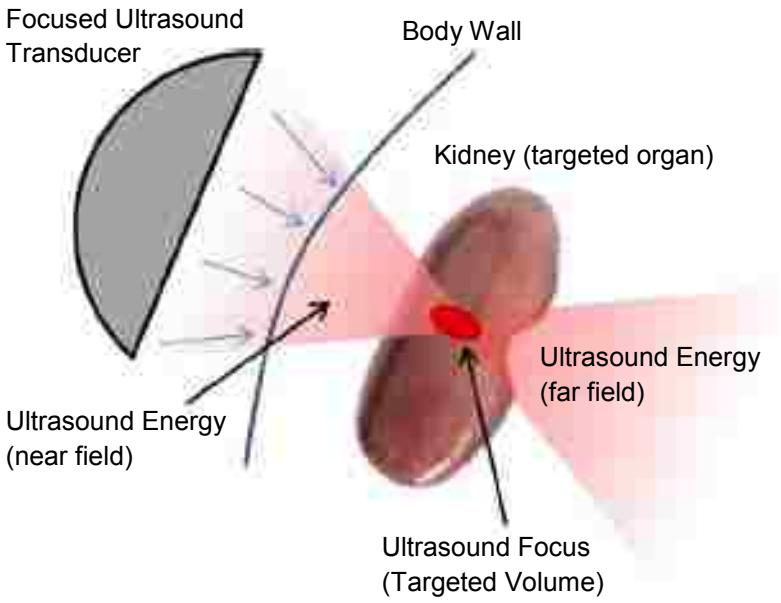

FIGURE 1.1: Focused ultrasound schematic, showing the well-defined treatment volume at the focus. Tissue in the near and far field will be unaffected by the ultrasound.

ultrasound, is its ability to be focused into a small, well-defined target region in the body and produce clinically significant effects without damaging the intervening tissue as shown in figure 1.1 [2], [3], [18]–[20]. Therapeutic ultrasound is often broken down into three categories: high intensity focused ultrasound (HIFU), shock wave lithotripsy (SWL), and drug delivery. While HIFU is the focus of this work, SWL and ultrasound-enhanced drug delivery will be briefly described here for completeness.

High Intensity Focused Ultrasound (HIFU)

A subset of focused ultrasound, high intensity focused ultrasound (HIFU) has been used to thermally necrose tumor tissues and cauterize blood vessels [2], [3], [18], [20]. In the well-defined HIFU focal volume, tissue absorption of the intense acoustic waves causes localized heating and protein denaturation [2], [3], [18], [19]. Guidance and monitoring of HIFU therapies are generally accomplished with B-mode ultrasound, x-ray, or magnetic resonance imaging (MRI) [2], [18]. While HIFU is already being clinically used to treat benign prostate hyperplasia and prostate cancer, clinical trials are underway for the treatment of breast cancer, uterine fibroids, and other tumors [21]–[25]. Intensities used in conventional HIFU therapies are generally 1000-10,000 W/cm^2 at the focus, which heats the tissue in a matter of seconds and causes local cell death through coagulative necrosis [2], [18].

An alternative to tissue denaturation is a mechanical version of HIFU that has the ability to cut through the heart septum [26] and to fractionate tissue by pulsed ultrasound cavitation or shock wave heating and millisecond boiling [8], [10], [11], [27]. These techniques utilize bubbles to fractionate tissue into submicron-size fragments (i.e. no remaining cellular structures), with sharp boundaries between the treated and untreated tissues. Histotripsy, or pulsed ultrasound cavitation therapy, fractionates tissue at the focus using microsecond pulses at very high acoustic pressures and pulse-repetition frequencies (PRFs) to create and maintain a cavitation bubble cloud on the order of several millimeters in size, composed of bubbles on the order of hundreds of microns in diameter [8], [10], [28]. On the other hand, shock wave heating and millisecond boiling, hereafter denoted as boiling histotripsy, uses millisecond pulses and lower PRFs, and acoustic pressures than cavitation cloud histotripsy to explosively expand a millimeter-

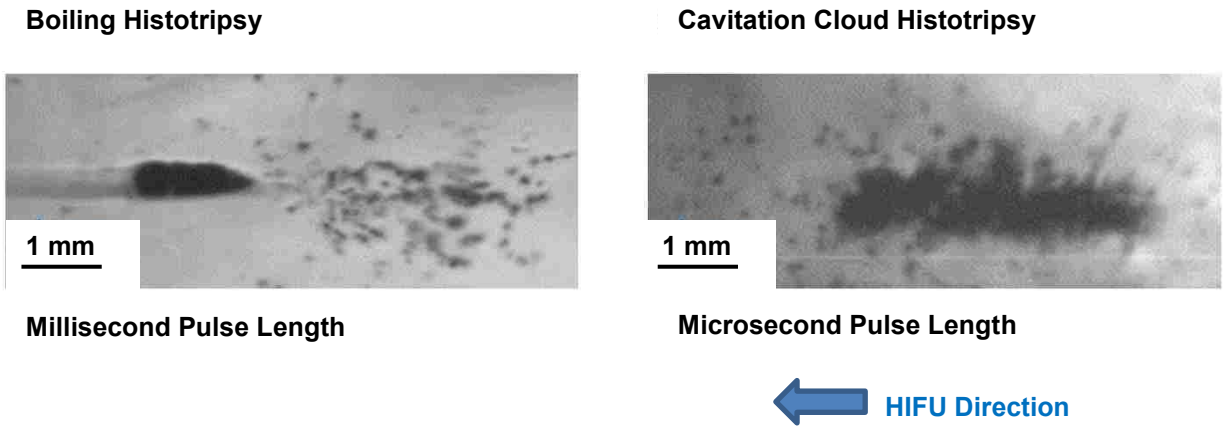

FIGURE 1.2: Images of the bubble patterns for (left) boiling histotripsy and (right) cavitation cloud histotripsy in a tissue-mimicking polyacrylamide gel. In boiling histotripsy, a millimeter-size boiling bubble explosively expands at the transducer focus, and cavitation bubbles form pre-focally. In cavitation cloud histotripsy, many cavitation bubbles of tens to hundreds of microns in diameter form a bubble cloud several millimeters in size.

size boiling bubble at the focus and fractionate tissue [11], [27]. Figure 1.2 shows the differences in the bubble fields between cavitation cloud histotripsy and boiling histotripsy in a tissue-mimicking polyacrylamide gel. While high-speed photography allows us to visualize the bubble fields for both types of histotripsy, it is unclear how millimeter-size boiling bubbles or cavitation bubble clouds can fractionate tissue into submicron-size fragments.

Shock Wave Lithotripsy (SWL)

SWL has been approved for clinical use in the US since 1985 to break kidney stones [29]. Lithotripters generate single, microsecond long shock waves outside the body which are focused to a fixed location. These shock waves are repeated thousands of times at 1-2 Hz to break the stone. SWL remains the principal treatment for kidney stones [30], despite increasing evidence that SWL causes significant damage to the kidney [31]–[35]. Cavitation, or bubble activity, has been shown to be necessary to break the stone; however cavitation also causes hemorrhagic lesions in the kidney [5]–[7], [36]–[38]. Additionally, after SWL, stone fragments often remain in the kidney, (especially in the lower pole because spontaneous stone clearance is rare due to gravity), which can act as nuclei for the formation of new stones [39]–[41]. The

fragments remaining in the lower pole after SWL has prompted the development of an ultrasonic propulsion device to move these fragments from the lower pole to the exit of the kidney [42]–[45].

Ultrasound-Enhanced Drug Delivery

Ultrasound-enhanced drug delivery uses the thermal and mechanical mechanisms of ultrasound to produce bio-effects that can improve targeting and delivery of chemotherapeutic agents. Generally, the intensity and frequency of ultrasound used to enhance drug delivery is lower than the intensity level of HIFU [2]–[4]. The only FDA-approved method for ultrasonically enhancing drug delivery is sonophoresis, which uses ultrasound transdermally to facilitate transport of drugs through the skin and into soft tissues and blood vessels [3], [46].

1.2.2. Ultrasonic Atomization

Ultrasonic atomization, or the emission of fine droplets from an acoustically excited thin liquid film exposed to air, has been the basis for commercial products such as air humidifiers and medical nebulizers. A well-known phenomenon since the landmark experiment by Wood and Loomis in 1927 [47], atomization can arise from either a plane or focused ultrasound wave in liquid encountering air. Tjan and Phillips have also suggested that atomization may play a role in lung tissue injury at diagnostic ultrasound levels [48], [49]. Even though ultrasonic atomization of liquids is well-known, the mechanism of atomization has not been fully elucidated.

Mechanism of Atomization in Liquids

While several hypotheses emerged primarily in the 1960's to explain atomization from plane and focused ultrasound waves, researchers have been unable to reach a consensus to describe the mechanism of atomization in liquids. The first hypothesis to explain atomization emerged in 1936, as a result of Söllner's series of experiments atomizing liquids of varying viscosity under decreased pressure and elevated temperature conditions [50]. This hypothesis was called the cavitation hypothesis, and described atomization as the emission of droplets from the violent collapse of bubbles.

However, Bisa, Dirnagl, and Esche observed the particle size distribution from atomization in a fountain and proposed an alternative hypothesis – a capillary-wave hypothesis [51], [52]. In the capillary-wave hypothesis, the liquid surface is parametrically excited with capillary waves at one-half the excitation frequency [53], [54]. As the surface continues to be sonicated, the capillary waves increase in amplitude until they become unstable, at which point small droplets pinch off from the crest of the waves (*i.e.* atomization) [52]. Experimental evidence published by Lang and theoretical studies by Peskin and Raco support the capillary wave hypothesis because of the strong relationship between the ultrasonic frequency (or indirectly the capillary wavelength) and the droplet diameter [55], [56]. Yet Antonevich concluded, based on high-speed experimental observations for low frequency planar ultrasound waves, that atomization was a combination of cavitation bubble collapses and capillary wave instabilities [57]. Antonevich further suggested that the size of the emitted droplets depends on the mechanism of release, with capillary waves producing the fine spray composed of droplets of consistent diameters and cavitation bubble collapse producing the larger droplets [57]. The end result of Antonevich's work is the cavitation-wave hypothesis of atomization, the most accepted hypothesis to describe atomization.

Several iterations of the cavitation-wave hypothesis exist for both plane and focused ultrasound waves and are shown graphically in figure 1.3 [53], [58]. One interpretation of the hypothesis for a plane ultrasound wave encountering a liquid surface, is that capillary waves are parametrically excited on the liquid surface at ½ the ultrasonic frequency. As the capillary waves grow in size, cavitation bubbles form within the peaks due to the focusing of the waves inverted from the pressure release liquid-air surface. The collapses of the cavitation bubbles along with the unstable cusps from the capillary waves cause droplets to pinch off in atomization. An interpretation for the cavitation-wave hypothesis of atomization from a focused ultrasound wave aligned with a liquid-air interface begins with radiation force from the focused wave bulging the liquid surface. The bulge on the surface focuses the ultrasound waves inverted by the pressure release interface, creating numerous cavitation bubbles within the bulging volume. Oscillations and collapses of these cavitation bubbles enhance microscale surface perturbations (capillary-waves) and facilitate the pinch-off of droplets (atomization).

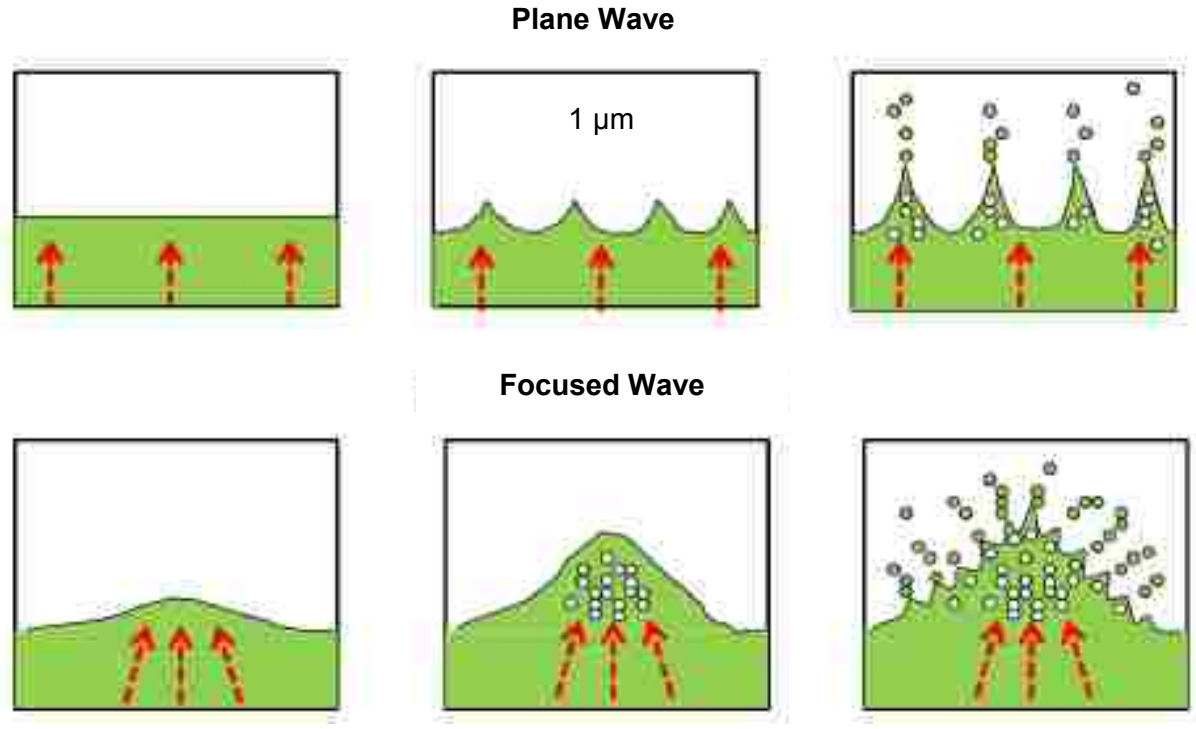

FIGURE 1.3: Schematic depicting the cavitation-wave hypothesis from (upper) a plane ultrasound wave and (lower) a focused ultrasound wave encountering a liquid-air interface. In the upper sequence of images, the plane wave parametrically excites capillary waves on the surface, which along with cavitation bubbles beneath the surface, become unstable and droplets pinch off in atomization. In the lower sequence of images, the focused wave bulges the liquid surface, focusing the wave inverted from the pressure release interface and causing cavitation bubbles to form. The cavitation bubbles along with capillary waves facilitate the pinch off of droplets (atomization).

While none of the three hypotheses (cavitation, capillary-wave, cavitation-wave) has been fully accepted by researchers, the cavitation-wave hypothesis seems to most accurately describe what is observed in liquid fountains formed by focused ultrasound [59]–[61].

1.3. Scope

The primary objective of this work is to increase our understanding of the thresholds and mechanisms of tissue injury by focused ultrasound. We begin by studying the mechanism of injury for one specific application of therapeutic ultrasound, namely tissue fractionation by boiling histotripsy (Ch. 2). After concluding that atomization is the mechanism of boiling histotripsy, we then consider the tissue properties that affect

atomization (Ch. 3) and the mechanism of atomization (Ch. 4). By developing an understanding of how atomization occurs and what properties influence atomization, we hope to be able to explain why boiling histotripsy is at times unsuccessful in fractionating tissue as well as develop techniques to make fractionation successful when it otherwise might not be. Besides exploring the mechanism of boiling histotripsy, we also evaluated the threshold for renal injury by focused ultrasound as there are many potential therapeutic applications of ultrasound in the kidney (Ch. 5). While this work is primarily experimental in nature, we include calculations as necessary to support our observations.

In Chapter 2, we test the hypothesis that ultrasonic atomization is the mechanism of tissue fractionation in boiling histotripsy. Previously, we noted that boiling histotripsy uses HIFU to superheat the tissue at the focus and produce a millimeter-size boiling or vapor bubble in several milliseconds which somehow fractionates the tissue into its submicron components [11], [27]. Here we conducted experiments to show that tissue can behave as a liquid such that a miniature acoustic fountain forms and atomization occurs within the millimeter-size vapor bubble produced by boiling histotripsy. High-speed photography was used to show that atomization and fountain formation occurs similarly in liquids and tissues. Gross observations of the tissue surface along with histology confirmed that the tissue is broken down into its submicron components.

After establishing atomization as the mechanism of tissue fractionation in boiling histotripsy, we wanted to determine which tissue properties affect atomization. In Chapter 3, we test the hypotheses that tissue wetness influences atomization and that atomization occurs similarly in *in vivo* and *ex vivo* tissues. We began by analyzing atomization and surface erosion in a wide range of tissues, gels, and fruits with different mechanical properties. Then, we submerged the tissue in a variety of solutions with varying salt and sugar concentrations to evaluate whether tissue wetness influenced atomization. Finally, we attempted atomization *in vivo* in a porcine animal model and compared the results to our *ex vivo* atomization experiments. The results from these experiments helped us begin to define a successful parameter space for atomization and hence, boiling histotripsy.

In order to be able to explain why some tissue will atomize and others will not, we needed to understand the mechanism of atomization. In Chapter 4, we test the hypothesis that bubbles are necessary for the atomization of liquids and tissues. Using high speed photography, atomization was observed in water and other liquids at various ultrasonic frequencies and acoustic intensities. After improving our understanding of atomization in liquids, we used high speed photography and B-mode ultrasound to observe atomization above and below the surface of viscoelastic solids. Then, to evaluate the necessity of bubbles, atomization was repeated in water and tissue under high static pressure conditions. The end result of this chapter was an improved understanding of how bubbles influence atomization in liquids and tissues.

In Chapter 5, the focus changes from boiling histotripsy and atomization to determining a threshold for renal tissue injury from therapeutic ultrasound. The motivation behind this work was to determine the safety of a novel ultrasonic propulsion device to reposition kidney stones. In the first study, 2 MHz focused ultrasound was applied directly to the kidney and three injury thresholds were established: one at a fixed 3.3% duty cycle with varying intensities; one at a fixed 100% duty cycle with varying intensities; and one at a fixed 9300 W/cm^2 intensity with varying duty cycle. In the second study, kidneys were analyzed after the ultrasound propulsion device was used transcutaneously to reposition stones that were implanted into porcine kidneys. In the final study, the long-term safety of the ultrasonic propulsion device was established by collecting and analyzing the tissue, blood, and urine one week after the ultrasound exposure. The results from these studies indicate that there exists a range of intensities above diagnostic levels but below tissue injury levels in which ultrasound can be used therapeutically. These studies were included in the Investigational Device Exemption (IDE) application to the FDA, to demonstrate the safety of the device before starting clinical trials.

CHAPTER 2:

Ultrasonic Atomization is the Mechanism of Tissue Fractionation in Boiling Histotripsy[1]

2.1. Introduction

Ultrasonic atomization, or the emission of droplets from an acoustically excited thin liquid film exposed to air, was first reported by Wood and Loomis [47]. More recently, McCubbin investigated the size of the droplets in the fog produced in a fountain formed by focused ultrasound [62]. Since then, ultrasonic atomization has been the basis for many air humidifiers and medical nebulizers and has been proposed to play a role in tissue injury in the lungs by diagnostic ultrasound [48], [49]. The main hypothesis of this chapter is that atomization and fountain formation by high intensity focused ultrasound (HIFU) occurs similarly in liquids and tissues. A further hypothesis is that tissue fractionation by HIFU is a result of atomization and fountain formation. This chapter reports experimental observations of these phenomena for planar interfaces and small cavities of tissue-air.

Acoustic atomization has been described by both cavitation and capillary-wave theories [53], which are described in detail in Ch. 1. The most accepted mechanism of ultrasonic atomization in liquids is the cavitation-wave hypothesis, which says a combination of cavitation and capillary waves cause atomization [53]. Several iterations of this hypothesis exist based on the results of Antonevich and Boguslavskii and

[1] Work published in part in:

Simon J, Sapozhnikov O, Khokhlova V, Wang Y-N, Crum L, and Bailey M (2012). "Ultrasonic atomization of tissue and its role in tissue fractionation by high intensity focused ultrasound," Phys. Med. Biol. 57, 8061-8078.

Simon JC, Sapozhnikov OA, Khokhlova VA, Wang Y-N, Crum LA, Bailey MR (2012). "Tissue atomization by high intensity focused ultrasound." IEEE International Ultrasonics Symposium Proceedings, Dresden, Germany October 7-10, pp. 1003-1006.

Éknadiosyants [57], [58]. One interpretation of the cavitation-wave hypothesis is that radiation force from the focused transducer causes the liquid surface to bulge, which focuses the waves inverted by the pressure release surface and causes numerous cavitation bubbles to form in the bulged volume of liquid. Oscillation and collapse of the cavitation bubbles enhance microscale surface perturbations (capillary waves), causing droplets to pinch off in atomization.

HIFU, which is also described in more detail in Ch. 1, has been used clinically to thermally coagulate tissue in a well-defined focal volume [2], [20]. An alternative to tissue denaturation is a mechanical version of HIFU that has the ability to cut through the heart septum [26] and to fractionate tissue by pulsed ultrasound cavitation or shock wave heating and millisecond boiling [8], [27], [63], [64]. Histotripsy, or pulsed ultrasound cavitation therapy, uses microsecond pulses at high pulse-repetition frequencies (PRFs) and acoustic pressures (peak positive pressure (p_+) of $p_+ > 80$MPa and peak negative pressure (p_-) of $p_- < 20$ MPa in water) to maintain a cavitation bubble cloud on the order of several millimeters in size, composed of bubbles on the order of hundreds of microns in diameter, which homogenizes the tissue in the focal volume [8], [28], [63]. On the other hand, shock wave heating and millisecond boiling, hereafter denoted as boiling histotripsy, uses millisecond pulses, low PRFs, and lower acoustic pressures than cavitation cloud histotripsy (peak pressures of $p_+ > 40$ MPa and $p_- < 10$ MPa in water) to explosively expand a millimeter-size boiling bubble at the focus and fractionate tissue [27], [64]. The end results of cavitation and boiling histotripsies are submicron-size tissue fragments [8], [65]; however, it is unclear how large (millimeter-size) boiling bubbles or cavitation bubble clouds create submicron-size tissue pieces.

The goal of this chapter is to present experimental evidence that acoustic atomization and fountain formation together form a possible mechanism by which the large, millimeter-size bubbles in boiling histotripsy produce submicron-size tissue fragments. To compare liquid and tissue fountains and atomization, flat interfaces between air and either a liquid or tissue were exposed to HIFU and filmed with high-speed videography. By modifying HIFU amplitudes, timing protocols, and number of pulses, the thresholds of atomization were established for several tissues. To relate to boiling histotripsy, the

possibility of atomization within a millimeter-diameter tissue-air interface was established. At the end of each exposure, the dimensions of the resulting tissue crater were measured and the volume of eroded tissue was calculated. An important result is an experimentally-tested mechanism of tissue fractionation by HIFU, which may lead to safer and more efficient tissue homogenization as the histotripsy techniques move to the clinical regime.

2.2. Methods

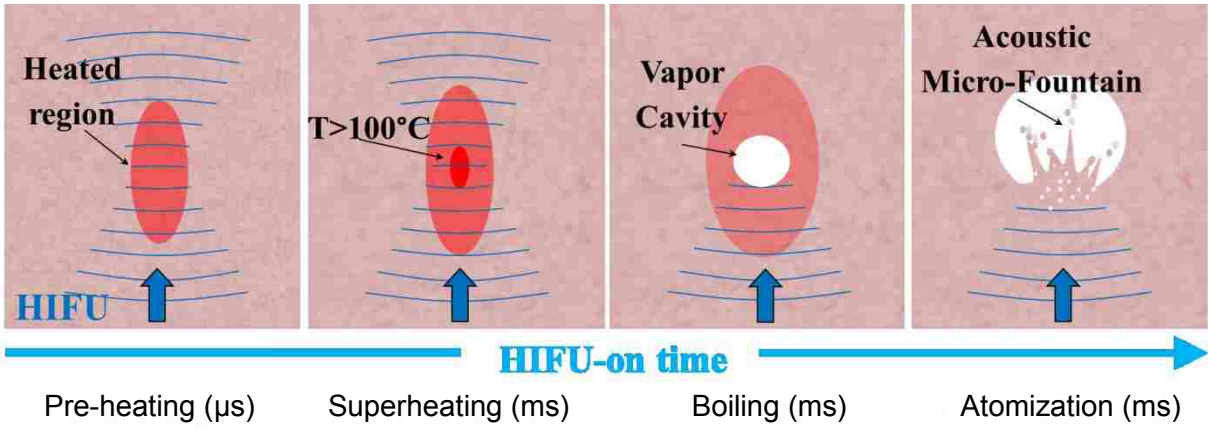

FIGURE 2.1: Proposed mechanism of tissue fractionation by boiling histotripsy.

Figure 2.1 illustrates the proposed mechanism of tissue fractionation in boiling histotripsy. As was stated previously, the tissue at the focus is heated rapidly, such that a millimeter-size boiling bubble is formed at the transducer focus in a predictable time [27]; however, it is unclear how the millimeter-size boiling bubble can produce submicron-size tissue fragments [64]. Some suggested mechanisms of tissue fractionation include explosive growth of a boiling bubble and tissue spallation due to reflection of a shock wave from the boiling bubble or bubble cloud with corresponding increases in negative pressure close to the interface [63], [64]. The idea proposed here is that the vapor-filled boiling bubble will be of sufficient size to act as a pressure-release interface, such that a miniature acoustic fountain will form and atomization will occur within the boiling bubble. In addition, atomization will be the process by which the large boiling bubble fractionates the tissue into submicron-size fragments. To experimentally test whether reflection from the bubble is similar to reflection from a flat

pressure-release interface, a cylindrical hole will be bored through tissue. While the cylindrical hole is not equivalent to the spherical bubble created by boiling histotripsy in bulk tissue, the hole allows for observation while maintaining a similar curvature in 2 dimensions as the boiling bubble shows in 3 dimensions. To reiterate, these experiments will begin with an existing void that simulates the void made by boiling in the more clinical case (*i.e.,* in bulk tissue). Then, as in the boiling histotripsy case, the void will continue to be insonified and the interaction between the focused sound and the void will fractionate the tissue.

2.2.1. Acoustic Characterization and Exposures

For all experiments in this chapter, the ultrasound transducer used was an air-backed, single-element, spherically focused piezoceramic crystal (PZ 26, Ferroperm Piezoceramics, Kvistgaard, Denmark), with an operational frequency of 2.165 MHz mounted in custom-built polycarbonate housing. A function generator (Model 33250A, Agilent, Palo Alto, CA, USA) and a linear radiofrequency (RF) amplifier (55 dB Gain, Model A300, ENI, Rochester, NY, USA) were used to drive the transducer. The diameter and radius of curvature of the transducer was 45 mm. Before the experiments, a fiber-optic probe hydrophone (FOPH 2000, RP Acoustics, Leutenbach, Germany) with 100-μm active diameter was used to measure the focal pressure waveforms in water. A similar transducer, with a slightly different operational frequency and housing, was thoroughly characterized in Canney *et al.* and used in previous boiling histotripsy studies [27], [64], [66].

Measurements were conducted in filtered and degassed room temperature (~20° C) water for increasing power outputs. A force balance was built in-house with a brush absorber, an Acculab VI-3mg scale (Columbia, MD, USA), and was controlled with Labview (National Instruments, Austin, TX, USA) programming. The measurements were conducted to ensure that power increased quadratically with voltage. Peak positive and peak negative pressures were obtained from pressure waveforms measured at the focus; focal intensities (I_L) were linearly scaled from low output measurements [66] and are reported in figure 2.2. The maximum acoustic output of the

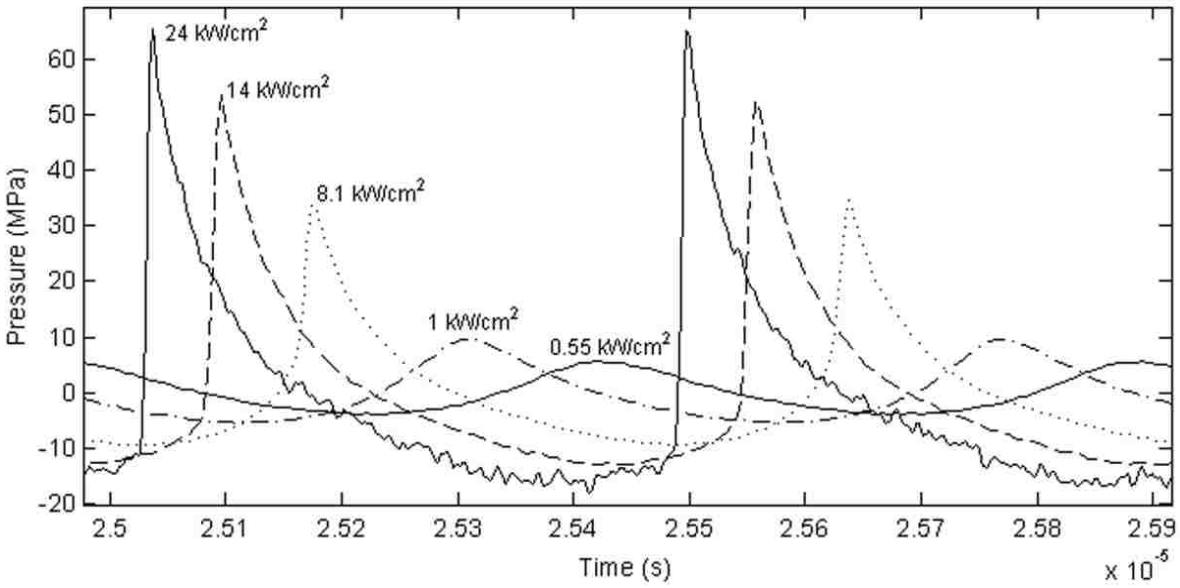

FIGURE 2.2: Waveforms with calculated linear intensities corresponding to select experimental conditions for the 2.165 MHz transducer.

transducer in water (figure 2.2) corresponds to an intensity at the focus of approximately I_L = 24,000 W/cm^2, with p_+ = 65 MPa and p_- = 16 MPa.

These measurements in water were translated to tissue using the previously developed derating methods for nonlinear high intensity focused ultrasound waves [27], [64], [67]. Briefly, the *in situ* intensities and peak pressures at the focus in tissue for a given output of the transducer corresponded to those measured in water for some lower power output. The scaling factor between outputs was calculated as exp(-2αL), where α is the attenuation coefficient in tissue at the operational frequency of the transducer and L is the tissue depth. As has been shown in previous studies, when the source outputs are scaled to account for linear attenuation losses in tissue, then both the peak pressure levels and intensity at the focus as well as the degree of nonlinear waveform distortion are similar in water and tissue [27], [64], [67]. Figure 2.2 shows the waveforms corresponding to the various experimental conditions.

For this study, an exposure consisted of one or several 10-ms pulses repeated at a 1 Hz pulse repetition frequency as in the previous boiling histotripsy studies [64]. All experiments were conducted at room temperature (~20°C) with water filtered to remove

particulates larger than 5 μm and degassed with a Liqui-Cel Extra-Flow 2.5 x 8 Membrane Contactor with the X50 fiber (Membrana, Charlotte, NC, USA) to less than 20% of saturation as measured with a dissolved oxygen meter (WTW Oxi 330i, Weilheim, Germany).

2.2.2. Experiments with a Plane Interface

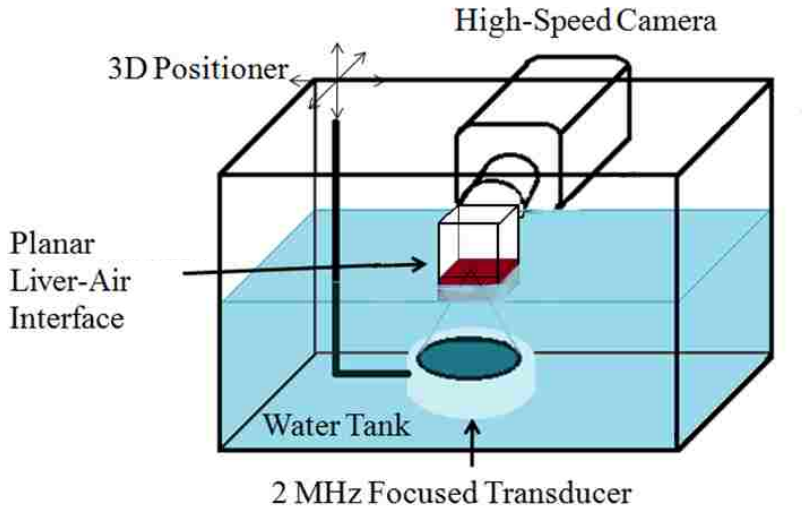

FIGURE 2.3: Macro experimental setup showing the planar tissue-air interface. Experiments are backlit (not shown).

The experimental arrangement for interrogation of liquids or flat tissue interfaces at the macro scale is displayed in figure 2.3. Tissue was placed at the focus of the transducer and filmed with a Photron APX-RS high speed camera (monochrome, Photron, San Diego, CA, USA). Liquids were held in a custom-designed container with an acoustically transparent, thin plastic film bottom; tissues were held in a similar plastic holder without the plastic film. To fit the container, the tissue was cut into pieces approximately 5.5 cm x 5.5 cm with a depth varying between 1 cm and 1.5 cm. The container was placed in water such that the bottom of the container was positioned just below the water surface. The thickness of the liquid layer was variable between 2-15 millimeters. The transducer was focused at the water or tissue surface using pulse echo with the timing recorded on a digital oscilloscope (Model LT432, Lecroy, Chestnut Ridge, NY, UA). The Photron high-speed camera was operated at 20,000 frames per second with a resolution of 256x512 pixels. A Carl Zeiss lens (Makro-Planar T* 2/100, Thornwood, NY, USA) with a bellows extension was used to provide a resolution on the order of 40 μm/pixel. A continuous, disperse light source

(Photogenic PowerLight 2500DR, Bartlett, IL, USA) positioned at an angle slightly off axis from the camera lens was used to backlight the water to air or tissue to air interface.

2.2.3. Experiments with a Bubble-Mimicking Interface

Figure 2.4 shows the experimental arrangement used to determine if tissue would atomize at a curved, millimeter-diameter, bubble-like interface. The same camera and acoustic equipment were used as has been described above; however, the tissue was prepared and held differently. The tissue was sectioned into samples approximately 8 cm x 8 cm x 2.5 cm and mounted into a custom-made holder that would suspend the tissue without interference to the acoustic field. Biopsy punches of 1-3 mm diameter were used to bore through the 2.5 cm of tissue at a position approximately 1.5 cm from the bottom surface of the tissue, creating a cylindrical tunnel. The transducer was focused at the bottom surface of the cylindrical tunnel using the pulse-echo technique.

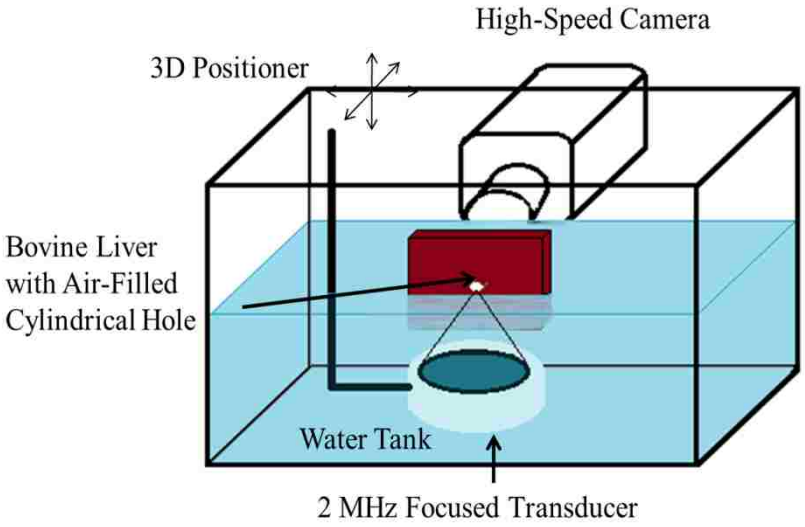

FIGURE 2.4: Macro experimental setup showing the cylindrical tunnel, a 2-dimensional bubble-like tissue-air interface. Experiments are backlit (not shown).

2.2.4. Experiments with a Micro-Tissue Setup

To examine the contents of the jet more thoroughly, and to obtain a more precise estimate of the commencement time for atomization, a micro setup was used as is illustrated in figure 2.5. With the tissue surface under interrogation placed parallel to gravity, the surface was filmed through an inverted microscope (TE2000-U, Nikon Inc.,

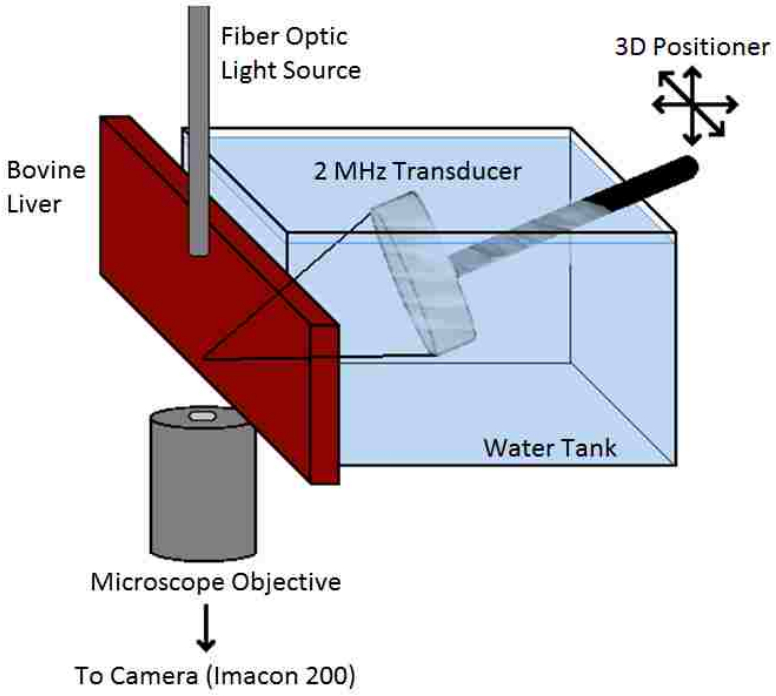

FIGURE 2.5: Micro experimental setup. The experiments are backlit.

Melville, NY, USA) with the Imacon 200 ultra-high-speed camera (DRS Hadland, Cupertino, CA, USA). The experiment was backlit with a fiber optic illuminator (Model 41500-50, Cole-Parmer Instrument Co., Vernon Hills, IL, USA) and positioned just in front of the tissue surface. The transducer was driven by a function generator (Model AFG3022B, Tektronix, Beaverton, OR, USA) and a linear RF amplifier (55 dB Gain, Model A150, ENI, Rochester, NY, USA). Because of space constraints, the transducer was positioned at 45° with respect to the tissue surface. As before, the transducer was focused at the surface using the pulse echo technique. For this experimental arrangement, the tissue was sectioned into samples of approximately 8 cm x 3 cm with a depth of 1 cm and placed under tension in a custom-designed tissue holder.

2.2.5. Tissue Preparation and Analysis

Two different biological samples were used in these experiments: bovine liver and porcine blood clots. Bovine liver was purchased from a local abattoir (Schenk Packing, Stanwood, WA, USA) and used within 8 hours of harvesting. The liver was kept on ice until arrival at the lab, where it was cut into the sizes specified for each experimental arrangement, taking care not to include blood vessels in the sample. The liver capsule was not present on the interrogated surface and surface imperfections such as vessels and kerf marks were avoided. After cutting, the liver was immersed in phosphate

buffered saline (PBSaline) and degassed for approximately one hour on ice in a desiccant chamber of -85 kPa. For nonlinear derating calculations in liver, the attenuation coefficient used was α=0.7 dB/cm/MHz [27].

Porcine blood clots were exposed to the experimental conditions as an intermediary between tissue and liquids. Blood was collected from a terminal porcine study conducted at the University of Washington and then placed in a holder and allowed to clot for approximately one hour at room temperature. Once the clot had formed, it was moved to the custom-designed holder described previously for the flat macro setup shown in figure 2.3. For nonlinear derating calculations in blood clots, the attenuation coefficient used was α=0.93 dB/cm/MHz [68].

Sizes of the emitted droplets and distances between jets were calculated from analysis of the high speed videos. In addition, calipers were used to measure, to the nearest half-millimeter, the erosion depth along with the horizontal and vertical diameters (with respect to the tissue piece) for the plane tissue-air interface (figure 2.3). The volume of eroded tissue was calculated assuming the shape of the eroded volume approximated a spherical cap. Furthermore, fountained and atomized tissue projectiles were collected from the micro setup by placing a glass slide beneath the fountain. The collected projectiles were allowed to dry on the slide, stained with Hematoxylin and Eosin (H&E), and analyzed using light microscopy.

2.3. Results

2.3.1. Plane Interface

To compare the observations from liquids to tissue, figure 2.6 depicts bovine liver and water at intensities just above their respective thresholds (I_L = 8,100 W/cm^2; p_+ = 35 MPa, p_- = 9.2 MPa derated in liver, I_L = 550 W/cm^2; p_+ = 5.5 MPa, p_- = 4 MPa in water) where atomization occurs in a relatively repeatable manner. As we hypothesized, liver flowed as a liquid such that an acoustic fountain formed and atomization occurred at the tissue-air interface. Upon comparison of the two image sequences, it was evident that the free liver surface only partly mimicked the behavior of water. In liver, an initial small volume of fine spray was ejected from the flat liver surface shortly before the tissue

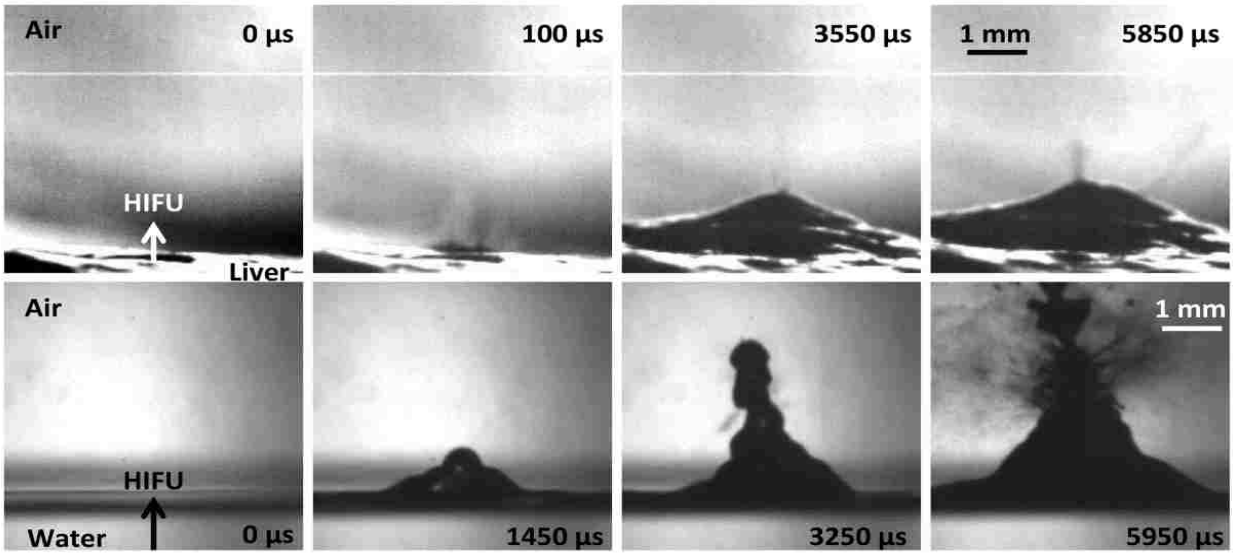

FIGURE 2.6: A direct comparison of liver (upper) and water (lower) at intensities slightly above their respective atomization thresholds (8100 W/cm^2 derated for liver and 550 W/cm^2 for water). In both cases, the first frame occurs 20 µs after the ultrasonic wave arrives at the interface. The second shows the initial spray of atomization in liver (upper) and the mound forming in water (lower) with no atomization. The third frame shows the small spray of atomization from the mound in liver and the first case of atomization for water; whereas the final frame shows atomization at its most significant. The timing is fairly similar between liver and water; the only difference is that liver has that initial spray of atomization before the mound forms and enhances atomization, while at this intensity water forms the mound before atomization occurs. In both cases, the total HIFU-on time was 10 ms.

started to bulge. As the acoustic pulse continued, the tissue mound became more distinct and more jets emerged, primarily from the top surface of the mound. In the course of one 10-ms pulse, the mound of liver reached 1.5 mm in height. The jets ejected from the liver surface at this intensity were fairly consistent in size with diameters in the 10s of microns range and velocities of approximately 13 m/s, although some of the initial jets reached velocities of 23 m/s. At this intensity, atomization began less than 70 µs after the acoustic wave-front arrived at the interface; however when the derated intensity at the focus was increased to the maximum of 14,000 W/cm^2, atomization was observable a minimum of 20 µs after the wave-front arrived at the surface. With each 10-ms pulse over the course of five pulses repeated at 1 Hz, atomization in liver becomes more dramatic, with an increasing number of jets being emitted from the surface. Conversely, in water (as shown in figure 4.6 (lower)) a fountain emerged first with a semblance of a drop-chain structure, but with no

atomization events occurring until the fountain was fully formed. As the water fountain propagated upwards, a few small atomization events occurred, the first of which was depicted in the third frame at 3.2 ms. However, once the first significant droplet collapse occurred, the fountain quickly degenerated into full-fledged atomization with jets emitted from the sides of the fountain. Interestingly, the jets from the side of the water fountain always emerged from a minimum of 1.2 millimeters above the surface of the water. Similar to liver, the velocity of the fine spray in water was approximately 12 m/s, with the droplets ejected from the water fountain varying in size from a few microns up to several hundred microns in diameter. A qualitative comparison between liver and water showed that the number of jets ejected from the water fountain greatly exceeded the number of jets ejected from the tissue fountain; however, in both cases, the formation of the mound substantially increased the number of emitted jets.

In a separate comparison, water and bovine liver atomization and fountains were imaged at the maximum *in situ* intensity of 14,000 W/cm^2. Figure 2.7 shows a series of frames taken in (a) water and (b) bovine liver. In water, significant atomization occurred by the second video frame. As the sonication continued, a bulge formed in the water surface and the number and size of the droplets emitted from the water surface increased until the camera field of view was almost completely obscured. However, in bovine liver a small spray of atomization was ejected by the third video frame, taken 120 μs after the ultrasound wave arrived at the interface. As in water, once a bulge formed in the liver surface, the number and size of ejected fragments increased significantly. The surface bulge took longer to form on the liver surface as compared to the liquid surface. Even at these intensities, the velocities of the projectiles and the overall size of the ejected fragments were comparable between water and bovine liver. Interestingly, the size of droplets emitted in bovine liver had a wider range of diameters at this intensity then at the previous 8100 W/cm^2 shown in figure 2.6. In this case droplet diameters ranged from 10s of microns to 100s of microns in diameter.

In an attempt to reconcile the differences observed between water and tissue fountains, blood clots were exposed to HIFU as an intermediary between tissue and liquid; blood clots form a protein network of fibrin without the structural proteins such as

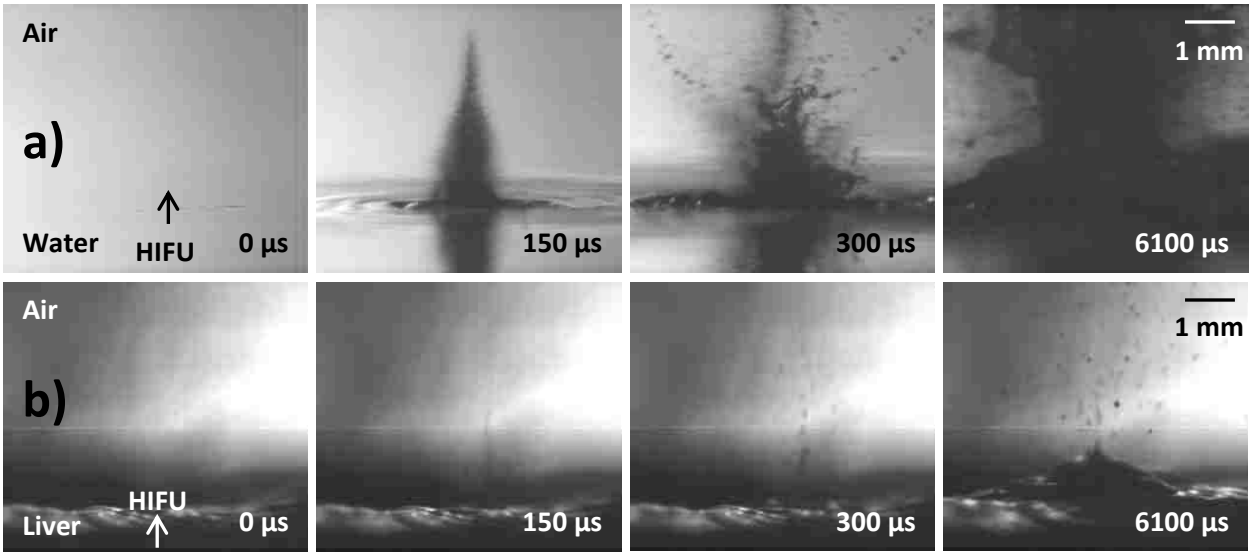

FIGURE 2.7: A high-speed photographic comparison between a) a water-air interface and b) a bovine liver-air interface for a 10-ms pulse at the maximum *in situ* intensity. The first frame in both instances is taken 20 µs after the ultrasound wave arrives at the surface. At 150 µs, the water shows well-developed atomization and height, while the liver surface shows only a couple of faint jets. At 300 µs, the water shows even more dramatic atomization with a larger average droplet size, while the bovine liver shows a slightly more developed surface spray. Finally, at 6100 µs into the 10-ms pulse, the amount of water being ejected from the surface has almost completely occluded the camera field of view, while in liver, a surface bulge has formed, which is accompanied by more dramatic atomization.

collagen and elastin that are present in tissues [69]. Figure 2.8 shows a blood clot exposed to I_L = 1000 W/cm^2 (p_+ = 8.7 MPa, p_- = 5.2 MPa) derated, an intensity above the atomization threshold. Here, the formation of the fountain looks like a hybrid between liver and water at intensities just above their respective atomization thresholds. Combinations of water and tissue fountain structures emerged; a drop chain formed well into the acoustic pulse (as was observed in the water fountain) from the top surface of a 0.4-mm high mound (similar to what was observed in the tissue fountain). The top droplet extended 1.5 mm above the surface of the blood clot after which the entire droplet detached from the blood clot. Jets were ejected from the blood clot at velocities of approximately 10 m/s. At these intensities, the initial spurt of atomization occurred more than 20 µs after the ultrasonic wave arrived at the interface. As in tissue, a short abatement of atomization occurred after the initial atomization spurt; once the mound formed, more significant atomization ensued. The initial spurt of atomization and the slight pause is thought to be due to excess liquid on the surface of the tissue, even

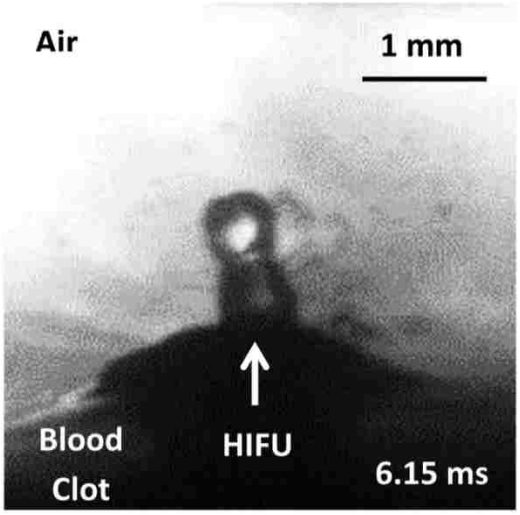

FIGURE 2.8: A drop-chain fountain emerging from the surface of a blood clot at 1000 W/cm^2, derated, an intensity just above the atomization threshold in blood clots. In this case, the total HIFU-on time was 10 ms.

though the tissue is carefully blotted with a paper towel before the exposure. The increase in atomization after the mound forms is likely due to the focusing of the waves reflected from the pressure release surface and the resulting increase in cavitation below the tissue surface.

2.3.2. Bubble-Mimicking Interface

Before atomization could be proposed as a mechanism for boiling histotripsy, it was necessary to show that the millimeter-size boiling bubble created by boiling histotripsy was large enough to act as a pressure-release interface similar to that seen when the plane tissue was interfaced with air (as in figure 2.6 upper, and 2.7(b)). Figure 2.9 shows atomization and fountain formation in a cylindrical, 2-dimensional bubble-like tunnel created in bovine liver at the maximum derated acoustic intensity of I_L = 14,000 W/cm^2 (p_+ = 53 MPa, p_- = 12.7 MPa). The size of the ejected fragments of a few microns up to several hundred microns in diameter and temporal progression of atomization were similar to what was seen with the flat liver-air interface. Jet velocities ranged from approximately 7.5 m/s for small, thicker jets up to 20 m/s for the long, thin, intermittently-released jets. At about 5 ms into the 10-ms pulse, the 1.5-mm diameter hole became occluded due to the formation of the tissue mound and the size and number of jets emitted from the tissue surface. Some pitting of the tissue was observed on the top surface of the tunnel, most likely due to the violent collision between the top tissue surface and the jets emitted from the lower surface. In addition, tissue erosion was observable on the lower surface of the cylindrical hole similar to what was seen on the flat tissue surface (see figure 2.10).

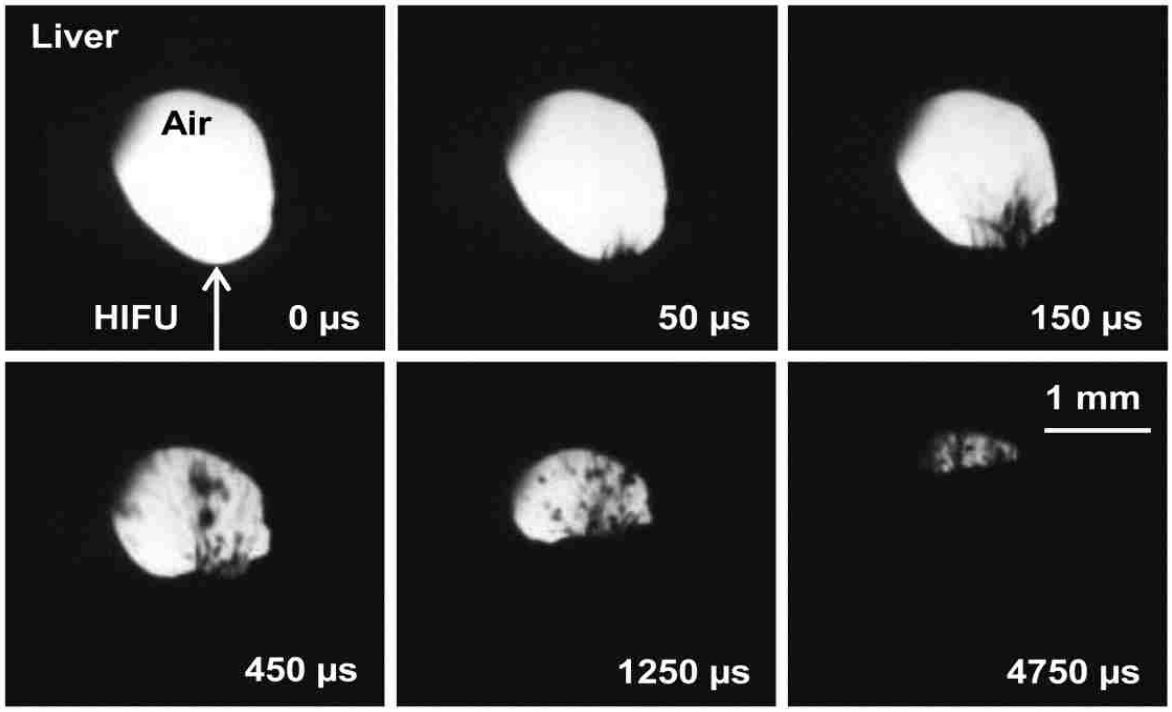

FIGURE 2.9: Cylindrical, bubble-like tunnel through bovine liver at linear intensity of 14,000 W/cm^2, derated. At this intensity, there is a spurt of atomization that becomes more pronounced as the mound forms in the tissue. After around 5 ms, the hole becomes occluded with the spray. In this case, the total HIFU-on time was 10 ms.

2.3.3 Tissue Fractionation

Thus far, it has been shown that atomization of tissue can occur; however, no evidence has been given that atomization of tissue results in the tissue fractionation that was observed in bulk cavitation cloud and boiling histotripsies [8], [64], [70]. Figure 2.10 shows erosion in a flat liver tissue surface from a varying number of 10-ms pulses at 1 Hz pulse repetition frequency. From the graph of erosion rate over time, it appears as if the volume of the hole is approaching saturation shortly after the number of 10-ms pulses exceeds 300. From the image of the tissue surface, it also appears that the surface dimensions (transverse to the ultrasound pulse direction) approaches saturation around 180 pulses; however from many experiments it was found that the depth of the hole continued to increase even up to 300 pulses and likely beyond, increasing the volume of eroded tissue.

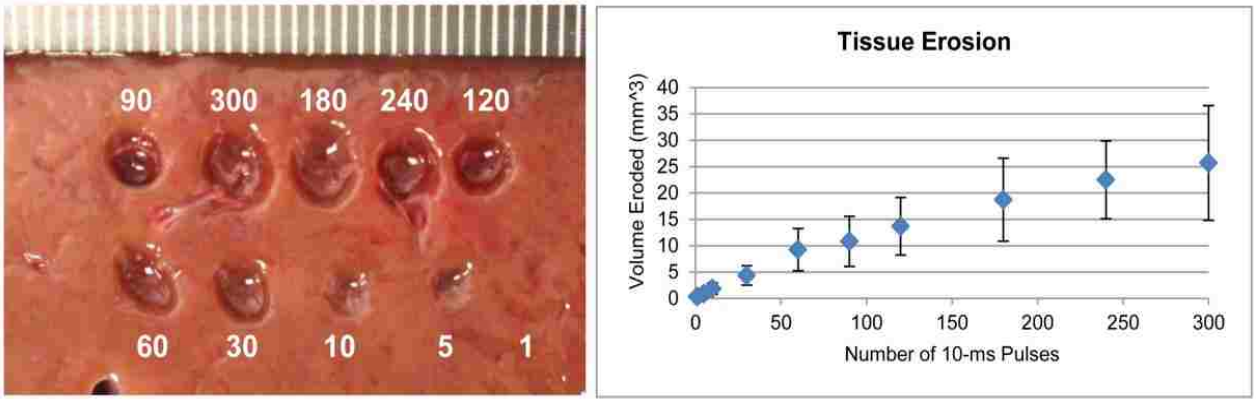

FIGURE 2.10: Left: Tissue erosion observed on the surface of bovine liver at the maximum acoustic intensity of 14,000 W/cm^2, derated, after a varying number of 10-ms pulses all at 1 Hz PRF. Right: A plot of the overall tissue erosion plotted as volume eroded per number of 10-ms pulses.

In order to look at the contents of the jets, the micro-setup described in figure 2.5 was used. Figure 2.11 shows two frames of a magnified view of several jets being emitted from the planar surface of bovine liver (I_L = 7100 W/cm^2 (derated); p_+ = 34 MPa, p_- = 8 MPa). From these images, it is clear that there is a large variation in the diameter of the jets. It is also evident in the jets on the right side of the frames that a fog is emitted (140 μs) slightly before the jet forms (260 μs), which is typical in the formation of jets.

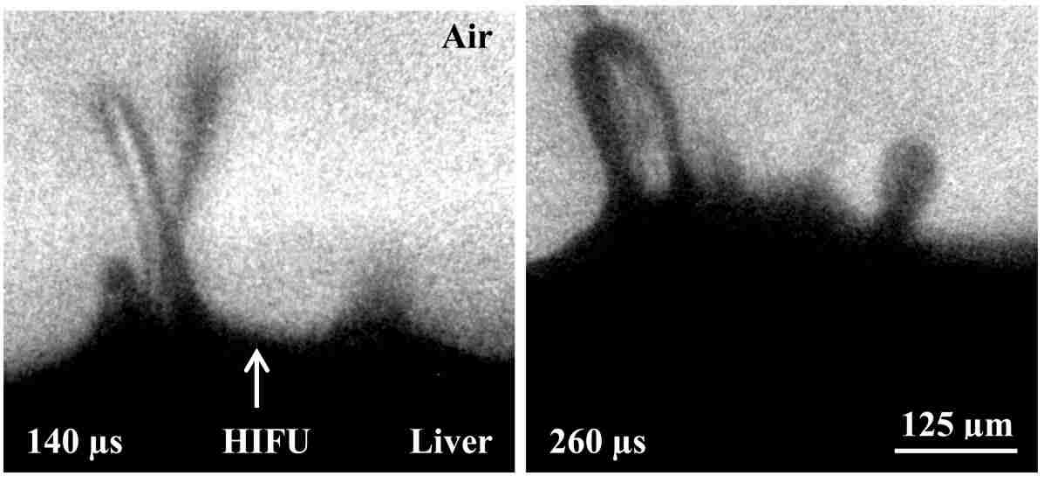

FIGURE 2.11: Magnified jets emitted from the surface of bovine liver. The jet(s) on the left side of each frame begin as thin streams and thicken over time. The jet on the right side of each frame shows how jets often start as the emission of a fog before developing into actual jets. In addition, the right frame shows more jets forming between the established jets. The total HIFU-on time was 10-ms.

Sometimes, jets combine from several smaller jets to produce a large jet, which is present on the left side of each frame. In addition, in the 260-μs frame, a fog is observed between the two mature jets, which may indicate the beginnings of new jets. The presence of several jets in the magnified frames is commonly observed. When the distance between jets is measured over many samples, an average center-to-center inter-jet distance emerges of 182±80 μm, which may be indicative of capillary waves on the tissue surface and could help elucidate the overall mechanism of tissue fractionation. Unfortunately the only equation for calculating the capillary wavelength is for liquids and it is expected that tissue elasticity will significantly change the expected wavelength; this equation is discussed further in Ch. 4. Furthermore, upon close examination of the left jet in the 260-μs frame, dark lines are observed within the jet. While this may just be due to light refraction, it could also be evidence of bubbles or eroded tissue within the jet.

The jet contents were collected by placing a microscope slide directly beneath the fountain in the micro-setup. An H&E stain of the fountain projectiles is shown in figure 2.12. This image contains whole and disrupted cells and nuclei. Cell clusters are often present, as is visible in the center of figure 2.12. Although these cells appear structurally intact, some of the nuclei show evidence of nuclear fading (karyolysis) indicating some damage. Dying single cells (black dashed circles) often show evidence of cell membrane disruption, chromatin condensation (pyknosis) and nuclear fragmentation (karyorrhexis). Red blood cells (white arrowheads) are also present. In addition, the insert shows an example of nuclear disruption and fragmentation (black arrowheads in the insert) that was observed throughout the sample. The presence of cells and nuclei was different from what was observed in histology of cavitation cloud histotripsy in bulk tissue, or for the same conditions used in the free tissue interface scenario (10-ms pulse, 1 Hz PRF) in boiling histotripsy of bulk tissue, where the cells and nuclei were completely homogenized such that no intact cells or nuclei remained [8], [65]. In addition, bubbles were found in many of the collected projectiles (black arrows), which could help elucidate the role of bubbles in tissue atomization. Modifying the pulse parameters, such as pulse repetition frequency, pulse length (down to 100 μs), and number of pulses did not significantly affect the appearance of whole cells and

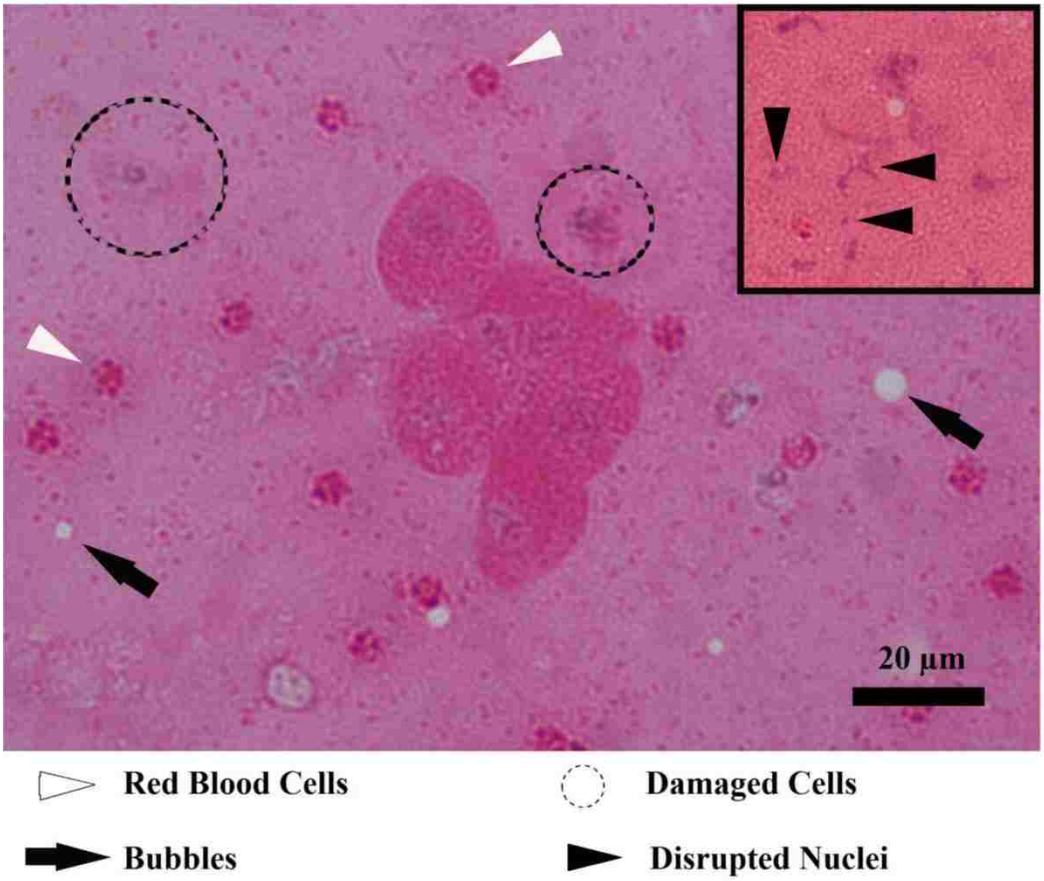

FIGURE 2.12: H&E stain of the collected fountain projectiles. In the center of the image, a cell cluster consisting of six whole cells is present. In addition, there are red blood cells (white arrowheads), damaged or dying cells (dotted circles), and vapor bubbles (black arrows). The insert shows smeared and fragmented nuclei (black arrowheads).

nuclei within the collected projectiles. The histological differences between atomization of a free tissue interface and bulk histotripsy, both cavitation cloud and boiling, need to be reconciled.

2.4. Discussion and Conclusions

The primary results from this study are that the application of HIFU to a tissue surface can result in the formation of a fountain and atomization, and that the result of this atomization is tissue erosion. However, tissue atomization and fountain formation does not entirely mimic what is typically seen in liquids. Tested parameters include: the acoustic threshold for atomization, the time for atomization to start, and the velocity of

the emitted jets. As expected, the threshold for bovine liver atomization (6200 W/cm^2) is much higher than in water (350 W/cm^2) and porcine blood clots (250 W/cm^2). Velocities of the projectiles are similar across all the species tested here that atomize and is on the order of 10 m/s.

An additional result of this study is that there is considerable evidence that tissue atomization and fountain formation is the mechanism by which tissue is fractionated in bulk tissue during boiling histotripsy. It is also possible that atomization might explain how cavitation-cloud histotripsy produces tissue emulsification within the 100 μm-size bubbles or within the cloud of bubbles. While we reported the threshold of atomization in liver in one 10-ms pulse (I_L = 6200 W/cm^2; p_+ = 25 MPa, p_- = 8 MPa), we have also observed atomization in liver after many 10-ms pulses at even lower derated intensities down to I_L = 1300 W/cm^2 (p_+ = 9.5 MPa, p_- = 5.5 MPa). Furthermore, it may be possible to extend the results from this study to diagnostic levels; these results seem to support the hypothesis proposed by Tjan and Phillips that atomization is the mechanism by which diagnostic ultrasound can damage lungs, a natural pressure-release interface that occurs in the body [48], [49]. By understanding the mechanism of tissue atomization, a means to protect the lungs may be devised so that ultrasound can be used to scan near the lungs without fear of causing tissue damage.

One possible explanation for the atomization and erosion of tissue is spallation [63], [64]. In other words, the wave reflects upon encountering the pressure release surface, causing significant cavitation just below the tissue surface. As these vapor cavities continue to form, fragments of tissue become separated from the bulk tissue by these cavitation clouds, at which time those fragments move in the direction of the gas. In the ideal case of reflection from the pressure release surface and submicron-size fragments, when the separation is complete, the velocity of the ejected pieces should equal double the particle velocity of the incoming wave. This mechanism would explain why we see whole and fragmented cells and nuclei in the collected projectiles; near the cavitation bubbles, the cells and nuclei could become fragmented due to the shear forces, but in the center portion of these fragments, the cells would be unaffected. This mechanism is evaluated and discussed further in Ch. 4.

FIGURE 2.13: Photo showing the tissue sample in the bottom of a pipette. The pipette will act as a container to recirculate the tissue as is predicted to occur in bulk boiling histotripsy.

Upon histological comparison between the fountain projectiles and bulk boiling histotripsy, it was noted that because whole cells and nuclei are still present in the collected projectiles, it differed from the histological analysis of cavitation cloud histotripsy and boiling histotripsy in bulk tissue [8], [65]. We believe the difference may be due to the confined space in the bulk tissue which causes the fountain projectiles to be recirculated rather than ejected from a surface. After several attempts, we found an experimental setup which allowed us to test this hypothesis. Briefly, a small tissue sample was placed in the bulb of a 1-mL polyethylene disposable pipette by cutting a hole in the pipette bulb wall as shown in figure 2.13. Some tape was placed over the hole to prevent fountain projectiles from escaping during atomization. A mosquito surgical clamp was placed slightly above the tissue piece to keep the tissue from being ejected from the transducer focus, while making sure an air interface existed for atomization to occur. The pipette was held via the mosquito clamp at the focus of the transducer, making sure the bulb of the transducer was placed just under the water surface for coupling to the transducer. When the amount of fractionated tissue occluded the tissue-air interface, the tissue sample was removed, and the remaining liquid was further circulated. Upon removal from the pipette, the recirculated liquid was smeared onto a microscope slide and stained with H&E. A representative histology picture from this study is shown in figure 2.14. Compared to the uncirculated fountain projectiles shown in figure 2.12, there remains only a few dying cells like the one shown to the upper-right of center in figure 2.14. This histology image is much more similar to what is observed after bulk boiling histotripsy than the histology images of the un-recirculated fountain projectiles. These results confirm our hypothesis that recirculation in bulk boiling histotripsy is necessary to break up the fountain projectiles into submicron cellular components.

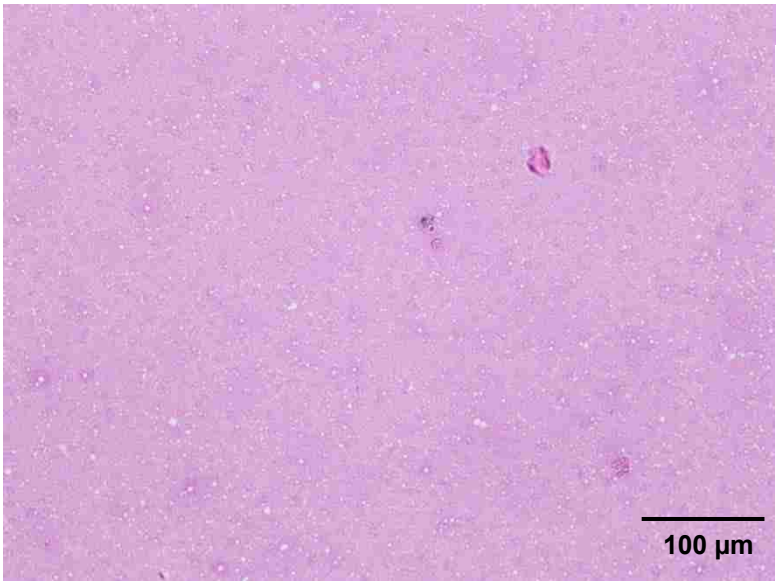

FIGURE 2.14: H&E stained histology slide showing cellular debris and bubbles after recirculating the fountain projectiles. A few dying cells remained in the sample, like the one apparent to the upper-right of center in this image. This histology image is much more similar to what is observed in bulk histotripsy than the histology images of the fountain projectiles.

One further observation made during the tissue studies is that the tissue wetness affects the tissue atomization and erosion rate. Standing liquid on the tissue surface, whether it be phosphate-buffered saline (PBSaline) or water, substantially enhances atomization and tissue erosion by decreasing the atomization threshold and time for atomization to occur. Blotting the surface to remove the excess liquid from the surface somewhat decreases the atomization and tissue erosion, while not soaking the tissue in PBSaline at all can almost completely inhibit atomization and tissue erosion. Our current hypothesis is that the thin liquid layer on the surface makes it easier for the surface capillary waves to form, lowering the cavitation threshold and thereby enhancing atomization and tissue erosion. However, since atomization and erosion are decreased by not soaking the tissue in PBSaline, it is possible that the PBSaline alters the tissue structural and the mechanical properties through absorption either in the cells or extracellular matrix. Another alternative is that by not soaking the tissue in PBSaline the air content of the tissue is increased such that it prevents ultrasound of sufficient intensity from reaching the surface, inhibiting atomization. Nevertheless, as increasing the soaking time of liver in PBSaline increases atomization and tissue erosion, it becomes evident that the process used to prepare tissue or create blood clots can substantially affect the atomization thresholds. Understanding the differences observed during atomization and fountain formation from different tissue preparation methods

may help us determine which tissues are candidates for *in vivo* tissue fractionation by boiling histotripsy.

Additionally, erosion rate and atomization threshold are easily affected by local inhomogeneities within the same liver, and even within the same liver sample. While erosion rate and thresholds can be affected by the tissue preparation methods as a whole, we found differences in the erosion rates and atomization thresholds from site to site. While some of these can be explained by the presence of small vessels and other visible structural inhomogeneities, other variations were not easily elucidated. One explanation may revolve around the small changes in tissue liquid content from site to site; while we attempt to maintain a consistent wetness on the tissue surface, variation at the cellular level may explain some of these discrepancies in the data. The method of liver preparation may also enhance or decrease these subtle differences. Further studies will be performed on tissue preparation techniques and cellular inhomogeneities in tissue to explain these variations.

Already, cavitation cloud histotripsy has been shown to be successful *in vivo* in the canine prostate [71], [72] and in the rabbit kidney [73]. Boiling histotripsy has also been shown to successfully emulsify porcine liver and murine melanomas *in vivo* with strong similarities between the *ex vivo* and *in vivo* results [74]. While the experiments in this chapter were conducted in *ex vivo* tissue samples, we expect similar instances of atomization and tissue fractionation when using *in vivo* tissues. The different distribution of gas nuclei in the living tissue may make atomization and tissue erosion less dramatic than has been observed in the *ex vivo* tissue because it could reduce the intensity of ultrasound reaching the atomization site; however if tissue wetness plays a factor in erosion and atomization, the blood that is present in living tissue might make atomization occur even easier than was found in the *ex vivo* case. Determining the factors that affect atomization and tissue erosion will be important as our work progresses toward *in vivo* studies and as we compare our results to *in vivo* boiling and cavitation cloud histotripsy studies. Furthermore, these factors may be important in predicting the success of boiling histotripsy in many different *in vivo* tissues and is the topic of the next chapter.

CHAPTER 3

Tissue Properties that Affect Atomization[2]

3.1. Introduction

Atomization and the formation of an acoustic fountain are complex processes in liquids that become even more complicated in tissues. The work in Rozenberg et al., shows that liquid and interfacial properties such as surface tension, density, speed of sound, and kinematic viscosity all influence atomization and the size of the emitted droplets [53]. Atomization becomes even more complicated in tissues when the elastic properties must be considered along with viscosity. In this chapter, we will experimentally determine which tissue properties most influence atomization with the goal of being able to predict which tissues can be successfully atomized. In addition, we will compare our *ex vivo* results from the previous chapter to atomization *in vivo* as we look towards transitioning boiling histotripsy or atomization into a clinical therapy.

One time consuming, but relatively easy way to determine which tissues can be successfully atomized is to try different types of tissue. Near the beginning of our study into tissue atomization, we used trial and error to help form more specific hypotheses as to what types of tissues can be atomized. Because tissues are primarily water with similar sound speeds and viscoelastic properties, we also explored atomization in fruits as well as tissue-mimicking gels. Atomization of the lungs was also considered because atomization has been mathematically proposed as a mechanism for lung damage at diagnostic ultrasound levels [48], [49]; however Tjan and Phillips did not directly propose atomization of tissue, rather they suggested that ultrasound could expel droplets from a tissue-liquid interface that could puncture the alveoli of the lung [48], [49]. The idea that tissue is punctured from droplets ejected across an air interface is

[2] Work published in part in:

Simon JC, Sapozhnikov OA, Khokhlova VA, Wang Y-N, Crum LA, Bailey MR (2013). "Ultrasonic atomization: a method of tissue fractionation." J. Acoust. Soc. Am. 133(5), 3316: Montreal.

different from the idea that tissue is atomized and ejected into an air pocket, which was presented in Ch. 2. These studies in a variety of tissues, fruits, and tissue-mimicking gels served as a starting point and specific hypotheses were formulated as a result.

One observation that emerged from the studies in numerous tissues, foods, and gels was that water content appeared to affect the success of atomization. As was mentioned in Ch. 2, we noticed that the amount of time a tissue spent in phosphate-buffered saline (PBSaline), a solution commonly used to preserve tissues for laboratory research, significantly affected the erosion volume. Submersion in PBSaline is known to cause tissue swelling over time, so the idea that tissue wetness affects atomization arose. Based on our understanding of the cavitation-wave theory of atomization in liquids (Ch. 1), which states that a combination of capillary waves on the surface along with cavitation bubbles beneath the surface cause atomization, an increase in the tissue wetness could make capillary waves easier to form on the tissue surface thereby enhancing subsurface cavitation and hence atomization. Understanding how water content affects atomization could lead to an understanding of which tissues can be successfully atomized.

In some of our peer-reviewed work, reviewers have expressed concerns about our observation that tissue wetness affects atomization because these observations were made using *ex vivo* tissues. It is often felt that *ex vivo* tissues are not alive, so do not accurately mimic the *in vivo* case. However, unpublished results by our lab indicate that the cells remain active and viable for many hours after tissue harvesting. In fact, organs such as kidneys can remain viable for transplant after being kept outside the body for 72 hours [75]! As we mentioned previously regarding the commonly used PBSaline solution, one of the concerns with cold storage of *ex vivo* tissues is the tissue swelling that occurs due to the changes in cellular metabolism and the differences in salt and sugar concentrations between the tissue and the solution [76]–[78] To address the issues of tissue wetness and preservation, we researched the solutions that are used for the transport and storage of organs destined for transplant. While the University of Wisconsin (UW) ViaSpan® solution continues to be the gold standard for organ transplant [77], it is cost-prohibitive to be used in a research setting. Other simpler

solutions were considered, including the basic phosphate buffered sucrose (PBSucrose) [79], [80] as well as phosphate buffered raffinose (PBRaffinose), as the smaller molecular weight sugars such as sucrose can freely penetrate into cells, while their larger counterparts rely on active transport [76]. By changing the salt and sugar concentrations in the preservation solutions, tissue swelling (water content) will be affected both intra-cellularly and extra-cellularly, in addition to pH and cell viability [81]. The results from these experiments, when compared to *in vivo* tissues, will not only describe the best way to store *ex vivo* tissues for ultrasound research but will also determine whether tissue wetness enhances atomization.

This chapter is broken down into three main experiments. In the first experiment, atomization was attempted in a variety of tissues, fruits, and tissue-mimicking gels. In the second experiment, tissue preservation solutions were varied to determine the effect of water content on atomization. Finally, in the third section, atomization was attempted *in vivo* in a porcine animal model. These experiments led to some general conclusions about the tissue properties that affect atomization and the tissue types that can be successfully atomized.

3.2. Atomization of Different Tissues

3.2.1. Methods

The same planar tissue setup was used as was described in Ch. 2 and is shown again here in figure 3.1. As before, a 2-MHz transducer was used along with an ENI A300 55 dB radiofrequency amplifier and an Agilent function generator. The samples were cut with a thickness of 1-1.5 cm (when possible), placed in a custom-designed holder, and partially submerged in water with the top surface exposed to air at the focus of the transducer. The water in the tank was filtered and degassed with a temperature of approximately 20 °C. In addition to the bovine livers and porcine blood clots that were atomized in Ch. 2, we also attempted to atomize porcine liver, esophagus, spleen, skeletal muscle, skin, and fat. To move away from organs, porcine tendons and ligaments were also attempted to be atomized in addition to various fruits and roots such as bananas (including the peel), potatoes, watermelon, and apples. Preparing a

list of which tissues and foods can and cannot be atomized will be a start to establishing the tissue properties that affect atomization.

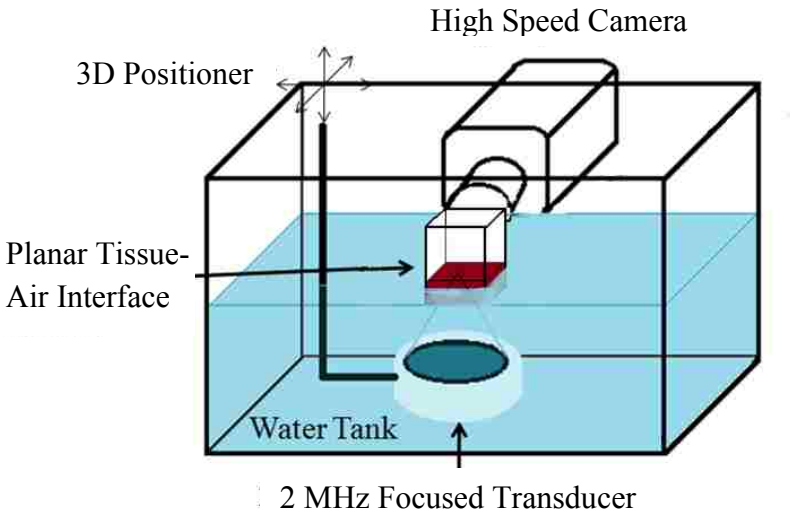

FIGURE 3.1: Experimental setup for all *ex vivo* tissue, food, and gel experiments detailed in this chapter.

In addition to foods and tissues, a tissue-mimicking polyacrylamide gel with 7% bovine serum albumin (BSA) was also atomized because the transparency of the gel allowed us to visualize atomization both above and below the gel surface. The gel was prepared as described in Lafon et al. [82]. Briefly, filtered water was mixed with a 40% w/v acrylamide solution (Sigma-Aldrich, St. Louis, Missouri, United States), a TRIS buffer with a pH of 8, and 7% BSA. The solution was degassed for at least one hour in a desiccant chamber before adding 10% w/v ammonium persulfate solution (Sigma-Aldrich), and N,N,N',N'-methylethylenediamine (Sigma-Aldrich). The complete solution was poured into a mold with a 1-2 cm thickness and allowed to set, which took approximately 20 minutes. The gel was placed into the same holder that was used for the tissue studies and has been described previously.

Besides just attempting to atomize a variety of foods and tissues, a goal has been to connect the tissue injury observed at internal air interfaces after diagnostic ultrasound exams to the injury we have observed at created air interfaces with higher acoustic intensities. The internal air interface of greatest concern during diagnostic ultrasound exams are the lungs. Several iterations of this experiment were attempted. In the first attempt, a syringe was used in an attempt to draw all of the air out of the lungs to create one, controllable, air interface. In the second attempt, we filled the lungs with PBSaline in an attempt to eliminate all of the air in the alveoli and have the single, controllable, air

interface. In the third attempt, the lungs were sectioned and injected with PBSaline to eliminate the air in the alveoli. With each attempt, the lungs were placed above the transducer in a similar setup as has been described previously and is shown in figure 3.1. For each of the three attempts, the lungs were exposed to ultrasound, starting with therapeutic HIFU levels and lowering the intensities until atomization did not occur. Should atomization be found to occur in the lungs at diagnostic levels, it may be possible to develop techniques to avoid or reduce damage to the lungs when ultrasound is used in the thoracic region.

3.2.2. Results

Our results in a variety of *ex vivo* tissues indicated that porcine liver in addition to esophagus, spleen, skeletal muscle, and fat could be atomized. Select frames from a high speed video of porcine skeletal muscle are shown in figure 3.2. It is interesting that the atomization of skeletal muscle looks fairly similar to the atomization of bovine liver (shown in Ch. 2), especially considering the vast difference in tissue structure between liver and skeletal muscle; however one noticeable difference is apparent in the size of the emitted droplets. In bovine liver at similar intensities, there is a large range in the sizes of droplets emitted from 10s to 100s of microns whereas in porcine skeletal muscle, the droplet sizes are much more consistent and in the 10s of microns range.

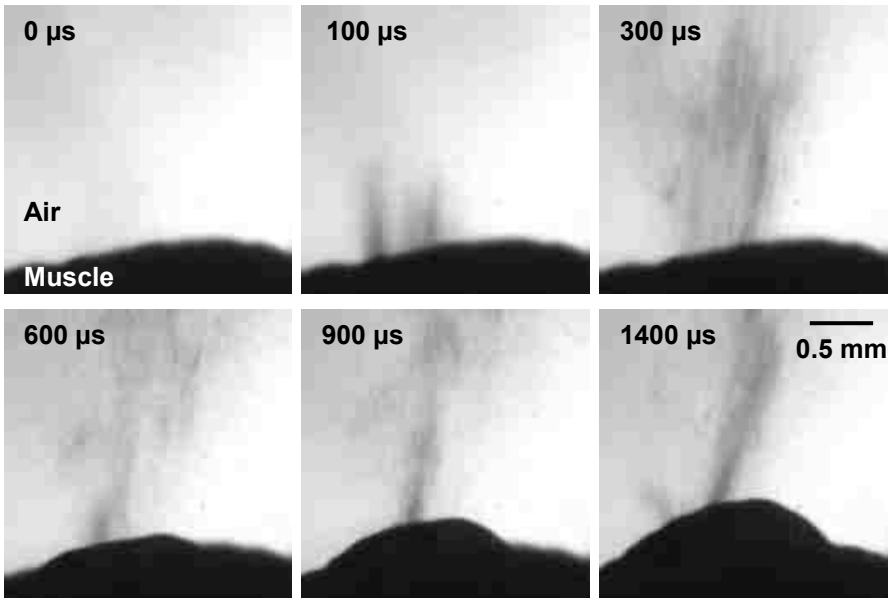

FIGURE 3.2: High speed video frames showing atomization in porcine skeletal muscle. Of interest, the droplets emitted from skeletal muscle are very small (~60 µm or ~1 pixel) in diameter and appear to be relatively consistent in size; no large droplets of 100s of µm are apparent. HIFU was on for 10-ms.

The velocity of the ejected fragments is approximately 13 m/s in porcine skeletal muscle. Also of interest in the frames shown in figure 3.2 is that no jets are emitted from the right hand side of the mound. The lack of jetting on the right hand side of the mound continued for the first 5, 10-ms pulses, though throughout those pulses the jets began to be emitted from the right hand side starting near the apex of the mound. It was not until the sixth pulse that jets were emitted from the lower sections of the right hand side of the mound; conversely, jets were emitted from the lower portions of the left hand side of the mound in the first 10-ms pulse. Other exposures in skeletal muscle showed jets from the entire surface of the mound in the first pulse. We expect the initial lack of jetting from the right hand side of the mound in figure 3.2 is due to the structural inhomogeneities in skeletal muscle. It is possible that the right hand side of the transducer focus was located more in the connective tissue between muscle fibers, rather than in the bulk fiber, making atomization more difficult on the right hand side of the mound. Nevertheless, this video showed that skeletal muscle could be successfully atomized.

As in bovine liver, the end result of atomization is tissue erosion, which is supported by the photographs shown in figure 3.3 where surface erosion is visible in porcine esophagus, skeletal muscle, and subcutaneous fat. In particular, from the depth of the hole in porcine subcutaneous fat, we can surmise that fat atomizes very efficiently. Thus far, porcine skin is the only soft tissue in which atomization has been completely unsuccessful. We expect this is due to the high acoustic attenuation of pig skin, which prevents ultrasound of sufficient intensity from reaching the surface [83], [84]. We also attempted to atomize two other tissues – porcine tendons and ligaments. Unfortunately,

FIGURE 3.3: A series of photographs showing erosion in A) porcine esophageal tissue (2 spots), B) porcine skeletal muscle, and C) subcutaneous porcine fat. All three tissues were successfully atomized and the resulting surface erosion is shown here.

the tissue setup made it virtually impossible to determine the success of atomization in porcine ligaments; the 1-2 mm thickness of even the largest ligaments harvested from the pig made it difficult to simultaneously submerge the lower surface of the ligament in water for coupling to the transducer while keeping the upper surface of the ligament exposed to air. While we were unsuccessful in atomizing ligament, we have some evidence that porcine tendons can be atomized as shown in figure 3.4. At the end of the exposure (50 pulses of 10-ms duration with a PRF of 1 Hz), there was a hole in the tissue; however it was very difficult to determine whether the hole was in the tendon or in the tendon sheath and surrounding fascia. We suspect that we actually atomized the some fascia and the tendon sheath rather than the actual tendon. Nevertheless, showing that even the tendon sheath can be atomized gives us some evidence that perhaps the tendon could be atomized, provided we could get access to the tendon, itself. The size of ejected fragments and velocities are similar to what we observed previously in bovine liver at similar intensities, with the size of the ejected fragments ranging from 10s of microns to 100s of microns in diameter and approximate velocities of 6 m/s. Many soft tissues were successfully atomized and all appeared remarkably similar in the high speed videos of atomization.

To explore a wider range of mechanical properties, atomization was attempted in a several different foods. The first food we successfully atomized was a banana, the

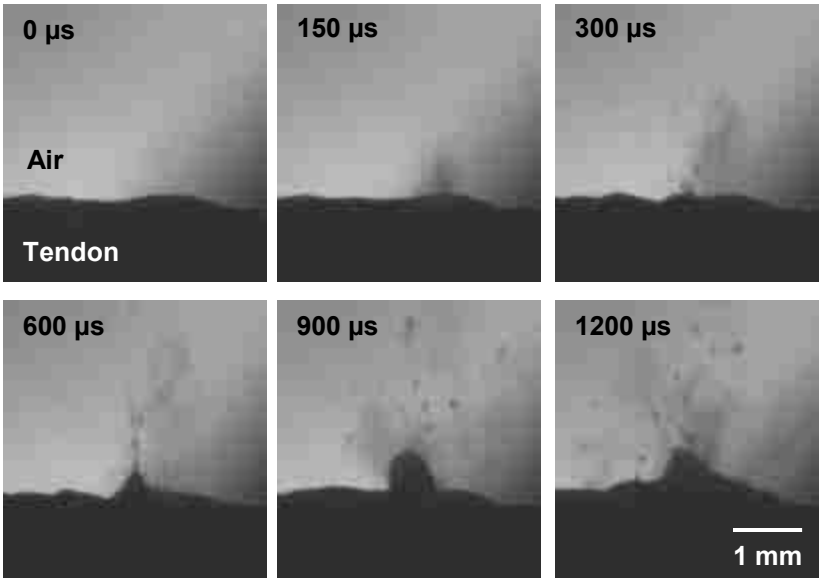

FIGURE 3.4: Selected frames from a high speed video of porcine tendon sheath atomization. The geometry of the tendon and the nature of the sheath surrounding the tendon made it very difficult to directly atomize the tendon. Nevertheless, there was a hole in the tendon sheath at the end of the exposure (50, 10-ms pulses).

results of which are shown in figure 3.5. From the picture, it appears that atomization is very efficient in bananas. Other foods, such as apples, potatoes, and watermelon did not atomize successfully, even when the peel was removed and the food was squeezed to break up some of the surface cells. We expect the lack of success was due to the difference in impedance between the water and the food which prevented ultrasound of sufficient intensity from reaching the pressure-release interface and causing atomization.

FIGURE 3.5: Photograph showing surface erosion after atomization of a banana. The hole in the banana is quite large compared to the tissues even though the exposure parameters were similar (10-ms pulses at a 1 Hz pulse repetition frequency).

As organs and foods often have significant discrepancies in their acoustical and mechanical properties between different animals, degrees of ripeness, etc., atomization was also attempted in a tissue-mimicking BSA polyacrylamide gel because the mechanical properties could be precisely controlled. In the first few gels, we found that surface erosion appeared to be intermittent; in some cases, a hole would appear in the gel surface, while in other cases, the surface would either bulge outward or show no surface evidence of the ultrasound exposure. After several gels, we realized that the gel surface dried out over time, which reduced or totally suppressed erosion of the gel surface. Figure 3.6 shows several frames from the high speed video of dry (upper) and wet (lower) polyacrylamide gel atomization. The dry surface was achieved by blotting the surface and leaving the gel exposed to air for about an hour until the surface was nappy instead of smooth to touch. For the video, the wet gel surface was achieved by spreading approximately 1-mL of water across the 2.5 cm x 2.5 cm gel surface. From the frames showing the dry gel surface in figure 3.6(a), it is apparent that while there is subsurface cavitation activity and mound formation, atomization does not occur; there is no jetting from the gel surface. Conversely, the frames from the wetted gel surface in figure 5.6(b) show significant atomization, with jet velocities of approximately 17 m/s

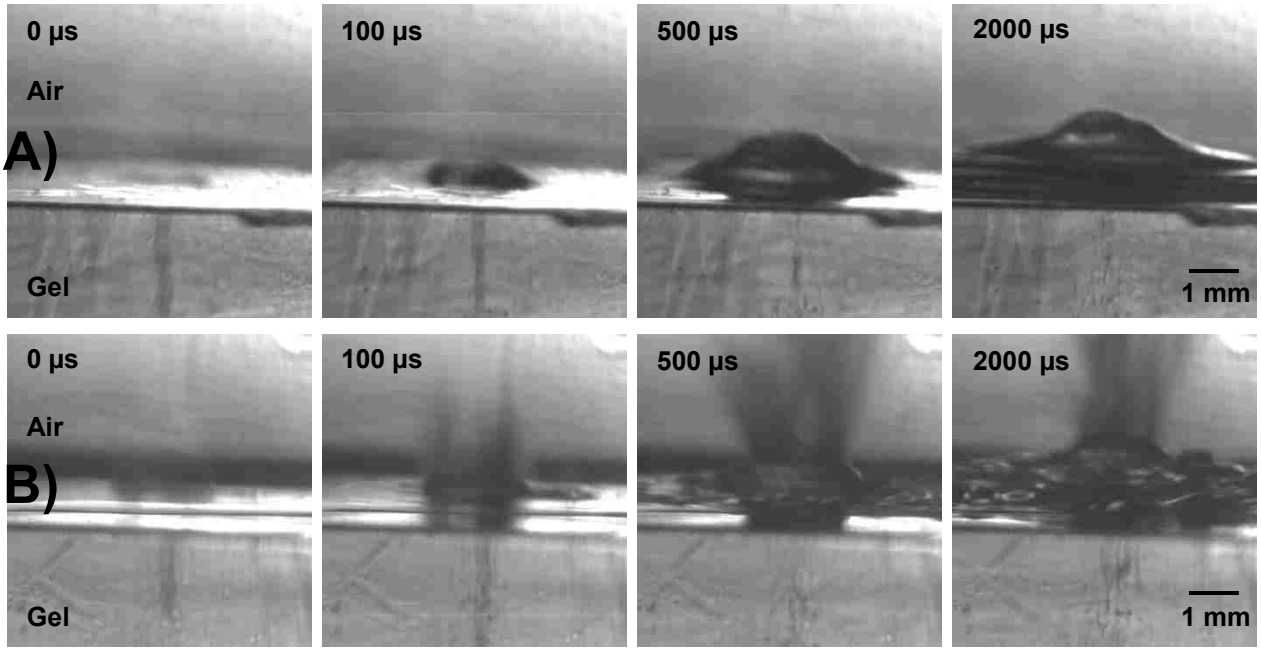

FIGURE 3.6: Selected frames from high speed videos of dry (A) and wetted (B) polyacrylamide gel. A) The dry polyacrylamide gel shows subsurface cavitation that is present in the first frame (labeled as 0 µs but actually 70 µs after the ultrasound wave encounters the gel-air interface). In the next frame, (100 µs) the mound has formed, though subsurface cavitation is still present. In the next two frames, subsurface bubble activity continues and the mound of gel continues to grow, but no jets are emitted from the gel surface. B) The water-wetted polyacrylamide gel also shows subsurface cavitation in the first frame (labeled as 0 µs but actually 70 µs after the ultrasound wave encounters the gel-air interface) as well as an initial spray of water from the surface. By the next frame, (100 µs) there is a slight mound forming, with jetting from the surface; subsurface cavitation is still visible. The final two frames shows still more atomization of the liquid and gel from a growing mound. Subsurface bubble activity seems to have subsided by the third frame (500 µs), though more bubbles have formed below the surface by the fourth frame (20000 µs). Both videos were taken at the maximum 24,000 W/cm^2 intensity and 10-ms HIFU exposures.

and a relatively homogenous particle size distribution, with diameters on the order of 10s of microns. Subsurface cavitation is also present in the wetted gel in addition to mound formation. In both the wetted and dry gels, subsurface bubble activity continues throughout the 10-ms exposure. The accompanying figure 3.7 shows photographs of the gel after the wet and dry atomization exposures. From the photo, it is apparent that atomization of the dry surface caused a slight bulge to form in the gel surface, whereas atomization of the wetted surface created a hole in the gel that extended several

FIGURE 3.7: Photographs showing side views of the dry gel (left) and the wetted gel (right) after 60, 10-ms pulses repeated at 1 Hz (transducer is positioned at the bottom of the photo shooting upwards). In the left photo of the dry gel, a bulge forms in the gel surface rather than a hole, with only a single subsurface bubble visible about 4 mm beneath the gel surface. The right image of the wetted gel shows the side view of the gel, with an inset showing the top gel surface. The hole formed when the gel is wetted is approximately 2 mm in diameter and 5 mm in depth.

millimeters into the gel. These observations support our hypothesis that tissue or gel wetness enhances atomization.

In an effort to link tissue injury in the lungs at diagnostic ultrasound levels to the tissue atomization that is observed at high intensities, we attempted to atomize the lungs. Three attempts were made to atomize the lungs and all were unsuccessful. It did not matter whether the lungs were intact (with the lungs deflated as much as possible), or whether the lungs were sectioned and injected with PBSaline – in all cases, the lungs would continue to float in the water tank and atomization would not begin. We expect that no matter which technique was used to purge the air from the lungs that there remained significant amounts of air which prevented the transmission of ultrasound to the controlled pressure-release interface. This conclusion was supported by little to no signal being received when using pulse-echo to focus the transducer at the surface.

3.2.3. Discussion

In this section, we began to establish which mechanical or acoustic properties affected atomization and erosion. We suspect that atomization was not successful in watermelon, apples, and potatoes due to the difference in impedance between water and the food, which prevented ultrasound of sufficient intensity for atomization from reaching the free surface. This same problem occurred when we attempted to atomize the lungs; however the difference of impedance was caused by the large volume of air in the lungs whereas in the fruits it was a combination of fruit hardness in addition to air that reduced ultrasound transmission. As far as porcine skin, we expect that the highly

collagenous nature of porcine skin prevented the skin surface from bulging enough to focus the wave and cause subsurface cavitation and hence atomization.

One interesting result from this section was that skeletal muscle could be atomized successfully. This was a surprising result as, thus far, skeletal muscle has been difficult to fractionate in bulk boiling histotripsy. One potential explanation for the lack of success in fractionating bulk skeletal muscle arises from the structure of skeletal muscle; it is possible that, while the pressures at the focus of the transducer move and stretch the tissue, the myofibrils or connective fascia do not actually pull apart to form a void. If no boiling bubble forms in the bulk tissue, atomization will not occur (as there will be no pressure release interface) and the tissue will not be fractionated. In our experiment, the flat tissue surface is exposed to air (i.e. an infinite bubble) so atomization and tissue erosion is successful. While we think the above explanation is the most feasible, one other possible explanation for the lack of tissue fractionation in bulk skeletal muscle is that the muscle (especially *ex vivo*) is too dry to atomize. We showed in the gels that atomization depends on tissue wetness and *ex vivo* skeletal muscle, in particular, is very dry, especially once the blood has been drained out. This reasoning is somewhat supported, as when we have purchased pork chops from the local marketplace for demonstrations, the tissue surface was relatively dry and atomization was not always successful; however, even when a thin layer of water was added, atomization was still not always successful in this tissue. Therefore, while both explanations are possible to link atomization to bulk boiling histotripsy, we expect that the first one, where the boiling bubble cannot be created, is most likely even though we have no proof to substantiate this claim.

One of our major conclusions from this section which helped steer much of the later research was that a thin layer of water on the gel surface caused atomization to be successful when it was otherwise unsuccessful. This supports the data we collected in Ch. 2, where we observed that the amount of time the tissue spent in PBSaline influenced the success of atomization. With histology, we could determine whether intracellular swelling or fluid in the extracellular matrix is most influential for atomization. This information may help elucidate the mechanism of atomization in tissues, which in

turn may help us develop techniques to enhance atomization and eventually boiling histotripsy. As far as clinical use, one easy way to enhance tissue wetness is to intentionally break small blood vessels near the treatment site. Further work is needed to understand how tissue wetness enhances atomization. The next section explores this hypothesis is more detail.

3.3. Tissue Wetness and Atomization

3.3.1. Methods

Solutions

In the previous chapter, we observed that storing tissue in PBSaline can significantly affect the success of atomization and the tissue erosion volume. As a result, we hypothesized that the difference in tissue wetness or water content is what caused the discrepancy. In this section, we submersed livers in several solutions of varying salt and sugar concentrations and compared the results to the gold-standard University of Wisconsin (UW) ViaSpan® organ transplant solution. Solutions tested include a phosphate-buffered sucrose (PBSucrose) [80], a phosphate-buffered raffinose (PBRaffinose), no solution, and phosphate-buffered saline (PBSaline). Both the phosphate-buffered sucrose and phosphate-buffered raffinose were prepared according to Lam et al. with 120 mmol/L of sodium, 60 mmol/L of phosphate, and 140 mmol/L of sucrose or raffinose [80]. The liver in the no solution group was wrapped in a PBSaline-wetted towel to prevent the tissue from completely drying out. The PBSaline solution contained 0.9% saline. All solutions were degassed in a desiccant chamber at -85 kPa for at least one hour before the liver was submerged.

To Degas or Not to Degas?

One side observation that was made during the initial atomization studies conducted in Ch. 2 was that degassing tissue in a desiccant chamber did not appear to affect atomization on the day the tissue was purchased. We hypothesized that, because the experiment relies upon exposing a tissue surface to air, that the air would diffuse into the tissue relatively rapidly compared to the focal dimensions of the transducer and the

length of the experiment, eliminating the need to degas the tissue. To support this hypothesis, we calculated the expected diffusion of air into bovine liver, using Fick's Law of diffusion in one dimension to calculate the diffusion length according to the equation:

$$L = 2\sqrt{Dt}$$

Where L is the diffusion length, D is the diffusivity, and t is time. As there were no available reported values of the diffusivity of air in bovine liver, we used the diffusivity of oxygen in rat liver of $3.6*10^{-5}$ cm^2/sec from MacDougall and McKabe for the calculation [85]. According to the calculation, in 5 minutes (the estimated time to focus the transducer at the liver surface), the diffusion length was approximately 2 mm, which is relatively large considering that half the axial -6 dB zone of the transducer is approximately 5 mm (which is of interest if we assume that the focus is precisely aligned with the surface of the tissue such that half of the focus is geometrically above the tissue surface and half of the focus is below the tissue surface). This calculation supports our preliminary results; however in this section we will more thoroughly test the hypothesis that degassing is not important for atomization studies by either degassing or not degassing the liver samples submerged in solution.

Experimental Protocol

A total of 15 groups were exposed to 1 of 5 solutions and split between day 1 and day 2 and degassed and non-degassed as indicated in table 3.1. Each of the 15 groups was repeated across a minimum of 3 livers, with 3 samples taken from each liver at randomly distributed locations. We assume that the 3 samples taken from the same liver are independent based on structural inhomogeneities and differences in vascularization that have been observed between different lobes and even different sections within the same liver lobe. Then, within each of the 3 samples, the ultrasound exposures were each repeated 3 times. This repetition of the ultrasound exposures within the same sample was not assumed to be independent for statistical purposes.

TABLE 3.1: Listing of the 5 solutions tested in 15 groups across degassing and day.

	Day 1		Day 2	
Solution	**Degassed**	**Not Degassed**	**Degassed**	**Not Degassed**
PBSaline	(Prelim only)	X	X	X
Nothing		X		X
PBSucrose	X	X	X	X
PBRaffinose		X	X	X
UW (ViaSpan)		X	X	X

Ten non-rinsed bovine livers were obtained from a local abattoir (Schenk Packing, Stanwood, WA, USA) for this study. The day of purchase was denoted day 1, with a maximum of 3 groups assigned to day 1, and a maximum of 3 groups assigned to day 2 for each liver. Immediately upon arriving at the lab, the liver was cut into pieces of approximately 5.5 cm x 5.5 cm, with a thickness between 1 cm and 1.5 cm and placed into 1 of 6 containers. Care was taken when cutting the liver to avoid major vessels within and on the surface of the samples; areas containing suspicious spots that could be parasitic were also avoided. The containers were pre-labeled and filled with 1 of the 4 solutions or a PBSaline-wetted towel for the no solution group. Any group that was specified as degassed on day 1 was placed into the -85 kPa desiccant chamber for at least one hour, while the other day 1 groups remained on the tabletop. The day 2 groups were submerged overnight in ice water. Gross observations of the liver quality and size were noted while cutting the samples.

Acoustic Measurements

After the liver samples were submerged in solution for at least one hour, the sound speed and attenuation were measured for the day 1 groups with the sample replacement technique [86]–[88]. Briefly, all three samples from the same liver were stacked and placed between a pair of 7 mm diameter PVDF transducers (Sonic Concepts, Woodinville, WA, USA) which are mounted on a set of calipers. (The samples were not measured individually because the minimum sample thickness for the caliper system is 1.5 cm, which is the maximum thickness of our liver samples.) The distance between the two transducers was set as close as possible to the thickness of

the liver samples without causing any flexion of the caliper arms. The liver samples remained in their solution for the measurement, with the solution coupling the transducer face to the liver surface. The acoustic measurements were controlled with LabVIEW software, where the user inputs the distance between the transducers and the temperature of the sample. The software then programs a function generator (Model 33120A, Agilent, Palo Alto, CA, USA) to send a 10 V, 10 μs long tapered chirp sweeping frequencies from 1-10 MHz. Based on the acoustic signal received by the opposite transducer that was measured and averaged 200 times with an oscilloscope (Model 9304CM, Lecroy, Chestnut Ridge, NY, USA), the program then writes a text file. The sound speed is calculated based on a time of flight comparison between the sample measurement and a water reference measurement according to the equation:

$$c_t = \frac{1}{\frac{\Delta t}{d} + \frac{1}{c_w}}$$

Where c_s is the sound speed of the sample, c_w is the sound speed of water, Δt is the difference in time of flight, and d is the distance between transducers. The sound speed measurements were then adjusted based on a curve published by Duck to an arbitrary 37 degrees to eliminate the discrepancies in sound speed caused by the difference in temperature between the liver samples [89]. The attenuation of the liver was also calculated using a power law curve fit of the fast Fourier transforms of the experimental data according to the equation:

$$Attn(f) = \frac{|F_{ref}(f)|}{|F_{sample}(f)|} = a * (f)^b$$

Where F_{ref} is the fast Fourier transform (FFT) of the signal from the reference measurement, F_{sample} is the FFT of the signal from the sample measurement, f is the frequency in MHz, a is the attenuation at 1 MHz and b is the power index. Each acoustic measurement was repeated in five different locations for each group. Reference measurements were taken in both water and the solution the liver samples were submersed in for all groups.

TABLE 3.2: Listing of the 4 acoustic exposures using the maximum acoustic intensity.

	Exposure A	Exposure B	Exposure C	Exposure D
Number of 10-ms Pulses at 1 Hz	10	30	60	120

Tissue Atomization

After measuring the sound speed and attenuation, the day 1 groups were atomized. The experimental setup that was used has been described previously (and is shown graphically in figure 3.1), with the tissue held within a container partially submerged in a water tank. A 2-MHz focused transducer with a 45-mm focal distance and radius of curvature was aligned with the surface of the tissue using pulse-echo. Four different acoustic exposures were chosen for all liver samples, based on our preliminary results. The four exposures are listed in table 3.2. The maximum linear *in situ* intensity of 14,000 kW/cm^2 (p_+ =53 MPa, p_- = 12.7 MPa) was used. As we stated previously, each of the four exposures were repeated three times throughout the sample, taking care to avoid any obvious vessels or surface disruptions and to spread out the exposures so that the same exposures were not right next to one another. The eroded tissue dimensions were measured after each exposure using calipers and an assumed precision of 0.5 mm. From these measurements, the erosion volume was calculated assuming a spherical cap geometry. The exposures were filmed with the Photron high speed camera for mechanical analysis.

Mechanical Analysis

To determine whether submersion in the various solutions altered the mechanical properties of the liver, the high speed videos were

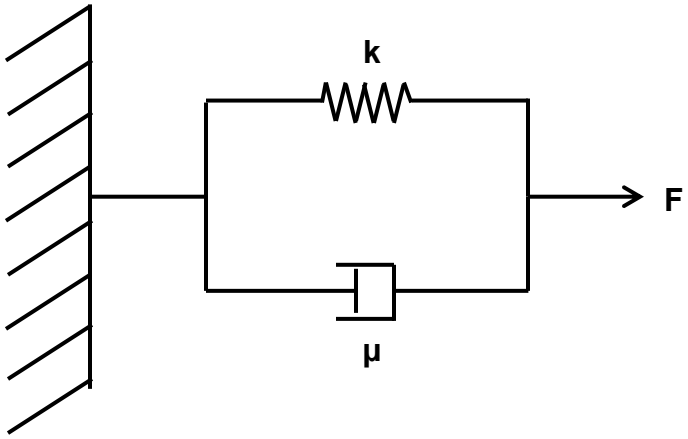

FIGURE 3.8: Schematic representation of the Kelvin-Voigt viscoelastic model.

analyzed to track the liver displacement over time. As liver can be described as a viscoelastic solid, the Kelvin-Voigt model was used to estimate the viscoelastic properties of the liver. The Kelvin-Voigt model consists of a spring and dashpot in parallel (figure 3.8), with the governing differential equation:

$$F = kx + \mu \frac{dx}{dt}$$

Where F is the applied force (acoustic radiation force in our case), k is the elastic constant, μ is the viscosity or the drag coefficient, x is the tissue displacement, and t is time. Assuming a constant force is applied at time=0, the solution to this equation is an exponential defined by the equation:

$$x(t) = \frac{F}{k}\left(1 - e^{-\frac{t}{\tau}}\right), \quad \tau = \frac{\mu}{k}$$

Once the applied force is removed, and the tissue is allowed to relax back towards its unperturbed state, the solution to the differential is:

$$x(t) = \frac{F}{k} e^{-\frac{t}{\tau}}, \quad \tau = \frac{\mu}{k}$$

From these equations, it is apparent that the time constant, τ should agree when the force is applied and when the force is removed. The time constants were calculated using the "cftool" command on MATLAB®, which fits an exponential to the data using the nonlinear least squares technique. For our experiment, we are most interested in comparing the time constants, both between livers and between groups as it provides information on the relationship between the viscosity and elasticity of individual samples. Comparing between livers should indicate differences in liver quality while the between groups comparison should indicate whether the solutions influence the mechanical properties of the tissue.

Tissue Wetness

The original hypothesis of this section was that tissue wetness enhanced atomization. To analyze the tissue wetness, small tissue sections were taken from each sample

within each group. The tissue sections were weighed and placed in a graduated cylinder to measure the volume of the liver sample. The samples were left exposed to air for at least one week and further dried out in a low heat oven. The weights and volumes of the samples were again measured. The percent change in the weights and volumes of each liver sample was calculated.

While the first technique gave us an idea of overall water content, it was not able to give us information as to the tissue quality. For that reason, additional tissue sections from each liver sample were taken and frozen-fixed in the optimum cutting temperature (OCT) compound. The frozen samples were then sliced in the cryostat in 8 μm thick sections. The slides were then stained with Hematoxylin and eosin (H&E) and examined with light microscopy. Qualitative comparisons were made between tissues in different solutions for different days.

Statistics

Due to the number of samples and the complexity of the statistical analysis, Dr. Ziyue Liu, a statistician from Indiana University, performed the analysis. A linear mixed effects model, which is a type of regression model, was used for the analysis because it can consider variation that is not attributable to the independent variables. The model is linear because the dependent variable (tissue erosion volume) was continuous; the model has mixed effects, which means some parameters have fixed effects and others random effects. As multiple samples were taken from the same liver, a random intercept was used to account for these correlations. Mean response levels were estimated by least square means, which essentially takes the mean of the mean for some independent variable. Most of the data were compared pairwise; however in the case of multiple comparisons, data were adjusted by Tukey's method, which uses the studentized range distribution to establish confidence intervals. These data were first analyzed by solution type as the combinations were not balanced across the five solutions. Then, the solutions were analyzed together to determine the effect of the solution. Due to the number of samples, p values < 0.01 were considered significant.

TABLE 3.3: List of the mean +/- standard deviation of the volume eroded (mm^3) per group

	Day		Degas		Ultrasound Exposure (# of 10-ms pulses)			
Solution	**1**	**2**	**Y**	**N**	**A (10)**	**B (30)**	**C (60)**	**D (120)**
PBSaline	X			X	3.1 ± 2.3	10.9 ± 8.2	20.5 ± 9.7	32.5 ± 16.1
PBSaline		X	X		3.7 ± 3.7	10.1 ± 8.9	24.3 ± 16.3	31.6 ± 18.2
PBSaline		X		X	2.7 ± 2.3	11.0 ± 6.6	25.1 ± 13.6	37.2 ± 18.2
Nothing	X			X	2.9 ± 1.5	12.5 ± 7.1	21.6 ± 12.0	30.9 ± 13.6
Nothing		X		X	2.3 ± 1.3	8.7 ± 6.9	24.4 ± 13.6	32.7 ± 12.2
PBSucrose	X		X		2.5 ± 1.5	9.8 ± 6.2	18.4 ± 9.6	28.4 ± 12.5
PBSucrose	X			X	2.5 ± 2.1	12.0 ± 9.5	20.5 ± 13.6	30.7 ± 18.0
PBSucrose		X	X		3.6 ± 2.9	15.2 ± 12.4	31.5 ± 15.1	37.6 ± 14.6
PBSucrose		X		X	1.7 ± 1.5	8.5 ± 6.9	20.3 ± 12.9	32.4 ± 18.1
PBRaffinose	X			X	2.0 ± 1.9	7.9 ± 6.7	15.7 ± 7.2	26.6 ± 9.9
PBRaffinose		X	X		2.8 ± 1.9	10.5 ± 7.2	27.7 ± 12.2	45.4 ± 24.9
PBRaffinose		X		X	2.4 ± 1.5	12.0 ± 8.1	25.2 ± 13.4	38.2 ± 18.2
UW (ViaSpan)	X			X	2.3 ± 1.4	11.4 ± 5.5	28.7 ± 14.4	41.2 ± 18.0
UW (ViaSpan)		X	X		3.0 ± 2.9	11.4 ± 7.5	26.3 ± 10.9	43.9 ± 15.6
UW (ViaSpan)		X		X	2.0 ± 1.4	7.3 ± 3.1	17.9 ± 7.0	36.6 ± 18.4

3.3.2. Results

Table 3.3 lists the mean and standard deviation of the eroded volume for each ultrasound exposure and group (solution, day, degas). An overall comparison across solutions was performed, where it was found that there is no difference in the tissue erosion volumes between solutions, regardless of day and degassing. If we compare the erosion volumes for each ultrasound exposure for each solution regardless of day and degassing (*i.e.* for PBSaline, all A's compared to all B's, all B's compared to all C's, etc.), we find that the erosion volume increases with the number of 10-ms pulses and that these increases are significantly different ($p=0.001$). Because the interactions between degassing and day are different across solution types, we were not able to separate the effects; however, we were able to conclude that the interaction of degassing and day significantly affects the tissue erosion volume for all ultrasound exposure levels ($p=0.0003$). While these results are interesting, we need to consider

TABLE 3.4: List of the averages +/- standard deviations for wetness, decay time constant, sound speed and attenuation.

Solution	Day 1	Day 2	Degas? Y	Degas? N	Wetness % Δ (weight)	Inverse Decay Time Constant (k/μ, sec^{-1})	Sound Speed m/s	Attenuation dB/cm
PBSaline	X			X	74.6 ± 1.1	0.24 ± 0.12	1597 ± 12	0.63 ± 0.19
PBSaline		X	X		77.3 ± 1.0	0.15 ± 0.04	1543 ± 22	0.72 ± 0.23
PBSaline		X		X	78.0 ± 2.5	0.14 ± 0.02	1572 ± 5	0.52 ± 0.12
Nothing	X			X	67.0 ± 4.5	0.19 ± 0.04	1596 ± 12	1.01 ± 0.14
Nothing		X		X	69.7 ± 4.3	0.13 ± 0.03	1580 ± 5	0.69 ± 0.23
PBSucrose	X		X		72.7 ± 1.4	0.16 ± 0.05	1584 ± 12	0.63 ± 0.14
PBSucrose	X			X	73.8 ± 3.5	0.17 ± 0.05	1598 ± 16	0.66 ± 0.13
PBSucrose		X	X		72.4 ± 4.8	0.17 ± 0.07	1551 ± 8	0.61 ± 0.24
PBSucrose		X		X	74.3 ± 1.0	0.13 ± 0.04	1551 ± 24	0.57 ± 0.10
PBRaffinose	X			X	70.8 ± 0.7	0.14 ± 0.05	1600 ± 9	0.70 ± 0.23
PBRaffinose		X	X		71.5 ± 3.1	0.11 ± 0.03	1559 ± 13	0.58 ± 0.13
PBRaffinose		X		X	72.2 ± 2.0	0.14 ± 0.06	1577 ± 16	0.66 ± 0.26
UW ViaSpan	X			X	72.4 ± 1.2	0.15 ± 0.04	1570 ± 28	0.67 ± 0.30
UW ViaSpan		X	X		72.7 ± 1.5	0.14 ± 0.04	1555 ± 18	0.50 ± 0.12
UW ViaSpan		X		X	73.8 ± 5.0	0.14 ± 0.02	1548 ± 21	0.57 ± 0.19

them in conjunction with the liver wetness, sound speed, attenuation and decay time constant from the Kelvin-Voigt model to be able to reach some meaningful conclusions.

Table 3.4 lists the mean and standard deviation of the wetness (percent change by weight), the inverse decay time constant fit from the Kelvin-Voigt model (units of inverse seconds, defined as the elastic coefficient divided by the viscous coefficient), the sound speed (in m/s) and the acoustic attenuation (dB/cm/MHz) for each group (solution, day, degas). For the purposes of analysis, only the percent change in water content by weight was considered as the volume measurements were not precise enough to detect small changes in the tissue volume. Also, only the decay time constant from the Kelvin-Voigt model was considered because the liquid jets on the tissue surface that were emitted during atomization caused inaccuracies in the tracked tissue displacements. Also, the tissue displacement approached but never reached a steady state value,

which represents a large source of error for model fitting. As our original hypothesis was that tissue wetness enhances atomization, we begin our analysis by considering how the various solutions influenced the tissue wetness. Interestingly, when the percent change in water content by weight was compared within solutions (so considering the effects of day and degassing), we found that only the PBSaline solution had any groups that were statistically different; for the PBSaline solution, we found that water content increased significantly between day 1 and day 2 when the tissue was not degassed ($p=0.0013$). While no other solutions showed significant differences between days, the percent water content in tissue ranged from 66% to 78% across the different solutions, which, along with the tissue erosion results, indicates that bulk tissue wetness does not influence atomization.

Then, we considered how the acoustic properties changed by day and degassing for each solution. As far as the acoustic attenuation, only no solution showed a significant difference between day 1 and day 2 ($p=0.0003$). Sound speeds showed more variation between groups for the same solution. In fact, only the UW ViaSpan and PBSucrose solutions had any groups that were not significantly different, and for these solutions only the sound speed on day 2 comparing degassing and not degassing were not significant. PBSaline also showed no significant difference between degassing and not degassing on day 2, though the p-value of 0.01 indicates that PBSaline is approaching significance. For all other solutions, a statistically significant difference was found for comparisons between days and degassing conditions with a maximum p-value of 0.003.

The final parameter of interest was the decay constant fit to the Kelvin-Voigt viscoelastic model, which gives an idea of the mechanical properties of the tissue. The decay constant has units of seconds and is a ratio of the viscous and elastic coefficients of tissue. In most cases, the curve fit to the tissue displacement was very good, with R^2 values above 0.95. An example of the liver displacement-time data is shown in figure 3.9. In this example, the displacement versus time looks reasonable for the rise and decay; however only the decay time constant was considered in this analysis. The analysis was performed for each solution to determine the effect of day and degassing on the mechanical properties of the liver. Only no solution showed any significant

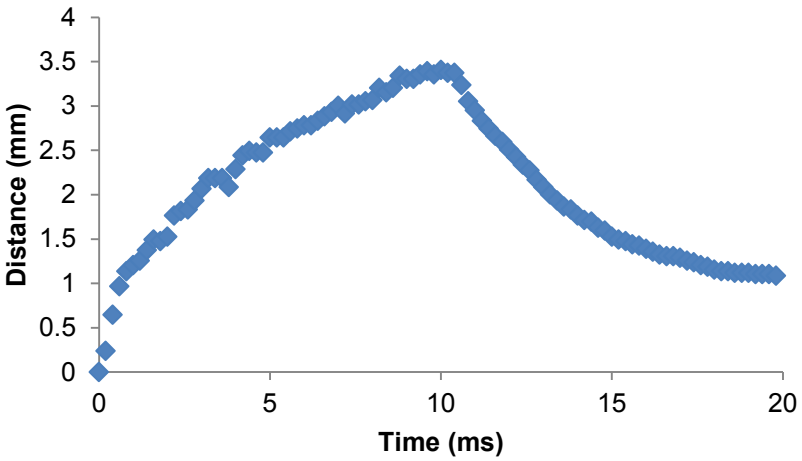

FIGURE 3.9: Plot showing the liver tissue displacement for a 10-ms HIFU pulse tracked for 20-ms with high speed video. This example was for PBSaline on day 1. Only the decay portion of the curve was considered for analysis, as the tissue rise only approaches, but never reaches, steady state.

difference between groups and that difference was found between day 1 and day 2 (the effect of degassing was not tested in no solution; p=0.004). The differences for the other solutions between groups (testing the effects of day and degassing) were not statistically significant.

Figure 3.10 shows erosion from the tissue surface after atomization. The pattern of holes on the liver surface show the typical pattern laid out for exposures; the design was meant to spread out exposures with the same conditions so that if there were hidden vessels in the sample, we had a good probability of missing the vessels for at least one of the exposures. As the liver is a highly vascularized organ, there were many vessels in the samples, even when we took care to avoid the vessels. When the vessels were obvious, we shifted the exposure pattern to try to avoid them. Nevertheless, we had to exclude some of the tissue erosion data when

FIGURE 3.10: Photograph showing the typical erosion pattern on the liver surface. From left to right on each line (the final line is split into 2 lines), exposures were completed in the order A (10 pulses), B (30 pulses), C (60 pulses), and D (120 pulses). The first exposure A in the upper left corner occurred on a vessel, so that exposure was excluded from the erosion analysis.

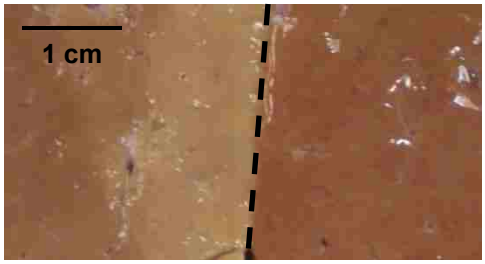

FIGURE 3.11: Photograph showing the visual difference in liver quality after a sample has been stored for 24 hours in PBSaline (left) and UW ViaSpan solution (right) as separated by the dotted line. The sample preserved in PBSaline has a noticeable color change about 1 cm from the edge, whereas the sample stored in the UW ViaSpan solution is a consistent, healthy color throughout.

vessels were noted at or near the exposure location and obviously influenced the eroded volume.

In this study, we also visually compared tissues preserved in the different solutions before and after the acoustic exposures. Figure 3.11 shows a comparison of a sample preserved for 24 hours in PBSaline (left) and the UW ViaSpan (right) solutions. In the photograph, we can see an observable color change in the sample stored in PBSaline approximately 1 cm from the edge, whereas the sample preserved in the UW ViaSpan solution is a consistent, healthy color throughout. As these samples were photographed together, taken from the same liver, and stored for similar times in their respective solutions, we can conclude that the color changes are due to the differences in solution rather than differences in the liver or lighting. If we look at the H&E histology slides under 20x magnification as shown in figure 3.12, there are no obvious differences in

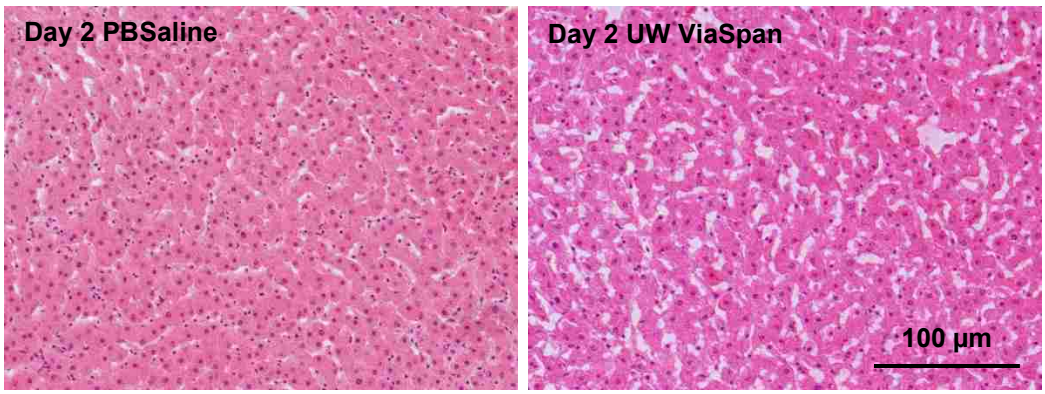

FIGURE 3.12: H&E histology slides showing the cellular morphology after 24 hours of cold storage in PBSaline (left) and UW ViaSpan (right). Besides a slight difference in the staining colors, there are no major differences between these samples. There are a few more frozen fixation artifacts (white spaces) in the UW ViaSpan solution, but that does not give any indication as far as liver quality or tissue wetness.

cellular morphology. The staining shows a little difference in color, but that is likely an artifact of the staining technique. Also, the UW ViaSpan solution has a few more frozen fixation artifacts than the PBSaline solution, which appears as white spaces between the cells. While it is important to analyze the samples histologically for changes in cellular morphology, we were not able to gain any more information as to the tissue wetness or quality.

3.3.3. Discussion

This section described a very thorough experiment designed to illuminate the influence of tissue wetness on atomization. From the results, we are able to make some broad conclusions regarding the effects of degassing, time, and solution on the acoustic and mechanical properties of tissue. Probably the most significant conclusion is that bulk tissue wetness does not appear to influence atomization. We say bulk tissue because the tissue was submerged in a solution, rather than just applying the liquid to the surface as was done in the tissue-mimicking gel in the previous section. The mean water content in tissue ranged from 66% to 78%, with no solution showing the lowest water content and PBSaline showing the highest water content; Duck reports a water content of 69% for fresh bovine liver [89]. As the statistics showed no significant differences between the erosion volumes across the different solutions or groups, we can conclude that the atomization is not affected by the wetness of bulk tissue, at least across the 12% change in liver water content that was tested here.

We were unsurprised to find that the PBSaline solution showed the highest water content, as our previous work indicated that tissue swells when submerged in PBSaline. Cellular metabolism slows during cold storage, changing the active ion transport mechanisms and causing cellular swelling [76], [78]. While 0.9% PBSaline is isotonic at body temperature, changes in cellular transport causes the sodium ions in the solution to be rapidly transported into the cell; water follows by osmosis to maintain equilibrium, causing cellular swelling [78]. For the sugar solutions (PBSucrose and PBRaffinose), the mean tissue wetness data follows the results by Kaboyashi et al., in that the mean water content in PBRaffinose, the higher molecular weight sugar, was lower than the mean water content of PBSucrose; however, our results differed from Kaboyashi et al.

in that the water content of the UW Solution tissue was more similar to PBSucrose than PBRaffinose [76]. This could be due to the differences in liver species (rat versus bovine) or the immediacy of adding the solution; Kaboyashi et al. perfused the liver *in vivo*, whereas the bovine liver was submerged in the solution at least one hour after harvest. As few labs have access to perfused organs, this result indicates that PBSucrose could be an excellent (and cheaper) alternative to the UW ViaSpan solution for the preservation and storage of *ex vivo* tissues for laboratory studies.

Another conclusion is that degassing the tissue is not important for atomization studies on the day of tissue harvesting. This supports our Fick's law diffusion calculations, which indicate that air diffuses about 2 mm into the tissue in 5 minutes. When the experiment takes approximately 25 minutes in total, with the tissue in air for at least 5 minutes before the first ultrasound exposure, it is not surprising that our experimental results indicate that degassing is not important on day 1. While the effect of degassing on day 1 was only evaluated for PBSucrose, this result follows our preliminary result with liver in PBSaline. These results are not included in this section because the preliminary tissue erosion data was taken with a malfunctioning transducer (water was leaking into the transducer housing and reacting with the copper wiring, reducing the transducer output by an unknown amount). As the preliminary results indicated degassing was not important on day 1, the decision was made to limit the use of the more costly solutions (PBRaffinose and UW ViaSpan) to test the effect of degassing on day 2, where statistically significant results were observed in the preliminary studies.

Overall, the results suggest that degassing the liver is important on day 2 (24 hours after harvesting). While we were statistically unable to separate the effects of degassing and day on the tissue erosion volume, our results in PBSucrose (the only complete dataset testing the effect of degassing across days), there is a statistically significant difference between the degassed and non-degassed samples on day 2 ($p<0.0001$). However, in the other three solutions where the effect of degassing was assessed only on day 2 there was no statistically significant difference in the erosion volume. From a physical prospective we would expect degassing to be important on the second day (but not on the first) because of tissue degradation and the resulting

release of gases from the tissue. These gases are expected to interfere with the transmission of ultrasound, reducing the intensity that reaches the surface. In the acoustic attenuation measurement, none of the solutions showed a difference in attenuation from degassing on the second day. One possible explanation is that the gas remained dissolved in the tissue so did not significantly affect the amplitude of the ultrasound wave. However, if we consider the sound speed measurements, which are influenced by tissue density, we find that PBRaffinose shows a significant difference in the sound speed from degassing on the second day and that the difference in PBSaline is approaching statistical significance; in both cases, the sound speed is higher when the tissue is degassed. This makes sense as the dissolved gas should slightly reduce the tissue density, thereby reducing the speed of sound. The fact that the sound speed did not change when the tissue was submersed in the UW ViaSpan and PBSucrose solutions suggests that these solutions maintained tissue quality over the 24 hours better than PBRaffinose and PBSaline.

Over the two day studies and regardless of degassing, we found that the mechanical properties of the tissue, as estimated from fitting the tissue stress relaxation curve to the Kelvin-Voigt model, was significantly different only for no solution. In fact, adding no solution was significantly different between days for the acoustic attenuation and sound speed measurements in addition to the Kelvin-Voigt decay time constant. Only the tissue erosion volume and the tissue wetness did not show significant differences between days. These were both surprising, as we expected the tissue to dry out overnight, causing atomization to be unsuccessful. In fact, we wrapped the tissue in PBSaline-wetted pads to prevent significant tissue desiccation, believing that the comparison between solutions would be more meaningful if the tissue was at least kept moist. It seems as if the PBSaline wetting was enough to cause tissue swelling; the mean tissue wetness actually increased overnight. If we surmise that the PBSaline only infiltrated the surface layers of the tissue, rather than the bulk, it would suggest the significance of surface wetness, as compared to bulk wetness, in atomization.

There are several major sources of error in these experiments which help explain the size of the standard deviations we observed particularly in the tissue erosion volume

dataset. The first source of error is the liver, itself. As we noted in the methods, some of the livers contained parasites, which likely influences tissue quality. These parasites would also increase the number of local inhomogeneities in the liver. In addition, we already mentioned that circumstances made it necessary to switch transducers between our preliminary work and the study presented here. We also had to switch transducers mid-experiment, as the piezoceramic element used initially for the complete study began to break down. The transducer that replaced it was made according to the exact same protocol, and measurements of the focal waveforms showed that the new transducer operated very similarly to the transducer that it replaced. No discernible discrepancies were found in the erosion volumes between transducers, which indicated that we were able to mitigate this potential source of error. Another major source of error in our erosion volumes was the focal position of the transducer. Due to the number of exposures, it was not feasible to precisely focus the transducer at the tissue surface for every exposure. While every attempt was made to keep the tissue surface as flat as possible with the transducer focus at the tissue surface, we noticed a difference in the erosion dimensions when the focus of the transducer was too far above or below the tissue surface. In most cases, the total calculated volume of the hole averaged out; however we found several outliers in the dataset that could be due to poor focusing or just due to local tissue inhomogeneities. In a few instances, we found boiling histotripsy-type holes beneath the surface when cutting the tissue for histology, which indicated that the transducer was not adequately focused for atomization. These exposures were excluded from the dataset.

This experiment was successful in that we were able to conclude that bulk tissue wetness does not influence atomization. While we were unable to statistically separate the effects of day and degassing, we do have evidence that degassing tissue is important on day 2, but not on day 1. These results in a variety of tissue preservation solutions stress the need for the consistent use of good preservation solutions in ultrasound studies where circumstances prevent the immediate use of harvested tissue. The commonly used 0.9% PBSaline solution does not sufficiently preserve tissue for studies conducted 24 hours after harvesting. We suggest the use of PBSucrose as cheaper alternative to the clinically used UW ViaSpan® solution for preserving tissue in

a laboratory setting. Our results from this section and the previous section suggest that surface tissue wetness is more influential for atomization than bulk tissue wetness; however more research is needed to understand why. The next section considers atomization in tissue where preservation or freshness is no longer a concern.

3.4. *In Vivo* Atomization

3.4.1. Methods

In vivo atomization is needed to validate our extensive *ex vivo* results. A porcine animal model was chosen, as we regularly have access to swine used in terminal kidney studies; these studies were approved by the University of Washington Institutional Animal Care and Use Committee (IACUC). Porcine liver was atomized *in vivo*, as the organ is fairly homogeneous and we have a large amount *ex vivo* data in both porcine and bovine livers.

The same acoustic exposures that were fully characterized in Ch. 2 were used here both *in vivo* and *ex vivo*. Briefly, the 2 MHz transducer was programmed to send 10-ms pulses at a pulse repetition frequency of 1 Hz. The transducer was operated at the maximum intensity of 14,000 W/cm^2, derated (p_+ = 53 MPa, p_- = 12.7 MPa). The amplifier and function generator did not change for the *ex vivo* studies, however a

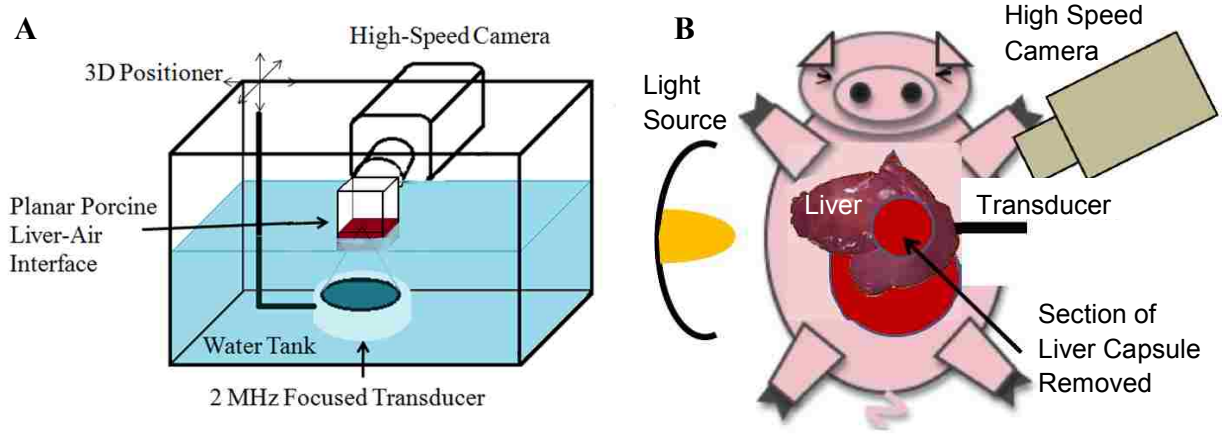

FIGURE 3.13: Experimental setups for A) the flat *ex vivo* porcine liver surface and B) a flat *in vivo* porcine liver surface. In both cases, the experiments were performed on sections of the liver with the capsule removed. The lighting was slightly different between the two cases – in A), the experiments were completely backlit, while in B) the lighting was a combination of back and side-lit.

different radiofrequency amplifier (ENI 400B, 55 dB gain) was used for the *in vivo* experiments as the size of the A300 ENI 55 dB used for the *ex vivo* experiments made it difficult to transport to the procedure room. With the change in amplifier, it was necessary to adjust the input voltage to the amplifier so that the intensity was similar between the *in vivo* and *ex vivo* studies.

A diagram of the experimental setups for *ex vivo* and *in vivo* tissues is shown in figure 3.13. The *ex vivo* setup has been described in detail in Ch. 2 and earlier in this chapter, so will not be repeated here. We began the *in vivo* experiment with the opening of the pig abdomen with electro-cautery. A retractor was then used to hold the body wall open while the liver was manipulated into a position slightly outside the abdominal cavity. A water-filled cone with a Tegaderm^{TM} membrane was used to couple the 2 MHz transducer to the underside of the liver surface. During the exposures, the transducer and liver were held in place by a lab member, who attempted to keep the transducer and liver as steady as possible. Liver sections that underwent atomization were kept at a thickness of approximately 1-1.5 cm, as the distance from the water-filled cone to the transducer focus was just over 1 cm.

As in the *ex vivo* experiments, the *in vivo* experiment was filmed with the Photron high-speed camera; however instead of the experiments being backlit only (as in the *ex vivo* livers), the *in vivo* experiments were back and side lit due to experimental setup constraints. Two types of exposures were conducted *in vivo* – one with the liver capsule intact and the other with the liver capsule carefully removed using a scalpel. When the liver capsule was left intact, water was routinely sprayed over the target surface to keep the tissue from drying out. When the liver capsule was removed, bleeding occurred, so the surface was blotted before atomization to remove the excess blood.

At the end of the *in vivo* exposures, pictures were taken of the liver surface and samples were removed and fixed in 10% neutral buffered formalin. After at least one week in the fixative, the liver samples were sent to a lab to be embedded in paraffin, sliced into 5 μm thick sections, and stained with H&E for histological analysis. No samples were

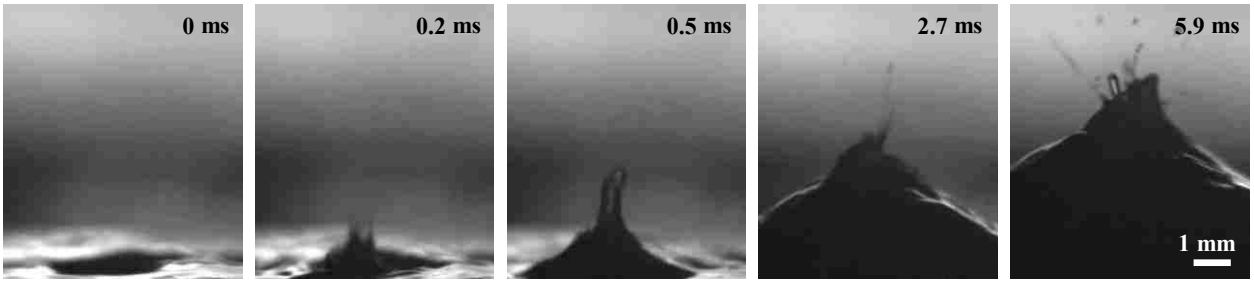

FIGURE 3.14: *Ex vivo* porcine liver without the capsule exposed to a linearly derated *in situ* intensity of 14,000 W/cm^2. The first frame shows the initial liver surface 70 μs after the ultrasound wave reaches the surface. The second frame shows the initial spray of atomization, which often occurs before the mound forms as shown in the third frame. In the fourth and fifth frame, atomization is becoming very dramatic, enhanced by the formation of the mound. The total exposure time was 10 ms.

taken from the *ex vivo* porcine livers as we already have extensive histological results in *ex vivo* bovine liver.

3.4.2. Results

Figures 3.14 and 3.15 show high speed images of atomization in porcine livers without the capsule *ex vivo* and *in vivo;* the timing of the high speed frames are similar between the two frame sequences. From figure 3.14, it is apparent that atomization begins as a fine spray very quickly after the ultrasound wave arrives at the surface. The initial atomization spray is followed by the formation of a mound at 0.5 ms, with a slight cessation of atomization. As the mound develops, atomization becomes more dramatic, as seen in the last two frames of figure 3.14. The velocity of the ejected fragments is on the order of 10 m/s, with the size of the ejected fragments ranging from tens to

FIGURE 3.15: *In vivo* porcine liver with the capsule removed at the maximum linearly derated *in situ* acoustic intensity of 14,000 W/cm^2. As in figure 3.14, the first frame was taken 70 μs after the ultrasound wave arrived at the surface. The second frame shows an initial spray of atomization that quickly becomes more dramatic (as seen in the third through fifth frames). The exposure was 10 ms in duration.

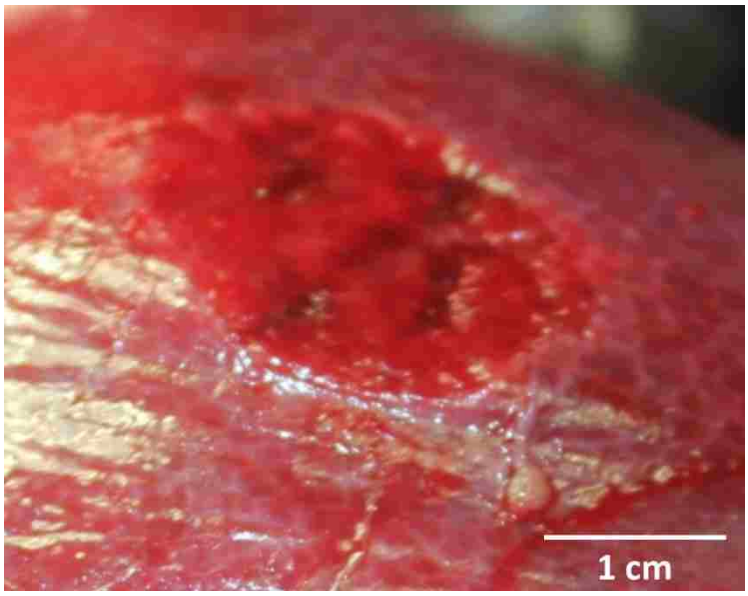

FIGURE 3.16: Photo showing erosion on the liver surface in the section without the capsule. From the presence of erosion tracks rather than a single hole in the liver surface, it is evident that the transducer was not kept very steady with respect to the liver surface.

hundreds of microns in diameter. When the 10-ms pulses are repeated at least 10 times at 1 Hz, the end result is a hole in tissue.

Figure 3.15 shows a sequence of high speed images (with the same time stamps as in figure 3.14) taken in *in vivo* porcine liver at the maximum *in situ* intensity of 14,000 W/cm^2. In figure 3.15, we see that atomization begins very quickly and becomes more dramatic with time. The spray looks liquid, most likely due to the presence of surface blood that appears when the liver capsule is cut. As compared to the *ex vivo* case where an obvious mound forms in tissue and enhances atomization, *in vivo* atomization becomes very dramatic with little to no mound forming over the duration of the pulse. The end result of *in vivo* atomization is surface erosion shown in figure 3.16. Unfortunately, the breathing motion of the pig makes it very difficult to keep the transducer steady so the same location is targeted with every pulse, hence the tracks shown in figure 3.16 as compared to discrete holes in tissue. When the liver without the capsule is viewed with the H&E stain as shown in in figure 3.17, we can see the pieces of liver that were torn away in addition to pooling of blood beneath the surface. There is no evidence of thermal injury near or below the targeted region and there is no evidence of subsurface boiling histotripsy.

The other *in vivo* exposure was with the liver capsule intact with water sprayed on the surface to keep it wetted. Thus far, no strong evidence exists to show that atomization can break the liver capsule *in vivo* or *ex vivo*. In several of the *in vivo* cases, the

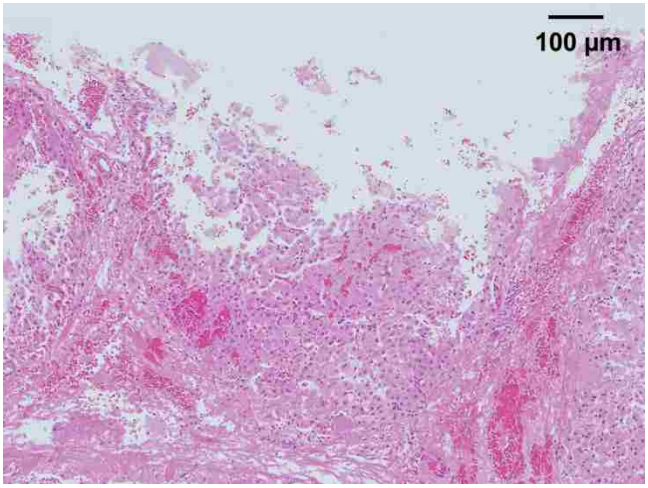

FIGURE 3.17: Light microscopy photo showing the H&E stained slide of liver erosion from the cut capsule liver surface. The top of the image shows where the tissue is pulled away from the bulk tissue, and around the eroded volume there is some evidence of blood pooling. The cells do not show any evidence of thermal damage and there is no fractionation of tissue beneath the surface.

histological results have indicated that a layer of 2-3 cells composing the liver capsule remain even after atomization (as shown in figure 3.18) with substantial fractionation of tissue below the liver capsule. In the case shown in the figure, fairly consistent but incomplete tissue fractionation extended 1.3 mm below the tissue surface, though patches of fractionated tissue continued to 2.5 mm. The length of the entire disrupted tissue (some blood pooling, fractionation, and perhaps even thermal injury) was 4.6 mm. In some cases (from which there are no histological results), a minute capsular breach was perhaps observed upon gross examination of the liver surface but was accompanied by significant thermal injury, making it difficult to confirm that the capsule was breached and not just cooked. These results agree with what has been observed in *ex vivo* porcine liver, namely that it is very difficult to break through the liver capsule

FIGURE 3.18: Light microscopy photo showing the H&E stained slide after atomization of the intact liver surface. The top surface shows where the 2-3 cells that compose the liver capsule remain intact, while the tissue beneath the surface is fairly well fractionated (some intact red blood cells and nuclei remain).

especially without causing any thermal damage. While these results confirm that liver atomizes similarly *in vivo* and *ex vivo,* it remains unclear why the collagenous liver capsule is difficult to breach.

3.4.3. Discussion

Our high speed video and erosion results *in vivo* indicate there is not a significant difference between *in vivo* and *ex vivo* atomization, at least for porcine liver. In both cases, atomization and surface erosion is successful when the liver capsule is removed. It is interesting to note that *ex vivo* porcine livers form a large tissue mound during atomization, whereas the *in vivo* porcine liver forms only a small mound. One potential explanation is that the holder used for *ex vivo* porcine liver simply holds the liver in a relaxed state, which allows for displacement of the liver sample; whereas the *in vivo* liver is, by necessity, pulled tight across the transducer's water cone to keep the targeted liver lobe outside of the body cavity. The difference in tension across the liver surface may explain the difference in mound heights. Another possible explanation is simply liver quality. While the *ex vivo* liver was used as soon as possible after sacrifice, there would be some tissue degradation even with storage in PBSaline. The livers for the two studies were also from different pigs. We observed in the previous section a large discrepancy between livers from different cows and would expect the same differences between livers from different pigs.

As we observed previously in the tissue-mimicking gel, surface tissue wetness appears to enhance atomization. From the lengths of the tracks in the *in vivo* porcine liver where the capsule was cut, it seems as if atomization is at least as efficient *in vivo* as *ex vivo* if not even more efficient. We expect this is due to the presence of blood, a wetting agent, on the tissue surface. An additional benefit *in vivo* is that the blood is continuously replaced, whereas *ex vivo*, the initial spray ejects the liquid and tissue must be fractionated before the liquid on the surface can be replaced. A study in erosion volumes is needed to compare the efficiency of tissue fractionation *in vivo* and *ex vivo.*

Also of interest, in both *ex vivo* and *in vivo* porcine livers it was very difficult to erode the liver capsule. The liver capsule is highly collagenous and elastic, and thus far, the only way we have been able to break through the capsule is when we cause significant amounts of thermal damage below the capsular surface. While there may not be a clinical reason to want to break through the liver capsule, there is some argument that breaking through a similar type of tissue would be useful in the kidney; if we could use ultrasound to break through the wall between the parenchyma and the collecting system, we would be able to drain the fractionated parenchymal tissue from the bulk kidney via the urinary system. Another highly collagenous tissue of interest is uterine fibroids. While HIFU is in clinical trials in the US to thermally ablate uterine fibroids, the end result of such a treatment is a benign mass or scar tissue within the body, which can cause pain or other complications [90]. By mechanically fractionating the fibroid, it could be allowed to harmlessly drain from the body. While we have been unable to obtain a sample of uterine fibroids, other groups have reported (unpublished) that it is difficult to create or maintain a bubble or bubble cloud within the fibroid. By atomizing a free tissue surface, we can (at least initially) circumvent the need to create or maintain a bubble in the tissue and can determine whether atomization can erode collagenous tissue. These are the reasons that we are particularly interested in our lack of success in atomizing the liver capsule and are working towards understanding atomization so we can develop techniques to become successful in eroding the liver capsule and hopefully other highly collagenous tissue.

Besides the fact that the capsule remains intact, it was interesting to note in our histology slides that the tissue injury extended 4.5 mm below the capsule surface. While there is some movement of the pig liver during the exposure from breathing and the experimental setup, the depth of partial fractionation leads us to believe that the capsule or free surface somehow alters the ultrasound wave to enhance subsurface fractionation. It is also possible that the radiation force of the ultrasound wave simply does not deform the capsular surface enough to break the cells. In the following chapter, we will look more closely at the mechanism of atomization and the predicted radiation forces and particle velocities that we can generate with our current transducers. With that careful study into the mechanism of atomization, we may be able

to explain why the liver capsule is particularly difficult to breach and develop techniques that will allow us to break through the liver capsule.

3.5. Summary and Conclusions

Establishing the tissue properties that affect atomization as well as finding the boundaries of tissue atomization (*i.e.* which tissues can and cannot be atomized) will help us determine not only the mechanism of tissue atomization, but will also help us work towards optimizing the parameters of atomization (i.e. pulsing sequence, frequency, etc.), and therefore boiling histotripsy. Between the tissues and foods tested, it was found that tissues that are very thick/tough such as pig skin would not atomize, and that hard foods such as potatoes, apples, and watermelon would not atomize. We expect the lack of atomization in the foods is due to transmission issues caused by the difference in impedances between water and the hard foods such as potatoes in addition to the amount of air within the fruits (which is significant in apples). As only bone in the body has a similar hardness, these preliminary results suggest that atomization could be successful in all soft tissues except bone. We also showed that a tissue-mimicking polyacrylamide gel would only atomize if a thin layer of water coated the surface. This supported our observation that submersion in PBSaline enhanced atomization, so we designed an experiment to more thoroughly test this hypothesis.

In the second section, we attempted to discern whether tissue wetness enhanced atomization. By submerging bovine liver in a variety of tissue preservation solutions composed of varying salt/sugar concentrations, we were able to conclude that bulk tissue wetness did not influence atomization. We were also able to conclude that degassing tissue is not important on the day of tissue harvesting; however tissue degassing becomes important 24 hours after harvesting, most likely due to the gasses that are released during tissue degradation. Finally, our acoustic attenuation and sound speed measurements suggested that PBSucrose could be a cheaper alternative to the clinically-used UW ViaSpan® solution to preserve tissue in laboratory settings. This study showed that bulk tissue wetness did not influence atomization while illustrating the need to either use tissue promptly after harvesting or store the tissue in a good tissue preservation solution to maintain tissue quality for ultrasound studies.

In the final section of this chapter, we compared our *ex vivo* atomization results to *in vivo* atomization. We found atomization occurred similarly *ex vivo* and *in vivo,* and perhaps was even more efficient *in vivo* due to the continuous leaking of blood to the surface of the cut capsule. We also were able to support our *ex vivo* results which indicated that the liver capsule was difficult to break with atomization without significant subsurface thermal injury. This led to the conclusion that highly collagenous tissues, such as liver capsules, are difficult to atomize. Hopefully, the next chapter that looks more deeply into the mechanism of atomization will shed some light into why the liver capsule is difficult to atomize, which could help us develop techniques to be able to atomize or erode highly collagenous tissue.

CHAPTER 4

The Mechanisms of Atomization[3]

4.1. Introduction

Atomization is a complex process when it arises from a plane ultrasound wave in liquid encountering a pressure-release interface; it becomes even more complex when a focused ultrasound wave encounters the pressure-release interface. As was pointed out in the two previous chapters, the mechanism of atomization is not well understood in liquids let alone in tissues. By determining the mechanisms of atomization in both liquids and tissues, we may be able to enhance atomization and perhaps even make tissue erosion by atomization successful when it otherwise might not be. The goal of this chapter is to better understand the role of bubbles in liquid and tissue atomization through high-speed photography and modeling.

The background section in Ch. 1 describes, in detail, the early work conducted to determine the mechanism of atomization in liquids and is briefly reprised here. Previously, researchers have considered the role of cavitation through sonoluminescence and the manipulation of ambient pressure, transducer frequency, temperature, surface tension, and viscosity [50]–[52], [91], [92]. The most accepted hypothesis to explain atomization is the cavitation-wave hypothesis, which was first proposed by Bisa, Dirnagl, and Esche [53]. In this hypothesis, a combination of capillary waves on the liquid surface in addition to the collapse of cavitation bubbles beneath the liquid surface result in the emission of a fine fog of droplets, or atomization (see figure 1.3). One version extends this hypothesis even further to state that the size

[3] Work published in part in:

Simon J, Sapozhnikov O, Khokhlova V, Wang Y-N, Crum L, and Bailey M (2012). "Ultrasonic atomization of tissue and its role in tissue fractionation by high intensity focused ultrasound," Phys. Med. Biol. 57, 8061-8078.

Simon JC, Sapozhnikov OA, Khokhlova VA, Wang Y-N, Crum LA, Bailey MR (2012). "Tissue atomization by high intensity focused ultrasound." Proceedings of IEEE UFFC Oct. 2012, Dresden, GER.

of the emitted droplets depends upon the mechanism of release; that droplets that are small and relatively consistent in size are emitted by capillary instabilities while the larger, more disperse droplets are emitted by cavitation bubble collapses [57]. While it is difficult to individually test these proposed mechanisms of atomization, we plan to vary ultrasonic parameters, liquids, and tissues to help elucidate the role of bubbles in liquid and tissue atomization.

In the decades since the initial studies on the mechanism of atomization in liquids, high speed imaging technologies have significantly improved. Conducting a reprise of the studies in water and other liquids will not only allow us to familiarize ourselves with the work, but the advance in imaging technology may allow us to observe an event that will shed some light as to the mechanism of atomization in a fountain. Observing the effects of varying ultrasonic frequency on atomization or even substituting other liquids for water may help indicate the effect of bubbles on atomization. Besides exchanging water with the traditional liquids such as glycerol and castor oil, we also plan to atomize 1,3-butanediol and olive oil, which were recently shown to have very high cavitation thresholds exceeding 30 MPa [93]. The primary advantages of 1,3-butanediol and olive oil over glycerol and castor oil are the similarities in the physical properties of olive oil and 1,3-butanediol to water; both olive oil and 1,3-butanediol have densities that are very similar to water of 915 kg/m^3 and 1005 kg/m^3, respectively and have shear viscosities that are significantly lower than the viscosities of glycerol and castor oil (84 cP for olive oil and 98 cP for 1,3-butanediol). Furthermore, the boiling points of olive oil and 1,3-butanediol are significantly higher than that of water (300 °C for olive oil and 200°C for 1,3-butanediol). In an attempt to distinguish between cavitation bubbles and boiling bubbles, substituting n-propyl alcohol for water is necessary because it has a boiling point of 97°C, which is similar to water, and a viscosity that is only double that of water (1.94 cP for n-propyl alcohol as compared to 1 cP for water). While atomization has been studied at different ultrasonic frequencies and in different liquids, by maintaining consistency in our experimental procedures, we may be able to provide more insight into the mechanisms of liquid atomization in a fountain.

When liquids are substituted for viscoelastic tissues, the mechanism of atomization in a fountain becomes even more complex. One of the difficulties with analyzing atomization in tissues is that we cannot observe atomization above and below the tissue surface with conventional photography. Therefore, we must substitute tissues for a transparent tissue-mimicking gel, which allows us to simultaneously observe the atomization below and above the gel surface with high speed photography. In addition, we can further test the idea that tissue wetness enhances atomization (as noted in the previous two chapters) by wetting the gel surface with liquids other than water to determine how surface wetting enhances atomization. However, even the best tissue-mimicking gels are not the same as real tissue. To link our subsurface observations in gels to tissue, B-mode ultrasound will be used. While it will be impossible to monitor for hyperechogenicity, or bubble activity, when the HIFU pulse is on, we expect the bubbles to persist for some time at the end of the HIFU exposure. The presence of hyperechogenicity, even at the end of the HIFU pulse, should help support our conclusions in gels about the influence of bubbles on atomization.

One of the best ways to assess the role of bubbles in ultrasonic atomization is to perform experiments under increased static pressure conditions to suppress bubbles [7], [94]–[97]. However, the necessity of an air interface for atomization makes building a high-pressure chamber dangerous. Fortunately, Brian MacConaghy, an engineer at CIMU has figured out what he believes is a safe way to build a chamber that can reach overpressures up to 2000 psi (13.8 MPa). While this amount of overpressure is not expected to totally eliminate boiling or cavitation (particularly because the ultrasound wave inverts on encountering the pressure release tissue- or liquid-air interface), that amount of overpressure should suppress cavitation and boiling enough to reveal the importance of bubbles in atomization. Observing atomization in a fountain with high speed photography under increased static pressure conditions will be a major step towards deducing the importance of bubbles in atomization.

The end result of this chapter will be a more thorough understanding of the mechanisms of atomization. By understanding the mechanism of atomization, we may be able to develop techniques to enhance atomization in tissues or to cause atomization to occur

in tissues that normally do not atomize. Through experimentation and modeling, we will test the hypothesis that bubbles are necessary for atomization. In liquids, we will change the ultrasonic frequency and atomize liquids of varying physical properties. In tissues and tissue-mimicking gels, we will monitor bubble activity beneath the tissue or gel surface with high speed photography and B-mode ultrasound. Finally, we will observe tissue and water atomization in a high static pressure chamber.

4.2. Water Atomization

4.2.1. Methods

Experiments

To determine the effect of ultrasonic frequency on water atomization, three different transducers were used with operational frequencies of 2 MHz, 1 MHz, and 155 kHz. All three transducers were air-backed, single-element, spherically focused piezoceramic crystals (PZ 26, Ferroperm Piezoceramics, Kvistgaard, Denmark) mounted in custom-built polycarbonate housings. Both the 2 MHz and 1 MHz transducers had 45-mm diameters and radii of curvature; the 155 kHz had a larger, 100 mm diameter and radius of curvature. A function generator (Model 33250A, Agilent, Palo Alto, CA, USA) and a linear radiofrequency (RF) amplifier (55 dB Gain, Model A300, ENI, Rochester, NY, USA) were used to drive the transducers.

Before the experiments, the focal pressure waveforms in water for the 2 MHz and 1 MHz transducers were measured with a fiber-optic probe hydrophone (FOPH 2000, RP Acoustics, Leutenbach, Germany) with 100-μm active diameter. The waveforms for the 2 MHz transducer were reported previously in Ch. 2. The 155 kHz transducer was not able to be mapped with the fiber optic hydrophone as the frequency was too low to get a decent signal; however, a calibrated Onda Reson hydrophone (Onda Corporation, Sunnyvale, CA, USA) was used to measure the signal at low input voltages and scaled to the voltages used for atomization. As we operated in the linear regime, the waveforms for the 1 MHz and 155 kHz transducer are not shown.

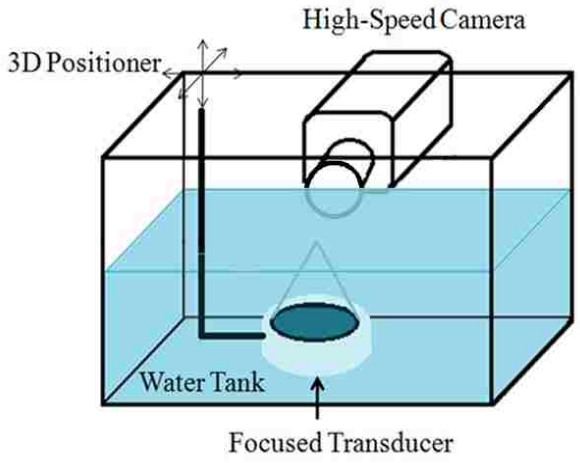

FIGURE 4.1: Experimental arrangement for atomization of water. Experiments are backlit (not shown).

Figure 4.1 shows the experimental arrangement for water atomization. The transducer was focused at the water surface using pulse echo with the timing recorded on a digital oscilloscope (Model LT432, Lecroy, Chestnut Ridge, NY, USA). A Photron APX-RS high speed camera (monochrome, Photron, San Diego, CA, USA) operating at variable frame rates from 5,000 to 30,000 frames per second was used to monitor atomization. A Carl Zeiss lens (Makro-Planar T* 2/100, Thornwood, NY, USA) with a bellows extension provided a resolution on the order of 40 μm/pixel. A continuous, disperse light source (Photogenic PowerLight 2500DR, Bartlett, IL, USA) was positioned at several angles to backlight the water to air interface in a combination of diffuse and direct lighting.

Theory

We can support our experimental observations with calculations that could help us discern the mechanism of atomization in water. The first equation gives us the capillary wavelength, which should equal the diameter of drops emitted from the fountain if capillary waves caused atomization. According to Sorokin and Eisenmenger [53], the capillary wavelength on a liquid surface excited by ultrasound waves and excluding gravity is governed by the equation:

$$\lambda_C = \sqrt[3]{\frac{8\pi\sigma}{\rho f^2}}$$

Where σ is the liquid-air surface tension, ρ is the liquid density, and f is the ultrasound frequency. For 20 °C water, the parameters used were σ=0.0728 N/m and ρ=1000 kg/m^3. As the capillary wavelength depends on frequency, we found that for ultrasound frequencies of 2 MHz, 1 MHz, and 155 kHz, the calculated capillary wavelengths were

7.3 μm, 11.9 μm, and 42.4 μm, respectively. These numbers can be compared to droplet diameters obtained from the high speed videos to confirm or eliminate the capillary wave mechanism of atomization.

In addition to the capillary wavelength, we can also calculate the approximate jet velocity using the equation for particle velocity:

$$v_p = \frac{p}{\rho c}$$

where p is the pressure of the ultrasound wave, ρ is the density of the liquid, and c is the speed of sound in the liquid. For water at 20 °C, we used a density of 1000 kg/m^3, and a sound speed of 1486 m/s. After calculating the particle velocities, we can also predict the maximum height of the jets using a simple energy balance. By balancing kinetic and potential energies, the equation to calculate the maximum height attained by the jetted particles (assuming vertical release) is:

$$h = \frac{v_p^2}{2g}$$

where v_p is the calculated particle velocity and g is the acceleration due to gravity. At the maximum acoustic output of the 2 MHz transducer, the peak positive pressure is 65 MPa, making the predicted particle velocity 43.7 m/s, and the maximum particle height around 97 m. If we assume linear wave propagation (instead of shocked wave), the peak pressure reduces to 26.7 MPa, in which case the particle velocity reduces to 18 m/s with a corresponding height of 16.5 m. When the acoustic pressures are reduced to 3 MPa, the predicted particle velocity becomes only 2 m/s and the height drops down to 20 cm. These predicted velocities and heights will be compared with observed particle velocities and heights measured from the high speed videos.

6.2.2. Results

As was previously observed in water [51], [91], for low acoustic intensities (I_L=180 W/cm^2; p_+ = 2.5 MPa, p_- = 2 MPa) at which atomization occurs intermittently in water, the fountain is a chain of drops and one or more drops explode (*i.e.,* atomize) as shown

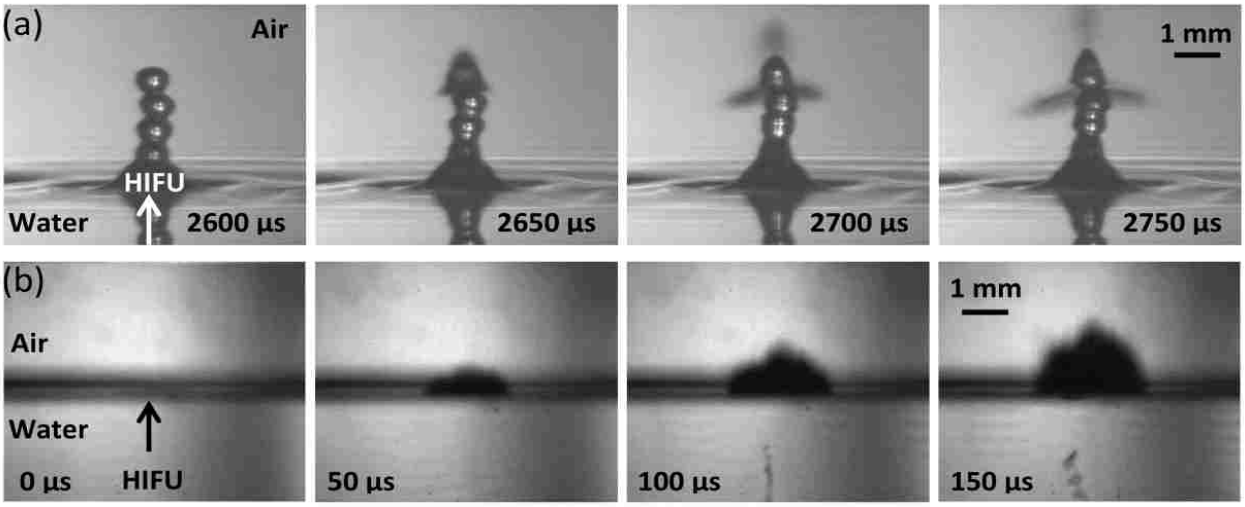

FIGURE 4.2: Air-water interface filmed with (a) the objective in air such that the reflections we see in the bottom of the frames are due to an optical reflection of the same jet and (b) the objective positioned so that half the objective is facing air and the other half facing water to observe effects in water and air simultaneously. (a) Shows a sequence of images taken at very low intensities (180 W/cm^2) with the camera positioned at a slightly downward angle to catch the surface of the water. Atomization does not occur until the drop chain emerges. At some point, the top drop becomes unstable and atomization jets are released. (b) A sequence of images showing the air to water interface at high acoustic intensities of 24,000 W/cm^2. Cavitation occurs before atomization or jetting and is faintly visible just to the right of the HIFU arrowhead in the first frame, which is taken 20 µs after the acoustic wave arrives at the water surface. As the ultrasonic pulse continues, the cavitation bubbles just below the water surface are joined by a cavitation bubble cloud further below the surface, possibly due to the standing wave pattern that develops upon the reflection of the acoustic wave. Total ultrasound exposure times were 10-ms.

in figure 4.2(a). While for this case, atomization occurred 2.65 ms into the pulse, in general, atomization does not occur in a predictable time at this intensity. The diameter of the drop chain is approximately 0.76 mm (this value oscillates slightly as the droplets compress and stretch while propagating upwards). The sizes of the individual emitted droplets are mostly less than a few microns, though a few emitted droplets reach up to 600 µm in diameter. In the sequence of images in figure 4.2(a), the drop becomes opaque 50 µs before the jets are emitted in a triangular pattern at a velocity of approximately 12 m/s in all directions. Possible explanations for such an explosive behavior of the droplet is discussed later in this chapter.

At the maximum focal acoustic intensity in water (I_L = 24,000 W/cm^2) cavitation bubbles appear beneath the surface of the water immediately before the violent ejection of

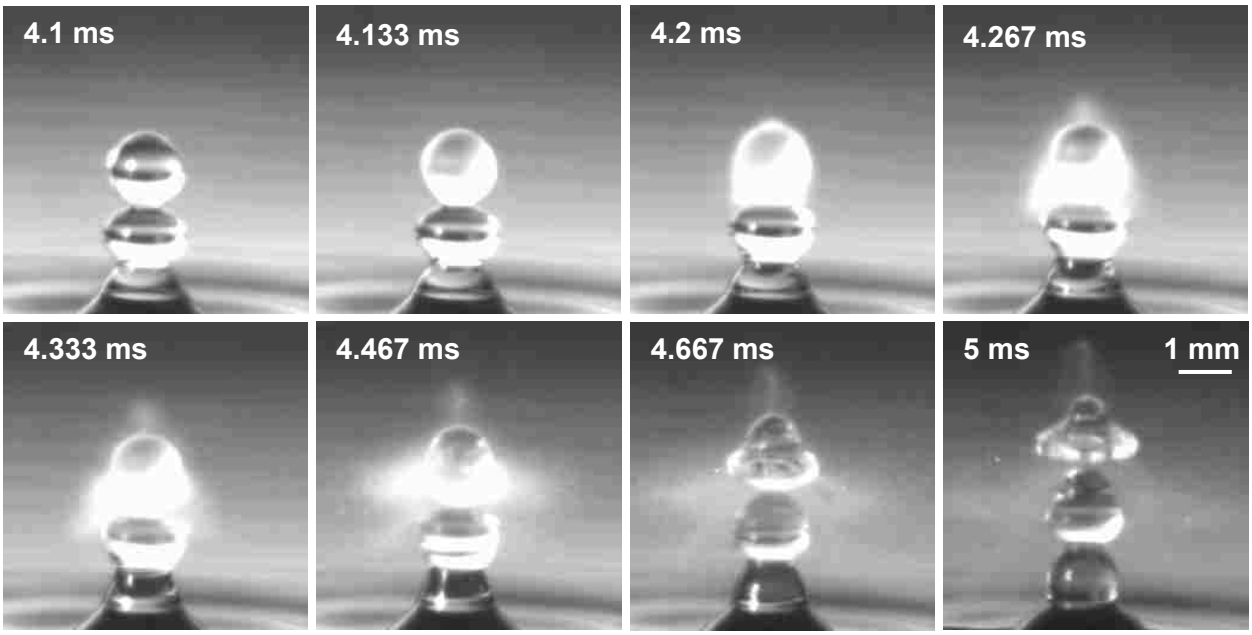

FIGURE 4.3: High speed video frames from the water-air interface exposed to 1 MHz focused ultrasound (p_+ = 3.1 MPa, p_- = 2.3 MPa) and filmed at 30,000 fps. The top water droplet in the first frame is very reflective, yet appears opaque 33 μs later as shown in the second frame. After the droplet becomes opaque, it begins to emit droplets in the same triangular pattern that was observed in the 2 MHz exposure (figure 4.2(a)). The fine mist of droplets continues to move away from the drop chain in the following frames. By the final frame, the top droplet in the drop chain is completely detached from the rest of the chain and is no longer even remotely spherical in shape. The entire atomization sequence takes place in less than 1 ms. The total ultrasound exposure was 10-ms in duration.

droplets from the surface as shown in figure 4.2(b). Standing waves can also be observed in the figure beneath the pressure-release interface. At this intensity, atomization, or the emission of fine droplets from the surface, occurs almost instantaneously, approximately 2 μs after the acoustic wave arrives at the interface. The jet velocity is approximately 11-15 m/s, which is on the same order as the jet velocity observed previously at very low intensities. As expected, the fountain heights in water depend on the acoustic intensity; the low amplitude fountain height is on the order of a few centimeters, while the high intensity fountain reaches the ceiling of the room positioned about 2 meters above the liquid surface.

When the ultrasonic frequency was changed to 1 MHz and operated at 245 W/cm^2 as is shown in figure 4.3, the drop chain diameter was 1.3 mm, which is about 0.5 mm greater than the drop chain diameter in the 2 MHz video. The emitted droplets ranged

in size from a few microns to tens of microns in diameter, with horizontal velocities of approximately 15 m/s, and vertical velocities of 7 m/s. For this video taken at 30,000 frames per second, the droplet changed from transparent/reflective to opaque in less than 33 μs, and the droplet explosion sequence occurred in less than 1 ms. While the original drop in the chain was spherical in shape, by the end of the atomization event, the droplet was vaguely ellipsoidal in shape and was separated from the rest of the drop chain. About 1 ms after this video within the same 10-ms ultrasonic exposure, the middle droplet (which has become the top droplet since the original top droplet disconnected) also explodes, exciting atomization events in droplets lower in the chain. Even though the high speed video frame rate for atomization at 1 MHz was 10,000 fps faster than was recorded for atomization at 2 MHz, atomization events appear remarkably similar between the two frequencies.

Figure 4.4 shows a sequence of high speed frames taken in water with the 155 kHz transducer operating at an intensity of 264 W/cm^2 ($p_+ = p_- = 2.8$ MPa). The high speed frame rate of 5000 fps was much lower than the frame rate used for the previous two figures, because of the larger dimensions of the drop chain (camera resolution is related to frame rate), and the length of pulse required for atomization to occur. The diameter of the drop chain was 7.8 mm and jet velocities were approximately 2-4 m/s. Most of the emitted droplets ranged from tens to hundreds of microns in diameters; however several of the emitted droplets exceeded one millimeter in diameter. When comparing atomization at 155 kHz to atomization at 1 MHz or 2 MHz, we find that atomization proceeds very differently. At 155 kHz in figure 4.4, an initial jet forms in the neck region between the top two droplets. This initial jet is very large and appears to travel up the side of the top drop in the chain. Between the third and the fourth frames, the droplet appears to become opaque; the lighting for this high speed video makes it difficult to be certain of the droplet opacity. In the fourth frame, we see a new jet that has formed on the same side (and in the same general area) of the drop chain as the initial jet. This new jet appears to excite a jet on the opposite side of the drop chain, as shown in the fifth frame; droplets continue to be released from these two jets positioned in the neck region between the top two drops in the drop chain. It is interesting to note that figure 4.4 shows jetting in only two directions as compared to the triangular jetting that was

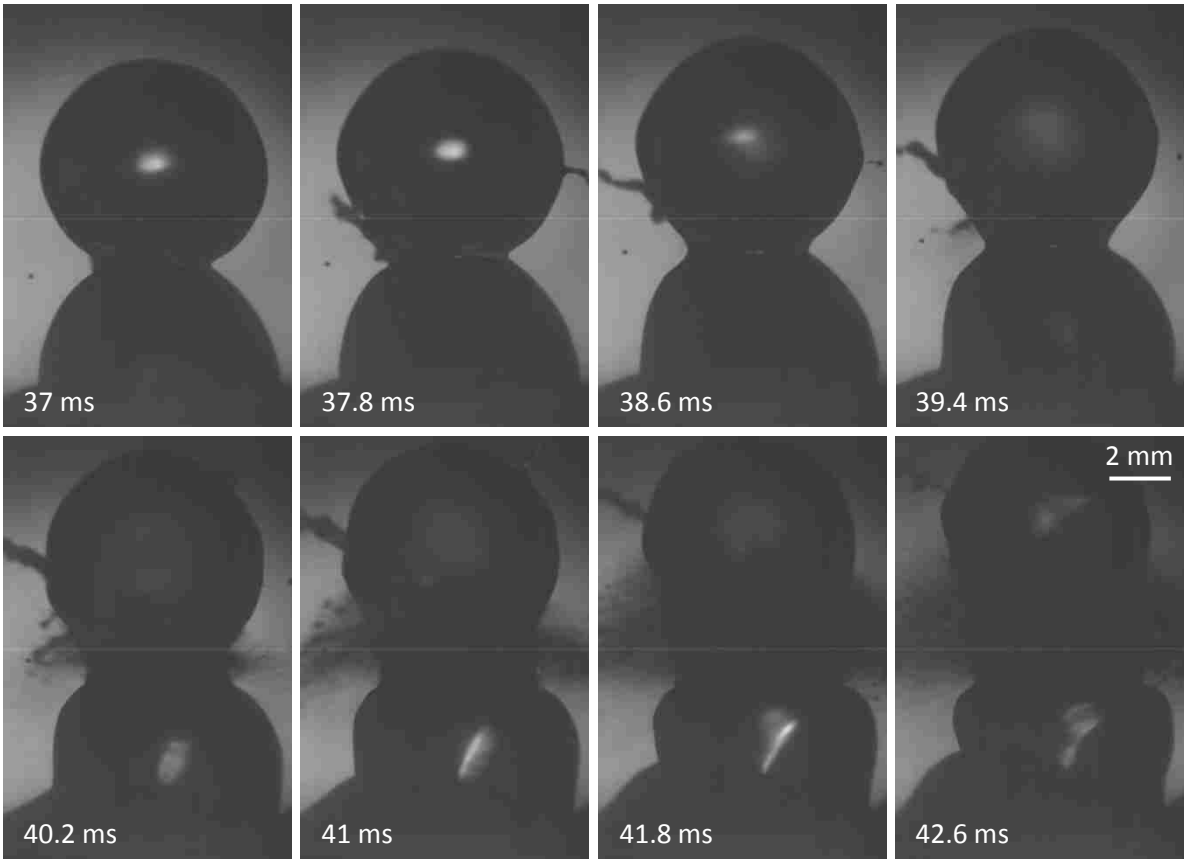

FIGURE 4.4: Selected frames from the high speed video of an air-water interface exposed to 155 kHz ultrasound at 264 W/cm^2 (p_+/p_- = 2.8 MPa) and filmed at 5000 fps. The first frame shows the drop chain with no jetting. In the second frame, a jet emerges from the right hand side of the top droplet, with some jetting from the neck region between the two droplets. While the jet on the right is released in the third frame, the instability on the left continues and moves upward. By the fourth frame, an additional jet has formed on the left side of the drop chain. The new jet is more developed by the fifth frame and excites a jet on the opposite side of the drop chain; the fifth frame also shows one additional jet being emitted from the upper right hand side of the top droplet. The sixth through eighth frames show that the jetting from between the top two droplets continues, releasing many fine droplets from the chain. The total ultrasound exposure time was 64.5 ms (10,000 cycles).

observed in figures 4.2(a) and 4.3. Also of note, the top droplet in the drop chain shown in figure 4.4 does not show the significant shape distortion that was observed at the other frequencies. Even though atomization at 155 kHz does not proceed in the exact same manner that was observed at 1 MHz or 2 MHz, the mechanism of atomization appears to be relatively similar across the frequencies observed here.

4.2.3. Discussion

In this section, we used high speed photography to show that changing the ultrasonic frequency at relatively low intensities does not significantly affect atomization. Unsurprisingly, we noted that decreasing the frequency of the transducer increases the droplet diameter in the drop chain fountain. In fact, if we calculate the wavelength in water for each frequency, we find the diameter of the drop chain and the calculated wavelength is approximately equal (at least for transducers where the f-number is one). We also calculated the capillary wavelength at the three different frequencies; however the resolution of the current camera setup made it difficult to determine whether the size of the emitted droplets equaled the capillary wavelength. As the videos show directional jetting or droplet release, we do not expect that capillary waves are a dominant mechanism of atomization, at least for focused waves at these intensities. Were capillary waves a dominant mechanism, we would expect a significant section of the droplet surface to be emitting the fine mist, rather than jetting from two to three isolated sections of the droplet in the chain.

We also calculated the particle velocity which is expected to be similar to the observed water jet velocity. At the low intensities for all three frequencies, the calculated particle velocity is 2 m/s; the velocities observed in the high speed videos ranged from 2-15 m/s. Interestingly, the jet emitted vertically from the drop chain during atomization at 155 kHz was very similar to the calculated particle velocity of 2 m/s, though the horizontally ejected particles had jet velocities of up to 4 m/s. However, when the frequency was increased to 1 MHz or 2 MHz, the particles were ejected at much higher velocities of 7 – 15 m/s. It is compelling to note that the observed velocities do not appear to depend on the ultrasonic intensity; when the intensity was increased at 2 MHz to 24,000 W/cm^2, jet velocities ranged from 11-15 m/s, a range which includes the observed velocity of jets emitted from the drop chain at the low intensity. The calculated particle velocity at the high intensity was 43.7 m/s, for the shocked wave, or 18 m/s for a linear wave of similar intensity. While the calculated particle velocity for the linear wave approaches the maximum observed jet velocity, we expect this is just coincidence as the maximum observed velocity should approach the particle velocity calculated for the shocked wave if the droplet release mechanism was related to the particle movement from the ultrasound wave.

Using the calculated and observed particle velocities, we predicted the maximum height of the atomized droplets. At the 24,000 W/cm^2 intensity, water jets were expelled over 2 m into the air (they reached the ceiling of the room); however the predicted height was almost 100 m when the shocked wave particle velocity was used. If we repeat the calculation using the observed jet velocity, the maximum droplet height reduces to about 3 m, which is much closer to our observed fountain height. At the lower intensities, the jet height calculated from the predicted particle velocity was 20 cm; however we observed a maximum jet height of only a several centimeters. In this case, it is very possible that the small atomized particles reached higher into the air than we could observe without magnification; however the small droplet size would make them particularly sensitive to air currents, which would prevent an accurate measurement of jet height. A summary of the calculated and observed drop chain diameters, capillary wavelengths/droplet diameters, and droplet/particle velocities are included in table 4.1.

One explanation for the explosive behavior of the droplets shown in figures 4.2(a), 4.3 and 4.4 is that they are a result of instabilities caused by the acoustical excitation of the droplet. When the droplet is formed, at some stage it becomes disconnected (or only slightly connected) from the neighboring droplets in the chain. Note that such a droplet becomes a highly excited spherical acoustic resonator because it has taken a portion of the acoustic energy that was initially in the fountain. Studies on the free oscillations of liquid droplets began more than one hundred years ago, first by Kelvin (1890) then Rayleigh (1894). Oscillations of liquid drops are of interest in many areas of science, *e.g.,* in chemical engineering; raindrop behavior is important in cloud physics. It is

TABLE 4.1: Comparison between calculations and observations for the 3 frequencies.

	Intensity (W/cm^2)	Acoustic Wavelength (Calculated)	Drop-Chain Diameter (Observed)	Capillary Wavelength (Calculated)	Calculated Particle Velocity	Observed Particle Velocity
2 MHz High	24,000	N/A	N/A	7.3 μm	43.7 m/s	11-15 m/s
2 MHz Low	180	0.69 mm	0.76 mm	7.3 μm	1.68 m/s	12 m/s
1 MHz Low	245	1.43 mm	1.3 mm	11.9 μm	2.09 m/s	7-15 m/s
155 kHz Low	264	9.59 mm	7.8 mm	42.4 μm	1.88 m/s	2-4 m/s

known that drop oscillation can become unstable; when non-spherical deformations of the drop shape develop, the drop can be broken into pieces. These instabilities are one possible reason for the observed explosion of droplets in a fountain. Another possible reason is that cavitation may occur inside the droplet that is oscillating radially (in a "breathing" mode). Such cavitation most probably starts in the center of the droplet, where the standing acoustic wave is at maximum amplitude. Before cavitation starts, the droplet oscillates in breathing mode, meaning periodic radial movement of liquid inwards and outwards from the droplet center. Once cavitation starts, the movement of liquid outwards from the center of the drop cannot be stopped and thus continues to move due to inertia; as a result, the droplet explodes. There is yet another possible explanation for the droplet explosion: boiling in its center. Such boiling may be a result of dissipation of the initial energy of the acoustically excited drop. The heat deposition is localized in the center of the droplet, especially when higher acoustic harmonics are developed. Superheating of the droplet may result in the center temperature exceeding 100 °C and forming a rapidly growing vapor bubble that makes the droplet explode. Narrowing these hypotheses to describe the explosive behavior of the droplet is a goal of this chapter.

In an attempt to discern the contribution of bubbles to atomization, particularly at low intensities, we made an effort to "see" within the droplet. By changing the lighting and filming parameters, we were occasionally able to observe a shadow within a droplet, which is thought to be a bubble, shortly before atomization commences. Several

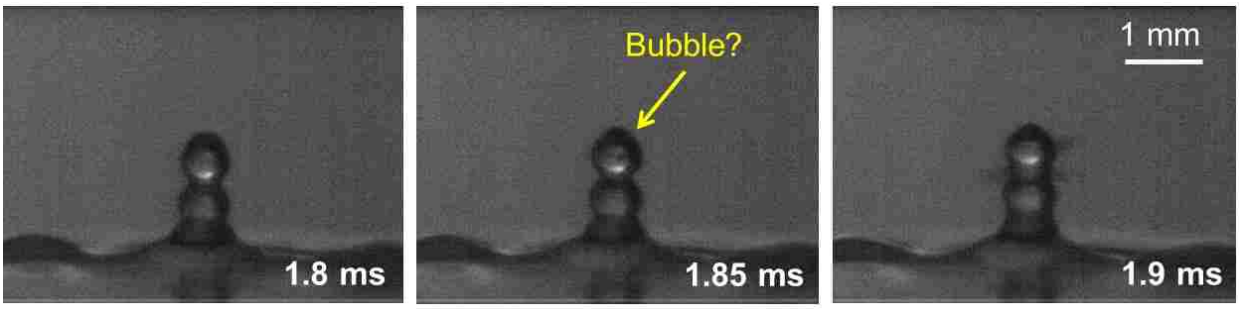

FIGURE 4.5: Diffusely-lighted air-water interface exposed to 2 MHz ultrasound at 180 W/cm^2 and filmed at 20000 fps. The first frame shows the drop chain with no jetting. The second frame shows a shadow in the top drop of the chain, which appears to be a bubble. In the third frame, which is taken only 0.1 ms after the initial frame, jets are being emitted from the drop chain at velocities up to 16 m/s. The total ultrasonic exposure was 10-ms.

frames from the video of this phenomenon is shown in figure 4.5. The exposure was conducted with the 2 MHz transducer operating at 180 W/cm^2 (p_+ = 2.5 MPa, p_- = 2 MPa). In the middle frame, a dark shadow appears near the center of the top droplet, and in the following frame (taken 50 μs later) jets are being emitted from the droplet at velocities up to 16 m/s. From this video, we can surmise that bubbles can cause atomization; however it is unclear whether bubbles are necessary for atomization, or whether bubbles are simply one form of droplet ejection in atomization. It is also unclear whether the bubble arose from cavitation or boiling. In the next section, we atomize liquids with various physical properties in an attempt to discern whether bubbles are essential for atomization.

4.3. Atomization of Different Liquids

4.3.1. Methods

Heated Water Atomization

Before atomizing different liquids, a simple experiment was conducted to determine whether boiling was a possible explanation for atomization in the drop chain. Water was heated to approximately 60 °C and allowed to cool. The same 2-MHz ultrasound transducer that has been described previously was used to fountain water at regular intervals while it cooled. A thermocouple was used to measure the water temperature for each exposure and the timing of atomization was recorded for two different acoustic intensities. The first intensity of 180 W/cm^2 was chosen because it was the intensity at which 20 °C water atomized inconsistently. A second, higher intensity of 350 W/cm^2 was chosen as 20 °C water consistently atomized at this intensity. The time for atomization to begin was plotted versus temperature for both intensities to determine whether a relationship might exist between heat and atomization. The same experimental setup that is shown in figure 4.1 was used for this experiment.

Atomization of Different Liquids

A reprise of the experiments conducted in the 1960's and 1970's was conducted here with a focus on manipulating the shear viscosity of the liquid using the experimental

arrangement shown in figure 4.6. Water (shear viscosity 0.0009 Pa·s), ethanol (0.001 Pa·s), castor oil (0.99 Pa·s), and glycerol (1.2 Pa·s) were placed at the focus of the 2 MHz transducer and filmed with the Photron APX-RS high speed camera. The liquid was held in a custom-designed container with an acoustically transparent, thin plastic film bottom. The container was placed in water such that the bottom of the container was positioned just below the water surface. The thickness of the liquid layer was variable between 2-15 millimeters. The transducer was focused at the liquid surface using pulse echo with the timing recorded on a digital oscilloscope (Model LT432, Lecroy, Chestnut Ridge, NY, USA). The same 2 MHz transducer, camera, lens, amplifier and lighting were used as were described in the previous section.

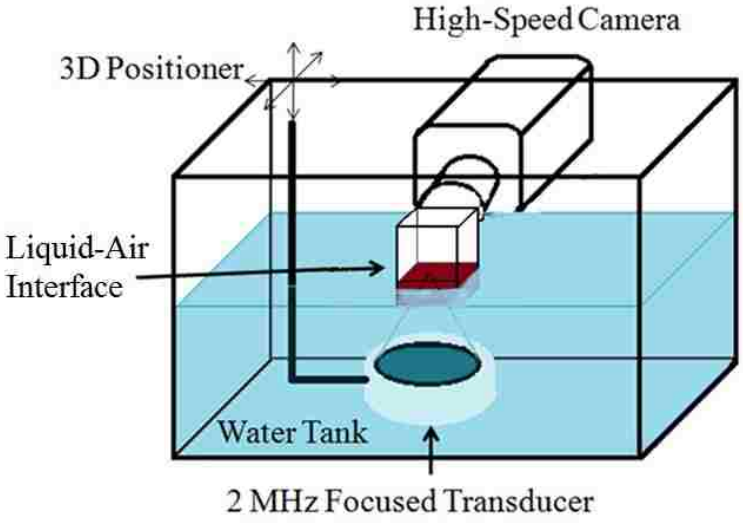

FIGURE 4.6: Experimental arrangement for atomization of various liquids. Experiments are backlit (not shown).

TABLE 4.2: Properties of liquids used at 25 °C and 2 MHz

Liquid	Density	Sound Speed	Boiling Point	Attenuation	Shear Viscosity	Surface Tension
	kg/m^3	m/s	deg. C	dB/cm	mPa·s	mN·m
Water	998	1486	100	0.0087	0.9	72.8
Ethanol	785	1144	78	0.0018	1	22
Castor Oil	960	1474	313	1.04	990	35.1
Glycerol	1260	1904	290	1.84	1200	64
n-Propanol	803	1205	97	0.0023	1.96	24
Olive Oil	915	1440	300	0.4	84	36
1,3-Butanediol	1000	1522	204	0.2	97	37

*From [93], [98], [99]

Three other liquids were used in this experiment, though shear viscosity was not the primary liquid property of interest. The full list of liquids used in this experiment and their physical properties are listed in table 4.2. The first liquid was n-propanol, which was chosen because the boiling point of n-propanol (97 °C) is similar to that of water (100 °C) and the shear viscosity of n-propanol (0.00196 Pa s) is only double that of water. The other two liquids of interest were olive oil and 1,3-butanediol as a recent paper by Maxwell et al. demonstrated that the cavitation threshold of both olive oil and 1,3-butanediol exceeded -30 MPa [93]. An advantage of these two liquids over castor oil and glycerol is that 1,3-butanediol and olive oil have densities and sound speeds that are similar to water.

4.3.2. Results

Heated Water Atomization

The plot showing the timing of the initial atomization event versus temperature is plotted for the two different intensities in figure 4.7. From the figure, a general linear trend is apparent; as the temperature increases the time to the commencement of atomization decreases. Interestingly, if a linear fit were performed for the data points of both intensities, the slope of the 180 W/cm^2 line is steeper. This is notable as atomization occurs inconsistently at that intensity when water is at 20 °C. However, while these

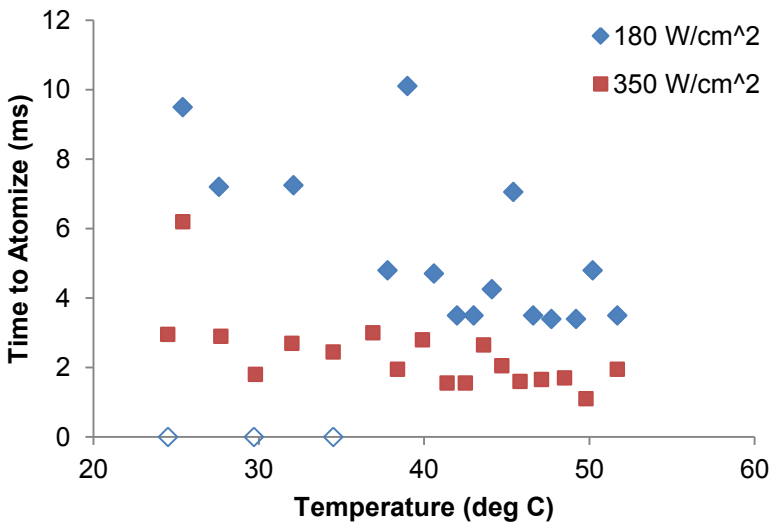

FIGURE 4.7: Plot showing the atomization timing versus temperature for water at two different intensities. The blue diamonds mark atomization timing at the 180 W/cm^2 intensity; the three blue diamond outlines at 0 ms are instances where atomization did not occur. The red squares show atomization versus temperature for the 350 W/cm^2 intensity. For both intensities, the timing for atomization decreases with increasing temperature.

results seem to support the boiling mechanism of atomization, the results are not conclusive as heat also affects the surface tension and viscosity of water, which change the cavitation threshold. Over the 40 °C temperature increase, the surface tension of water decreases by 7 mN/m and the shear viscosity is halved, changing from 0.9 mPa s at 20 °C to 0.553 mPa s at 50 °C [99]. Therefore, while these results suggest the importance of bubbles in the explosive atomization of the drop chain fountain, we are unable to completely eliminate cavitation to conclude that boiling causes atomization in a drop chain.

Atomization of Different Liquids

When high viscosity liquids such as castor oil and glycerol are placed at the transducer focus as in figure 4.8(b,c), a fountain forms but atomization does not occur, even for very thin liquid layers (~2 mm) exposed to the maximum acoustic intensity of 24,000 W/cm^2. In 70% ethanol (figure 4.8a), which has a viscosity approximately equal to that of water but one-third of the surface tension (72 mN/m in water and 22 mN/m in ethanol), atomization occurs relatively similar to water; at the 180 W/cm^2 intensity in ethanol, there are a few relatively large droplets (~200 μm in diameter) ejected at a velocity of approximately 2.4 m/s. Overall, the droplets emitted from 70% ethanol are much larger the droplets emitted from water (for the same acoustic intensity) and the larger droplet size is accompanied by a decrease in the droplet velocity.

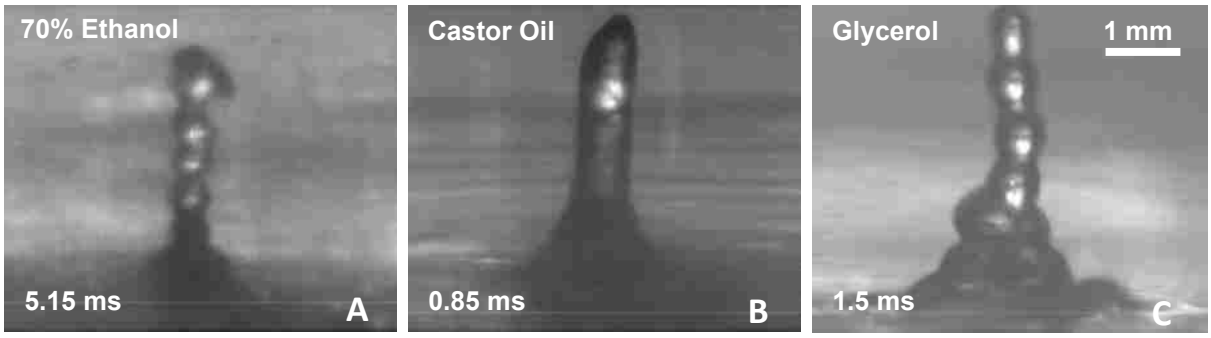

FIGURE 4.8: Frames taken from the high speed videos of A) 70% ethanol at a 180 W/cm^2 acoustic intensity, B) castor oil at a 24,000 W/cm^2 intensity, and C) glycerol at a 24,000 W/cm^2 intensity. In ethanol (A), the intensity was just above its atomization threshold; on the upper left just under the"70% ethanol" label, you can see a droplet that was ejected from the fountain. In both castor oil (B) and glycerol (C), the intensity was at the maximum output of the transducer and atomization did not occur (*i.e.* no droplets were emitted from the fountain).

Comparing the fountains in figure 4.8 to what has been observed previously in water, ethanol and glycerol form drop chain fountains similar to water; however the sides of the castor oil fountain are smooth, with no drop chain structure. The diameter of the drop chain in glycerol is 0.78 mm, and the diameter of the fountain in castor oil is 0.77 mm, both of which are very similar to water. In contrast, the diameter of the drop chain of ethanol is smaller at only 0.54 mm. Additionally, at the maximum acoustic intensity, the drop chain in glycerol propagates vertically at 2 m/s, while the fountain in castor oil propagates vertically slightly faster than glycerol at 2.4 m/s. It is interesting that both the fountain diameters and velocities are similar for castor oil and glycerol, even though the glycerol fountain has a drop-chain structure while castor oil does not.

When the thresholds for consistent atomization in one 10-ms pulse excited by 2 MHz ultrasound were compared for water, 70% ethanol, glycerol, bovine liver, and porcine blood clots, it was found that the *in situ* intensity thresholds increased in the order: ethanol (180 W/cm^2) < blood clot (250 W/cm^2) < water (350 W/cm^2) < liver (6200 W/cm^2); glycerol and castor oil did not atomize (details in table 4.3). If we separate the liquids from the tissues, the atomization threshold basically increases with the increase in shear viscosity. At intensities near the threshold, the liquids formed a drop-chain fountain before atomization (shown in previous studies [51]). For all species that atomized, the average jet velocity at the maximum intensity (24 kW/cm^2 in water) were similar and on the order of 10 m/s. Furthermore, we determined that the jet velocities were inversely related to the size of the ejected droplets.

TABLE 4.3: Summary of atomization and fountain results for 6 materials[a]

Material	Threshold Intensity	Max Mound Width at Base[b]	Time to Atomize	Fountain Height	Jet Velocities
Water	350 W/cm^2	4.0 mm	2 µs	< 1 mm	11 m/s
Castor Oil	NA	8.5 mm			
Glycerol	NA	8.6 mm			
70% Ethanol	180 W/cm^2	3.1 mm	~ µs	< 1 mm	25 m/s
Blood Clot	250 W/cm$^{2,\,c}$	3.2 mm	> 20 µs	1.5 mm	10 m/s
Liver	6200 W/cm$^{2,\,c}$	5.5 mm	20 µs	1 mm	13 m/s

[a] Unless otherwise specified, results are for the maximum acoustic intensity (24,000 W/cm^2) and 1 10-ms pulse
[b] Base width measured at threshold intensity
[c] *In situ* intensity

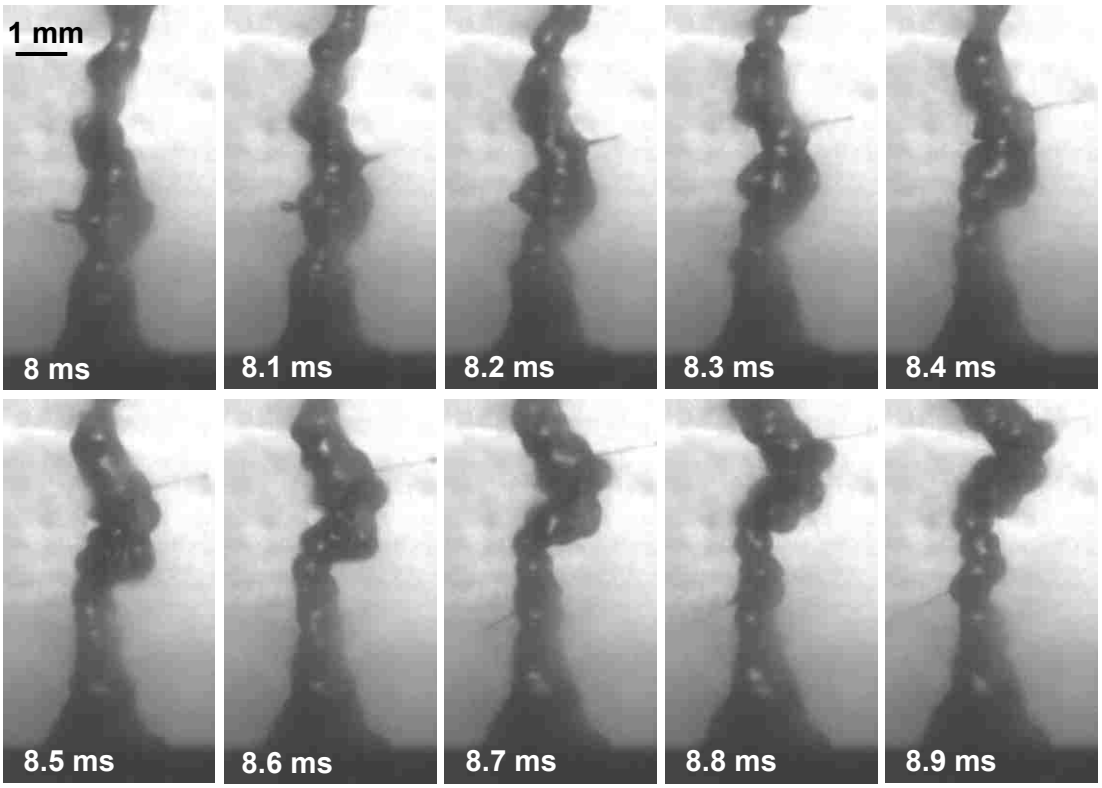

FIGURE 4.9: Frames taken from the high speed video (10,000 fps) of olive oil when exposed to 550 W/cm^2 (p_+ = 5.5 MPa, p_- = 4 MPa), the threshold of atomization for olive oil. From the image sequence, we can see a jet being emitted from the drop chain on the right hand side starting at 8.1 ms. The jet velocity is 3.7 m/s. In the frame taken at 8.7 ms, we can see a jet emitted from the left hand side of the drop chain with a velocity of 5.3 m/s. The emission of jets in olive oil looks qualitatively different from the drops emitted from the water drop chain. The total ultrasonic exposure time was 10-ms.

After analyzing the effect of shear viscosity on atomization, olive oil and 1,3-butanediol were tested for atomization because of their relatively low shear viscosities but very high cavitation thresholds [93]. Figure 4.9 shows a sequence of high speed video frames in olive oil with the 2 MHz transducer operating at an intensity of 550 W/cm^2 (p_+ = 5.5 MPa, p_- = 4 MPa), the threshold for atomization in olive oil. In the second frame taken at 8.1 ms, a thin jet is emitted from the right hand side of the drop chain at 3.7 m/s. The emitted droplet is approximately 70 μm in diameter. Another jet is emitted in the 7th frame at 8.7 ms with a velocity of 5.3 m/s. Both of these jets look very different from the jets observed during water atomization at any intensity. Nevertheless, the diameter of the drop chain in olive oil is 0.76 mm, which is approximately equal to the drop chain diameter in water at its threshold intensity. Atomization in 1,3-butanediol at

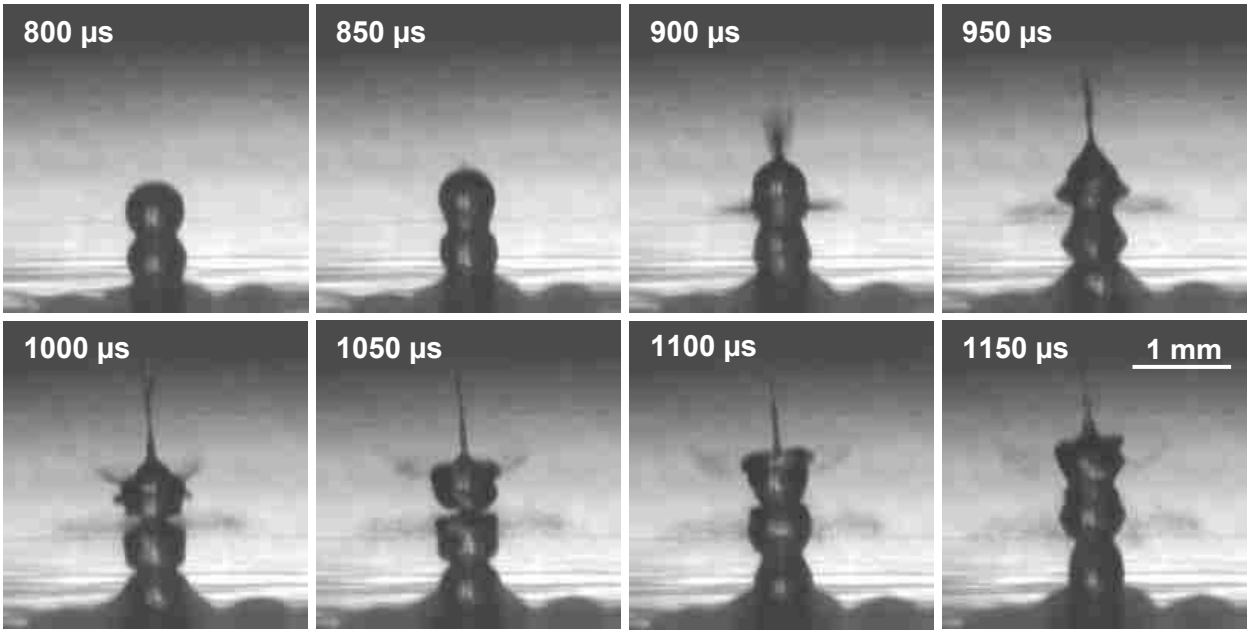

FIGURE 4.10: Frames taken from the high speed video (20,000 fps) of n-propanol at 365 W/cm^2 (p_+ = 4 MPa, p_- = 3 MPa). The first frame taken at 0.8 ms shows the drop chain. In the second frame (taken 50 µs after the first frame) the top droplet of the chain is already starting to atomize, as seen by the shading just above the droplet. The third frame shows triangular atomization, which is very similar to what was observed in water. The triangular atomization causes more atomization to occur at the 1 ms time point. The total ultrasonic exposure time was 10-ms.

2 MHz (not shown) appears qualitatively very similar to olive oil atomization. The atomization threshold is slightly higher than olive oil at 1000 W/cm^2 (p_+ = 9.6 MPa, p_- = 5.4 MPa), and jet velocities range from 2-7 m/s. As in olive oil, the diameter of the drop chain is 0.7 mm, which is again very similar to that of water. In both olive oil and 1,3-butanediol at the 550 W/cm^2 intensity, the drop chain propagates vertically at approximately 3.5 m/s (3.4 m/s for 1,3-butanediol, and 3.7 m/s for olive oil), which is notably higher than the drop chain velocity of 2.9 m/s observed in water at the same intensity. Nevertheless, with the reported cavitation threshold of more than 30 MPa in olive oil and 1,3-butanediol [93], it was very interesting that atomization occurred at all, let alone at such low acoustic intensities.

Atomization was tested in one other liquid, n-propanol, because it has a boiling point of 97 °C, which is almost equal to that of water. Figure 4.10 shows frames from a high speed video of n-propanol when exposed to 2 MHz ultrasound at an intensity of 365 W/cm^2 (p_+ = 4 MPa, p_- = 3 MPa). The first frame of the figure shows the drop chain

fountain; the top droplet of the chain begins to atomize 50 μs later. In the third frame, we can see that atomization occurs in a triangular pattern, which appears very similar to that of water (shown in figure 4.2(a)). The triangular atomization excites two more atomization events, which are shown at the 1 ms time point. The velocity of the jets range from 5.6-10.2 m/s, with the upper end of the range corresponding to the velocity of the jets emitted from the top droplet in the triangular pattern and the lower end corresponding to the velocity of the secondary side jets (5.6 – 7.1 m/s). During the exposure, the drop chain propagated vertically at a fairly constant 2.5 m/s and the drop chain diameter was 0.62 mm. Except for the long thin jet ejected from the uppermost surface of the top droplet, the atomized droplets are very small and on the order of tens of microns in diameter (measurement limited by camera resolution). The qualitative and quantitative similarities between the atomization of n-propanol and water suggest that boiling may explain atomization within the drop chain.

4.3.3. Discussion

In our first experiment in this section, we found that when water was heated, the time for atomization commencement decreased with increasing temperature. This led to the conclusion that atomization was due to either cavitation (as the cavitation threshold in water decreases with heating [100]), or it was due to boiling. According to Herbert et al., the cavitation threshold decreases by 4 MPa when water is heated from 20 °C to 50 °C; however differences in water quality and cavitation detection techniques make it difficult to find concurring water cavitation thresholds in the literature [100]. Besides affecting the cavitation threshold, Li et al. has found that water fountains can cause significant heating [101]. If we assume that the acoustic intensity remains constant (without potential focusing effects from the spherical drop in the chain) increasing the water temperature by 30 °C, reduces the time to boil by approximately 40% (when thermal diffusion is neglected). While the results from our water heating experiment suggest the involvement of bubbles in the atomization of the water drop chain, without a thorough understanding of how the drop chain affects the acoustic wave propagation, it is difficult to determine whether boiling or cavitation causes the explosion in the drop chain.

In the second experiment, we tried to atomize liquids with varying shear viscosities and found that as the shear viscosity increased, the atomization threshold increased. These observations of fountain formation and the commencement (or lack) of atomization in liquids of varying viscosity concur with the lack of atomization seen by previous researchers upon increasing the static pressure or lowering the gas content in the liquid [50], [92], [102]. Unfortunately, changing the viscosity or static pressure of the system affects both cavitation and boiling bubbles, causing these results to really only highlight the importance of bubbles in atomization.

In an effort to isolate the effects of cavitation and boiling, atomization was attempted in three additional liquids. While atomization occurred in both 1,3-butanediol and olive oil, liquids that have been previously shown to have very high cavitation thresholds, the jets appeared qualitatively very different to atomization of water. Instead of fractionating into small droplets, olive oil and 1,3-butanediol released long, thin jets from the drop chain; however, both liquids had drop chain diameters and velocities that were similar to water at their respective threshold intensities. Even though the reported cavitation thresholds of 1,3-butanediol and olive oil are well beyond the maximum output of the transducer used here, atomization could still be explained by cavitation if one considers the potential for standing waves from the acoustic reflections within the drop chain. The qualitative differences observed in the jetting between olive oil/1,3-butanediol and water could be explained by the differences in physical properties between the liquids.

The final liquid of interest was n-propanol because it has a boiling point that is almost equal to water, but a shear viscosity that is double that of water. Atomization of the n-propanol drop chain appeared remarkably similar to water atomization; the atomized droplets were emitted in a triangular pattern from the top droplet, and had similar velocities and droplet sizes to water (for 2 MHz ultrasound at similar intensities). As n-propanol has a similar boiling point to water, but double the dynamic viscosity and approximately one-third the surface tension, these results seem to indicate boiling as the mechanism of atomization in drop chains. Clearly, more research into the mechanisms of atomization is needed.

While a variety of liquids have been atomized in this section, the results are inconclusive as to whether cavitation or boiling is the primary mechanism of atomization in liquids. Overall, the results appear suggest that boiling is the driving mechanism of atomization in a drop chain; however it is difficult to totally eliminate cavitation as a mechanism of atomization in a fountain. Additionally, in some of the high speed videos, it appears as if spherical resonance and modal instabilities of the drop chain drive atomization. While these studies in a variety of liquids are necessary as we attempt to understand atomization in a liquid fountain, the results remain inconclusive. In the next section, we complicate the mechanism of atomization even further by considering atomization in viscoelastic materials.

4.4. Atomization in Viscoelastic Solids

While the exact mechanism of atomization remains unclear in liquids, the novelty of this work is the evidence that atomization can occur in tissues or viscoelastic solids. In this section, we will endeavor to understand the importance of bubbles in tissue atomization.

4.4.1. Methods

Atomization in Tissue-Mimicking Gels

In the previous chapter, we showed that wetting the surface of the tissue-mimicking polyacrylamide gel with water caused atomization to become successful in eroding the gel surface. To investigate how surface wetting increases erosion, we wetted the gel surface with the same liquids of varying physical parameters that were used in the previous section. As we already know whether or not the liquid, itself, atomizes, we expect that observing atomization with the high speed camera above and below the gel surface in addition to monitoring surface erosion will help us to elucidate the mechanism of atomization in tissues. Even though we described the process used to make the gel in the previous chapter, we will briefly reprise it here for completeness. The gel was prepared as described in Lafon et al. [82]; filtered water was mixed with a 40% w/v acrylamide solution (Sigma-Aldrich, St. Louis, Missouri, United States), a TRIS buffer with a pH of 8, and 2% BSA. The solution was degassed for at least one hour in a desiccant chamber at -85 kPa before adding 10% w/v ammonium persulfate solution

(Sigma-Aldrich), and N,N,N',N'-methylethylenediamine (Sigma-Aldrich). The complete solution was poured into a mold with surface dimensions of 2.5 cm x 2.5 cm and a thickness of 1-1.5 cm and allowed to solidify. The experimental setup was the same as described in the previous section (without the thin plastic film on the bottom of the holder) and shown in figure 4.6.

Seven separate gels were poured from the same gel mixture, one for each of the seven different wetting liquids (water, 70% ethanol, castor oil, glycerol, n-propanol, olive oil, or 1,3-butanediol). For each gel, the surface was dried and atomization was attempted to ensure that the surface had been dried enough that atomization was not successful. Then, 1 mL of the wetting solution was added to the gel surface. The gel was then exposed immediately to 10 pulses of 10-ms duration repeated at 1 Hz with the 2 MHz transducer at the maximum intensity (24,000 W/cm^2 in water). The exposure was filmed with the Photron APX-RS camera. Approximately five minutes after the first exposure (the time it took for the first video to save), a new location in the gel surface was exposed to 60 pulses (same parameters) and filmed with the high speed camera to monitor whether atomization changed after the wetting liquid interacted or settled on the gel surface. Videos were recorded at 10,000 fps with backlighting by the Photogenic light source (as described in section 4.2.1). While the same camera objective was used for this experiment as has been described previously, the f-number was adjusted as high as possible to allow for clear focusing both below and above the gel surface. At the end of the exposures, the gel was removed from the container and photographed to record the size of the eroded volume.

Subsurface Observations of Liver Atomization

While the polyacrylamide gel is acoustically very similar to tissue (when the BSA concentration is 7%) and is transparent, which allows us to observe atomization below the viscoelastic surface, structurally the gel is very different from tissue. To relate our results in gel to tissue, we used B-mode ultrasound to observe atomization below the tissue surface. Even though we cannot observe atomization beneath the tissue surface during atomization with B-mode because of interference from the HIFU pulse, we can see whether any bubbles persist at the end of the HIFU pulse. This experiment is the

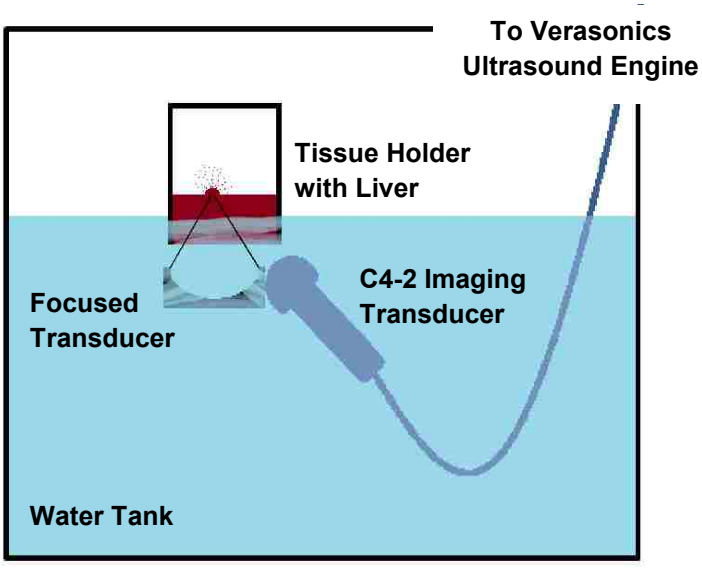

FIGURE 4.11: Experimental setup showing the alignment of the tissue sample, the 2 MHz focused transducer, and the C4-2 imaging transducer. The imaging transducer was connected to the Verasonics Ultrasound Engine which controlled the ultrasound pulsing and mapped the received signals.

next step towards determining the influence of bubbles in tissue atomization.

A Philips C4-2 (Bothell, WA, USA) ultrasound transducer and the Verasonics® Ultrasound Engine (Verasonics, Inc. Redmond, WA, USA) were used to image the tissue during atomization. The same 2 MHz HIFU transducer that has been described previously was used to atomize the tissue with 10-ms pulses repeated at 1 Hz at the maximum *in situ* intensity of 14,000 W/cm^2. The ultrasound imaging transducer was placed at an angle within the water below the tissue sample and out of the HIFU propagation path as shown in figure 4.11. The imaging frequency was 3 MHz and the frame rate of the ultrasound image was 20 fps; however the video recording software captured fewer frames. B-mode videos were saved for later analysis. Liver was purchased the day of experimentation from Schenk Packing (Stanwood, WA), transported on ice, and stored in phosphate-buffered saline until use.

4.4.2. Results

Atomization in Tissue-Mimicking Gels

After confirming that the surface of the 2% BSA tissue-mimicking polyacrylamide gel was dry enough to prevent atomization and erosion, 1 mL of one of the seven solutions (water, 1,3-butanediol, n-propanol, castor oil, glycerol, 70% ethanol, and olive oil) was

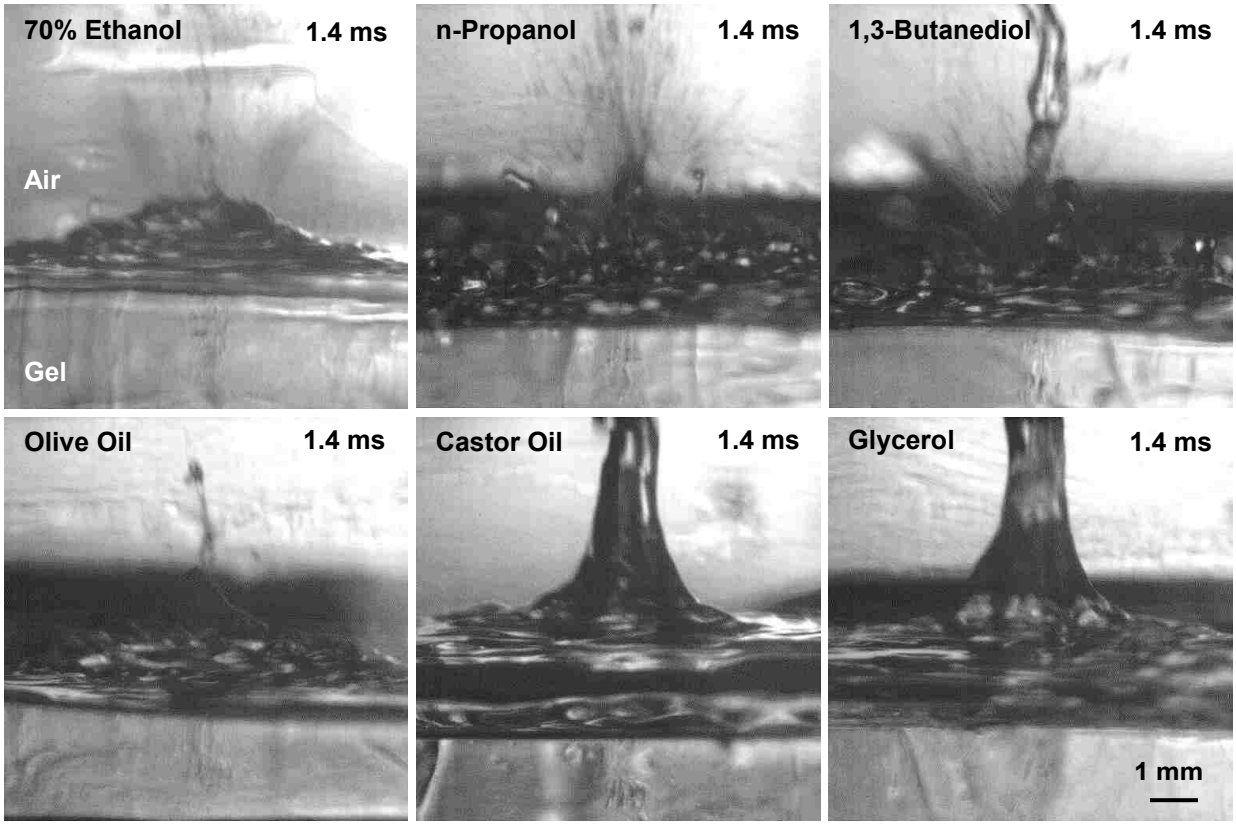

FIGURE 4.12: Frames taken 1.4 ms into the HIFU pulse from the high speed videos immediately after 70% ethanol, n-propanol, 1,3-butanediol, olive oil, castor oil, or glycerol was added to the surface of the tissue-mimicking polyacrylamide gel. From the images, it is apparent that the liquid fountain on the gel surface looks very similar to the liquid-only fountains observed previously. The exception is 70% ethanol where the low boiling point of ethanol caused rapid evaporation from the gel surface. Even though the amount of liquid on the gel surface obscures our view of the gel surface, all of the videos show at least some degree of bubble activity within the gel. HIFU exposures were with the 2 MHz transducer at the maximum acoustic intensity of 24,000 W/cm^2 (p_+ = 65 MPa, p_- = 16 MPa).

added to the gel surface and immediately atomized. The exposures were filmed with the high speed camera and one frame (taken at 1.4 ms) from each liquid-wetted gel is shown in figure 4.12. (As the atomization of the dry gel surface and the water-wetted gel surface are shown in figure 3.6, they will not be included in this section.) In general, the fountain formed in the liquid on the wetted gel surface looks very similar to the liquid-only fountains shown in section 4.3. The primary exception is 70% ethanol, for which the low boiling point and large surface area causes the ethanol to evaporate rapidly, drying the surface of the gel. In these immediate exposures, the amount of liquid on the surface at the transducer focus obscures the activity of the gel surface.

Nevertheless, cavitation bubble activity is evident beneath the gel surface. The end result of the 10, 10-ms pulses repeated at 1 Hz was surface erosion for all solutions; however with only 10 pulses, it was difficult to distinguish any differences in the erosion dimensions.

Because the liquid fountain on the gel surface looked so similar to the liquid-only fountains, exposures were repeated approximately five minutes after the 1 mL was added to the gel to give the solutions time to interact with the gel and spread into a thin layer across the surface. Figure 4.13 shows frames from the high speed videos taken approximately 5 minutes after the gel was wetted with 1,3-butanediol, olive oil, 70% ethanol, n-propanol, castor oil, or glycerol. The timing and scale of individual frames are the same for each wetted gel, with frames at 200 μs, 900 μs, 1900 μs, 4900 μs. Atomization and fountaining occurred for all wetting liquids, though in the case of castor oil, atomization occurred later into the 10-ms pulse than is shown in the figure (atomization began at around 8 ms). Starting with 1,3-butanediol, the high speed video shows initial wispy jetting as the ultrasound wave encounters the surface before the mound begins to form. Atomization continues as the mound forms, with one large liquid fountain forming and then detaching from the surface of the mound. Jet velocities primarily spanned 5-8 m/s, although some of the initial, wispy jets reached 16 m/s. Most of the emitted droplets are in the upper tens to lower hundreds of microns in diameter; a few droplets approached diameters of 350 μm. Atomization of the olive oil wetted gel proceeds relatively similarly to 1,3-butanediol without the initial jetting or the large liquid jet. Jet velocities primarily ranged from 4-7 m/s, though some of the wispier jets reached velocities up to 13 m/s. The diameters of the emitted droplets are mostly 100-200 μm in diameter. The alcohol-wetted gels (70% ethanol and n-propanol) atomize relatively similar to one another; for both alcohols, initial jetting is followed by the formation of a mound which enhances atomization. Jet velocities for both 70% ethanol and n-propanol are similar and range from 6-8 m/s, although in the 70% ethanol wetted gel the velocity of the initial jets reached 13 m/s. For the castor oil-wetted gel, no atomization occurs within the selected frames. There is no initial jetting, although a mound forms and a large liquid fountain forms. Once atomization begins (approximately 8 ms into the 10-ms pulse), jets are emitted with velocities of 2-4 m/s;

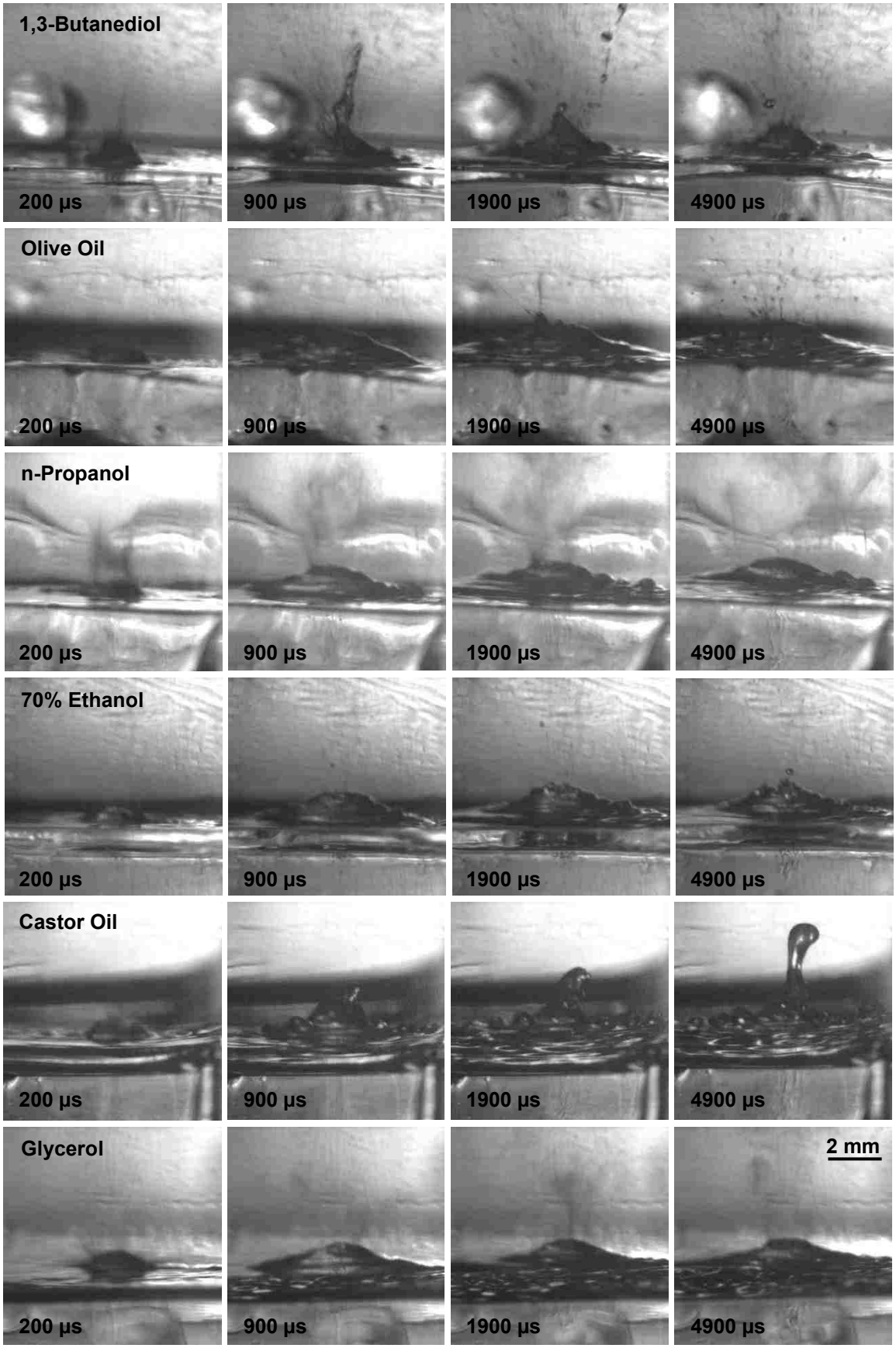

FIGURE 4.13 (on previous page): Frames taken from the high speed videos of polyacrylamide gel wetted approximately five minutes prior to the 2 MHz HIFU exposure with 1,3-butanediol, olive oil, n-propanol, 70% ethanol, castor oil, or glycerol. For each wetting liquid, the timing of the frames shown in the figure is the same. 1,3-butanediol and olive oil, which have relatively similar physical properties, emitted droplets that were mostly in the upper 10s to low 100s of microns in diameter at velocities of 4-8 m/s (though some of the wispy jets reached velocities of 13-16 m/s). The alcohols (70% ethanol and n-propanol) had velocities that were mostly in the 6-8 m/s range and very small droplets on the order of one to several pixels in diameter, which corresponds to diameters in the lower 10s of microns in diameter. Glycerol and castor oil, both of which did not atomize as liquids, caused atomization to occur in the tissue-mimicking gel with jet velocities primarily between 3-6 m/s (though for castor oil atomization occurred later in the 10-ms pulse than is shown here). The diameters of the droplets in castor oil were large - in the 100-400 micron range, with the droplet diameters in glycerol primarily on the order of 10s of microns with several droplets reaching 300 μm. The end result of 60, 10 ms pulses repeated at 1 Hz was holes in the gel surface for all 7 wetting liquids.

several of the wispy jets reached velocities of 7 m/s. The droplet diameters ranged from 100-400 μm, although one droplet released from the large liquid jet was 1.5 mm in diameter. Surprisingly, atomization of the glycerol-wetted gel was more similar to the atomization of alcohols than to castor oil. With glycerol, a fine mist was ejected before the mound forms and enhances atomization. The diameters of the droplets were very small, with most of them on the order of several pixels or 10s of microns; a few droplets reached 300 μm in diameter. Jet velocities were 4-6 m/s, though a few jets reached 10 m/s. In all videos, cavitation activity was visible beneath the gel surface. These findings are summarized in table 4.4.

TABLE 4.4. Liquid-wetted polyacrylamide gel atomization and erosion descriptors.

	Jet Velocity*		Emitted Drops*		Mound**		Eroded Hole***	
Liquid	Range	Max	Range	Max	Width	Height	Width	Depth
1,3-Butanediol	5-8	16	60-200	350	2.6	0.9	2	3
Olive Oil	4-7	13	100-200	200	3.5	1.1	1.5	2.5
n-Propanol	6-8	8	10-50	50	3.2	1.1	2	5.5
70% Ethanol	6-8	13	10-50	150	3.1	0.8	2	3
Castor Oil	2-4	7	100-400	1500	2.9	1.2	2	6
Glycerol	4-6	10	10-90	300	3.1	0.9	2	4

*Ranges for jet velocities and emitted drops are the most common jet velocities and droplet diameters, though the range goes up to the maximum jet velocity or drop diameter.

**Mound dimensions were taken at 7.4 ms into the 10-ms pulse.

***Eroded hole dimensions are to the nearest 0.5 mm, and were measured after 60, 10-ms pulses repeated at 1 Hz. The exposure began at least 5 minutes after the liquid was added to the gel surface.

The end result of 60, 10-ms pulses repeated at 1 Hz is a hole in the gel surface for all seven of the wetting liquids. Figure 4.14 shows side views of the hole in gel for each wetting liquid. Interestingly, the holes from the oils (castor oil and olive oil) were rimmed with white. We expect this happens because the water-based polyacrylamide gel hydrolyzes the oil, causing the white fatty acids to be deposited on the gel surface. For all liquids expect olive oil, the surface dimensions of the hole were similar and 2 mm in diameter; the surface diameter for olive oil was slightly smaller at 1.5 mm. The depth of the holes had more variation. For water, n-propanol, castor oil, and glycerol hole depths were similar and between 4 and 6 mm. The holes for 1,3-butanediol, 70% ethanol, and olive oil were slightly shallower and 2.5-3 mm deep. Table 4.4 includes the hole dimensions of the gel for each wetting liquid.

Subsurface Observations of Liver Atomization

Figure 4.15 shows selected frames from a B-mode ultrasound video of liver atomization. The frames have been flipped so that the ultrasound images look similar to the high-speed video images; for each frame, the HIFU source is positioned below the tissue sample and focused at the tissue-air interface as shown red in the first frame. The tissue block is also outlined in yellow for clarity. The imaging transducer is positioned in the plane of the paper, angled so it is focused through the tissue to the focal zone on

FIGURE 4.14: Photographs showing the holes in polyacrylamide gel when the surface was wetted with 1 of 6 liquids after an exposure to 60, 10-ms pulses repeated at 1 Hz delivered with 2 MHz ultrasound operating at 24,000 W/cm^2. For all exposures, the transducer was positioned at the bottom of the page and pointing towards the top of the page (the free gel surface). While the scales are similar for these photographs, the camera angle differs between the gels. For example, the hole in gel when wetted with 70% ethanol was only 3 mm deep, while the hole in castor oil extended 6 mm into the gel, even though in the photographs, the depths look similar. The measured dimensions of the eroded gel volumes are included in table 4.4.

the surface as shown in figure 4.11. Even though the video recording software made the exact timing of individual frames difficult, we were able to discern which HIFU pulse corresponded to which frame. In the second frame of figure 4.15, we can see that the tissue surface is slightly at the transducer focus than at time zero. By the third frame (or 4th pulse) there is a hyperechoic spot on the tissue surface indicative of bubble activity. In the fourth frame, we were able to capture the HIFU interference; to the right of the interference, we find a relatively large hyperechoic region at the tissue surface corresponding to the transducer focus. While some of the hyperechogenicity has faded by the 5th frame, when the HIFU interference is again shown in the ultrasound image as in the 6th frame (11th pulse) the hyperechogenicity is more pronounced. The 7th frame is interesting, as it does not show any hyperechogenicity at the tissue surface. We expect that this frame was taken near the end of the HIFU off-time, which shows that the bubble activity is fading between pulses. It may also indicate that there is no hole on the tissue surface or that the hole is not large enough to be detected with these B-mode imaging parameters. The next four frames (42nd, 73rd, 103rd, and 177th pulses) show the progression of hyperechogenicity. As before, when the HIFU interference is contained in the frame, the hyperechoic region is larger. Interestingly, comparing the 73rd and 177th pulses, we see that the hyperechoic region extends further into the bulk tissue as the pulsing progresses. This is expected as we found in Ch. 2 that the depth of the holes in tissue increase with the number of pulses. The final frame shows the tissue several seconds after the end of the 180 HIFU pulses. In this frame, hyperechogenicity is still present at the tissue surface. We expect that this is due to the hole in the tissue surface. This video confirms the presence of bubbles below the tissue surface during atomization and supports the high speed videos taken in the tissue-mimicking polyacrylamide gels.

4.4.3. Discussion

In this section, we found that the properties of the liquid wetting the surface of a tissue-mimicking polyacrylamide gel did not matter; even liquids that did not atomize on their own (i.e. glycerol and castor oil) caused atomization and erosion when spread on the gel surface. This is particularly interesting, as when the gel surface is dry atomization

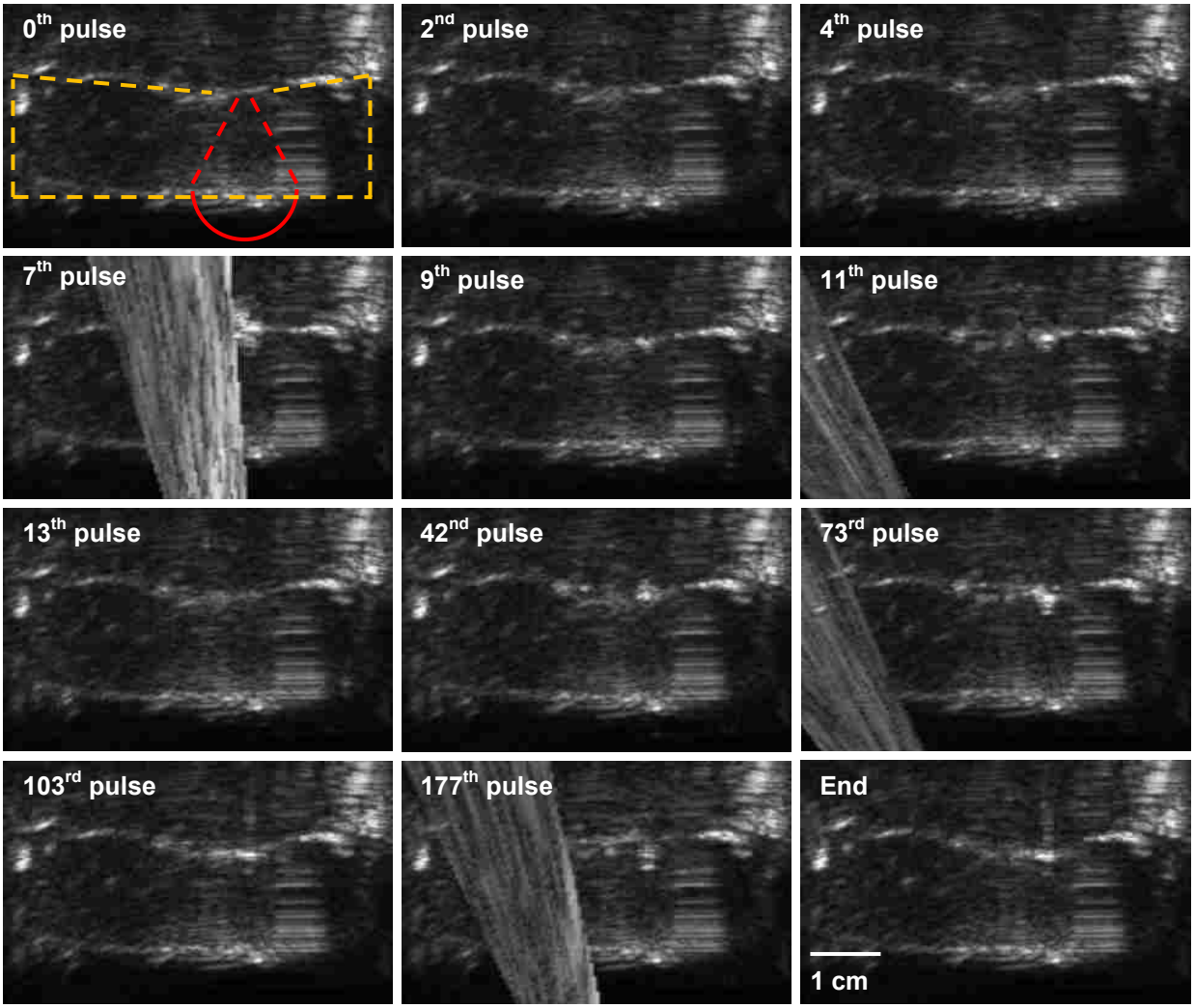

FIGURE 4.15: Frames taken from a B-mode ultrasound video of atomization with the 2 MHz HIFU transducer at the maximum *in situ* intensity of 14,000 W/cm^2 (p_+ = 53 MPa, p_- = 12.7 MPa). Pulses were 10-ms in duration and repeated at 1 Hz. While the video recording technique precluded the exact timing of atomization, we were able to distinguish which pulse corresponded to which frame, even though discerning the timing within the pulse was not possible. The first frame shows the outlines the tissue sample in yellow, with red indicating the position of the HIFU transducer and the approximate focal location at the tissue surface. The imaging transducer was positioned in the plane of the paper. The second frame shows that the tissue surface was brighter after the second HIFU pulse. By the third frame, or 4th HIFU pulse, we can see a hyperechoic region at the tissue surface. The fourth frame shows interference from the HIFU pulse, and we can see an intense hyperechoic region at the tissue surface just to the right of the HIFU interference. The next two frames (9th and 11th pulses) show the hyperechoic region getting larger and more intense, yet by the 7th frame (13th pulse) the hyperechogenicity is gone. We expect that this frame was taken near the end of the HIFU off-time, as it appears that bubble activity has ceased. The frames corresponding to the 42nd, 73rd, 103rd, and 177th pulses show the growth of the hyperechoic region at the tissue surface as the pulse number increases. The final frame shows that the hyperechoic region at the surface remains, even several seconds after the last HIFU pulse, and corresponds to the hole that was formed in the tissue surface.

does not occur and the gel surface is not eroded. In all cases, even for the case of dry gel (shown in figure 3.6) subsurface cavitation or bubble activity is present, yet since atomization and surface erosion does not occur when the gel surface is dry, it is unclear how cavitation relates to atomization. As the polyacrylamide gel is structurally very different from tissue, we used B-mode ultrasound to confirm the presence of bubbles beneath the tissue surface during atomization. Even though we could not monitor the tissue during the HIFU pulse, the B-mode video clearly shows hyperechogenicity beneath the tissue surface as the HIFU pulse passes. At first, the hyperechogenicity fades between the HIFU pulses, yet by the end of a set number of pulses, the hyperechogenicity remains and coincides with the presence of a hole in the tissue surface. While our observations of bubble activity beneath the tissue and gel surfaces confirm our hypothesis that bubbles are present during atomization, we have yet to determine the role bubbles play in tissue atomization.

Our observations of atomization in a variety of liquids from the previous section seem to support one version of the cavitation-wave hypotheses originally laid out by Pohlman and Lierke and Boguslavskii and Éknadiosyants [53], [58]; however, in tissue, no definite mechanism of atomization and tissue erosion has been validated. In Ch. 2, we hypothesized that spallation could explain the atomization and erosion of tissues. While spallation could explain some of the jetting in tissue, it does not explain why the dry gel or dry tissue surface does not erode, especially when, in the case of the gel, we see cavitation bubbles beneath the surface. If spallation were the mechanism, why would wetting the gel surface, even with liquids that have not been shown to atomize themselves, cause atomization and erosion of the gel surface? One possible reason is that the liquid on the gel surface lowers the cavitation threshold, due to either a lower interfacial surface tension or through the formation of capillary waves (or other types of surface waves) in the liquid. It is possible that these surface waves, which are faintly observable in the wetted gel atomization videos in figure 4.13, actually refocus the reflected and inverted wave closer to the gel surface. This hypothesis is crudely sketched in figure 4.16. When the viscoelastic surface of the gel or liver capsule is dry, the mound curvature causes the reflected and inverted wave to be focused deep within the tissue as shown in figure 4.16(a), causing atomization and surface erosion to be

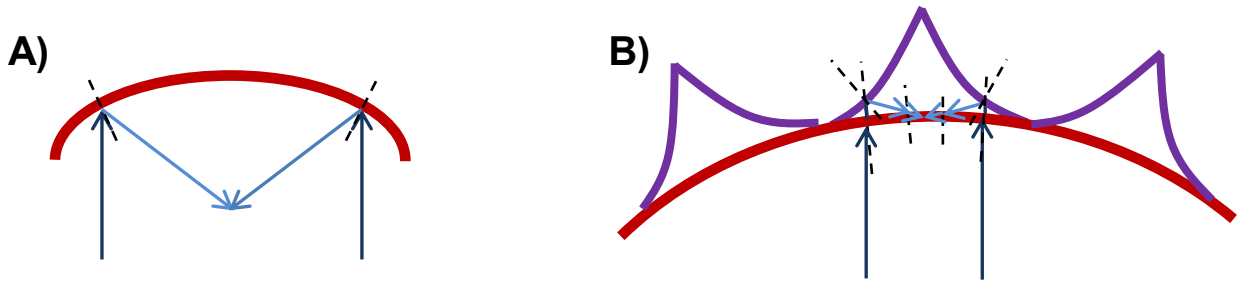

FIGURE 4.16: Sketches showing the acoustic wave diagram for an incoming acoustic wave (black arrows) approaching a curved, pressure release interface (red). A) Shows a diagram of the acoustic wave approaching an interface with a curvature approximating that of the dry gel surface or the porcine liver with an intact capsule. When the wave reflects (light blue arrows) from the pressure-release interface, the wave refocuses beneath the surface. If we approximate a scale, the focus is approximately 4.5 mm below the surface of the mound. B) Shows the same curved interface (magnified for improved visualization) with capillary waves shown in purple on the elastic gel or tissue surface. This wave diagram is more complex. When the wave encounters the gel-liquid interface, there is a little bit of refraction due to the differences in sound speed. Then, the wave reflects upon encountering the fountain-air interface (light blue arrows), which refocuses the wave at or near the original curved surface (in this case the gel surface). In both cases, the reflected wave is inverted because the tissue-air and liquid-air interfaces are pressure-release, meaning significant cavitation activity would be expected at the focus of the reflected wave. For these diagrams, the liquid- or tissue-air interfaces were considered a perfect pressure-release interface. In B), waves reflected from the gel-glycerol interface were neglected to maintain the clarity of the figure.

unsuccessful; however when the elastic surface is wetted, fountains or surface waves form in the liquid on the gel surface which reflect and refocus the wave at or near the gel surface as sketched in figure 4.16(b). The intense cavitation that is expected at the focus of the inverted wave causes fractionation below the surface (when dry) or atomization of the gel surface (when wetted). This could explain why atomization was successful both immediately after the liquid was added to the gel surface and after waiting five minutes so that the gel surface is not visibly wetted (figure 4.13); in both cases, fountains and/or surface waves are visible in the high-speed videos.

With the discovery that particularly castor oil and glycerol on the gel surface caused atomization and eroded the gel surface, we decided to revisit atomization of the porcine liver capsule. In the previous chapter, we described atomization of the *in vivo* porcine liver without the capsule and showed that when the capsule was left intact, we were unable to breach the 2-3 cells composing the liver capsule, even when water was sprayed on the liver surface. We also noticed from the histology samples of intact liver capsule atomization that the extent or depth of the damage to the tissue (either

fractionation or bruising) extended 4.6 mm below the tissue surface, which is significantly larger than the focal zone of the transducer, even accounting for breathing motion and inexact focusing of the transducer at the liver surface. The depth of tissue damage along with the shallow curvature of the liver mound when the capsule is intact, made us think of the wave diagram in figure 4.16; we theorized that even when water was added to the liver surface, the inverted and reflected HIFU wave was focused too deep into the tissue. We hypothesized that lowering the surface tension of the liquid added to the liver surface could refocus the inverted and reflected HIFU wave closer to the liver capsule surface by decreasing the capillary wavelength, potentially breaking through the liver capsule. We tested this hypothesis in the *in vivo* porcine model in two pigs with a setup exactly the same as was described in the previous chapter (section 3.4.1). We chose to test this hypothesis directly *in vivo* rather than *ex vivo* where we can control alignment more precisely because when the capsule is breached *in vivo*, bleeding occurs. This will give us instantaneous feedback, circumventing the need to find either visually or histologically, small fissures or breaks in the liver capsule. The liquid chosen for having a lower surface tension than water was soapy water. A study showed that when Dawn dishsoap was mixed in water at 20 mL soap to 80 mL water ratio, the surface tension was 24.5 mN/m [103], which is approximately 1/3 the surface tension of water. This change in the surface tension would lower the predicted capillary wavelength from 7.3 μm in water to 5.1 μm in surfactant-water. We already have extensive data indicating our lack of success in breaching the dry intact capsule and the water-wetted intact capsule, when pulsing (10-ms, 1 Hz) up to five minutes; however we repeated the experiments in these livers for completeness.

During the soapy-water exposures, three of the five treatment locations began to bleed after approximately three to four minutes of continuous HIFU pulsing. The bleeding was wispy and was quickly washed away by the stream of soapy water. During the exposure, we observed a significant amount of bruising beneath the capsule surface before the capsule was breached. This is similar to what we observed when the liver capsule surface was wetted with water, though the capsule never breached. In the case of the dry liver surface, the tissue below the capsule appears blanched, or heat-related, rather than bruising or mechanical damage. Frames from a high speed video

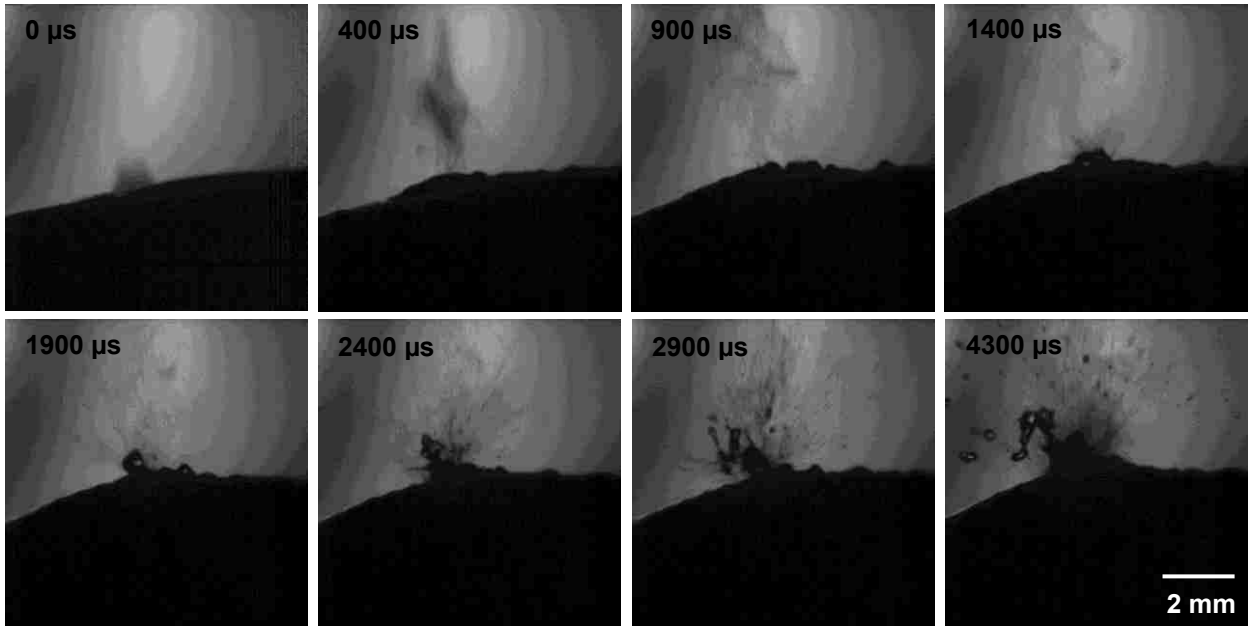

FIGURE 4.17: High speed video frames of atomization of the intact *in vivo* liver capsule when wetted with soapy water. The first frame shows that the initial fine spray is emitted as the ultrasound wave encounters the liver surface (70 µs prior to the frame). The second and third frame shows the mound forming in the tissue surface with atomization continues. In the fourth frame (1400 µs), we see the soapy water fountain beginning to form. As the fountain forms, it atomizes very dramatically. In the 6th and 8th frames, if we backtrack along the direction of many of the jets, we can see that they appear to be originating at or near the liver capsule surface. We expect this is what caused the liver capsule to be breached. 2 MHz HIFU operating at the maximum *in situ* intensity of 14,000 W/cm^2 (p_+ = 53 MPa, p_- = 12.5 MPa) was pulsed with 10-ms pulses at 1 Hz.

taken during the soapy water-wetted HIFU exposure of the intact liver capsule are shown in figure 4.17. In the figure, we can see that atomization begins with the initial jetting of fine particles followed by the formation of a mound. As the 10-ms pulse continues, a soapy water fountain and surface waves form on the liver capsule and substantially increase atomization. The end result of the exposure was a small breach in the liver capsule. The jet velocities in this video were around 10 m/s, with ejected droplets ranging from 10s of microns up to 720 microns in diameter. For comparison, one frame from each of the high speed videos of the saline-wetted liver capsule and dry liver capsule atomization are shown in figure 4.18. Saline-wetted liver capsule atomization proceeds relatively similarly to soapy water atomization without as many explosive atomization events. Jet velocities were a little slower and approximately 6 m/s, though a few jets reached up to 9 m/s. Most of the droplets ejected are in the 10s

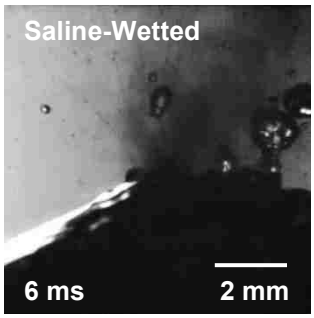

FIGURE 4.18: High speed video frames of the *in vivo* liver capsule with *Left:* saline wetted and *Right:* dry surfaces. *Left:* This frame shows the curvature of the liver surface and saline atomization on the surface; no clear saline fountain or obvious surface waves form that are able to reflect the wave back to the capsule surface. *Left:* This frame shows the bulge in the dry liver surface. The line to the upper right of the bulge is an artifact, not a jet. 2 MHz HIFU operating at 14,000 W/cm^2 (*in situ)* with 10-ms pulses was used for both exposures.

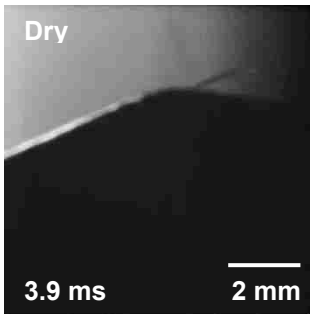

of microns in diameter, though larger droplets reached 1 mm in diameter. The dry liver capsule basically shows the bulge in tissue (we expect the dark line that appears on the upper-right side of the fountain is a hair, as it remains for the entire pulse without moving except as the liver flexes). While this particular frame of dry liver capsule atomization shows a little spray that is ejected from inertia as the wave encounters the surface, we expect it was because the liver surface was still slightly wet from the soapy water. Figure 4.19 shows a photograph of the liver surface after a soapy water-wetted exposure. Only localized bruising is visible upon gross examination of the liver; no capsular breach is apparent even though bleeding was observed during the HIFU exposure.

Our result in the *in vivo* porcine liver when soapy water was added to the surface of the liver capsule indicates that we may be on the right track as far as determining the mechanism of atomization in tissues. While these results may not be useful for bulk boiling histotripsy exposures, it begins to explain why some tissues can be atomized and others not. In particular, it explains why highly elastic tissues do not atomize;

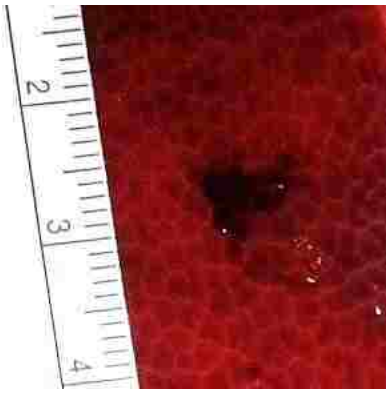

FIGURE 4.19: Photograph taken after the soapy water exposure in the *in vivo* pig liver. Fairly localized bruising is apparent. While bleeding occurred during the ultrasound exposure indicating a capsular breach, no evidence of a break in the capsule is visible upon gross examination.

the large radius of curvature that forms in the “infinite bubble” scenario focuses the reflected and inverted wave too deeply into the tissue to cause atomization and erosion. This may also explain the difficulties of fractionating some tissues in bulk boiling histotripsy; even if a bubble can be formed in the tissue, if the tissue properties do not allow for focusing of the inverted wave near the lower surface of the bubble, fractionation will not occur. It is interesting to note that all of our hypotheses for atomization of tissues (and even somewhat for liquids) involve bubbles. In the next section, we will use an overpressure chamber to test whether bubbles are necessary for atomization to occur in liquids (water) and in tissue. The results from the section should help elucidate the role of bubbles in liquid and tissue atomization.

4.5. Atomization in a High Pressure Chamber

4.5.1. Methods

High Pressure Chamber

This final study was considered the key study to illustrate the importance of bubbles in liquid and tissue atomization. The studies leading up to this point have suggested the importance of bubbles while being unable to completely eliminate either bubbles or one of the other potential mechanisms. The high static pressure chamber is shown in figure 4.20. Designed and built by Brian MacConaghy, the aluminum chamber with acrylic windows was hydraulically tested up to 2500 psi (17.2 MPa). A 2 MHz transducer was built into the bottom of the chamber using a flat piezoceramic source approximately 40 mm in diameter and an aluminum lens with center thickness of 10.8 mm. For the atomization experiments, overpressure was driven by a compressed air cylinder (Praxair, Seattle, WA) and controlled with a regulator (ProStar 4092, Praxair, Seattle, WA). Water level was controlled with a hydraulic syringe and could be adjusted under pressure. A mesh platform with a center cutout was used for tissue atomization. The mesh platform was placed on an acrylic cylinder which was designed to fit around the aluminum lens of the transducer. The setup was designed for a 1.5-cm thick piece of tissue to be at the transducer focus; however expecting tissue to be somewhat compressible a system was designed to raise and lower the mesh platform. A tightly-

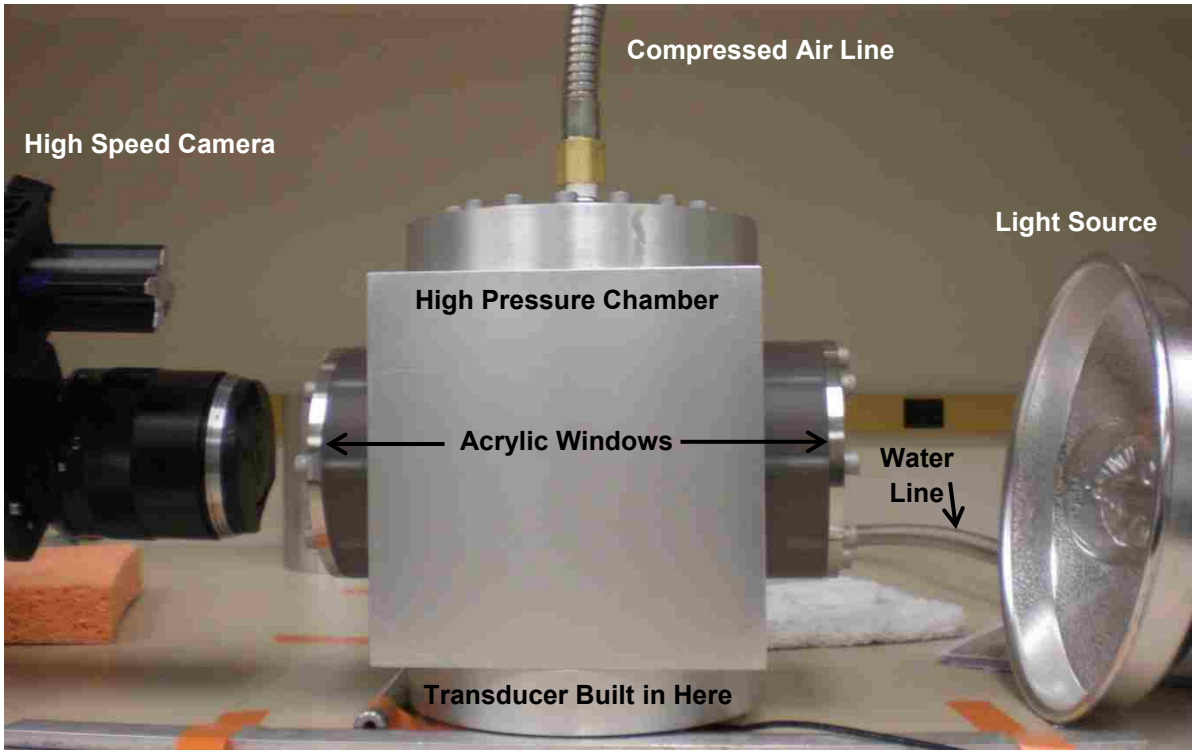

FIGURE 4.20: Photograph of the high static pressure chamber. The lens of the high speed camera is visible on the left side of the photo, with the light source visible on the right. Filming occurred through the side acrylic windows. The compressed air line is piped through top lid of the container, with the water line piped on the back side near the bottom of the container. The transducer is aluminum-lensed and built into the bottom lid of the container. Thirty-two screws and two O-rings seal the top and bottom lids of the container, with an additional eight screws sealing each of the side acoustic windows.

fitted O-ring was placed in the groove between the aluminum lens of the transducer and the wall of the chamber, underneath the acrylic cylinder. The piping for the water line was placed underneath the O-ring so that hydraulic pressure could be used to raise and lower the tissue, even under high static pressure conditions. This was essential as once the chamber was sealed, the tissue could not be otherwise manipulated.

Before experimentation, the waveforms of the aluminum-lensed transducer were measured in filtered water with the fiber optic probe hydrophone (FOPH 2000, RPI Acoustics, Leutenbach, Germany). The transducer was driven by an Agilent function generator (Model 33250A, Palo Alto, CA, USA) and a linear radiofrequency amplifier (55 dB gain, Model A300, ENI, Rochester, NY, USA). The measured delay to the focus was found to be 29 μs, which is slightly longer than the predicted 27 μs for a curved 40-mm

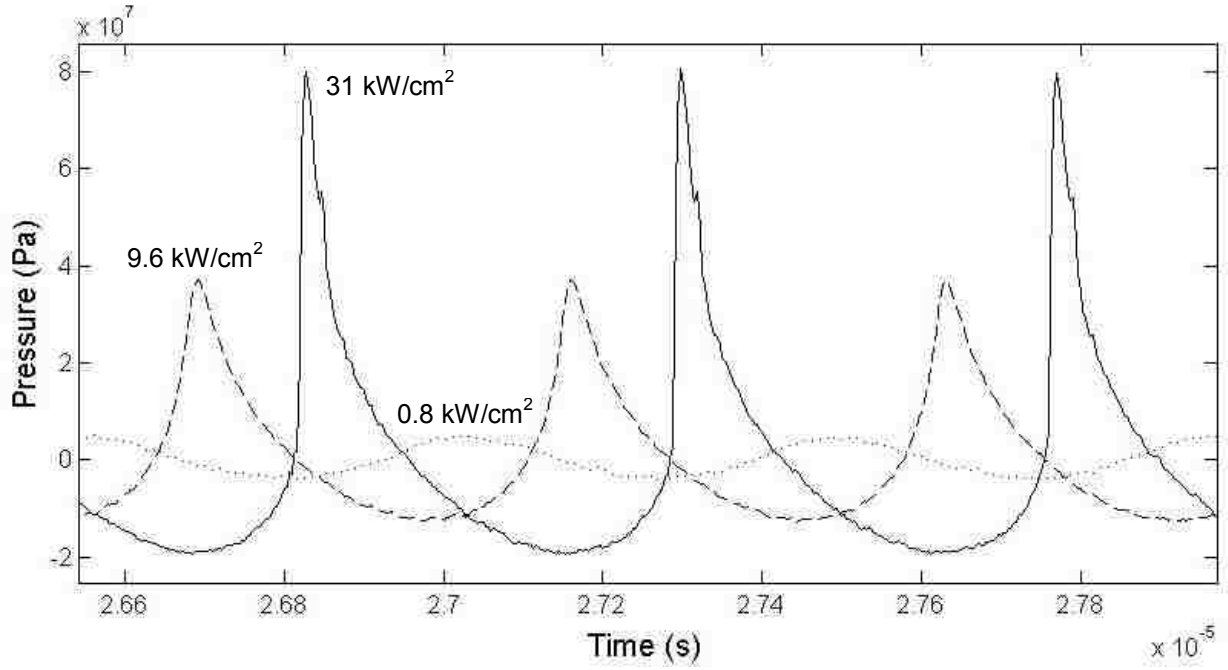

FIGURE 4.21: Selected waveforms measured in water with the fiber optic probe hydrophone of the 2.127 MHz aluminum-lensed, flat piezoceramic source built into the high pressure chamber. A matching network was used to increase the impedance of the transducer from approximately 2 ohms to 80 ohms. The 9.6 kW/cm^2 intensity was the maximum that could be achieved using the A300 amplifier. The 31 kW/cm^2 waveform was measured when using the 400B amplifier.

source with an f-number of one. The -6 dB focal dimensions of the transducer were measured near the shocked regime and found to be 0.5 mm transverse and 2.9 mm axial for positive pressures. The peak linearly-calculated intensity that could be achieved with the A300 amplifier was only 9600 W/cm^2 (p_+ = 38 MPa, p_- = 13 MPa) and is shown with a dashed line in figure 4.21. As these pressures were not sufficient for atomization of bovine liver, a more powerful 400B amplifier (55 dB gain, ENI, Rochester, NY, USA) was used. With that amplifier, the linearly-calculated intensity increased to 31 kW/cm^2 (p_+ = 80 MPa, p_- = 19.5 MPa). Figure 4.22 shows the results of a Comsol Multiphysics® model of the predicted von Mises stresses in the aluminum lens and the predicted acoustic focal pressures in water when 100 V was sent across the piezoceramic element. The predicted peak acoustic pressure (38.5 MPa) was in good agreement with the measured peak pressure with 100 V across the element (just below the maximum output of the A300 amplifier) of 37.9 MPa.

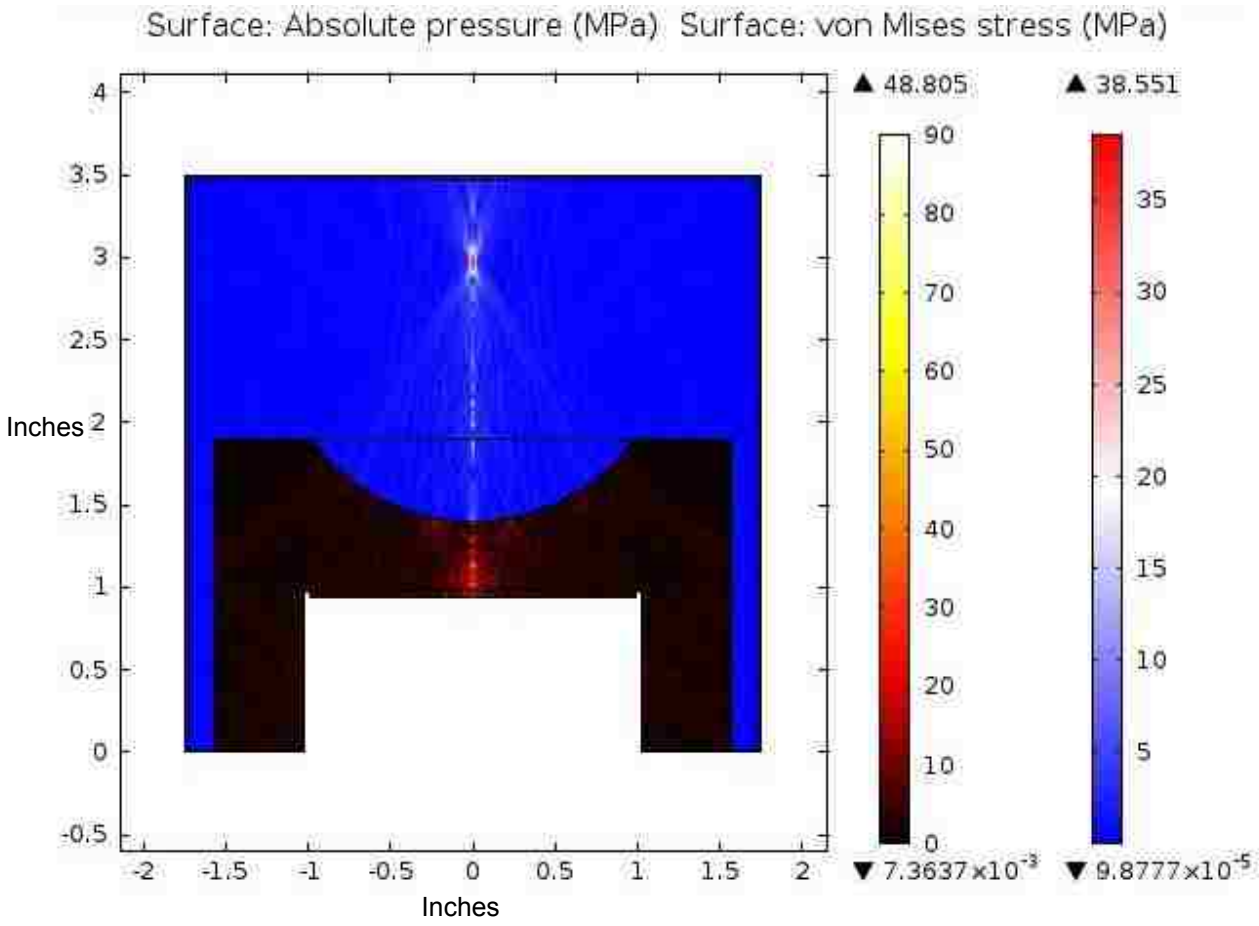

FIGURE 4.22: Comsol model programmed by Brian MacConaghy of the surface pressures in the aluminum lens (left scale), and the predicted focal pressures when 100 V is applied across the piezoceramic element (right scale). There is good agreement between the observed and predicted focal pressures; the 100 V across the element is just below the maximum that can be achieved using the A300 amplifier (as measured with a high voltage probe).

Experiments

Our first experiments in the high pressure chamber were conducted in filtered 20 °C water. The water was not degassed as the diffusion coefficient of air in water is 0.282 cm^2/s at atmospheric pressure [104], which will only increase as the static pressure of the system increases. The A300 amplifier was used for water atomization because it provides sufficient pressures for the atomization of water and has cleaner waveforms than the 400B amplifier (the 400B amplifier waveforms show lower and higher harmonics). Atomization was filmed through an acrylic window with the Photron APX-

RS high speed camera operating at 10,000 fps with a resolution of 17 μm/pixel. Experiments were backlit with the Photogenic light source. Pulse echo was used to focus the transducer at the water surface; the received signal was found to be very sensitive to the position of the pressure-release interface. Beginning at atmospheric pressure with the chamber sealed, atomization was recorded starting with low acoustic intensities that produce the drop chain and increasing the intensity to the maximum output of the transducer with the A300 amplifier. The static pressure of the system was then increased, and the same range of acoustic intensities was repeated. Static pressures tested were 200 psi (1.4 MPa), 350 psi (2.4 MPa), 500 psi (3.4 MPa), 1000 psi (6.9 MPa), 1200 psi (8.3 MPa), 1500 psi (10.3 MPa), and 2000 psi (13.8 MPa); pressures above 1000 psi were only used on an as-needed basis. After reaching the maximum pressure, the chamber was returned to atmospheric pressure and exposures were repeated to ensure that atomization did not change.

After atomizing water, bovine liver was obtained from a local abattoir (Schenk Packing, Stanwood, WA, USA) for atomization. The liver was used on the day of harvesting and was cut into sections approximately 5 cm x 5 cm, with thicknesses between 1-1.5 cm. The liver was placed on the mesh screen in the high pressure chamber. As the A300 amplifier did not provide enough power to atomize liver at atmospheric pressures, the 400B amplifier was used to atomize the tissue. All liver exposures consisted of 60, 10-ms pulses repeated at 1 Hz at the maximum linear intensity in water of 31,000 W/cm^2 (*in situ* intensity of 22,000 W/cm^2, assuming 1 cm of tissue and the previously reported liver attenuation coefficient of 0.7 dB/cm/MHz [27]). As in water, the liver was first exposed at atmospheric pressure. The static pressure was then increased to 200 psi (1.4 MPa), 350 psi (2.4 MPa), 500 psi (3.4 MPa), and 1000 psi (6.9 MPa); we did not exceed a static pressure of 1000 psi in liver. Between each pressure and exposure, the chamber had to be returned to atmospheric pressure and opened to reposition the liver. Pulse-echo was used for each exposure to ensure that the liver was positioned at the transducer focus after the pressure was increased. If needed, the height of the liver was adjusted to ensure proper alignment. As in water, exposures were filmed with the Photron high speed camera operating at 10,000 fps and backlit with the Photogenic light

source. At the end of each exposure, the liver surface was photographed, and samples were taken for histological analysis.

Histology

Liver samples were frozen-fixed in Tissue-Tek® O.C.T. (optimum cutting temperature) compound. Samples were sliced in 8 μm serial sections and alternating slides were stained with Hematoxylin and Eosin (H&E) to evaluate cellular morphology and stained with nicotinamide dinucleotide diaphorase (NADH-d) to evaluate enzymatic activity. Slides were examined for injury by an expert histologist using light microscopy.

Theory

To support our experimental results, we can repeat some of the calculations made in water (section 4.2.1. *Theory*) in bovine liver. Specifically, we compared the observed diameters and velocities of the emitted jets to the calculated capillary wavelengths and jet velocities. In addition, we estimated the height of the mound in tissue and compared the calculations to experimental results. As tissue is mostly liquid, we assumed that the surface tension of bovine liver was the same as water (0.0728 N/m). The speed of sound of bovine liver is 1597 [89], and the density is 1099 kg/m^3 [105]. Additionally, the Young's Modulus of bovine liver has been found to be approximately 31 kPa [106]. The attenuation coefficient of bovine liver that was used to derate the pressure and intensity was 0.7 dB/cm/MHz.

The capillary wavelength can be calculated according to $(8\pi\sigma/\rho f^2)^{(1/3)}$ as stated previously. The capillary wavelength for bovine liver is 7.2 μm, which is not appreciably different from water (which makes sense as we are using the surface tension of water, and the density of liver is not significantly different from that of water). If we calculate the particle velocity according to the equation p/ρc as stated previously, using the derated peak positive pressure of 61.9 MPa, we predict the particle velocity to be 35.2 m/s. If we assume linear wave propagation, the predicted particle velocity drops to 13.3 m/s; even assuming linear wave propagation, the predicted height of the particles is over 9 meters. The capillary wavelength and particle velocity will not be significantly affected by increased static pressure. While the exact influence of increased static

pressure on tissue is unknown, bovine liver is 69% water [89], so if we assume it is affected similarly to water, we would expect small changes in both the speed of sound and density of < 2% [96], [107] over the 6.8 MPa change in the ambient pressure.

Additionally, we can estimate the height of the fountain or mound that forms in tissue using an energy balance and a modified Bernoulli equation. The four forces we took into consideration are the applied ultrasonic radiation force, surface tension, gravity, and tissue viscoelasticity. As the interface between the liquid and air is pressure release, or a perfect reflector, the equation to calculate the radiation pressure is:

$$P_{Rad} = \frac{2I}{c}$$

Where I is the acoustic intensity at the interface and c is the speed of sound in the liquid. The surface tension between the liquid and air will attempt to counteract the applied acoustic radiation force. The equation for the Laplace pressure can be calculated according to the equation below:

$$P_{Lap} = \frac{2\sigma}{R}$$

Where σ is the interfacial surface tension and R is the radius of curvature between the two surfaces. For our case, we are assuming that the radius of curvature is approximately equal to the height of the curved mound. Since the surface tension between bovine liver and air is not known, we assume a surface tension of water, since bovine liver is almost 70% water. The static fluid pressure due to gravity is simply ρgh. The final restoring force of consideration is the tissue viscoelasticity. Assuming that the tissue response is dominated by elasticity, (so neglecting tissue viscosity), the tissue response takes the form of:

$$P_{Tissue} = E\epsilon(t)$$

Where E is the Young's modulus of bovine liver and ε is the tissue strain. To put this equation in terms of mound height, we can assume that the transducer is perfectly focused, such that half of the -6 dB axial focus is beneath the tissue surface. This also

means we assume that the tissue is not displaced except in the -6 dB focus. While these assumptions might not be quite valid, this will give us a broad estimate of the predicted fountain height. If we know the initial length, we can rearrange the equation to:

$$P_{Tissue} = \frac{E}{L}h$$

With L equal to one half of the -6 dB axial focal length. When balancing the applied and restoring energies, we arrive at the equation:

$$P_{Rad} = P_{Lap} + P_{Grav} + P_{Tissue}$$

Substituting in the above equations yields the equation in terms of mound height of:

$$\left(\rho g + \frac{E}{L}\right)h^2 - 2\frac{I}{c}h + 2\sigma = 0$$

Where g is the acceleration due to gravity. At the maximum intensity that can be output by the 2 MHz transducer, we estimate a mound height in liver of 12.7 mm. Upon increasing the static pressure of the system, the mound height should not change appreciably as the 6.8 MPa increase in static pressure has only a small influence on the speed of sound and density of the tissue. These calculations serve as an approximation of the mound height in tissue and will be compared to experimental observations.

4.5.2. Results

Water Atomization

Figure 4.23 shows atomization at 350 W/cm^2 (p_+ = 3.5 MPa, p_- = 3 MPa) for atmospheric pressure and 200 psi overpressure. At atmospheric pressure, the threshold for consistent atomization of 350 W/cm^2 and the qualitative appearance of atomization is the same as was observed previously (section 4.2.2). From the frames in the figure (which were taken at the same time points), it is apparent that while atomization occurred at atmospheric pressure, atomization does not occur when the

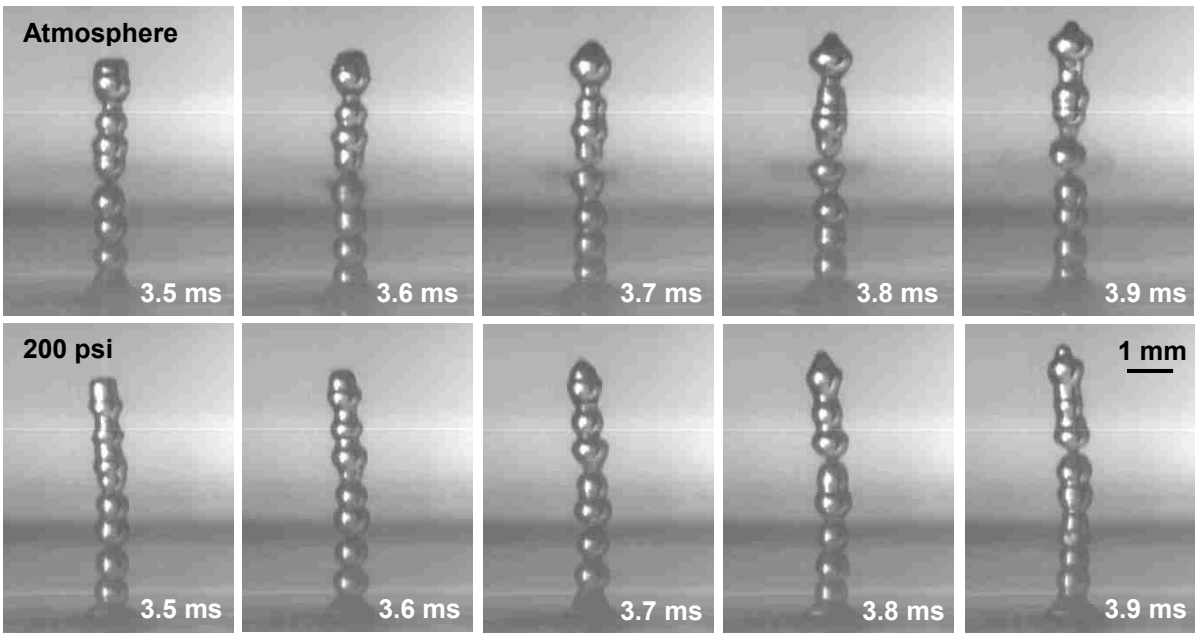

FIGURE 4.23: Frames taken from high speed videos of water atomization at 350 W/cm^2 (p_+ = 3.5 MPa, p_- = 3 MPa) at atmospheric pressure (upper) and with 200 psi of overpressure (lower). The timing is the same in both sequences of images. In the upper image sequence at atmospheric pressure, atomization occurs in the fifth droplet from the top. As we have seen previously in water, a fine spray is released from both sides of the droplet in the chain. However, in the lower image sequence, no atomization occurs – not just in these frames but throughout the 10-ms pulse. In both cases, the drop chain velocities are similar and on the order of 2.6 m/s. Droplet diameters are approximately 0.72 mm, which is similar to what we observed previously at the 2 MHz excitation frequency.

static pressure is increased to 200 psi. The atomization event at atmospheric pressure is actually the second atomization event in the video; however, the first event is not as clear and releases several large droplets rather than the fine spray. At both pressure levels the drop chain diameter is 0.72 mm, which is similar to what was observed previously at 2 MHz and the drop chain propagates vertically at 2.6 m/s. For the atomization event recorded in the figure at atmospheric pressure, the velocities of the atomized jets are approximately 5 m/s, which is less than half of the jet velocities that were observed in section 4.2.2.

When the ultrasonic intensity is increased to 850 W/cm^2 (p_+ = 5.5 MPa, p_- = 4.5 MPa), droplets began to be ejected from the fountain at the 200 psi of overpressure. It is interesting to note, however, that the diameters of the droplets emitted at 200 psi fall on the upper end of the droplet diameter range at atmospheric pressure. At 14.7 psi (or

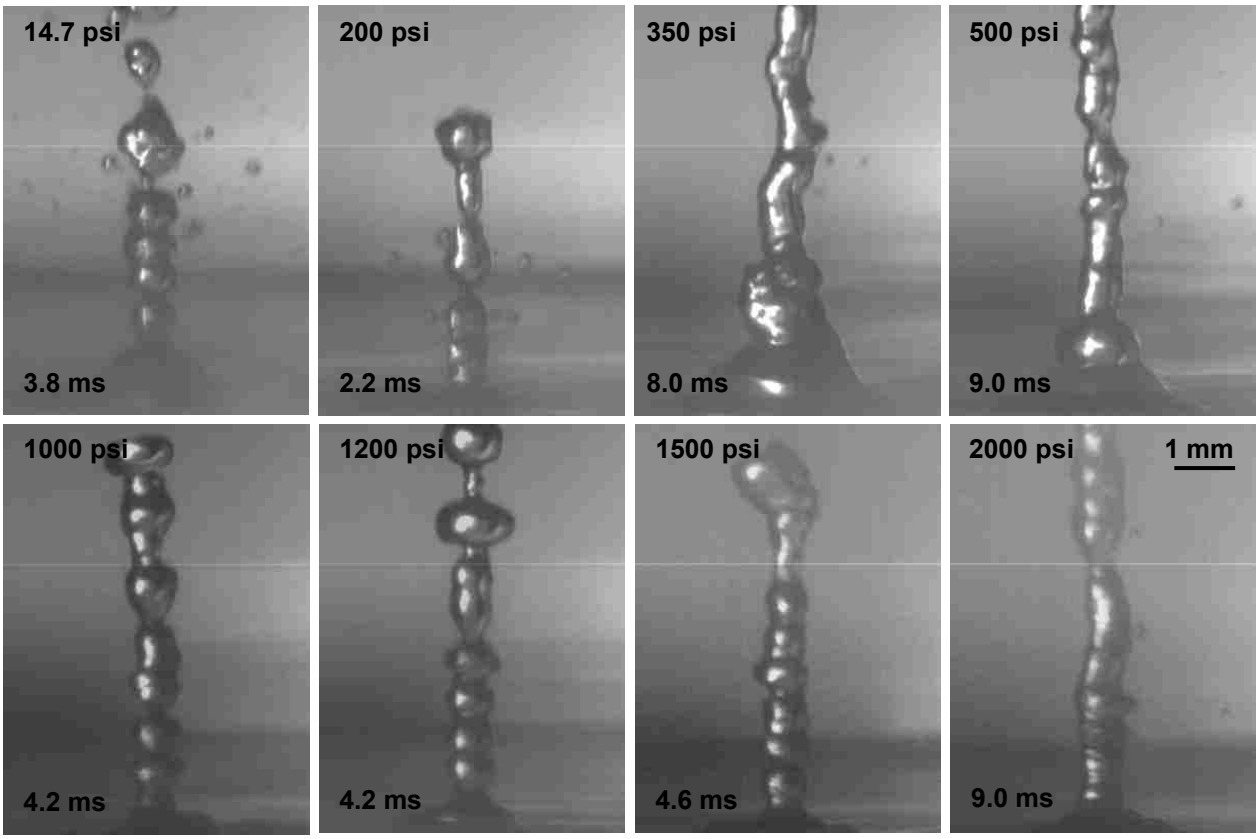

FIGURE 4.24: Selected frames of the high speed videos of water atomization under high static pressure conditions at an acoustic intensity of 850 W/cm^2 (p_+ = 5.5 MPa, p_- = 4.5 MPa). At atmospheric pressure or 14.7 psi, the emitted droplets span a range between approximately 20 µm (1 pixel) to 370 µm in diameter with velocities of 2-8 m/s. Once 200 psi of overpressure is applied, primarily large droplets (160-300 µm) are released with velocities of 2-10 m/s. As the static pressure is increased even further to 350 psi or 500 psi, fewer droplets (100-200 µm) are emitted at around 2-3 m/s. No droplets are released at 1000 psi, 1200 psi, or 1500 psi. It is not until 2000 psi of overpressure is applied that droplets are again released; these droplets are 100-200 µm in diameter with velocities of 1-2 m/s. For all levels of static pressure, the drop chain propagated vertically at approximately 2 m/s. Exposures were 10-ms in duration.

atmospheric pressure) droplets range from 1 pixel (20 µm) to 370 µm in diameter, whereas, at a static pressure of 200 psi the droplet diameters range from 160-300 µm. Ejection velocities are similar for both 14.7 psi and 200 psi and range from 2-10 m/s. When the static pressure is increased to 350 psi or 500 psi, large droplets (100-200 µm) are emitted at 2-3 m/s for the same 850 W/cm^2 intensity, though fewer droplets are released than in the cases of 200 psi or 14.7 psi. Once the static pressure is increased even further to 1000 psi, the release of droplets completely ceases. This continues for

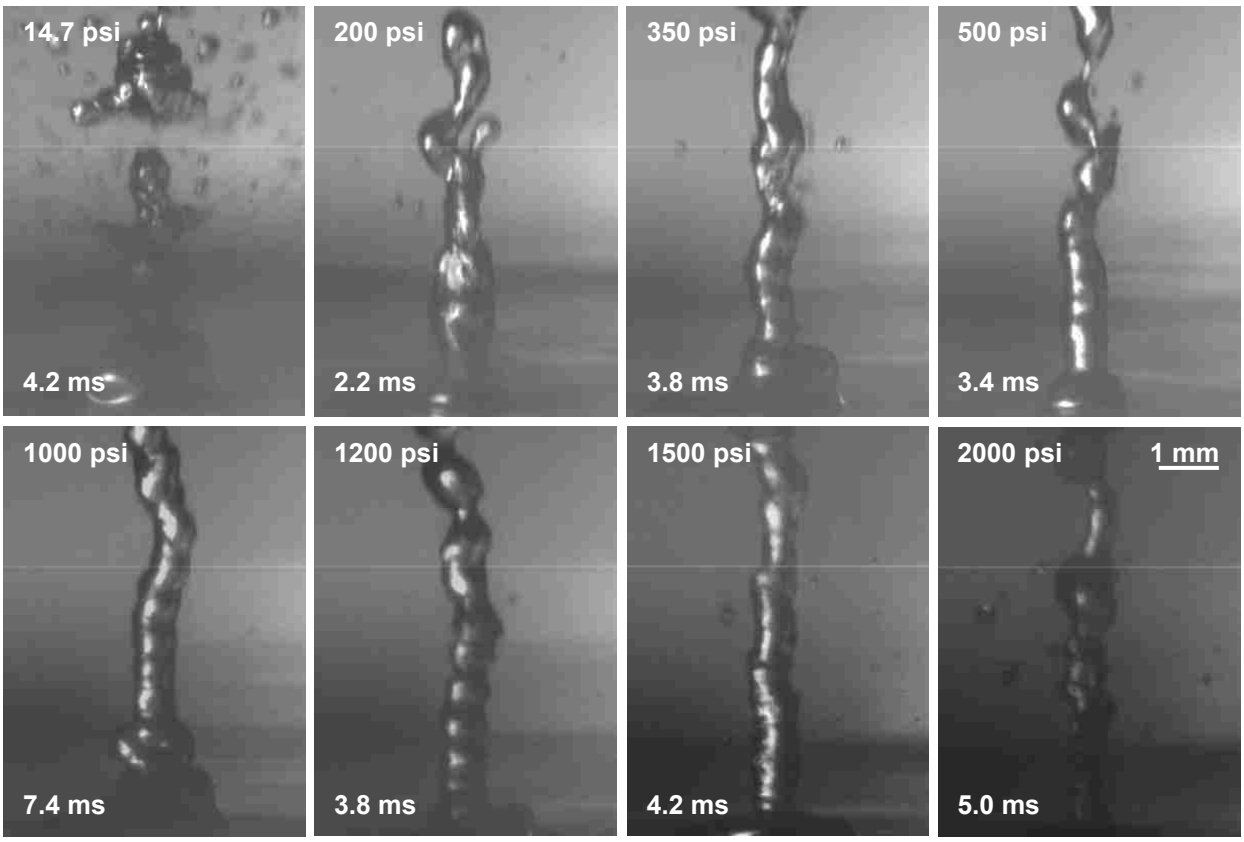

FIGURE 4.25: Frames from high speed videos of water atomization under high static pressure conditions when exposed to 2 MHz focused ultrasound operating at 1200 W/cm^2 (p_+ = 6.8 MPa, p_- = 5.3 MPa). At 14.7 psi (atmospheric pressure) atomization is very dramatic with a range of droplet diameters from 1 pixel (~20 μm) to 550 μm and jet velocities reaching 11 m/s. When the static pressure is increased to 200 psi, the number of emitted droplets decreases dramatically with droplet diameters reaching 200 μm and velocities of 5-7 m/s. At overpressures of 350 psi and 500 psi, jet velocities range up to 7.5 m/s and drop diameters range from a few pixels up to 400 μm. As the static pressure increases still further to 1000 psi or 1200 psi, the droplet diameters are on the order of a few pixels in diameters, with slow velocities of approximately 2 m/s. At 1500 psi and 2000 psi of overpressure, droplet diameters are again larger (100-400 μm) with jet velocities of 1-2 m/s. Exposures are 10-ms in duration and the drop chain propagates vertically at 2-3 m/s.

the 1200 psi and 1500 psi levels of overpressure. Interestingly, however, droplets are emitted again once an overpressure of 2000 psi is reached. These droplets are relatively large (100-200 μm) and are released at very slow velocities of 1-2 m/s. Selected frames from the high speed videos at this intensity are shown in figure 4.24. Exposures are 10-ms in duration and the drop chain propagates vertically at around 2 m/s for all levels of static pressure.

As the acoustic intensity is increased still further in water to 1200 W/cm^2 (p_+ = 6.8 MPa, p_- = 5.3 MPa), a combination of large and small droplets are emitted at atmospheric pressure (20-550 μm) and at 200 psi of overpressure (up to 200 μm). Once the static pressure reaches 350 psi or 500 psi, the number of emitted droplets is sharply reduced. Drop diameters range from a few pixels up to 400 μm in diameter, with velocities reaching 7.5 m/s. Even fewer droplets are released at 1000 psi and 1200 psi. These droplets are small and on the order of a few pixels in diameter and released at velocities of approximately 2 m/s. Surprisingly, a larger number of droplets are released when the pressure is increased to 1500 psi, which increases even further when the static pressure reaches 2000 psi. The droplet diameters are larger and range from 100-400 μm, but are released at very slow velocities of 1-2 m/s. Representative frames from the high speed videos showing the type and number of released droplets are shown in figure 4.25. The drop chain propagates vertically at 2-3 m/s for all static pressure levels.

If we increase the acoustic intensity to the maximum that can be achieved with the A300 amplifier of 9600 W/cm^2 (p_+ = 38 MPa, p_- = 13 MPa), we find that the fountain becomes narrower with increasing static pressure and the number of released droplets is reduced. Figure 4.26 shows representative frames of the fountain and emitted droplets from the high speed videos of atomization at the 9600 W/cm^2 acoustic intensity for the entire range of static pressures. The number of droplets emitted at 14.7 psi, 200 psi, and 350 psi makes it difficult to get an idea of the fountain width; however, when the static pressure is increased to 500 psi, there is a significant decrease in the number of emitted jets and the fountain, itself, appears narrower, with a diameter of approximately 1 mm. As the static pressure is increased even further to 1000 psi or 1500 psi, the width of the fountain is the same as the drop chain diameter at low intensities and is approximately 0.72 mm. The fountain appears to become wider as the pressure is increased even further to 1200 psi or 1500 psi, with a width of approximately 1.2 mm. Initial jet velocities are around 10 m/s, with the initial jet at atmospheric pressure having the highest velocity of 13.5 m/s and the initial jet at 500 psi having the lowest initial velocity of 8 m/s. The number of emitted droplets makes it difficult to determine an exact range of droplet diameters; however it is apparent that the droplets range from

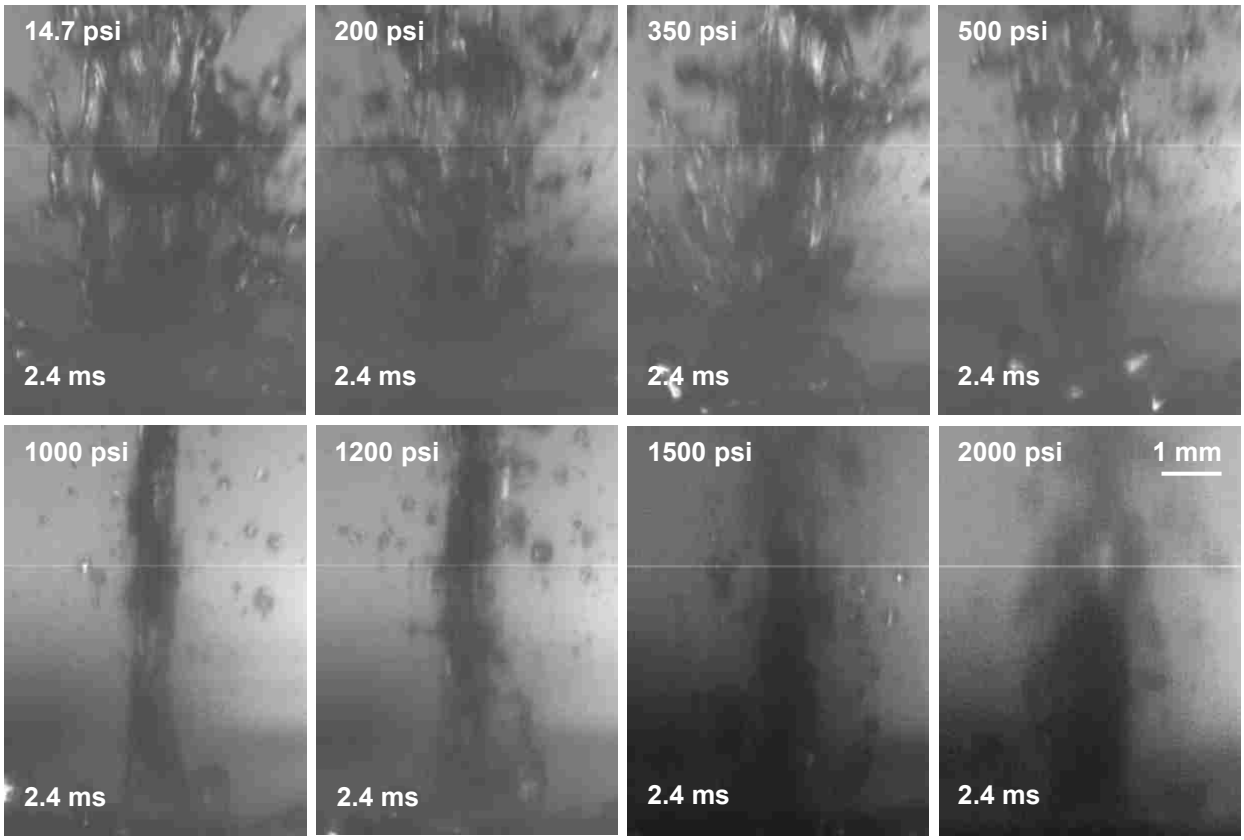

FIGURE 4.26: High speed video frames of water atomization at 9600 W/cm^2 (p_+ = 38 MPa, p_- = 13 MPa) for different static pressure levels. All frames were taken 2.4 ms into a 10-ms pulse. The number of droplets that are emitted at 14.7 psi, 200 psi, and 350 psi, make it difficult to get an idea as to the width of the actual fountain; however, when the static pressure is increased to 500 psi, we see a significant reduction in the number of emitted droplets and we see that the fountain appears to be getting narrower. As we increase the static pressure even further to 1000 psi or 1200 psi, the drop chain becomes even narrower with fewer droplets being released. If the pressure is increased still further to 1500 psi or 2000 psi, the fountain appears to be getting wider again, though there is not a noticeable increase in the number of emitted droplets.

approximately 20 microns (1 pixel) up to hundreds of microns in diameter for all static pressure levels.

After increasing the static pressure to the maximum 2000 psi, the pressure was reduced to atmospheric levels and water was again atomized at the various acoustic intensities. After returning to atmospheric pressure, water atomization proceeded relatively similarly to atomization at atmospheric pressure before the pressure was increased. Figure 4.27 shows an example of atomization at 350 W/cm^2 when the static pressure is returned to atmospheric levels. This video shows one of the middle drops in the chain emitting

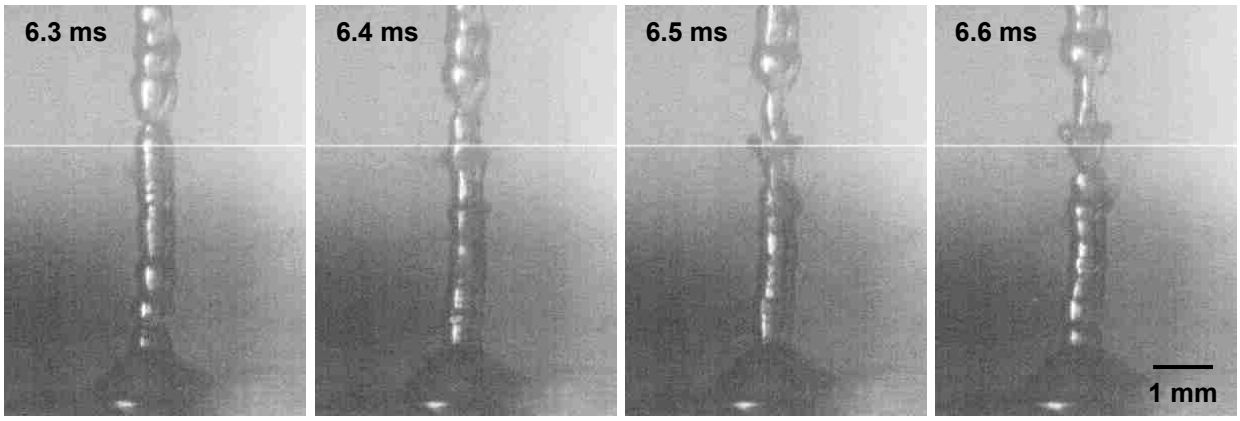

FIGURE 4.27: Selected frames from a high speed video of water atomization when the static pressure was reduced to atmospheric after being exposed to 2000 psi of overpressure. In this case, one of the middle droplets explodes and releases jets out to either side of the drop chain. The droplets that are emitted are less than one pixel in size (20 μm), and are emitted with a velocity of 6 m/s. The drop chain is approximately 0.75 mm in diameter and propagates vertically at 1.75 m/s. The ultrasound exposure was 10-ms in duration with an intensity of 350 W/cm^2 (p_+ = 3.5 MPa, p_- = 3 MPa).

small droplets to either side of the chain. The emitted droplets are less than one pixel in diameter (20 μm) and are ejected with a velocity of 6 m/s. The drop chain diameter is 0.75 mm, which is very similar to what was observed before overpressure was applied. The main difference between atomization of water before overpressure and after overpressure is consistency; at the original threshold intensity of 350 W/cm^2 before overpressure, atomization occurred in every video, whereas once overpressure was released, atomization only occurred in one of three videos (which happens to be shown in figure 4.27). We expect this is due to the number of bubbles that are present in water when the pressure is released. This hypothesis is somewhat confirmed because the drop chain propagates upwards at approximately half the velocity when pressure was reduced to 14.7 psi than was observed before increasing the pressure (1.75 m/s upon return to 14.7 psi as compared to 2.6 m/s before the pressure was increased) for the 350 W/cm^2 intensity. Even though the bubbles in the liquid upon return to atmospheric pressure changed the consistency of atomization and the drop chain velocity, the qualitative appearance of atomization remains the same.

Bovine Liver Atomization

After studying atomization in water under increased static pressure conditions, we switched to bovine liver. We know from our previous work in bovine liver that the atomization threshold is above the maximum output of the transducer with the A300 amplifier, so we used the more powerful 400B amplifier for liver atomization. At the maximum linear *in situ* intensity of 22,000 W/cm^2 (p_+ = 67.4 MPa, p_- =16.4 MPa) and at atmospheric pressure, atomization of bovine liver with the aluminum-lensed transducer proceeds similarly to what has been observed previously (as shown in figure 4.28). However, when the static pressure is increased even to 200 psi, atomization of bovine liver looks qualitatively very different as shown in the second line of figure 4.28. The emitted droplets are much smaller and more uniform in size and the mound itself appears to have a more shallow curvature. The same small and uniform droplet distribution and decrease in mound curvature continues as the static pressure increases. When the pressure is again reduced to atmospheric pressure as shown in the final line of images in figure 4.28, atomization again appears similar to what was observed previously at atmospheric pressure, though is perhaps slightly less dramatic. Due to the difference in curvature of the liver surface, it is difficult to get an accurate measurement of mound width at the base; however the mound height is similar across all static pressures and varies between 2.5 mm and 3 mm. At atmospheric pressure, the velocities of the projectiles generally range from 5-7 m/s, with the droplets less than 1 pixel (~20 μm) up to 180 μm in diameter. While it is difficult to get an accurate velocity measurement of the fine droplets, the estimated velocity at all levels of overpressure (200-1000 psi) is between 2 and 3 m/s. The videos at both 200 psi and 350 psi of overpressure do not have any emitted droplets larger than approximately 1 pixel; however at 500 psi and 1000 psi of overpressure, the videos show one or several droplets that have diameters approaching 130 μm.

Figure 4.29 (left) shows the liver surface after 60, 10-ms pulses at 1 Hz for each pressure level. While we still find a hole in the tissue surface at atmospheric pressure, when the static pressure is increased, we find a heated mound at the exposure site. Visually, there are no obvious differences between the exposure sites on the liver surface for the different levels of overpressure (ranging from 200-1000 psi). On the right side of figure 4.29, we see that when the liver surface is blotted (which removes

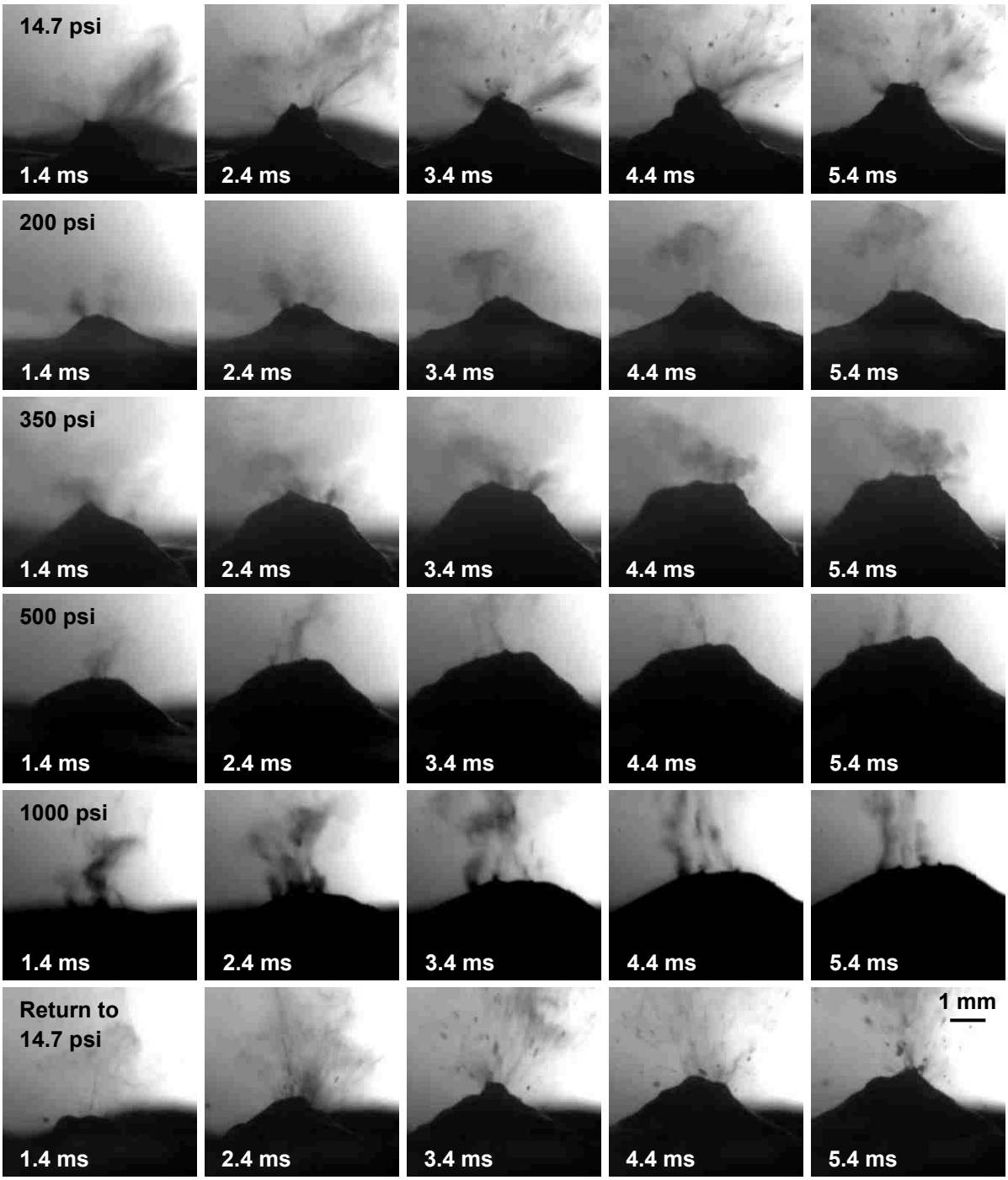

FIGURE 4.28: Frames from high speed videos of bovine liver atomization from exposure to 2 MHz ultrasound at an *in situ* linear intensity of 22 kW/cm^2 (p_+ = 67.4 MPa, p_- =16.4 MPa) under high static pressure conditions. Even increasing the static pressure from 14.7 psi to 200 psi, we notice that the emitted droplets are smaller and more uniform in diameter. This trend continues up to the 1000 psi of overpressure. When pressure is reduced again to 14.7 psi as shown in the final line of the figure, atomization appears very similar to what was observed initially at atmospheric pressure. The increase in static pressure changes the mound dimensions so that the mound is wider at the base and flatter at the top, though there appears to be no significant change in mound height. The timing is similar between frames for all 10-ms exposures.

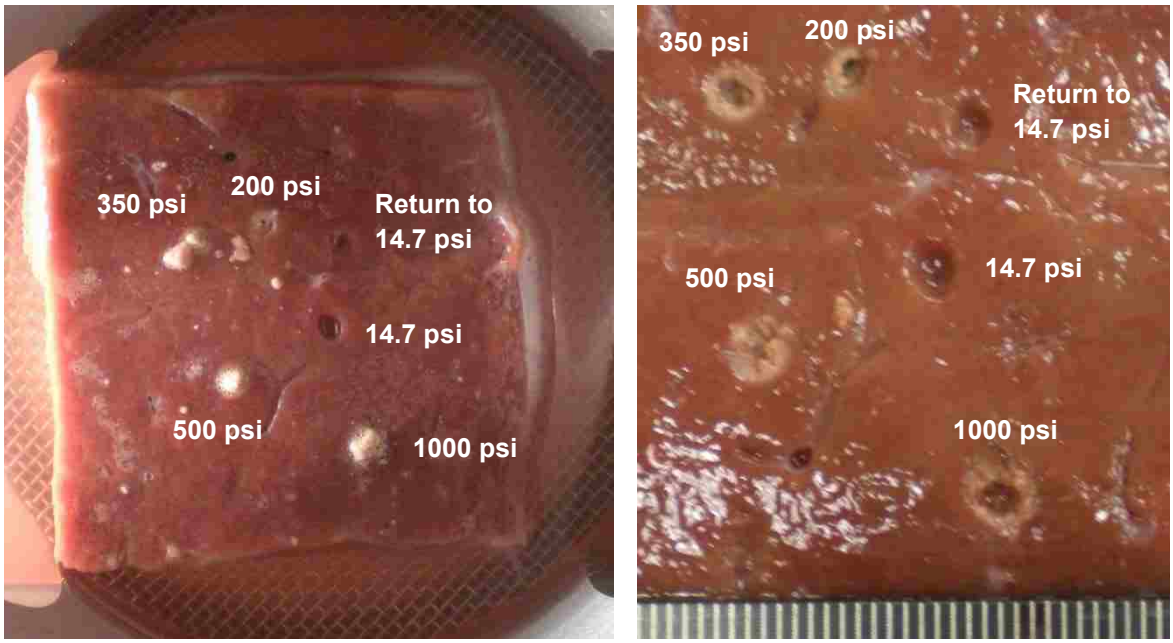

FIGURE 4.29: Photos of the surface of bovine liver after being exposed to 60, 10-ms pulses at the maximum linear *in situ* intensity of 22 kW/cm^2. The left image shows the liver in the high pressure chamber. Mounds of thermally denatured tissue are visible at the overpressure exposure sites with cooked debris near mounds. In this photograph, it is difficult to tell whether the cooked mound from the 200 psi exposure is not evident due to the ultrasound exposure or whether the area was disturbed when manipulating the tissue slice. The image on the right shows the same piece of bovine liver after it was removed from the chamber and the surface blotted to remove excess liquid. As you can see, when the cooked mounds of tissue are removed from the overpressure exposure locations, a hole with a thermal border is visible in the liver surface. In both images, the exposures at atmospheric pressure left a divot in the tissue with no obvious thermal boundary; no obvious differences were apparent in the holes created at atmospheric pressure before or after overpressure.

the cooked mound of tissue), there is a hole in the tissue surface, surrounded by a thermal border for all levels of overpressure. No thermal border is evident upon gross examination of the hole in tissue from the exposures at atmospheric pressure.

Figure 4.30 shows H&E and NADH histology images of samples taken from the liver surface after exposure to the 60, 10-ms pulses at atmospheric pressure. From the H&E image, it is evident that the hole in the tissue surface is about 3 mm in diameter and approximately 2 mm in depth. The hole contains both homogenized cellular debris in addition to some intact cells. When we look at the NADH-stained sample, we see some sections of lighter staining, indicating lower enzymatic activity, or thermal damage to the tissue. This lighter staining is evident in some of the cellular debris within the void and

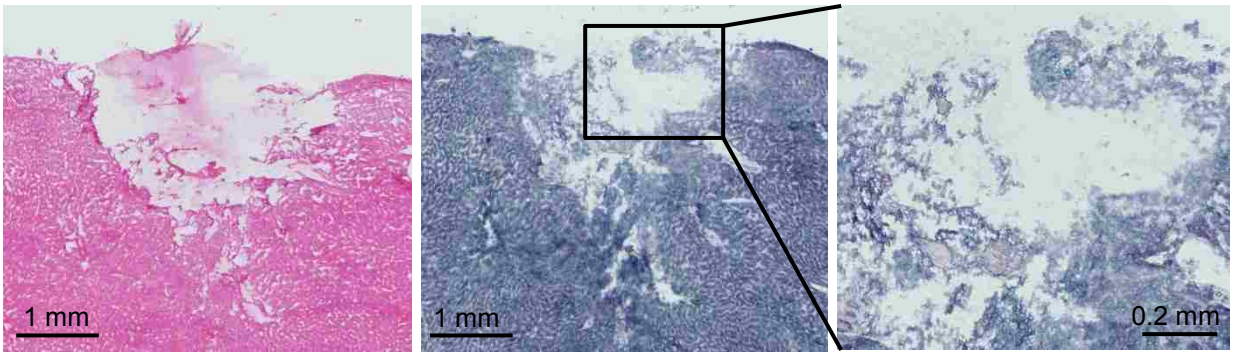

FIGURE 4.30: Microscopy images showing (*right*) H&E stained and (*center and left)* NADH stained samples of the 60, 10-ms pulse exposure at atmospheric pressure in bovine liver. The H&E image shows the outline of the hole with some cellular debris within the hole. The center NADH image shows the same hole, with some loss of enzymatic activity in some of the cellular debris within the void and some of the cells at the edges of the void. The right image shows a magnified section of the center photo, which more clearly shows the lighter staining (lower enzymatic activity) in the cellular debris near the top of the hole.

in some of the cells at the edge of the void. If we magnify a section of the NADH slide, we can see that cellular structure remains in the debris, though the lighter staining indicates some thermal damage. Some of the cells in the magnified image show blurring between the borders, indicating that the cells have been partially homogenized.

Figure 4.31 shows histology images of the liver after exposure to 60, 10-ms pulses for 350 psi and 1000 psi of overpressure. The 350 psi sample shows a hole beneath the tissue surface that extends approximately 3.5 mm into the tissue; however the hole does not reach the tissue surface. Rather, it appears as if cellular debris is pushed up so it extends above the liver surface, but never gets ejected from the exposure area. The NADH slide shows that the debris is enzymatically inactive – the cells are thermally damaged. When we magnify different areas of the NADH-stained slide, we see that deeper in the tissue (closer to the void), even though the cells are thermally damaged, cellular structure remains; however when we magnify the tissue that has been pushed above the liver surface, we still see thermal damage, but there is little to no cellular structure remaining. This indicates that the tissue above the liver surface was homogenized or partially homogenized before it was cooked. The thermally damaged tissue deeper beneath the liver surface has cellular structure, indicating that it was cooked before homogenization occurred. When the overpressure levels are increased to 1000 psi, the degree of tissue fractionation is reduced. Tissue below the surface was

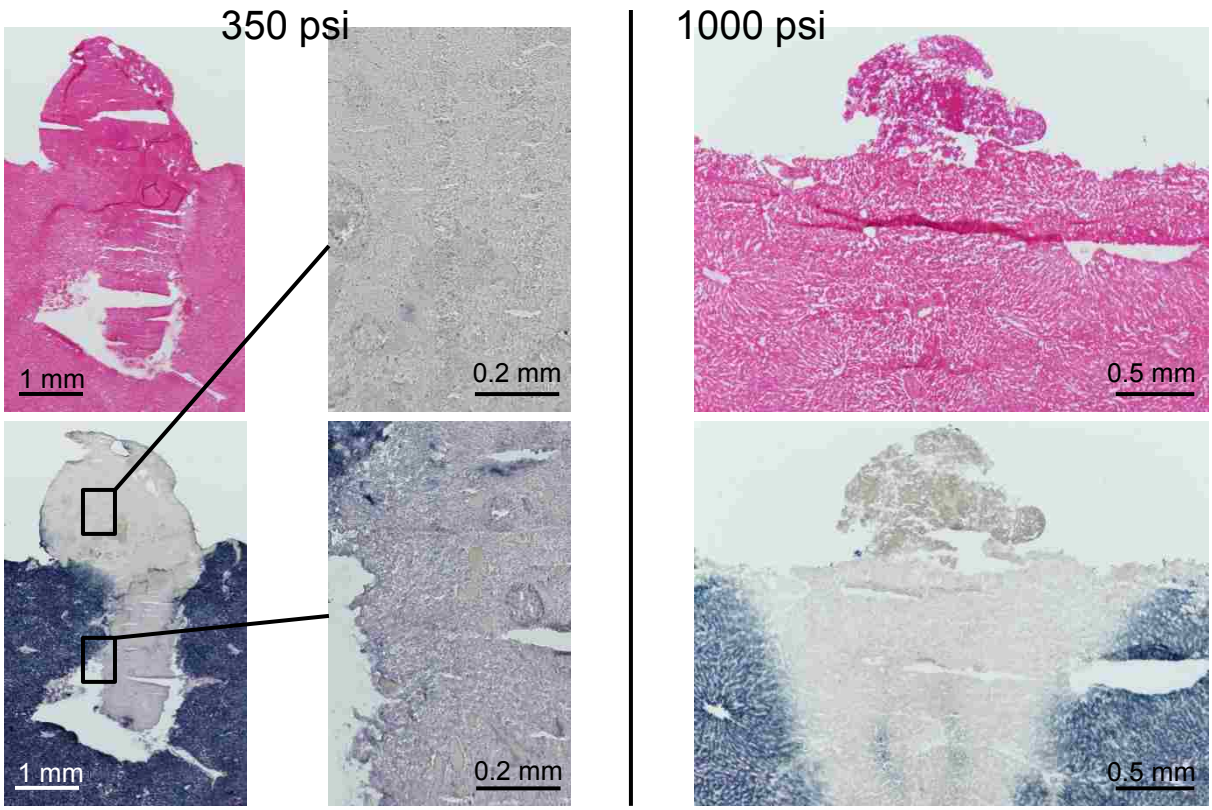

FIGURE 4.31: A combination of H&E and NADH images from the 60, 10-ms pulses at 350 psi (*left)* and 1000 psi (*right)* of overpressure. On the far left, we see the H&E (*upper*) and NADH (*lower*) stained sections showing the extent of cellular damage at 350 psi. Beneath the liver surface is a hole in tissue that is partially filled with cellular debris that has been pushed up through, but not ejected from, the liver surface. The middle images show magnified sections of the NADH-stained slide from the 350 psi exposure. It is interesting that some cellular structure remains in the lower image, which was taken from the lower portion of the injured area; however, the upper image, taken from the cellular debris that had been pushed above the liver surface, shows no remaining cellular structure, suggesting that the tissue was homogenized before it was heated. The images on the far right show H&E stained (*upper)* and NADH-stained (*lower)* images of liver after the 1000 psi exposure. In this case, there is no obvious void below the tissue surface, and the thermal damage to the tissue extends well below the liver surface (as indicated by the lighter staining in the NADH section). Additionally, the tissue pushed above the liver surface shows some cellular structure, suggesting heating before homogenization; however the tissue below the surface, even the sections that were heated, show clear cellular definition and no homogenization.

thermally damaged but not fractionated. The mound above the tissue surface shows thermal injury with some cellular structure, indicating that the tissue was at least partially cooked before fractionation. Histology images from 1000 psi show no hole beneath the liver surface, and show a different pattern of thermal damage than was observed at 350 psi. This could be due to either the differences in boiling temperature or differences in the cavitation threshold at the different levels of overpressure.

4.5.3. Discussion

In this section, we showed that increasing the static pressure of the system alters atomization in both water and bovine liver. Even though high static pressure conditions have been shown to increase the boiling temperature, increase the bubble dissolution rate, and decrease the amplitude of bubble oscillations [96], these results are inconclusive as to the effect of bubbles on atomization in water and in liver. In water, it was surprising to find that atomization ceased at 1000 psi for the 850 W/cm^2 or 1200 W/cm^2 applied acoustic intensities, yet atomization began once again when the static pressure was increased to 2000 psi (13.9 MPa). Even assuming constructive interference between the forward and reflected, inverted, ultrasound wave at 1200 W/cm^2, the maximum tensile pressure is 12.1 MPa. Compared to the 1000 psi of overpressure, the applied acoustic wave exceeds the overpressure by almost a factor of 2, so cavitation bubble is still possible within the drop chain. However, at 2000 psi, the applied overpressure of 13.9 MPa exceeds the maximum tensile pressure of the applied acoustic wave, which means that cavitation bubble activity is highly unlikely, yet droplets are being emitted. It is unclear why atomization ceased at 1000 psi but began again at 2000 psi. The most likely explanation for atomization at 2000 psi are acoustic instabilities and resonance within the drop chain. While the drops in the chain oscillate at the 1000 psi of overpressure, the drops never atomize or release droplets. However, at 2000 psi, the drop chain is less consistent and has less definition; at times, the fountain sides appear smooth, before a drop chain structure again begins to merge. Relatively large droplets appear to be released when the drop chain transitions from smooth-sided to drop chain. These transitions in and out of the drop chain structure are likely due to interactions between reflected waves and incoming waves within the water column. The difference in reflection pattern with increasing static pressure could be due to the small changes in sound speed of water or the change in the acoustic impedance of air. A well-defined model with exact fountain dimensions could help support this hypothesis and explain why droplets are not released at 2000 psi but are released at 2000 psi for these specific acoustic intensities.

In bovine liver, atomization is significantly reduced and looks qualitatively different as the static pressure is increased, even though the amount of overpressure is much less than the applied acoustic pressures. At static pressures of 200 psi, 350 psi, and 500 psi, our histology slides showed a hole in tissue approximately 3 mm beneath the surface with cooked and partially fractionated tissue spanning the distance between the hole and the tissue surface and extending above the tissue surface. It was not until the static pressure reached 1000 psi that a hole was not consistently observed beneath the tissue surface, although histology still indicated partially homogenized and cooked tissue above the tissue surface and cooked tissue below the tissue surface. One explanation for the hole in tissue is boiling; at 500 psi, the boiling temperature of water is 242 °C [99]. According to weak shock theory (described more fully in the following chapter) with an *in situ* shock amplitude of 70 MPa, boiling is predicted in approximately 8 ms. When the static pressure is 1000 psi, the boiling temperature of water increases to 285 °C [99], in which case boiling is predicted in approximately 10 ms. As individual HIFU pulses are only 10-ms in duration, this calculation appears to support the hypothesis that boiling forms the void in tissue; however, it is also possible that the increase in cavitation threshold with increasing static pressure explains the void that is formed beneath the tissue surface. The location of the void (3 mm beneath the tissue surface) closely matches the maximum height of the mound, meaning the reflection of the ultrasound wave from the mound could cause intense cavitation down to that depth, forming the void. With this experiment, it is difficult to discern whether cavitation or boiling formed the void in tissue; reducing the HIFU pulse length could help make a distinction between cavitation and boiling.

At 200 psi, 350 psi, and 500 psi of overpressure, we noted that the cooked mound above the tissue surface appeared to be fractionated before cooking because of the homogeneity and liquidity observed in the H&E and NADH-stained slides. At 1000 psi, however, the cooked mound had granular and liquid components in the NADH and H&E-stained slides, indicating that the tissue was at least somewhat cooked before homogenization. The reduction in tissue homogenization with increasing static pressure indicates that tissue fractionation is likely related to bubble activity; however it is unclear why the fractionated tissue becomes cooked rather than ejected from the tissue surface

when the static pressure is increased. One possible explanation is that cavitation within the mound fractionates the tissue. At atmospheric pressure, cavitation bubble collapse along with radiation force causes the liquefied tissue to be ejected from the surface; however, when the static pressure is increased, bubble oscillations are reduced [96], slowing the rate of tissue fractionation and ejection of the liquid from the tissue surface. Thermal denaturation or cooking occurs when the fractionated tissue is not ejected fast enough; the change in acoustic and mechanical tissue properties with heating further reduces jetting. After one or several HIFU pulses, the fractionated and cooked tissue extends above the tissue surface and influences the wave propagation and reflection of subsequent HIFU pulses. Between the altered wave dynamics and the reduction in jetting, tissue beneath the surface which would have been ejected at atmospheric pressure also becomes thermally denatured and partially fractionated, extending the thermal injury pattern well beneath the tissue surface. It is also possible that the reduction in bubbles from the elevated static pressure allows higher acoustic intensities to reach the tissue surface, which in turn increases the tissue heating rates. Then, as before, the fractionated tissue becomes thermally denatured before ejection from the tissue surface, forming a mound of cooked, liquefied tissue. However, the difference between the acoustic pressures and the applied overpressure makes the expected change in bubble dynamics relatively minor, which means it is unlikely that bubbles are the reason the tissue is cooked rather than denatured. More research is needed to understand this phenomenon.

In the high speed videos, jetting from the tissue surface continues even when the static pressure is increased. When the pressure is increased to even 200 psi, the emitted drops become uniformly small in diameter and are emitted at less than half of the velocity that was observed at atmospheric pressure. It is unlikely that thermal denaturation of the tissue explains the change in the observed jets as the change in ejection mechanism began at the start of the high speed videos, before tissue cooking is expected to occur. Also, our photographs of the liver surface show small pieces of cooked tissue near the cooked mounds of tissue indicating that at least some jetting occurred once the tissue was thermally denatured. It is unlikely that capillary waves describe the mechanism of droplet release because the droplets are emitted primarily

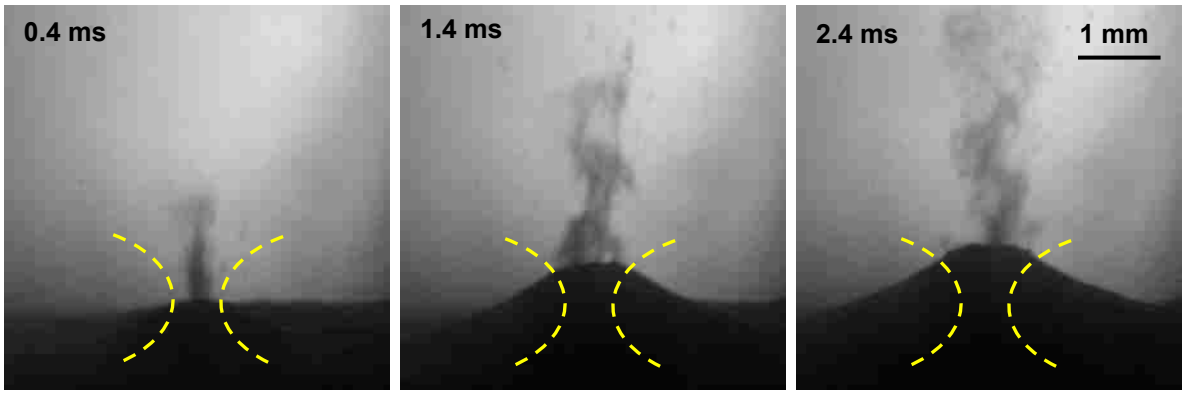

FIGURE 4.32: Frames from high speed videos of bovine liver atomization from 2 MHz ultrasound at 22 kW/cm^2 (p_+ = 67.4 MPa, p_- =16.4 MPa) when exposed to 350 psi of overpressure. The yellow dotted line shows an approximation of the -6 dB focal curvature. The figure shows that as mound height increases, the length of mound surface that atomizes increases, approximately following the -6 dB focal area of the transducer.

from the peak of the liver mound; if capillary waves were the release mechanism, we would expect the droplets to be emitted from the entire mound surface. Rather, we hypothesize that spallation, (which is likely one of the ejection mechanisms at atmospheric pressure), becomes the dominant mechanism of particle release under increased static pressure conditions. If spallation is the mechanism of atomization, we would expect that the jets will be emitted from the surface of the mound approximately following the -6 dB focal area of the transducer. Figure 4.32 shows atomization with increasing mound height at 350 psi overpressure. From the yellow dotted line in the figure, it is evident that the width of atomization from the mound surface approximately follows the -6 dB focal area of the transducer. Near the beginning of the exposure, the mound height and the jetting width is approximately 0.3 mm. In the second frame of the figure, the mound height is now 0.8 mm and the jetting width from the liver surface is now 0.7 mm. Finally, in the third frame of the figure, the mound height and the jetting surface width is 1.1 mm. This relation between the -6 dB focal area of the transducer and the width of jetting supports our spallation hypothesis; as the tissue forms a mound, the focal area that encounters the pressure release interface begins to spread, causing jetting to occur from a larger surface area.

When we compared our observed mound height to our calculated mound height, we found that the observed mound height of approximately 3 mm was only ¼ the calculated mound height of 12 mm. We expect that some of this error came from neglecting viscosity in the calculation as the relatively fast height change (~ 1 m/s) will increase the influence of viscosity on our mound height. Also, our decay time constant fitted to the Kelvin-Voigt model in the previous section indicated that viscosity is a dominating force in the stress relaxation of the fountain, which means that neglecting it should cause an overestimation in the calculated mound height. An additional source of error is our choice of the applicable length when considering the tissue strain. We used ½ of the -6 dB peak positive focal area of the transducer; however, that is not necessarily correct as the focal volume of the transducer actually has a pressure gradient and the ring-up in our pulse echo measurement makes it is difficult to know exactly where the tissue surface lies in the focal volume. The values used for the Young's modulus, attenuation coefficient, and attenuation length also constitute potential sources of error. For the calculations we used the smallest liver thickness of 1 cm, yet some of our samples were closer to 1.5 cm thick. As far as the values for Young's modulus and attenuation for the liver, even though these values were from literature, we have noticed large differences in mechanical properties, acoustic properties, and quality of the liver, even when purchasing from the same supplier. These sources of error caused an overestimation of the observed liver mound height; however the calculation did provide an order of magnitude estimation of the mound height while affording us the opportunity to consider the forces influencing the mound height in liver.

Observing atomization in a high static pressure chamber created more questions than it answered as far as the mechanism of atomization in water and liver. In liver, we found that the degree of tissue fractionation decreased when the static pressure was increased, allowing us to conclude that bubbles cause tissue fractionation. We were also able to conclude that spallation explains at least one mechanism of liver atomization, as the jetting surface followed the -6 dB focal area of the transducer for all levels of overpressure and cooked tissue pieces or spall surrounded the cooked mounds from the overpressure exposures. However, the fact that the tissue is cooked when even a small amount of overpressure is applied (as compared to the applied

ultrasonic pressures) makes it difficult to say that bubbles are necessary for atomization. More research is needed to understand why the fractionated tissue is cooked rather than ejected from the liver surface when the static pressure is increased. In addition, the results from water atomization suggest that dynamic instabilities in addition to cavitation and likely boiling bubble activity explain atomization in a drop chain. The cessation and then restart of atomization when the static pressure increased from 1000 psi to 2000 psi for certain applied acoustic intensities made it impossible to rule out surface waves to conclude that bubbles are necessary for atomization in a liquid fountain. A detailed model is needed to understand these experimental results.

4.6. Summary and Conclusions

The purpose of this long chapter was to increase our understanding of the mechanisms of atomization in liquids and tissues. We began by observing atomization in water with a high speed camera at different ultrasonic frequencies. We were able to conclude that the drop chain dimensions depend directly on the ultrasonic wavelength. Then, at a fixed 2 MHz frequency, we atomized liquids with varying viscosities, boiling points, and cavitation thresholds. From the results, we surmised that boiling described atomization in a drop chain, as the timing of atomization decreased with increasing temperature and n-propanol (which has a similar boiling point to water) atomized very similarly to water. In the third section, we changed from the atomization of liquids to viscoelastic solids. In tissue-mimicking gels, we found that the wetting liquid on the surface did not matter, and from this result hypothesized that waves in the wetting liquid on the gel surface caused the reflected wave to refocus at or near the gel surface to cause erosion. This hypothesis was supported by an *in vivo* porcine liver experiment, where it was found that changing the surface wave dimensions by wetting the liver capsule with soapy water allowed us to breach the liver capsule. Finally, we atomized water under high static pressure conditions and showed that it was difficult to separate the effects of bubbles from dynamic instabilities to explain atomization in a drop chain fountain. We also atomized bovine liver under high static pressure conditions and showed that while bubbles were necessary for tissue fractionation, it was unclear whether bubbles were necessary for atomization as the tissue was thermally denatured rather than ejected

from the liver surface when the static pressure was increased. More research is needed in both water and in tissues to understand the mechanisms of atomization. In the next section, we change gears somewhat to look at the threshold of renal tissue injury.

CHAPTER 5

Establishment of an Injury Threshold for Therapeutic Ultrasound[4]

5.1. Introduction

Due to the wide variety of bioeffects that can be produced in tissues, the clinical uses of ultrasound span diagnostic to therapeutic levels. However, the potential for tissue damage from ultrasound has prompted the need for safety guidelines. The initial guidelines for diagnostic ultrasound were established in the 1970s and were based around thermal bioeffects [108]. It wasn't until the late 1980s, that the mechanical effects of ultrasound entered the discussion, with the definition of the mechanical index ($MI = p_{-} / (f^{0.5})$) being introduced into the clinical ultrasound world in 1991 [14]. After almost 6 decades of use in the clinic, safety for B-mode ultrasound imaging has been fairly well established; however, no safety guidelines for ultrasound at the therapeutic levels have been adopted by the FDA [109]. With the emergence of new diagnostic and

[4] Work published in part in:

Wang Y-N, **Simon JC,** Cunitz BW, Starr F, Paun M, Liggitt DH, Evan AP, McAteer JA, Liu Z, Dunmire B, and Bailey MR (2013). "Focused ultrasound to displace renal calculi: threshold for tissue injury." J. Therapeutic Ultrasound Submitted August 5, 2013.

Connors BA, Evan AP, Blomgren PM, Hsi RS, Harper JD, Sorensen MD, Wang Y-N, **Simon JC,** Paun M, Starr F, Cunitz BW, Bailey MR, and Lingeman JE (2014). "Comparison of tissue injury from focused ultrasonic propulsion of kidney stones versus extracorporeal shock wave lithotripsy," J. Urol. S0022-5347(13)05053-2.

Sorensen MD, Bailey MR, Hsi RS, Cunitz BW, **Simon JC,** Wang Y-N, Dunmire BL, Paun M, Starr F, Lu W, Evan AP, and Harper JD (2013). "Focused ultrasonic propulsion of kidney stones: Review and update of preclinical technology," J. Endourology 27(10), 1183-1186.

Harper JD, Sorensen MD, Cunitz BW, Wang Y-N, **Simon JC,** Starr F, Paun M, Dunmire B, Liggitt HD, Evan AP, McAteer JA, Hsi RS, and Bailey MR (2013). "Focused ultrasound to expel calculi from the kidney: safety and efficacy of a clinical prototype device," J. Urol. 190, 1090-1095.

Shah A, Harper JD, Cunitz BW, Wang Y-N, Paun M, **Simon JC**, Lu W, Kaczkowski PJ, and Bailey MR (2012). "Focused ultrasound to expel calculi from the kidney." J. Urol. 187(2) 739-743.

therapeutic ultrasound hybrids, patient safety needs to be carefully evaluated for each individual application until the FDA collects enough data to be able to publish overall safety guidelines for therapeutic ultrasound.

The current limits set by the FDA for diagnostic ultrasound, are derated spatial-peak, pulse average-intensity (I_SPPA) < 190 W/cm^2, Mechanical Index (MI) < 1.9, derated spatial-peak, temporal-average intensity (I_SPTA) < 720 mW/cm^2 [13]. These values are derated by the constant 0.3 dB/MHz/cm defined by the FDA [13], [110]. The only other FDA-approved, ultrasound-related device is the shock wave lithotripter, which generates a shock wave outside the body and focuses them to break up kidney stones. The peak pressures of clinical shock wave lithotripters (SWLs) are 37-115 MPa peak positive and approximately 10 MPa peak negative, with a total energy dose of 100-200 J [111]. As of right now, therapeutic ultrasound devices trying for a 510k FDA approval must track under either diagnostic ultrasound or SWL. As the therapeutic ultrasound field is advancing rapidly, new FDA safety guidelines are sorely needed.

An example of one such diagnostic and therapeutic device uses ultrasound to expel renal calculi from the kidney [42], [43]. The prevalence of kidney stones in the United States is increasing, affecting more than 10% of the population; within 5 years, 50% of those patients will have a recurrence of stones [112]. SWL remains the principle

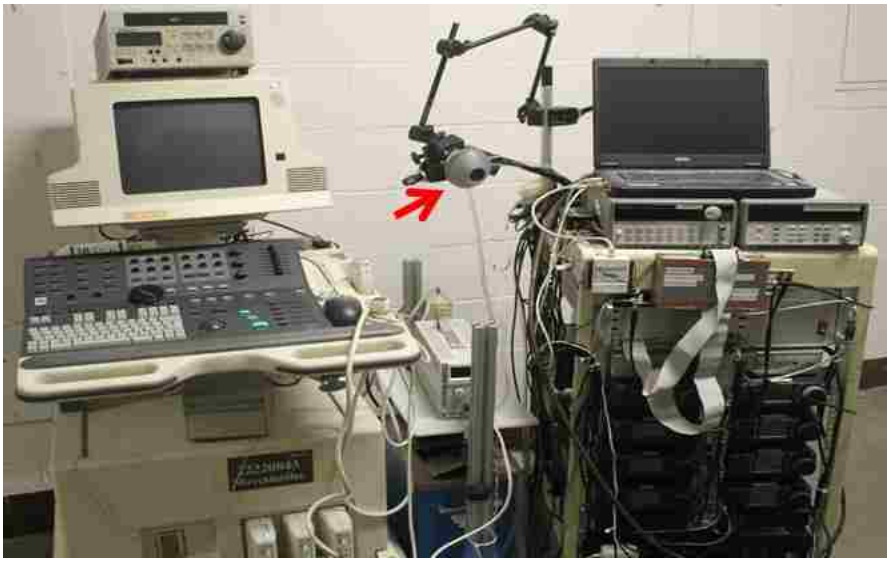

FIGURE 5.1: Image showing the first generation array device used in the threshold study. On the left is the HDI 5000, which collects an image of the kidney with a coaxially aligned P4-2 transducer. In the middle is the water cooling and circulation system, and on the right is the custom-built array device. The red arrow indicates the 2 MHz array transducer with the water-coupling cone.

treatment for kidney stones [30], despite increasing evidence that SWL causes significant damage to the kidney [31]–[35]. Unfortunately, after SWL stone fragments often remain in the kidney (especially in the lower pole where spontaneous stone clearance is rare due to gravity), which can act as nuclei for the formation of new stones [39]–[41]. Other treatments for kidney stones include ureteroscopy, percutaneous nephrolithotomy, or pharmaceutical interventions such as potassium citrate, but the risks involved with some of these treatments (or the mixed success rates) make them not as commonly used [113]. A need exists for non-invasive therapies that can aid the spontaneous passing of small stones and that can assist with residual stone fragments after SWL. Using ultrasound to non-invasively move stones or stone fragments out of the kidney could reduce the use of SWL and other invasive therapies and, if used in conjunction with standard stone treatments, could improve the stone-free rates of many patients.

FIGURE 5.2: Photo of the second generation clinical device. The Verasonics® Ultrasound Engine (in silver on the right) and ultrasound transducer (P4-1 shown in front of the keyboard) is used to both image and move stones. The PC (on the left) communicates with the Verasonics via MATLAB® software.

Previously, we reported the use of a first generation custom array device (shown in figure 5.1) to expel renal calculi [43]. This device consists of an eight-element annular array therapy transducer and a coaxially aligned commercial transducer controlled with the HDI 5000 ultrasound imager. Due to the tissue damage that has been observed after SWL treatments, one of our first goals was to establish a safe parameter-space for moving stones. To that end, the first section of this chapter reports a threshold for *in vivo* porcine kidney injury using the first generation custom array device. While the threshold work was progressing, a second generation hybrid diagnostic/therapeutic device was built on the Verasonics® Ultrasound Engine platform (shown in figure 5.2). With the ultimate goal of clinical use,

this device uses a single, commercially available transducer to move and image the stone. The second section of this chapter reports the safety and efficacy of the second generation device when moving stones within *in vivo* porcine kidneys. Based on the results from this second study in addition to further bench-work, the stone pushing sequence was then updated to reduce the number of ultrasound pulses that missed the stone. The new pulsing sequence along with the potential for delayed-onset injury prompted the need for an *in vivo* porcine survival study, which is the topic of the third section of this chapter. We hypothesized that the novel second generation diagnostic/therapeutic device operated at intensities well below the kidney injury threshold.

5.2. Establishment of an *In Vivo* Porcine Kidney Injury Threshold

5.2.1. Methods

First Generation Array Device

As the second generation clinical device was operating at its peak output in early studies, the custom-built, first generation, ultrasound array system that could produce pressures well beyond those produced by the clinical system was used for this study. The device shown in figure 5.1 consists of a 2 MHz, 8 element annular array with a diameter of 6 cm and curved to fit a natural focus of 6 cm (H-106, Sonic Concepts, Bothell, WA). Eight SC-200 radiofrequency synthesizers (Sonic Concepts) and individual 100 W IC-706MKIIG amplifiers (Icom®) were synchronously used to excite the eight elements of the array. A Dell laptop computer was used to operate MATLAB® software that controlled the excitation timing of each element, allowing the user to control the focal depth from 3.5 cm to 9.5 cm.

The treatments were image-guided using a coaxially aligned P4-2 imaging transducer and HDI-5000 ultrasound imaging system (Philips ATL®), which allowed the operator to manipulate the probe so that the proximal parenchyma was at a depth of approximately 6 - 6.5 cm with respect to the transducer. These two depths were selected based on the depths of the maximum output of the array and because they put the transducer focus about 1-1.5 cm beneath the surface of the kidney in the proximal parenchyma of

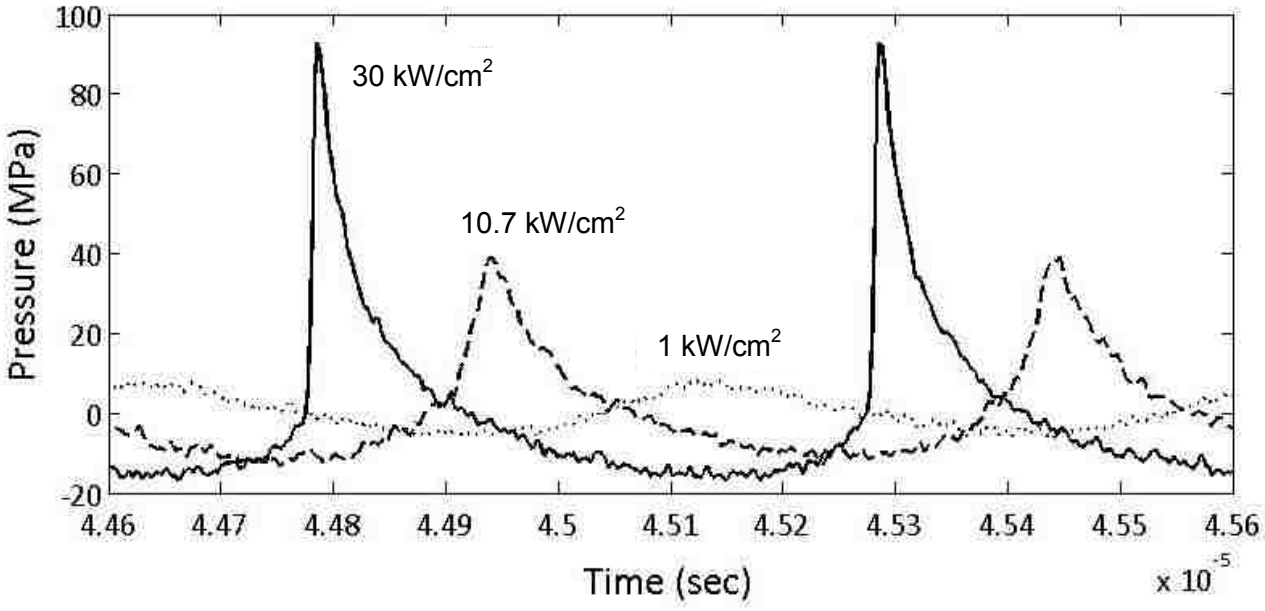

FIGURE 5.3: Image showing selected waveforms collected from the array device as measured with the fiber optic probe hydrophone (FOPH) in water.

the porcine kidney (when the water-filled coupling cone was used). The array system was programmed to the desired settings and a foot switch was used to start and stop the focused ultrasound. A water cone of approximately 5 cm in length with a 0.01 inch, thick silicone rubber membrane, was used to couple the transducer to the animal. A custom-built water cooling system and pump was used to keep the transducer surface cool, with the water temperature set at about 8 °C.

The output of the device was measured in filtered and degassed room temperature water (~20°C) with a fiber-optic probe hydrophone (FOPH 2000, RP Acoustics, Leutenbach, Germany). The cone was on the transducer head to help align the hydrophone and to check whether the cone interfered at all with the acoustic field; the membrane that fits on the cone was not used. Figure 5.3 shows select measured waveforms. Since shocks were present in the higher amplitude waveforms, the nonlinear spatial peak pulse averaged intensities were calculated using previously developed methods [66]. Briefly, a number of cycles where the transducer had reached

a steady state were selected. Then, the nonlinear spatial peak pulse-averaged intensity was calculated from the measured waveforms according to the formula:

$$I_{SPPA} = \frac{1}{\rho_0 c_0 (t_2 - t_1)} \int_{t_1}^{t_2} |p|^2 \, dt$$

The maximum intensity that could be achieved with the device was found to be 30,000 W/cm^2 in water with corresponding peak positive pressure *(p_+)* of 96 MPa, peak negative pressure *(p_-)* of 16 MPa.

These measurements in water were translated into tissue using the previously developed derating methods for nonlinear HIFU waves [27], [64], [67]. Briefly, the *in situ* intensities and peak pressures at the focus in tissue for a given output of the transducer corresponded to those measured in water for some lower power output. The scaling factor between pressure was calculated as exp(-αL), where α is the attenuation coefficient in tissue at the operational frequency of the transducer and L is the tissue depth. As has been shown in previous studies, when the source outputs are scaled to account for linear attenuation losses in tissue, then both the peak pressure levels and the intensity at the focus as well as the degree of nonlinear waveform distortion are similar in water and tissue [27], [64], [67]. For our case, the length was 1 cm, which was the distance the ultrasound propagated through tissue to reach the focus. The attenuation coefficient used to calculate the *in situ* pressure and intensity was 0.3 dB/cm/MHz (as defined by the FDA). We chose to follow the FDA documentation rather than the attenuation coefficient reported for renal tissue (approximately 0.5 dB/cm/MHz [114] to simplify our comparison between this device and the novel hybrid diagnostic/therapeutic device for moving kidney stones (i.e. the Rolling Stones device).

Animals

The renal parenchyma of domestic swine was treated *in vivo* following a protocol approved by the Institutional Animal Care and Use Committee at the University of Washington. A total of 29 female pigs weighing 101-141 lbs were sedated with an intramuscular injection of Telazol (4 mg/kg). Swine were used as pig kidneys are more similar to human kidneys in anatomy, function, and size than most other animal species.

Anesthesia was maintained with Isoflurane at 1.5-3% via an endotracheal tube. The abdomen was opened with electro-cautery to reduce bleeding, and the intestines were pulled to the side for better access to the kidney. The renal fascia was removed and the kidney was raised and immobilized on a bed of gauze, making sure to keep the gauze out of the ultrasound propagation path. The abdominal cavity was filled with degassed phosphate buffered saline (PBS) to couple the transducer to the kidney, though in some cases where the abdominal anatomy made it difficult to keep the kidney fully submerged, ultrasound transmission gel was also used. As previously stated, the ultrasound transducer was positioned so the proximal renal parenchyma was about 6 cm to 6.5 cm from the transducer. Exposure settings were randomly chosen for each treatment site, with a maximum of seven distinct targeted sites per kidney. During the treatment, the ultrasound image was monitored for signs of hyperechogenicity (except for the 100% duty cycle exposures because the interference from the focused ultrasound made it impossible to monitor the target site during the treatment). After each exposure, the kidney was carefully examined and photographed, and the targeted site was marked with histology ink for later processing.

Exposures

Exposure conditions were defined around the expectations for the clinical stone-moving protocol. All of the exposures were 10 minutes in duration, as that length of time was considered to be the maximum time in push mode required to move a stone from within the kidney to the exit. Three sets of data were collected: one set at 3.3% duty cycle with 100 μs pulses repeated every 3 ms and varying intensity (defined based on the original stone pushing parameters); one set at 100% duty cycle with varying intensity (of interest in case the machine malfunctioned and was operating continuously in “push” mode); and one set at an intensity of 9,319 W/cm^2 with varying duty cycle (of interest in case it was found that another duty cycle could more efficiently move stones). Table 5.1 shows the list of the three datasets with the number of samples in each set.

The sample counts are the highest for the 3.3% duty cycle group as this exposure was expected to be the most appropriate for the kidney stone pushing application and in some cases these samples showed very subtle injury. The lowest sample counts in

Table 5.1. List of injury exposures and the number of samples for each plot.

3.3% Duty Cycle		100% Duty Cycle		$I_{SPPA.3}$ = 9,319 W/cm^2	
$I_{SPPA.3}$ (W/cm^2)	Samples	$I_{SPPA.3}$ (W/cm^2)	Samples	Duty Cycle (%)	Samples
0	29	0	13	0	13
934	12	467	3	2	7
2529	14	934	6	6	5
4094	10	2529	7	10	8
6,031	10	4094	8	25	3
9,319	12	6031	5	50	5
12,233	11	9319	4	100	4
16,618	14				
21,000	11				
26,128	10				

both the 100% duty cycle and the 9,319 W/cm^2 groups are 3 samples, as the injury type and the tissue fixation/staining method allowed for easier interpretation and because these were not the primary focus of this study. The exact exposures were arbitrarily chosen based on the capabilities of the machine and the anticipated results.

The temperature rise in kidney tissue at the transducer focus was estimated using weak shock theory and the heat transfer equation as published in Canney et al [27]. The weak shock theory equation is listed below:

$$q = \frac{\beta f A_s^3}{6 c_0^4 \rho_0^2}$$

Where β is the nonlinearity parameter, f is the transducer center frequency, A_s is the shock amplitude, c_0 is the speed of sound, and ρ_0 is the tissue density [27]. Using the maximum pressure measurements of the transducer along with the parameters for kidney found in [89], focal heating was calculated with β=7.1, f=2 MHz, A_s = 89 MPa (*in situ*), c_0=1560 m/s, and ρ_0=1050 kg/m^3. Neglecting diffusion, as heating is expected to occur very rapidly such that the heat loss from diffusion is expected to be insignificant, the heat transfer equation can reduce to:

$$\Delta T = \frac{qt}{c_v}$$

Where ΔT is the change in temperature from the ambient temperature of the tissue, q is the heating rate at the focus estimated by weak shock theory, t is the time, and c_v is the specific heat capacity per unit volume [27]. At the maximum intensity of 26,000 W/cm^2, derated, and a 3.3% duty factor composed of 100 μs pulses repeated every 2.9 ms, the temperature rise is approximately 6.5 °C per pulse. In the 2.9 ms where the transducer is off, there will also be some cooling due to perfusion and diffusion of less than 1/10th of a degree per off time, (based on calculations using values from Cornelis et al. [115]). When the transducer is run at the maximum for the other two plots (9,319 W/cm^2 derated intensity and 100% duty cycle), 13.3 ms of continuous ultrasound is required for the tissue temperature at the focus to reach 100 °C. These values were calculated assuming an ambient temperature (body temperature of the pig) of 37 °C.

In most of the pigs, both kidneys were used for this threshold study; however in a few cases, the contralateral kidney was used for other studies. After the kidney(s) were treated, they were either removed for frozen histological analysis (for the 100% duty cycle and the 9,319 W/cm^2 groups) or perfusion fixed *in situ* (for the 3.3% duty cycle group) before removing for histological analysis. In the case of frozen histological analysis, individual treatment locations marked with histology ink and separate control tissue were individually embedded in TissueTek® Optimum Cutting Temperature Compound (Sakura Finetek, Torrance, CA, USA). Sections approximately 8 μm thick were sliced and stained with nicotinamide dinucleotide diaphorase (NADH-d) to evaluate for thermal injury in addition to Hematoxylin and Eosin (H&E). These frozen-fixed sections were scored by only one blinded expert, as injury was easily identifiable because of the fixation methods. In the case of perfusion-fixed histological analysis, whole kidneys were perfusion fixed *in situ* with a 2% glutaralydehyde in a 0.1 M cacodylate buffer. The kidneys were then submerged in 10% neutral buffered formalin for at least one week, before the treatment locations marked with histology ink and separate control tissue samples were individually placed in containers. Samples were then embedded in paraffin, sectioned at about 5 μm thick, and stained with H&E and

periodic acid Schiff (PAS). These perfusion-fixed histology slides were randomized and reviewed by three independent, experienced reviewers blind to the experimental conditions. The slides were judged to be either normal or showing signs of injury, in which case the reviewer described the observed injury. From these notes, sections were placed into a scoring rubric as defined in Table 5.2.

Statistics

An expert statistician, Dr. Ziyue Liu from Indiana University, performed the statistical analysis on these data. The agreement between our three independent blinded

Table: 5.2. The injury scoring rubric.

0	No injury (including only background lesions)
1	Degenerative injury - marked by tubular damage
2	Focal degeneration and necrosis
3	Focal degeneration with hemorrhaging

histology experts was calculated using the intra-observer correlation coefficient (ICC). The determination of agreement between scorers was: stated as poor if the ICC is 0-0.2; considered fair if the ICC is 0.3-0.4; considered moderate if the ICC is 0.5-0.6; stated as strong if the ICC is 0.7-0.8; and was considered almost perfect if the ICC is > 0.8. The threshold for injury was calculated using the plateau model, a special case of the change point model where the slope is zero. The suitability of the model was determined by parameter estimates with a $p < 0.05$ being considered significant. The same method was used to determine the injury thresholds for the 100% duty cycle group and the nonlinear intensity of 9,319 W/cm^2.

In addition, the threshold for the hyperechogenicity of the 3.3% duty cycle group was determined using a generalized linear mixed effects model, as the outcomes were binary (either positive or negative for hyperechogenicity). Again, parameter estimates with a $p < 0.05$ were considered significant. Furthermore, the reviewer scores were compared to gross observations of injury for all three groups. The injury threshold was recalculated considering the gross observations of injury in addition to the scores by the

reviewers. The same plateau model was used as described previously with parameter estimates showing $p < 0.05$ being considered significant.

5.2.1. Results

3.3% Duty Cycle

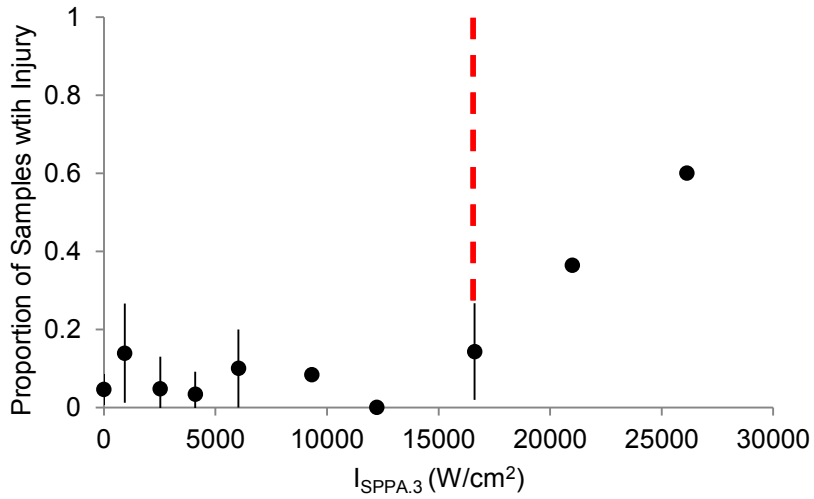

FIGURE 5.4: Plot showing the proportion of samples with injury versus intensity at a 3.3% duty cycle. Each point is the average proportion from the three reviewers and the error bars are one standard deviation. The red dashed line indicates the threshold for injury at approximately 16,600 W/cm^2.

Figure 5.4 shows the results from the three reviewers for the 3.3% duty cycle group plotted as proportion of samples showing injury versus intensity. The red line on the graph indicates the injury threshold, which was found by the statistician to be 16,618 W/cm^2, derated. The majority of the injury observed above this threshold intensity included emulsification, necrosis, and hemorrhage; lesion size was on the order of several millimeters in diameter. Figure 5.5 shows a few samples of the types of injury the types of injury observed above the threshold. Below the threshold, the probability that injury was observed remained constant and was below 0.2. Most of the injury observed below the threshold was background inflammation consisting of focal cell and tubular swelling and/or degeneration. Figure 5.6 shows examples of normal tissue and the types of background injury observed in tissues below the injury threshold. The scorers were in almost perfect agreement, with the intra-class correlation value calculated to be 0.86.

A variation in the 3.3% duty cycle graph includes our observations of gross injury at the treatment site and is shown in figure 5.7. The primary type of injury that was present

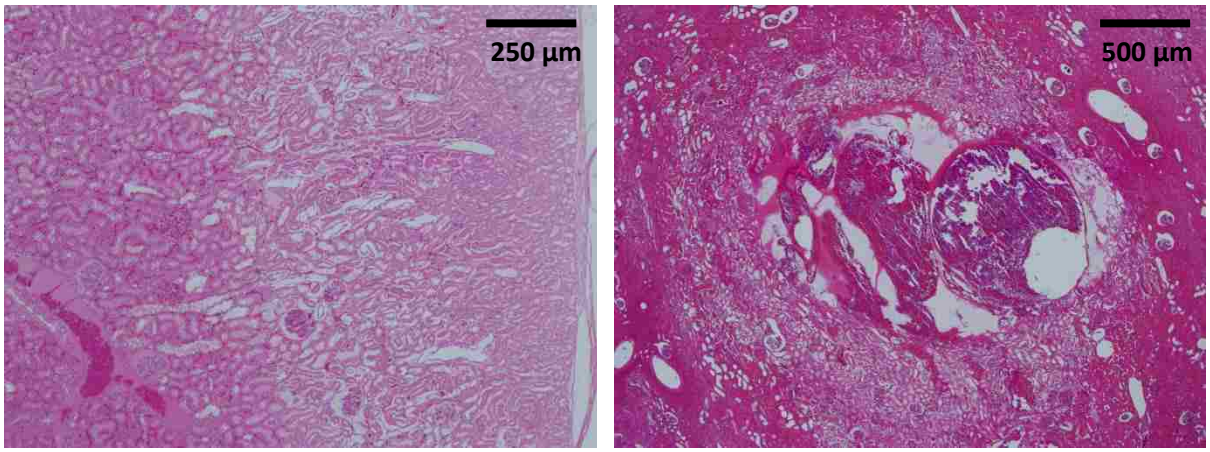

FIGURE 5.5: Two H&E stained histology images showing types of injury observed above the threshold of injury at 3.3% duty cycle. The image on the left was scored both 2 and 3, and shows evidence of necrosis and hemorrhage. The image on the right was scored a 3 by all reviewers and shows evidence of emulsification in addition to necrosis and hemorrhage.

upon gross examination was surface bruising that could have faded by the time of tissue collection. Figure 5.8 shows an example of the surface bruising that was observed at the time of experimentation that was not apparent in the scores by the reviewers. When these samples are included in the dataset as evidence of injury, the plateau model gives an injury threshold of 4094 W/cm^2, derated, which is about ¼ the intensity threshold calculated without the observations of gross injury.

An additional figure 5.9 shows the proportion of samples showing hyperechogenicity

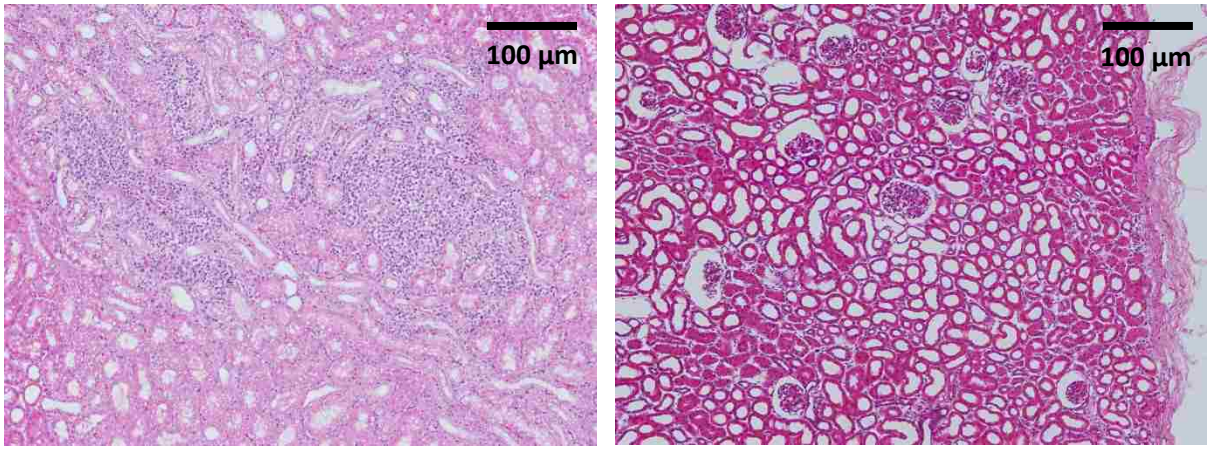

FIGURE 5.6: Two H&E stained histology images showing what was observed below the injury threshold at the 3.3% duty cycle. On the left, the image shows background inflammation that was often observed in the pigs. The right image shows a control image with very good fixation.

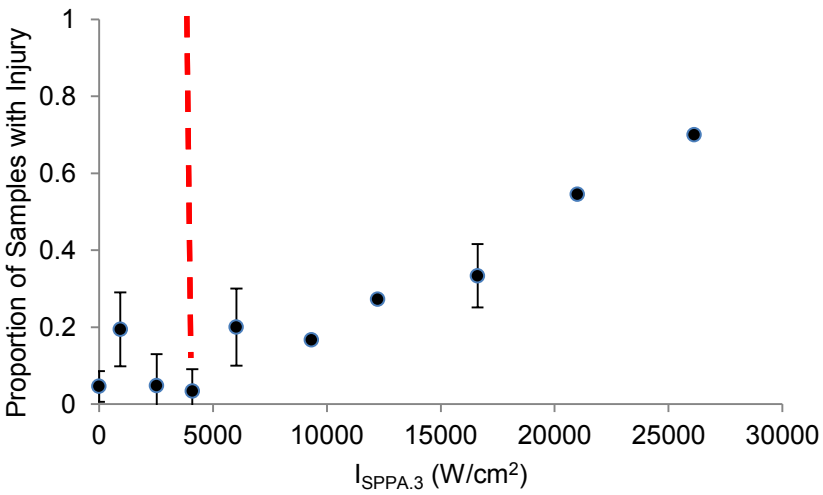

FIGURE 5.7: Plot showing the proportion of samples with gross and histological injury versus intensity at a 3.3% duty cycle. Each point includes the observations of the three reviewers in addition to the gross injury observed in photographs taken at the time of the study. As before, the red line indicates the injury threshold, which is at about 4000 W/cm^2 in this case.

plotted versus the intensity. Comparing figure 5.9 to figures 5.4 and 5.7, you can see there is a fairly good correlation between the proportion of samples showing injury and the proportion of samples with hyperechogenicity; however, the raw data indicates that the individual samples that show hyperechogenicity do not necessarily show injury. The threshold for hyperechogenicity calculated with the generalized linear mixed effects model was found to be 4094 W/cm^2, derated. This threshold agrees with the injury threshold calculated when the gross injury from notes is included.

100% Duty Cycle

Figure 5.10 shows the proportion of samples showing injury for the 100% duty cycle frozen-fixed samples that were scored by a single blinded expert. The last data point is a little odd as we had one instance where no injury was found at the 9,319 W/cm^2 exposure. This occurrence of no injury is most likely due to a machine malfunction; it is unlikely we missed collecting the exposure location as all other instances using the maximum exposure of the array resulted in large lesions that oftentimes cooked through the entire kidney with large thermal lesions visible on both surfaces as

FIGURE 5.8: Photograph of a bruise on the kidney surface taken at the time of the study. These types of injury were not always apparent in the histology slides.

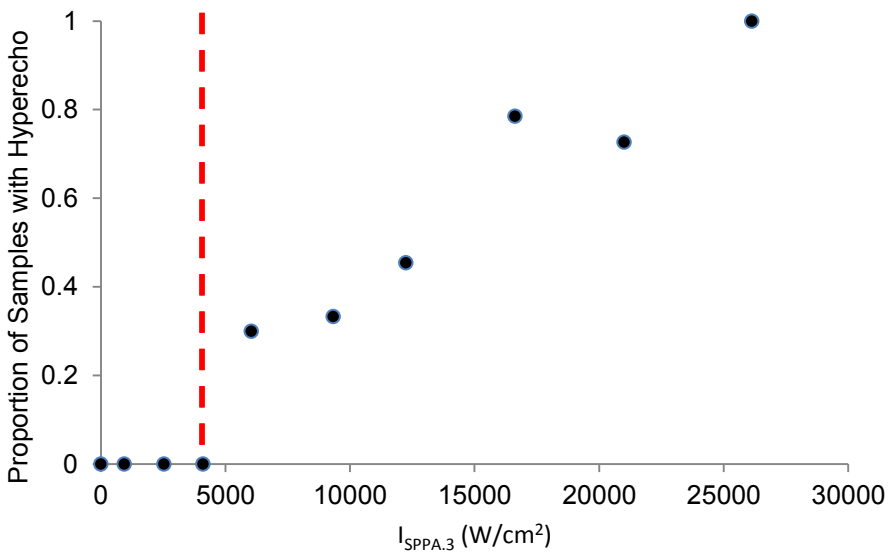

FIGURE 5.9: Plot showing the proportion of samples with hyper-echogenicity versus intensity at a 3.3% dutycycle. As before, the red line indicates the threshold, which is at about 4000 W/cm^2 in this case.

shown in figure 5.11. The threshold for injury was found to be 467 W/cm^2, derated. In this case, there is no noise below the threshold since the threshold is our first non-zero data point. Figure 5.12 shows an example of the type of injury seen above the threshold as viewed on a NADH-stained slide.

9319 W/cm^2 Intensity

Figure 5.13 shows the proportion of samples showing injury versus duty cycle for a fixed nonlinear intensity of 9319 W/cm^2. Again, the last point, which is actually the same

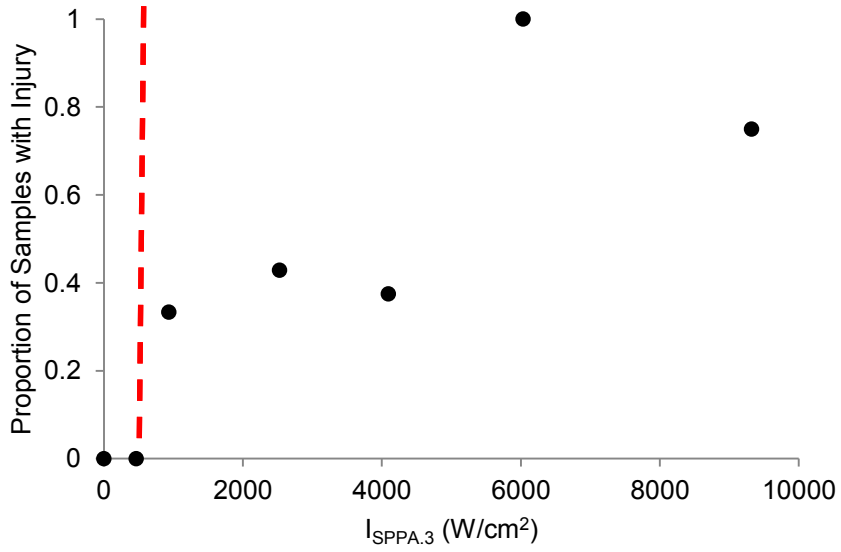

FIGURE 5.10: Plot showing the proportion of samples with injury versus intensity at a 100% duty cycle. In this case, there was only one scorer, as the frozen fixation and NADH staining method made the presence of injury very obvious. As before, the red line indicates the injury threshold, which is at about 500 W/cm^2 for this case.

exposure as the last point in the 100% duty cycle plot (see figure 5.10), has a lower proportion of injury than we would expect; again we believe that this one instance of no injury at those setting was due to machine malfunction, but as we have no concrete evidence to support this claim, we did not exclude the sample from the dataset. The threshold for injury using the plateau model was found to be at the 2% duty cycle for this graph. Figure 5.14 shows another example of injury observed with the NADH-stained histology. From these images, it is apparent that injury is definite, which is why only one expert scored this slides.

FIGURE 5.11: A photo showing the typical level of gross injury observed for the 9300 W/cm^2 exposure at 100% duty cycle.

5.2.3. Discussion

In this chapter, we have presented a range of therapeutic ultrasound intensities at which there exists a low probability for causing injury to the kidney. These data were taken at a single frequency of 2 MHz, as, due to the depth involved, it is the frequency most likely to be used for imaging or treating the kidney. We were fortunate to have access

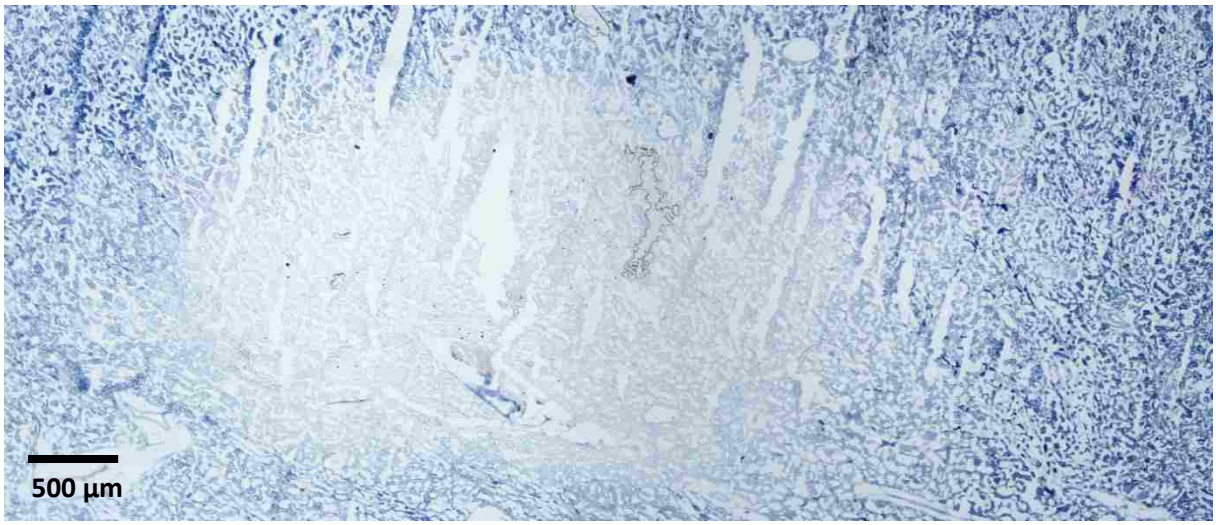

FIGURE 5.12: A large thermal injury as observed by the lack of blue staining in the middle of the slide. The exposure to create this injury was 6000 W/cm^2 and the 100% duty cycle. The maximum dimension of the injury is approximately 5 mm.

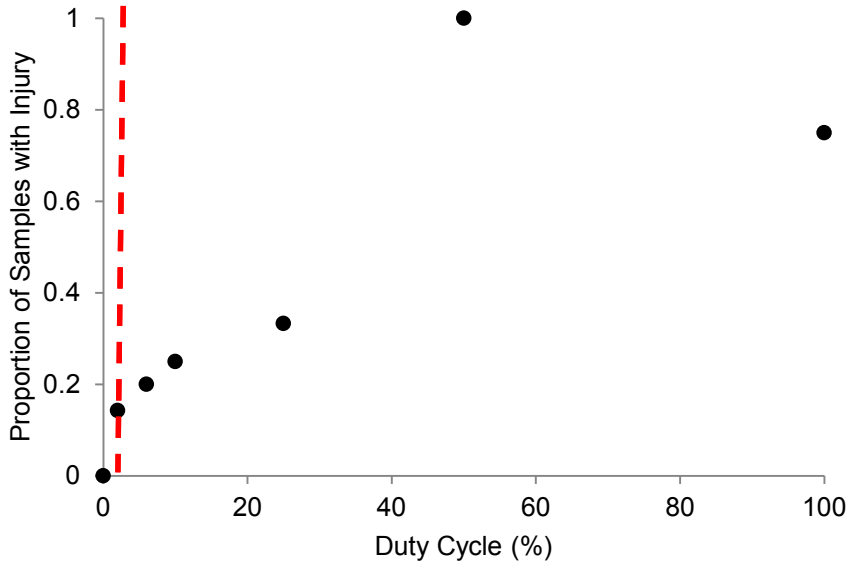

FIGURE 5.13: Plot showing the proportion of samples with injury versus duty cycle at an intensity of 9300 W/cm^2. As with the 100% duty cycle graph, there was only one scorer, as the frozen fixation and NADH staining method made the presence of injury very obvious. The red line indicates the injury threshold at a 2% duty cycle.

to the array device as few machines could have handled the 288 exposures at the intensities used in this experiment with little to no mechanical failure. As a result of this experiment, there are now published thresholds for injury at a 3.3% duty cycle, a 100% duty cycle, and at a fixed intensity of 9319 W/cm^2. These results may be useful to the FDA as they work towards establishing guidelines for safety of therapeutic ultrasound devices.

From the SWL literature [34], [116], [117], it is well-known that the lithotripsy firing rate affects the amount of injury found in the kidney. Pretreating the kidney with some shocks was found to reduce kidney damage, likely due to vasoconstriction. As the study conducted here involved many exposures on the same kidney and in the same pig, vasoconstriction was a concern. However, there was no indication of vasoconstriction in the ultrasound images, and there was no evidence, upon thorough examination of the data, that the order of

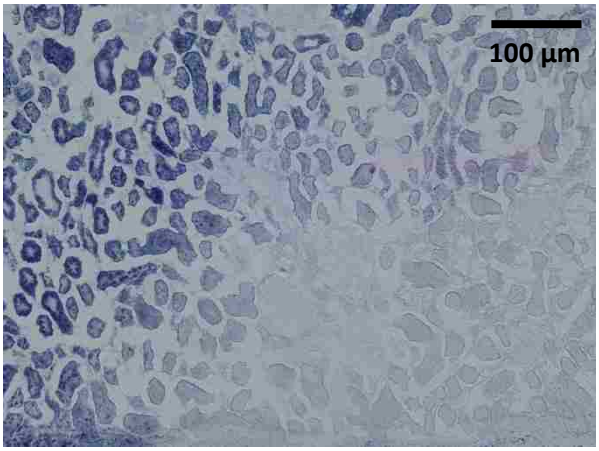

FIGURE 5.14: NADH-stained histology slide showing injury (by the lack of staining in the lower right hand corner of the image). This sample was taken for a 9300 W/cm^2 exposure at a 100% duty cycle.

the exposures on an individual kidney or pig affected the presence or type of injury.

In addition, researchers have shown that increasing the static pressure or eliminating the tensile component of shock waves reduces or eliminates cavitation (which is visible by hyperechogenicity on B-mode images) thereby reducing renal injury in SWL [7], [38]. Hyperechogenicity is explained by the presence of either boiling or cavitation bubbles [97]. In this study, hyperechogenicity, or bubble activity, was monitored on the B-mode image during the exposures, and it was found that overall, hyperechogenicity correlated well with injury at the 3.3% duty cycle. Oddly, though, injury in individual samples, did not match as well with our observations of hyperechogenicity. A thorough analysis of the types of injury that did not show echogenicity might explain the mismatch in those individual samples. At the highest intensities, hyperechogenicity often appeared almost immediately, though at lower intensities, it was at times quite late into the exposure that echogenicity appeared. Canney et al. showed that shock wave heating could cause boiling to occur in milliseconds [27]. At the maximum intensity of 26,000 W/cm^2, derated, boiling occurs in less than 1 ms for a continuous exposure. Along with our previous calculations of heating, even at the 3.3% duty cycle, we would expect boiling in less than 1 second, which leads us to believe that even when hyperechogenicity appeared almost immediately, it likely was due to boiling (at least at the higher intensities). This is supported by histological results, where the injury patterns at the higher intensities are very similar to what has been observed in shock wave heating and millisecond boiling [64]. While the presence of hyperechogenicity is not in itself a determinant of injury, hyperechogenicity is related to some types of injury and should be avoided when the goal is to avoid tissue disruption.

There are several potential sources of error that individually could cause underestimation or overestimation of the tissue injury thresholds. For example, the focal location of the exposure may have been missed either when marking or slicing the tissue, which could cause an overestimation of the injury threshold. However, due to the differences in the sizes and anatomies of the pigs, several programmable depths of the array system were used which correspond to slightly different intensities. As the results were plotted using the highest intensities of the depths that were used, this

would cause an underestimation of the injury threshold, perhaps partially cancelling out the overestimation from mismarked exposure locations. Additionally, the derating method and values used for derating were not specific to kidney tissue and assumed a linear attenuation with frequency. These would result in underestimation of the injury threshold. However, the waveform measurements, especially at the upper intensities where the waves are highly shocked, are limited by the bandwidth of the fiber optic hydrophone. This would result in an underestimation of the peak positive pressure output by the array and therefore an underestimation of the tissue injury thresholds. Other potential sources of error come from the fixation methods. With the high pressure perfusion fixation, artifact such as blown blood vessels and poor fixation could be attributed by the scorers as injury caused by the device. With the frozen fixation, the addition of ice crystals caused by the fixation process causes artifacts in the slides which at times could be attributed to injury caused by the device. Overall, the potential sources of error seem to balance out, giving us confidence in our reported renal injury thresholds.

The results from this study may help the FDA develop and publish standards for therapeutic ultrasound devices such as acoustic radiation force imaging, ultrasonic stone propulsion, and histotripsy. As for the second generation ultrasonic propulsion system, even at the maximum device settings with the original pulsing sequence injury is not expected in the kidney, where the derated intensity is 2400 W/cm^2 (at a depth of 7 cm, which corresponds to the approximate depth of a human kidney). With the 3.3% duty cycle setting, the second generation device has a safety margin of at least double the maximum intensity before bruising is expected and a margin of at least six times the maximum intensity before significant injury is expected. Since this study was completed, a new, updated pulsing sequence has been found to be more efficient in moving stones. In the new pulsing sequence, the duty cycle is approximately 75% and contained in one 50 ms pulse. With the new push pulse sequence, the second generation device is much closer to the level at which injury could be expected; however, this exact duty cycle and pulse length were not tested in this study. Further research is needed to verify the safety of the second generation device, considering the

effect of the new pulsing sequence, the effect of stones in the kidney, and the difference in transducer geometry and design.

5.3. Acute Safety and Efficacy of the Second Generation Clinical Device

5.3.1. Methods

Animals

All animal experiments were performed with the approval of the University of Washington Institutional Animal Care and Use Committee. Eight female domestic swine approximately 6 months old and weighing 90-120 lbs were used for this study. Swine were chosen over other animal models as pig kidneys are more similar to human kidneys in anatomy, function, and size than most other animal species [118]. Animals were sedated with an intramuscular injection of Telazol at a concentration of 4 mg/kg. Anesthesia was maintained using Isoflurane at a concentration of 1.5-2.5% via an endotracheal tube. Since the ultrasound will be applied through the skin for this study, the torso of the animal was shaved and further depilated using Nair® for improved ultrasound transmission. Electrodes were placed on depilated areas located on the right and left shoulder and haunch to observe the vitals of the animal. The skin beneath the electrodes was sprayed with an adhesive to attach the electrodes, and a contact gel was added to the electrodes to improve signal detection. An ear vein Angiocath was inserted to maintain fluid homeostasis and a Bair Hugger® in addition to a water circulating heating pad was used to maintain the core body temperature of the animal.

Fourteen of the sixteen kidneys were implanted with human kidney stones (2-8 mm calcium oxalate monohydrate (COM)) and beads (2.5 mm sterling plated nickel) using retrograde ureteroscopy with a nitinol basket, as pigs do not naturally grow stones; the other two kidneys were used as controls. A reference bead was placed in the upper pole of the kidney to allow us to distinguish between stone/bead displacements from pig repositioning as compared to the stones/beads that were repositioned ultrasonically. A series of beads and 2-8 mm stones coated with tantalum powder (to improve stone visualization under fluoroscopy) were placed in the middle or lower pole calyx of the

kidney for ultrasonic repositioning. Stone position and movement was monitored ultrasonically, fluoroscopically, and endoscopically.

Second Generation Clinical Device

The second generation clinical device (shown in figure 5.2) to image and move kidney stones was built on the Verasonics® Ultrasound Engine platform and was programmed to operate with the Philips/ATL C5-2 or Philips/ATL P4-1 transducers. In this study, the original push pulse sequence was used and was composed of bursts approximately 100 μs long followed by 2.9 ms of silence (3.3% duty cycle). These bursts were repeated to fill a total user-defined push time that ranges from 0.1 ms to 1 sec. The original push pulse sequence is shown graphically in figure 5.15. The focus of each individual burst was varied over a 4-mm width to reduce the intensity delivered to a single location in the kidney; the goal was to reduce kidney injury while increasing the probability of the energy hitting the stone. The transducer frequency was set at a fixed 2.3 MHz. Even though the maximum power available to physicians for human studies will be limited to 50 V, for this study, the push pulse power was allowed to range from 0-90 V and was controlled by the user. When the system power was set to its maximum 90V, the *in situ* spatial peak pulse averaged intensity was 2,400 W/cm^2, derated at 0.3 dB/cm/MHz over 7 cm with corresponding peak positive pressure (p_+) = 20 MPa (11 MPa, derated) and peak negative pressure (p_-) = 7 MPa (4 MPa, derated).

The imaging settings for the second generation device were optimized to visualize the stone or bead. The push pulse power (0-92 V) and duration (0.1 ms to 1 sec.) were controlled by the user, as in the original design of the device. B-mode imaging was interleaved within the push pulse to provide real-time stone imaging. All system parameters, including output voltage, duration of the push burst, and location of the push focus were recorded for each push attempt.

Protocol

As the goal of this study was to mimic the clinical protocol, an expert sonographer placed the ultrasound transducer on the skin of the pig and identified the target stones, using ultrasound gel to improve the coupling of the transducer to the pig. The

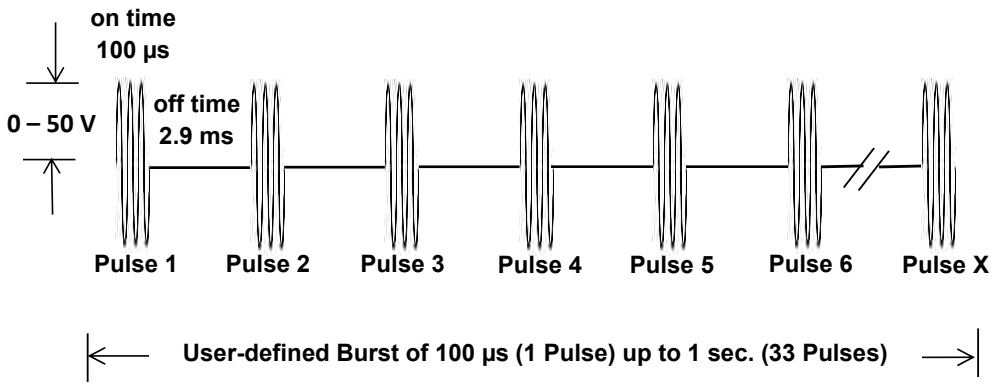

FIGURE 5.15: Schematic showing the original push pulse sequence for the second generation clinical stone propulsion system. In this push sequence, the user controls the push pulse length from 0.1 ms to 1 sec. which is then composed of 100-µs on-time separated by 2.9 ms of off-time and repeated to fill the defined push pulse length.

sonographer then carefully aligned the transducer, so that when the push pulse was activated, the stone moved out of the calyx and towards the renal pelvis, ureteropelvic junction (UPJ), or the ureter. Stone motion was visualized and recorded using fluoroscopy (GE OCE 9800), the ureteroscope, and the ultrasound imager in real-time. If several push pulses at the same transducer angle and location were unsuccessful, the sonographer moved the transducer to a new position or angle and repeated the targeting and treatment. If the stone still would not move, the pig was repositioned with fluoroscopic images of the stone recorded before and after pig movement to monitor whether shifting the pig resulted in stone movement. Repositioning the pig allowed the sonographer to utilize gravity to help move the stones in addition to providing room to try more transducer angles. Once all of the stones or beads were pushed to their maximum extent (except for the reference beads in the upper pole), the abdomen of the animal was opened with electro-cautery to prepare for perfusion fixation of the kidneys to preserve the tissue for later injury analysis.

Perfusion-Fixed Tissue Injury Analysis

All 16 kidneys from the 8 pigs were perfusion-fixed with 2% glutaralydehyde solution in a 0.1 M sodium cacodylate buffer. To prepare for perfusion fixation, the aorta, vena cava, and intestines were tied off above and below to isolate the renal vessels. Then,

catheters were inserted in both the aorta and vena cava. First, approximately 1 L of heparinized sodium phosphate under pressures up to 300 mm Hg was pushed through the kidney, followed immediately by approximately 2 L of the glutaralydehyde solution at similar pressures, taking care to proceed quickly and avoid air bubbles that could rupture the smaller vessels. After euthanizing the pig, the kidneys were removed and placed in 10% neutral buffered formalin fixative for at least seven days. After submersion in the formalin, the kidneys were either placed in containers of water for storage or set aside for injury analysis.

The four kidneys exposed to the longest treatment times and one control kidney (treated transcutaneously with the second generation clinical system without any beads/stones inserted) were selected for injury analysis by experts at Indiana University. (The exception was kidney 54L, from which the remaining stones and beads were unable to be removed from the kidney). Before the kidneys could be shipped to Indianapolis, any and all remaining stones and beads were removed from the kidney by filling them with water and shaking them, or using the ureteroscope with the nitinol basket. Our colleagues at Indianapolis have developed a technique to quantify injury by a volumetric injury evaluation technique [119]. Briefly, the technique consisted of infiltrating and embedding the entire kidney in paraffin, sectioning the kidney into 40-μm thick slices, and imaging each section with a digital camera [119]. The size of hemorrhagic lesions in each slice were measured and summed to determine the total lesion volume as a percentage of the total functional volume of the kidney [119].

5.3.2. Results

In this study, 14 kidneys of 8 pigs (2 controls) were implanted with 2-3 human kidney stones (tantalum-coated COM) or beads via retrograde ureteroscopy. The second generation clinical device was used to move the beads/stones with the original push sequence (100 μs pulses repeated every 2.9 ms) and user-controlled power (0-92 V) and push pulse duration (0.1 ms -1 sec.). Overall, 17 of the 26 (65%) implanted objects were successfully relocated from a middle or lower pole calyx to the renal pelvis (n=3), UPJ (n=2) or ureter (n=12). Two other objects were moved out of the calyx but stopped in the infundibulum. The remaining 7 stones/beads were lodged in their original calyx,

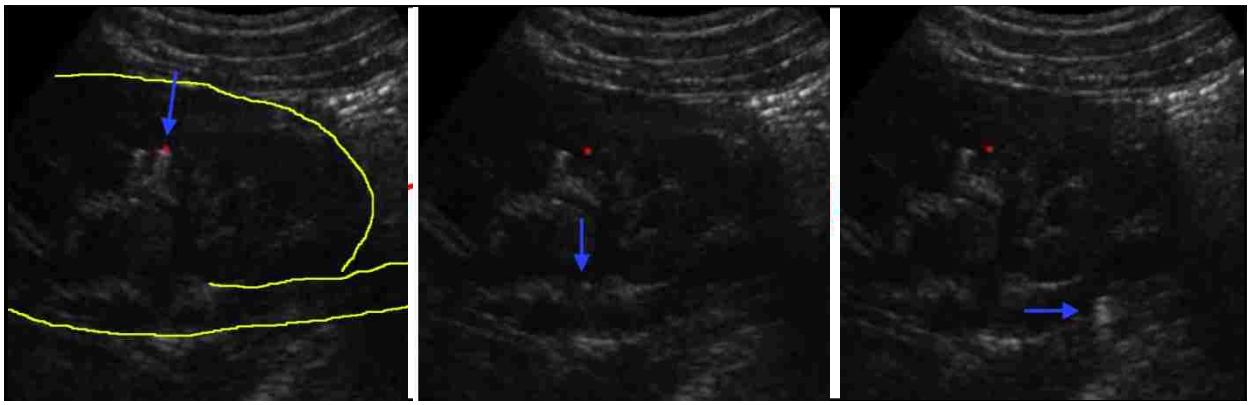

FIGURE 5.16: Real-time B-mode image of a stone pushed from the kidney. The blue arrow indicates the stone and direction of stone motion in the collecting system. After targeting (red dot), a single 0.5 sec. burst of ultrasound pulses is applied and the stone moves from the calyx to the ureter. All motion occurs in about 1 sec.

and while they were observed to shudder when the push pulse was applied, they could not be dislodged from their calyx. Figure 5.16 shows an example of a stone moving in the eighth pig from a middle pole calyx to the ureter from a single 0.5 sec. push pulse sequence.

The average procedure time to successfully displace each object was 14.2 ± 7.9 minutes and required 23 ± 16 pushes. The mean time between successive pulses was 41 ± 13 seconds. Most push attempts resulted in no object movement; however when successful, few pulses were necessary to result in object clearance. The average displacement was estimated to be 5.6 ± 2.7 linear centimeters as measured from the fluoroscopy images taken before and after treatment. Thirty-six percent of the upper pole reference beads were dislodged during the experiment, most likely due to changes in the pig body position (stomach, back, or side).

FIGURE 5.17: Bruises in the middle to upper pole of pig 54-4 from wire pokes during ureteroscopy surgery. The one on the left side of the image appears to have completely penetrated the parenchyma of the kidney.

Injury evaluation of the 5 kidneys (4 receiving the maximum treatment, one control) revealed a total of four sites of hemorrhage in

three of the kidneys, all of which could be attributed to wire pokes during the retrograde ureteroscopy surgeries. Figure 5.17 shows a photo of bruising on the upper pole of a perfused kidney, which is evidence of a wire poke. In the three kidneys showing injury, the injury volume was less than 1% of the total functional volume of the kidney. The other treated kidney and the control (10 minutes of pushing at the maximum power with 1s on – 10s off – 1s on – 10s off – 1s on – 90s off and no stones implanted) showed no evidence of gross or histological injury. Visual inspection of the intervening tissues and the kidney identified only one instance of bruising on one kidney which could have been attributed to the ultrasound exposure.

5.3.3. Discussion

This section established that the second generation clinical device could be used to safely and effectively reposition kidney stones in domestic swine. As far as the efficacy, this study showed us that the angle and alignment of the transducer were the most important factors for stone movement. To that end, a successful device operator needs to have the skills to visualize the open spaces of the kidney from a B-mode ultrasound image and to be able to determine the proper alignment to move the stone. Additionally, we observed over the month-long intensive study that there is a learning curve involved with using the device; in the later studies, stones were moved with significantly shorter imaging times and fewer push pulses. While part of this improvement came from the development of spatial perception and kidney anatomy, the procedure to find the correct treatment angle was also streamlined. No more than three attempts were made to free the stone from the same location before the angle of approach was changed either by moving the transducer or moving the animal. Therefore, providing training courses on using the clinical device may be an essential component of the device marketing strategy.

Additionally, even though we observed some injury that was attributed to the surgical stone insertion, the lack of ultrasound-induced injury observed in these kidneys agree with the threshold study conducted in the first section. There was some concern that the presence of the stone would increase tissue injury either from stone motion or from the direct or indirect interactions of the ultrasound wave with the stone; however that

was not in evidence in the volumetric injury analysis or in the samples taken for histology. Unfortunately the injury that we have attributed to the surgical procedure is unavoidable as there is not a well-defined pig model that can naturally grow kidney stones.

Besides causing trauma directly to the kidneys from wire pokes, the surgery introduces air into the system in addition to inflating the ureters and causing general trauma to the entire urinary system. Also, while the stones may be from humans, they were also exposed to air before being stored in water. While the larger volumes of introduced air seemed detrimental to moving stones as it reflected the push pulse and made stone identification difficult, it is possible that small bubbles on the stone surface makes moving stones easier because of the acoustic radiation force.

Besides exposure to air, another concern with surgical stone insertion is that the stone could be attached to the kidney wall *in situ.* One of the projected uses of the clinical device is to aid with the passage of *in situ* human kidney stones which are attached to the wall. As the force required to detach the stone would depend on a variety of parameters, it is difficult to predict whether the clinical device will be able to assist in the passage of small stones before surgical intervention. There is no immediate solution to this problem besides moving to humans, where stones form naturally. There is one pig model being developed in Wisconsin where pigs are being fed a special diet to grow stones naturally [120]; however the stones tend to be very small and not connected to the kidney. Additionally, the process to induce pigs to grow stones is very expensive, requiring at least 20 days for even crystal deposits to show in the kidney [120].

This section demonstrates the acute safety and efficacy of the second generation clinical device with the original pulsing sequence and surgically inserted kidney stones. The final section of this chapter will evaluate the safety of the second generation clinical device with the updated pulsing sequence in a porcine survival study.

5.4. Survival Study Safety Evaluation of the 2nd Generation Clinical Device

5.4.1. Methods

Animals

To evaluate the long-term effects from using the second generation clinical device, survival studies were conducted. Five male and five female clean Hanford™ Miniature Swine from Sinclair (5-9 months old, 55-100 lbs.) were used for this study. The pigs were randomly assigned to 3 different groups; two groups were treatment groups and the other was a control group. Group A was treated with the high clinical dose, which consists of 3 sites each treated for 20 minutes per site for a total of 60 minutes; Group B was treated with the moderate clinical dose, which consists of 2 sites each treated for 10 minutes for a total of 20 minutes; Group C was the control group which received no treatment. The groups and their dosing protocol are laid out in table 5.3.

Animals were sedated with an intramuscular injection of Telazol at a concentration of 4 mg/kg. Anesthesia was maintained using Isoflurane at a concentration of 1.5-2.5% via an endotracheal tube. Since the ultrasound will be applied through the skin for this study, the torso of the animal was shaved and further depilated using Nair® for improved ultrasound transmission. Electrodes were placed on depilated areas located on the right and left shoulder and haunch to observe the vitals of the animal. The skin beneath the electrodes was sprayed with an adhesive to attach the electrodes, and a contact gel was added to the electrodes to improve signal detection. An ear vein Angiocath was inserted to maintain fluid homeostasis and a Bair Hugger® in addition to a water circulating heating pad was used to maintain the core body temperature of the animal. Blood and urine were collected throughout the study; blood was collected from a Doppler-guided percutaneous femoral puncture and urine was collected via transcutaneous bladder puncture. Anesthesia time was kept to a minimum in order to survive the animals with minimal complications.

Study Protocol

To control bias, each animal judged acceptable was assigned to either the right kidney or left kidney treatment group using a computer-generated random number list. An assignment of 1 corresponded to a right kidney treatment and an assignment of 2

corresponded to a left kidney treatment. These assignments were independent of the dose group assignment.

TABLE 5.3: Treatment groups for the survival studies.

Group	Number of Kidneys per Group M/F	Device	Treatment Designation	Total Treatment (Time)	Termination
A	3/3	2nd Generation Clinical Device	High Clinical Dose	60 minutes	Day 7
B	3/3	2nd Generation Clinical Device	Moderate Clinical Dose	20 minutes	Day 7
C	1/1	None	Control	No Treatment	Day 7

The day of treatment was designated Day 0. On the treatment day, the pigs proceeded in the dosing order as described above (high group then moderate group with control interspersed). Groups A and B received ultrasonic treatment with group C serving as the control. Animals were anesthetized and blood and urine samples were collected for clinical pathology evaluation. The animals were prepared for treatment in the manner described above. The randomly selected kidney was treated according to table 5.3, starting with group A as detailed above. At the end of the exposure, additional blood and urine samples were collected for clinical pathology evaluation. Animals were survived for seven days; at the end of seven days, a third set of blood and urine samples were collected for clinical pathology evaluation and the animals were euthanized. Necropsies with tissue collection were conducted on all animals.

Treatments were performed transcutaneously to mimic the treatment route in the clinical setting. The kidney designated for treatment was imaged for no more than 20 minutes with the Philips/ATL C5-2 ultrasound probe; the same transducer that was used for treatment. The ultrasound probe was positioned so that the collecting system of the kidney was 4-cm from the transducer, a depth which corresponds to the maximum amplitude of the second generation clinical device. For all exposures, the updated push pulse (50 ms duration) was repeated every 30 sec. with the machine set at the

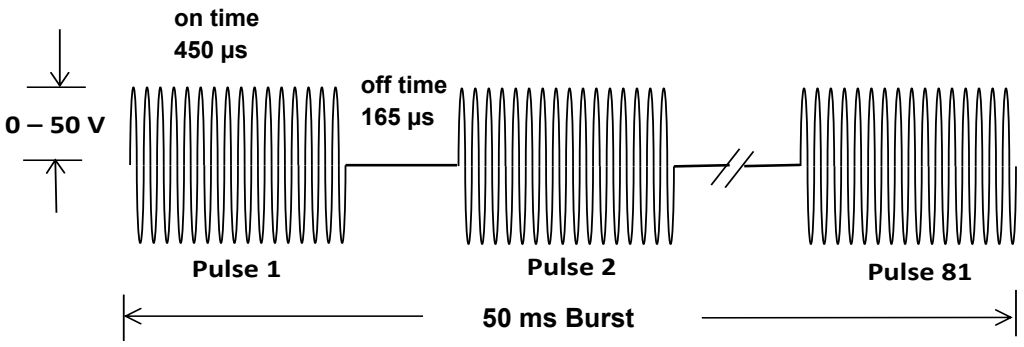

FIGURE 5.18: Updated push pulse sequence of the second generation clinical ultrasonic propulsion device. The frequency and amplitude of the updated push pulse sequence are the same as the original push pulse sequence. The difference is that now the push pulse is a 50-ms burst, composed of 81 450-µs pulses of on-time separated by 165-µs of off-time.

maximum power (90V). The updated push pulse uses the same 2.3 MHz frequency as the original pulsing sequence, but each 50-ms push pulse is composed of 81 repetitions of 450 µs of on-time followed by 165 µs of off-time as shown in figure 5.18. For all dosing groups, the probe or treatment location in the image was repositioned at least one time to simulate the stone moving from the lower pole towards the exit of the kidney.

Evaluation of Injury

The blood and urine collected throughout the study for clinical pathology were evaluated by Phoenix Laboratories (Seattle, WA) for pH, hematocrit, leukocytes, creatinine, albumin, etc. (for the entire list, see Appendix A). After euthanizing the animal, tissues in the treatment path and control tissues were collected and preserved in 10% neutral buffered formalin. The tissues from the treatment path were embedded in paraffin, sectioned at 5 µm, and stained with H&E; the rest of the collected tissues will only be analyzed if needed. A blinded veterinary pathologist performed the tissue analysis. A complete list of collected tissue samples and clinical pathology tests are included in Appendix A.

5.4.2. Results

No animals died during the course of the study and no clinical signs indicative of any

TABLE 5.4: Summary of histological findings from the survival study.

Tissue	Finding/Diagnosis	Control (n=2)	Maximum (n=2)	Extreme (N=6)
Liver	NSL (No Significant Lesion)	2/2	2/2	6/6
Kidney L	NSL	2/2	2/2	6/6
Kidney R	NSL	2/2	2/2	6/6
Adrenal gland	NSL Congestion (incidental)	1/2 1/2	2/2	6/6
Pancreas	Minimal scattered saponification, acinar cell degeneration with rare karyolysis, peracute/agonal, peracute, (incidental; not treatment related): NSL	2/2	2/2	6/6
Spleen	NSL Congestion (barbiturate euthanasia related)	2/2 2/2	2/2 2/2	6/6 6/6
Skin	NSL	2/2	2/2	6/6
Body wall	NSL	2/2	2/2	6/6
Rib	NSL	2/2	2/2	6/6
Spinal cord	NSL	2/2	2/2	6/6

adverse effects of the treatment were observed. While mild changes were observed in the pancreas and adrenal gland, these were determined to be unrelated to treatment as similar changes were observed in the control pigs that did not receive treatment. The summary of the histological findings are shown in table 5.4.

Figure 5.19 shows selected representative histology sections for the kidney and the pancreas from control and high dose groups. The kidney and pancreas are of particular interest because the kidney is the targeted organ which receives high blood volumes (20-25% of the cardiac output [121]) and damage to the pancreas can result in diabetes mellitus. Fortunately, the kidneys remain undamaged in both the high and moderate dose groups, with only background lesions apparent in the pancreas. The skin was also

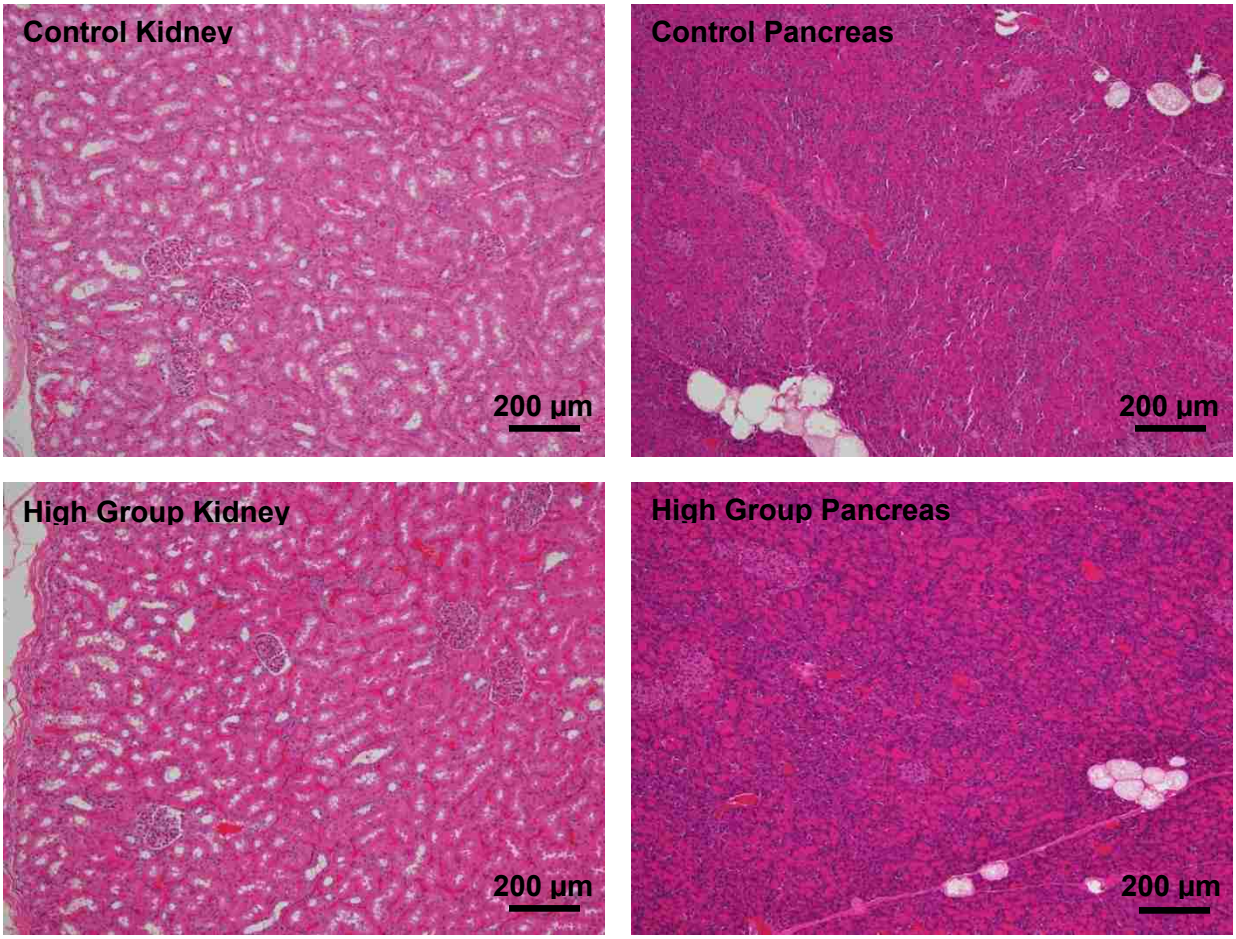

FIGURE 5.19: Hematoxylin and Eosin-stained samples from the kidney (left) and pancreas (right) from the control (upper) and high treatment (lower) groups. The kidney samples look very similar between the control and high treatment groups with no significant treatment-related injury. The pancreas samples also look very similar between the control and high treatment groups, though the samples contain saponification and some cellular degeneration.

of particular interest as transducer overheating and skin burns were an early. Gross and histological samples of the skin are shown in figure 5.20; no evidence of injury is seen in either our gross observations or histological samples of skin, which supports our probe heating measurements.

The results from our hematology and urinalysis are shown fully in Appendix A. While there was some minor variations in hematologic and clinical chemistry parameters of all animals and groups, a few of which were statistically significant, the changes are not significantly different from control animals. Some variations in hematologic and clinical

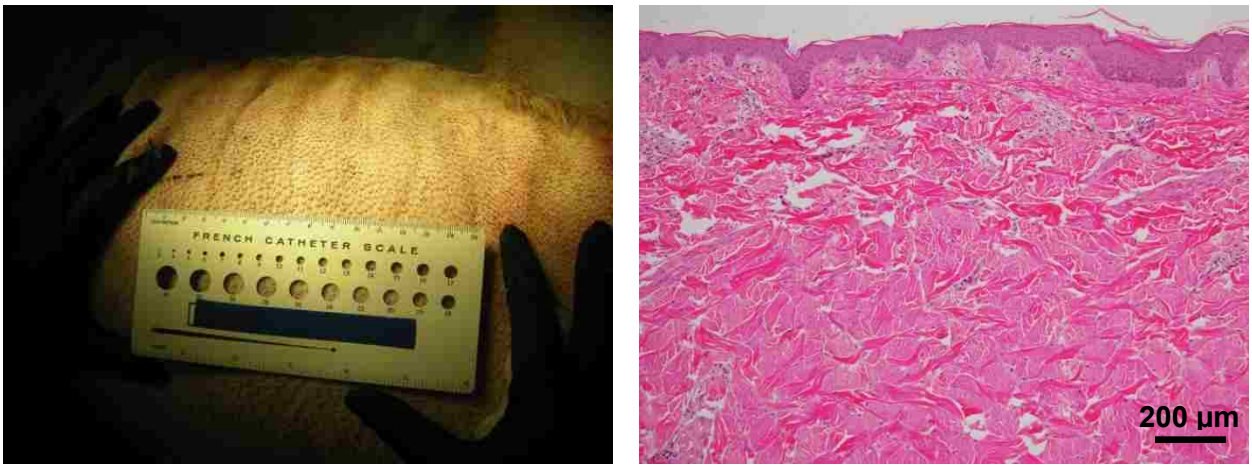

FIGURE 5.20: *Left:* Photo taken showing the pig skin of a high treatment group recipient. The black dots faintly visible above the scale were placed immediately after the treatment and identify the location of the transducer. *Right:* H&E stain of the pig skin. No significant lesions are apparent, indicating that the transducer did not damage the skin.

chemistry in large species are considered to be normal events, particularly when coupled with the stress of handling and anesthesia. No changes were considered to be related to the use of the device and there were no histopathologic correlates. Urinalysis also demonstrated no device-related effects.

5.4.3. Discussion

Based on the findings from this pre-clinical safety study performed in pigs, we anticipate no substantial tissue changes in humans, even if the procedure exceeds the maximum number of pulses by a factor of three (the maximum clinical dose is limited to 40 pulses or 20 minutes of continuous (push pulses separated by 30 seconds) of treatment). These findings support the evidence of no renal injury that was predicted in the initial threshold study and was observed in the efficacy and safety study where stones were moved.

This study constituted a major portion of our Investigational Device Exemption (IDE) application to the FDA. Special “clean” Hanford swine were used for this study with the idea of eliminating any possible background lesions to ensure that any injury caused by the second generation clinical device could be identified. Unfortunately, even these

pigs had or developed background pancreatic lesions in addition to one instance of a background adrenal lesion. Nevertheless, the results from this study indicate it is safe to proceed to human clinical trials.

5.5. Summary and Conclusions

The three studies included in this chapter tested the safety and efficacy of ultrasonic propulsion of kidney stones in swine. In the first section, several thresholds for kidney injury were established for a 2-MHz focused ultrasound source using the first generation array device. In the next section, the acute safety and efficacy of the second generation clinical device using the original push pulse sequence was established when stones were surgically implanted in pigs. In the final section, the long term safety of the second generation clinical device with the updated push pulse sequence was evaluated in clean swine.

To our knowledge, the threshold data collected in the first section of this chapter represent the first set of data indicating that ultrasound is safe beyond the limits set by the FDA. This opens up a whole regime between the traditional imaging and therapeutic ultrasound levels that could be safely used for therapies like ultrasonic propulsion or acoustic radiation force imaging (ARFI). More research is needed to determine the exact safe parameter space, namely exploring different tissues, frequencies, and pulse lengths. The research included in this chapter represent a major effort to establish the safe operating levels in porcine kidneys and filling in the all of the gaps to be able to define the safe parameter space will likely require decades of work.

Specifically regarding ultrasonic propulsion, the gross, histological, and chemical results from all three sections agree that ultrasonic propulsion is safe in pigs; however even though pig kidney collecting system anatomy and size are very similar to human kidneys, they are not completely the same [118], [122]. The vasculature is quite different between pigs and humans [118], [122], which means that ultrasonic propulsion in humans could cause more hemorrhaging than was observed in pigs. While there is no way to determine whether there is an increased risk of hemorrhage except by using ultrasonic propulsion in humans, we expect that the factor of six safety margin we

observed in the threshold study will ensure that any hemorrhaging will be minor and recoverable. Some of the other treatments for kidney stones include ureteroscopic surgery or lithotripsy, both of which have been shown to cause trauma to the kidney [123]. In this case, the benefits of aiding kidney stone/fragment passing thereby reducing stone recurrence rates outweighs the risk of potential bruising or other minor kidney damage that may result from using this device.

One additional question related to ultrasonic propulsion that we have been unable to answer in these studies is whether or not it is painful for the kidney stones to be moved. With the second generation clinical device, our goal would be for physicians to move stones in an office visit without anesthesia. Unfortunately, there is no way to gauge potential pain from these studies in pigs. Therefore, a big component of our clinical trial will involve patient feedback as to whether the device causes pain.

In conclusion, this chapter demonstrates that we have established a threshold for tissue injury by focused ultrasound as it specifically relates to ultrasonic propulsion of kidney stones. All three sections concur that the second generation ultrasonic propulsion clinical device is expected to be safe to use in humans. In fact, the FDA also agrees with our conclusions and has given us permission to conduct clinical trials in humans.

CHAPTER 6

Summary and Future Directions

6.1. Summary

Therapeutic ultrasound has advanced exponentially since Langevin first observed fish death while developing sonar. Now, therapeutic ultrasound is used clinically worldwide to treat diseases ranging from uterine fibroids to osteoarthritis. While many of the therapeutic effects of ultrasound are elicited by hyperthermia, bubbles can also interact with tissue to produce beneficial effects. For example, bubbles are used in boiling histotripsy to de-bulk tissue and are used in shock wave lithotripsy to help break kidney stones. However, the same bubbles that break kidney stones also damage the kidney, which is why bubble damage is a concern in every ultrasound application including fetal imaging. While the Mechanical Index predicts the likelihood of cavitation, interactions between bubbles and tissues are complex, making it difficult to establish safety guidelines for therapeutic ultrasound. Whether the aim is to emulsify a tumor or image a fetus, identifying the thresholds and mechanisms of tissue injury by bubbles in an ultrasound field is important for all ultrasound applications and was the goal of this research.

While boiling histotripsy has been shown to emulsify bulk tissue, it has been unclear how the millimeter-size boiling bubbles fractionate the tissue into its submicron components. To solve this conundrum, the mechanism of boiling histotripsy was investigated, where it was determined that ultrasound atomization described tissue fractionation by boiling histotripsy. Using high speed photography, it was shown that the millimeter-diameter boiling bubble was large enough to act as a pressure release interface between tissue and air or vapor, such that a miniature acoustic fountain formed and atomization occurred within the boiling bubble. The end result of the exposure was a hole in tissue; when the fountain projectiles were recirculated as would

be expected in bulk tissue, histological analysis showed that few to no intact cells remained.

With ultrasonic atomization established as the mechanism of tissue fractionation in boiling histotripsy, new questions arose as to the tissue properties that influenced atomization and the mechanism of atomization, itself. Results from the initial atomization studies suggested that tissue wetness influenced atomization, so tissues were preserved in solutions of varying salt and sugar concentrations to alter bulk water content. It was determined that bulk tissue wetness did not enhance atomization. A subsequent study in the tissue-mimicking polyacrylamide gel showed that surface wetness is what enhanced atomization. When the gel surface was dry, atomization and erosion did not occur; however, when the surface was wetted, even with liquids that did not atomize on their own, atomization and surface erosion were observed. Analysis of the high speed videos led to the supposition that deformation of the liquid on the tissue or gel surface caused the inverted and reflected ultrasound wave to refocus at or near the tissue or gel surface enhancing atomization and erosion. This hypothesis was then tested in an *in vivo* porcine liver with the capsule intact. Previous studies in porcine liver indicated that while atomization was successful *in vivo* and *ex vivo* when the liver capsule was removed, when the capsule was left intact, atomization was not successful even with the surface was wetted with water. In addition, histology slides showed tissue injury extending over 4 mm below the surface when the liver capsule was intact. To test the idea that the wetting agent can refocus the inverted and reflected wave at the liver capsule, the liver surface was wetted with soapy water because of the lower surface tension. The result was bleeding from a capsular breach. One additional experiment – atomization in a high pressure chamber - was performed to determine whether bubbles were necessary for atomization. The results showed that tissue was cooked when the static pressure was increased, and while small droplets were emitted, the tissue surface showed a cooked mound rather than a hole. This experiment showed that bubbles are necessary for tissue fractionation; however it remains unclear whether bubbles are necessary for atomization as the tissue fragments were thermally denatured rather than expelled from the tissue surface.

The final chapter of this dissertation changes gears somewhat to determination of the thresholds for renal tissue injury by focused ultrasound. Thermal and mechanical, or bubble-driven, injury thresholds were established for focused ultrasound exposures applied directly to *in vivo* porcine kidneys. While the motivation behind this work was to establish the safety of an ultrasonic propulsion device to reposition kidney stones, this was also the first known work to comprehensively define renal injury thresholds for a specific range of ultrasound parameters. Then, the safety of the ultrasonic propulsion device was established in transcutaneous studies. In the first study, stones were inserted into the pig kidney via retrograde ureteroscopy, repositioned with ultrasonic propulsion, then harvested and evaluated for injury. In the second study, the long-term safety of the device was established in a week-long porcine survival study. Both studies along with the threshold study were presented to the FDA in an Investigational Device Exemption (IDE) and approval was granted to begin clinical trials in humans.

Whether the goal is to move kidney stones or image a fetus, ultrasound can cause unwanted tissue injury. In techniques such as boiling histotripsy, tissue injury is the goal; however understanding the levels at which injury occurs and the mechanisms of injury is important for developing safe and reliable therapies.

6.2. Future Work

While the original goal of the majority of this dissertation was to determine the mechanism of tissue injury in boiling histotripsy, the work has evolved to perhaps explain how tissue is damaged in cavitation cloud histotripsy and even in naturally occurring air interfaces at diagnostic ultrasound levels. Even though the experiments in the lungs were unsuccessful in showing atomization, the soft, moist lung tissue is expected to atomize very easily and injure the lungs. If the smallest gas interface at which atomization occurs could be established, it would be a step towards explaining tissue fractionation by cavitation cloud histotripsy as well as explaining damage in the lungs. Alveoli in the lungs are individually approximately 300 μm in diameter [69] and individual bubbles in the cavitation cloud are 10s to 100s of microns in diameter [8], [63]. Should atomization occur at interfaces of this size, it would be very exciting as it

could relate back to all the bubble jetting work [124] and form a complete, unifying picture of bubble-induced damage.

When atomizing viscoelastic solids, a hypothesis emerged that tissue wetness enhanced atomization by refocusing the ultrasound wave at the tissue or gel surface. While an *in vivo* experiment showed that wetting the porcine liver capsule with soapy water caused atomization and a breach of the liver capsule, controlled experiments and modeling of acoustic wave propagation is needed to support this hypothesis. Then, the results from these experiments and modeling need to be related back to bulk boiling histotripsy. Recent studies in bulk boiling histotripsy have shown that 2 MHz appears to be the optimum frequency to create the boiling bubble and cause fractionation. A model of tissue deflection and wave propagation could be used to illustrate why 2 MHz is the ideal frequency. In addition, a model along with experimentation could be used to evaluate whether forming a large bubble with low frequency ultrasound and then atomizing with ultrasound of a higher frequency could be more efficient in fractionating a large volume of tissue.

With the increased understanding as to the mechanisms of boiling histotripsy and atomization, it may be possible to develop techniques to fractionate highly elastic tissues such as uterine fibroids or the kidney sinus. Uterine fibroids would be a highly desirable clinical niche for boiling histotripsy. Experiments should be conducted in elastic tissues such as uterine fibroids to determine whether atomization or the formation of the boiling bubble (pressure release interface) limits tissue fractionation. If atomization is what limits tissue fractionation, it may be possible to increase tissue or surface wetness by inducing bleeding or injecting a wetting liquid into the fibroids to improve atomization and hence fractionation. More experiments conducted in a variety of especially *in vivo* tissues will help determine whether bleeding can enhance atomization or bulk tissue fractionation.

Thus far, the future work has focused on explaining tissue injury; however questions still remain as to the influence of bubbles and dynamic instabilities on atomization in water at low intensities and in tissues or viscoelastic gels. The various experiments included in this dissertation suggest that boiling causes water atomization from the drop chain,

yet it is not possible to completely eliminate cavitation. Experimentally, shorter ultrasound pulses could be used to add more weight to the boiling hypothesis in tissues and water, but the expected reflections and interactions of the wave in the drop chain fountain could confound the results. A model is needed to predict wave propagation, reflections, and focusing in the drop chain. This model could also be used to describe why atomization in the drop chain ceases at 1000 psi, but again releases droplets at 2000 psi.

As far as the injury thresholds, there is a large parameter space that could be filled in by varying ultrasonic frequency, pulse length, intensities, and duty cycles as well as the tissue type. A study of this magnitude is not likely to occur, except as needed for FDA approval to translate research devices into clinical therapies. It is expected that the tissue thresholds depend on many parameters, and it may not ever be possible to publish general guidelines for tissue injury at therapeutic ultrasound levels. As far as the specific application of ultrasonic propulsion of kidney stones, the next step is clinical trials to show the efficacy and safety of stone repositioning in humans.

REFERENCES

[1] K. F. Graff, “A History of Ultrasonics,” in in *Physical Acoustics*, Vol. 15., M. and Thurston, Ed. Academic Press, 1981, p. Chapter 1.

[2] M. R. Bailey, V. A. Khokhlova, O. A. Sapozhnikov, S. G. Kargl, and L. A. Crum, “Physical mechanisms of the therapeutic effect of ultrasound (a review),” *Acoust. Phys.*, vol. 49, no. 4, pp. 369–388, Jul. 2003.

[3] V. Frenkel, “Ultrasound mediated delivery of drugs and genes to solid tumors,” *Adv. Drug Deliv. Rev.*, vol. 69, pp. 1193–1208, 2008.

[4] R. Deckers and C. T. W. Moonen, “Ultrasound triggered, image guided, local drug delivery.,” *J. Control. Release*, vol. 148, no. 1, pp. 25–33, Aug. 2010.

[5] W. Sass, M. Braunlich, H. Dreyer, E. Matura, W. Folberth, H. Priesmeyer, and J. Seifert, “The mechanisms of stone disintegration by shock waves,” *Ultrasound Med. Biol.* vol. 17, no. 3, pp. 239–243, 1991.

[6] N. G. Holmer, L. O. Almquist, T. G. Hertz, A. Holm, E. Lindstedt, H. W. Persson, and C. H. Hertz, “On the mechanism of kidney stone disintegration by acoustic shock waves,” *Ultrasound Med. Biol.* vol. 17, no. 5, pp. 479–489, 1991.

[7] O. A. Sapozhnikov, V. A. Khokhlova, M. R. Bailey, J. C. Williams, J. A. McAteer, R. O. Cleveland, and L. A. Crum, “Effect of overpressure and pulse repetition frequency on cavitation in shock wave lithotripsy,” *J. Acoust. Soc. Am.*, vol. 112, no. 3, p. 1183, 2002.

[8] J. E. Parsons, C. A. Cain, G. D. Abrams, and J. B. Fowlkes, “Pulsed cavitational ultrasound therapy for controlled tissue homogenization.,” *Ultrasound Med. Biol.*, vol. 32, no. 1, pp. 115–29, Jan. 2006.

[9] M. S. Canney, V. A. Khokhlova, O. V Bessonova, M. R. Bailey, and L. A. Crum, “Shock-induced heating and millisecond boiling in gels and tissue due to high intensity focused ultrasound.,” *Ultrasound Med. Biol.*, vol. 36, no. 2, pp. 250–67, Feb. 2010.

[10] A. D. Maxwell, T.-Y. Wang, C. A. Cain, J. B. Fowlkes, O. A. Sapozhnikov, M. R. Bailey, and Z. Xu, “Cavitation clouds created by shock scattering from bubbles during histotripsy.,” *J. Acoust. Soc. Am.*, vol. 130, no. 4, pp. 1888–98, Oct. 2011.

[11] T. D. Khokhlova, M. S. Canney, V. A. Khokhlova, O. A. Sapozhnikov, L. A. Crum, and M. R. Bailey, “Controlled tissue emulsification produced by high intensity

focused ultrasound shock waves and millisecond boiling.," *J. Acoust. Soc. Am.*, vol. 130, no. 5, pp. 3498–510, Nov. 2011.

[12] "Radiation-Emitting Products: Ultrasound Imaging," *Food and Drug Administration*, 2012. [Online]. Available: http://www.fda.gov/Radiation-EmittingProducts/RadiationEmittingProductsandProcedures/MedicalImaging/ucm115357.htm.

[13] R. Phillips and G. Harris, "Guidance for Industry and FDA Staff Information for Manufacturers Seeking Marketing Clearance of Diagnostic Ultrasound Systems and Transducers," 2008.

[14] R. E. Apfel and C. K. Holland, "Gauging the likelihood of cavitation from short-pulse, low-duty cycle diagnostic ultrasound," *Ultrasound Med. Biol.*, vol. 17, no. 2, pp. 179–185, 1991.

[15] K. Ng and Y. Liu, "Therapeutic Ultrasound : Its Application in Drug Delivery," *Medicinal Research Reviews,* vol. 22, no. 2, pp. 204–223, 2002.

[16] K. G. Baker, V. J. Robertson, and F. A. Duck, "A review of therapeutic ultrasound: biophysical effects.," *Phys. Ther.*, vol. 81, no. 7, pp. 1351–8, Jul. 2001.

[17] J. Driller and F. L. Lizzi, "Therapeutic applications of ultrasound: a review.," *IEEE Eng. Med. Biol. Mag.*, vol. 6, no. 4, pp. 33–40, Jan. 1987.

[18] S. Vaezy, M. Andrew, P. Kaczkowski, and L. Crum, "Image-Guided Acoustic Therapy," 2001.

[19] G. ter Haar and C. Coussios, "High intensity focused ultrasound: Physical principles and devices," *Int. J. Hyperth.*, vol. 23, no. 2, pp. 89–104, Jan. 2007.

[20] G. ter Haar, "High Intensity Ultrasound," *Surg. Innov.*, vol. 8, no. 1, pp. 77–89, Mar. 2001.

[21] N. T. Sanghvi, R. S. Foster, R. Bihrle, R. Casey, T. Uchida, M. H. Phillips, J. Syrus, A V Zaitsev, K. W. Marich, and F. J. Fry, "Noninvasive surgery of prostate tissue by high intensity focused ultrasound: an updated report.," *Eur. J. Ultrasound*, vol. 9, no. 1, pp. 19–29, Mar. 1999.

[22] A. Gelet, J. Y. Chapelon, R. Bouvier, O. Rouvière, Y. Lasne, D. Lyonnet, and J. M. Dubernard, "Transrectal high-intensity focused ultrasound: minimally invasive therapy of localized prostate cancer.," *J. Endourol.*, vol. 14, no. 6, pp. 519–28, Aug. 2000.

[23] K. Hynynen, O. Pomeroy, D. N. Smith, P. E. Huber, N. J. McDannold, J. Kettenbach, J. Baum, S. Singer, and F. A. Jolesz, "MR imaging-guided focused

ultrasound surgery of fibroadenomas in the breast: a feasibility study.," *Radiology*, vol. 219, no. 1, pp. 176–85, Apr. 2001.

[24] A. G. Visioli, I. H. Rivens, G. R. ter Haar, A. Horwich, R. A. Huddart, E. Moskovic, A. Padhani, and J. Glees, "Preliminary results of a phase I dose escalation clinical trial using focused ultrasound in the treatment of localised tumours.," *Eur. J. Ultrasound*, vol. 9, no. 1, pp. 11–8, Mar. 1999.

[25] L. Mencaglia, R. Guidetti, D. Tonellotto, and A. Fanfani, "Energy focused ultrasound for the clinical treatment of uterine myoma," *Ultrasound Med. Biol.*, vol. WFUMB '00 , p. A207, 2000.

[26] N. B. Smith and K. Hynynen, "The feasibility of using focused ultrasound for transmyocardial revascularization," vol. 24, no. 7, pp. 1045–1054, 1998.

[27] M. S. Canney, V. A. Khokhlova, O. V Bessonova, M. R. Bailey, and L. A. Crum, "Shock-induced heating and millisecond boiling in gels and tissue due to high intensity focused ultrasound.," *Ultrasound Med. Biol.*, vol. 36, no. 2, pp. 250–67, Feb. 2010.

[28] T.-Y. Wang, Z. Xu, T. L. Hall, J. B. Fowlkes, and C. A. Cain, "An efficient treatment strategy for histotripsy by removing cavitation memory.," *Ultrasound Med. Biol.*, vol. 38, no. 5, pp. 753–66, May 2012.

[29] FDA, "Division of Medical Assistance: Extracorporeal Shock Wave Lithotripsy," *FDA*, pp. 0–4, 2007.

[30] Kidney.org, "Kidney Stone Treatment: Shock Wave Lithotripsy," 2013. [Online]. Available: http://www.kidney.org/atoz/content/kidneystones_ShockWave.cfm.

[31] L. R. Willis, A. P. Evan, B. A. Connors, R. K. Handa, P. M. Blomgren, and J. E. Lingeman, "Prevention of lithotripsy-induced renal injury by pretreating kidneys with low-energy shock waves.," *J. Am. Soc. Nephrol.*, vol. 17, no. 3, pp. 663–73, Mar. 2006.

[32] J. A. McAteer and A. P. Evan, "The acute and long-term adverse effects of shock wave lithotripsy.," *Semin. Nephrol.*, vol. 28, no. 2, pp. 200–13, Mar. 2008.

[33] A. P. Evan, D. Ph, L. R. Willis, B. A. Connors, J. A. Mcateer, J. E. Lingeman, M. D, and E. E. T. Al, "Injury by Extracorporeal Shock Wave Lithotripsy," vol. 5, no. 1, 1991.

[34] B. A. Connors, A. P. Evan, P. M. Blomgren, R. K. Handa, L. R. Willis, S. Gao, J. A. McAteer, and J. E. Lingeman, "Extracorporeal shock wave lithotripsy at 60 shock waves/min reduces renal injury in a porcine model.," *BJU Int.*, vol. 104, no. 7, pp. 1004–8, Oct. 2009.

[35] J. V. Kaude, C. M. Williams, M. R. Millner, J. M. Scott, and B. Finlayson, “Renal morphology and function immediately after extracorporeal shock wave lithotripsy,” *Am. J. Roentgenol*, vol. 145, pp. 305–313, 1985.

[36] A. J. Coleman, M. J. Choi, and J. E. Saunders, “Detection of acoustic emission from cavitation in tissue during extracorporeal lithotripsy,” *Ultrasound Med. Biol. Am.* vol. 22, no. 8, pp. 1079-1087, 1996.

[37] D. Dalecki, C. H. Raeman, S. Z. Child, D. P. Penney, R. Mayer, and E. L. Carstensen, “The influence of contrast agents on hemorrhage produced by lithotripter fields," *Ultrasound Med. Biol.,* vol. 23, no. 9, pp. 1435–1439, 1997.

[38] A. P. Evan, L. R. Willis, J.A. McAteer, M. R. Bailey, B. A. Connors, Y. Shao, J. E. Lingeman, J. C. Williams, N. S. Fineberg, and L. A. Crum, “Kidney damage and renal functional changes are minimized by waveform control that suppresses cavitation in shock wave lithotripsy.,” *J. Urol.*, vol. 168, no. 4 Pt 1, pp. 1556–62, Oct. 2002.

[39] J. E. Lingeman, Y. I. Siegel, B. Steele, A. W. Nyhus, and J. R. Woods, “Management of lower pole nephrolithiasis: A clinical analysis,” *J. Urol.*, vol. 151, pp. 663–667, 1994.

[40] S. B. Streem, A. Yost, and E. Mascha, “Clinical Implications of Clinically Insignificant Stone Fragments After Extracorporeal Shock Wave Lithotripsy,” *J. Urol.*, vol. 155, no. 4, pp. 1186–1190, Apr. 1996.

[41] N. P. Gupta, D. V Singh, a K. Hemal, and S. Mandal, “Infundibulopelvic anatomy and clearance of inferior caliceal calculi with shock wave lithotripsy.,” *J. Urol.*, vol. 163, no. 1, pp. 24–7, Jan. 2000.

[42] A. Shah, N. R. Owen, W. Lu, B. W. Cunitz, J. D. Harper, and M. R. Bailey, “Novel ultrasound method to reposition kidney stones,” *Urol. Res.*, vol. 38, no. 6, pp. 491–495, 2010.

[43] A. Shah, J. D. Harper, B. W. Cunitz, Y.-N. Wang, M. Paun, J. C. Simon, W. Lu, P. J. Kaczkowski, and M. R. Bailey, “Focused ultrasound to expel calculi from the kidney.,” *J. Urol.*, vol. 187, no. 2, pp. 739–43, Mar. 2012.

[44] J. D. Harper, M. D. Sorensen, B. W. Cunitz, Y.-N. Wang, J. C. Simon, F. Starr, M. Paun, B. Dunmire, H. D. Liggitt, A. P. Evan, J. a McAteer, R. S. Hsi, and M. R. Bailey, “Focused ultrasound to expel calculi from the kidney: safety and efficacy of a clinical prototype device.,” *J. Urol.*, vol. 190, no. 3, pp. 1090–1095, Sep. 2013.

[45] M. D. Sorensen, M. R. Bailey, R. S. Hsi, B. W. Cunitz, J. C. Simon, Y.-N. Wang, B. L. Dunmire, M. Paun, F. Starr, W. Lu, A. P. Evan, and J. D. Harper, “Focused

ultrasonic propulsions of kidney stones: Review and update of preclinical technology," *J. Endourol.*, vol. 27, no. 10, pp. 1183–1186, 2013.

[46] R. Rao and S. Nanda, "Sonophoresis : recent advancements and future trends," *Rev. Lit. Arts Am.*, pp. 689–705, 2009.

[47] R. W. Wood and A. L. Loomis, "Physical and biological effects of high-frequency sound-waves of great intensity," *London, Edinburgh, Dublin Philos. Mag. J. Sci.*, vol. 4, no. 22, pp. 417–436, 1927.

[48] K. K. Tjan and P. W. R. C., "On the impulsive generation of drops at the interface of two inviscid fluids On the impulsive generation of drops at the interface of two inviscid fluids," *Proc. R. Soc. A*, vol. 464, pp. 1125–1140, 2008.

[49] K. K. Tjan and W. R. C. Phillips, "On impulsively generated inviscid axisymmetric surface jets, waves, and drops," *J. Fluid Mech.*, vol. 576, pp. 377–403, 2007.

[50] B. Y. K. Sollner, "The mechanism of the formation of fogs by ultrasonic waves," *Trans. Faraday Soc.*, vol. 32, pp. 1532–1536, 1936.

[51] L. D. Rozenberg and O. K. Eknadiosyants, "Kinetics of ultrasonic fog formation," *Sov. Phys. - Acoust.*, vol. 6, no. 3, pp. 369–374, 1960.

[52] E. L. Gershenzon and O. K. Eknadiosyants, "The nature of liquid atomization in an ultrasonic fountain," *Sov. Phys. - Acoust.*, vol. 10, no. 2, pp. 127–132, 1964.

[53] L. D. Rozenberg, Ed., *Physical principles of ultrasonic technology Vol. 2*, English - . New York: Plenum Press, 1973, pp. 4–88.

[54] M. Faraday, "On a peculiar class of acoustical figures: and on certain forms assumed by groups of particles upon vibrating elastic surfaces," *Philos. Trans. R. Soc. London*, vol. 121, pp. 299–340, 1831.

[55] R. J. Lang, "Ultrasonic atomization of liquids," *J. Acoust. Soc. Am.*, vol. 34, no. 1, pp. 6–8, 1962.

[56] R. L. Peskin and R. J. Raco, "Ultrasonic atomization of liquids," *J. Acoust. Soc. Am.*, vol. 35, no. 9, pp. 1378–1381, 1963.

[57] J. N. Antonevich, "Ultrasonic atomization of liquids," *Ultrason. Eng. Trans. IRE Prof. Gr.*, vol. 6, no. 1, pp. 6–15, 1959.

[58] Y. Y. Boguslavskii and O. K. Eknadiosyants, "Physical mechanism of the acoustic atomization of a liquid," *Sov. Phys. - Acoust.*, vol. 15, no. 1, pp. 14–21, 1969.

[59] M. N. Topp, “Ultrasonic atomization - a photographic study of the mechanism of disintegration,” *Aerosol Sci.*, vol. 4, pp. 17–25, 1973.

[60] J. D. Bassett and A. W. Bright, “Observations concerning the mechanism of atomisation in an ultrasonic fountain,” *J. Aerosol Sci.*, vol. 7, pp. 47–51, Jan. 1976.

[61] F. Barreras, H. Amaveda, and A. Lozano, “Transient high-frequency ultrasonic water atomization,” *Exp. Fluids*, vol. 33, pp. 405–413, 2002.

[62] J. K. McCubbin Jr., “The particle size distribution in fog produced by ultrasonic radiation,” *J. Acoust. Soc. Am.*, vol. 25, no. 5, pp. 1013–1014, 1953.

[63] A. D. Maxwell, T.-Y. Wang, C. A. Cain, J. B. Fowlkes, O. A. Sapozhnikov, M. R. Bailey, and Z. Xu, “Cavitation clouds created by shock scattering from bubbles during histotripsy.,” *J. Acoust. Soc. Am.*, vol. 130, no. 4, pp. 1888–98, Oct. 2011.

[64] T. D. Khokhlova, M. S. Canney, V. A. Khokhlova, O. A. Sapozhnikov, L. A. Crum, and M. R. Bailey, “Controlled tissue emulsification produced by high intensity focused ultrasound shock waves and millisecond boiling.,” *J. Acoust. Soc. Am.*, vol. 130, no. 5, pp. 3498–510, Nov. 2011.

[65] Y.-N. Wang, T. Khokhlova, M. Canney, V. Khokhlova, L. Crum, and M. Bailey, “Histological and biochemical analysis of emulsified lesions in tissue induced by high intensity focused ultrasound,” *J. Acoust. Soc. Am.*, vol. 129, p. 2477, 2011.

[66] M. S. Canney, M. R. Bailey, L. A. Crum, V. a Khokhlova, and O. A. Sapozhnikov, “Acoustic characterization of high intensity focused ultrasound fields: a combined measurement and modeling approach.,” *J. Acoust. Soc. Am.*, vol. 124, no. 4, pp. 2406–20, Oct. 2008.

[67] O. V. Bessonova, V. A. Khokhlova, M. S. Canney, M. R. Bailey, and L. A. Crum, “A derating method for therapeutic applications of high intensity focused ultrasound,” *Acoust. Phys.*, vol. 56, no. 3, pp. 354–363, May 2010.

[68] V. Nahirnyak, S. Yoon, and C. Holland, “Acousto-mechanical and themal properties of clotted blood,” *J. Acoust. Soc. Am.*, vol. 119, no. 6, pp. 3766–3772, 2006.

[69] D. U. Silverthorn, *Human Physiology: An Integrated Approach*, 3rd ed. San Francisco: Pearson Education Inc., 2004, pp. 71–74; 536–540; 547–568.

[70] M. Canney, T. Khokhlova, V. Khokhlova, M. Bailey, J. H. Hwang, and L. Crum, “Tissue erosion using shock wave heating and millisecond boiling in HIFU fields,” *ISTU-2009, AIP Conf. Proc.*, vol. 1215, pp. 36–39, 2010.

[71] T. L. Hall, C. R. Hempel, K. Wojno, Z. Xu, C. A. Cain, and W. W. Roberts, “Histotripsy of the prostate: dose effects in a chronic canine model.,” *Urology*, vol. 74, no. 4, pp. 932–7, Oct. 2009.

[72] C. R. Hempel, T. L. Hall, C. A. Cain, J. B. Fowlkes, Z. Xu, and W. W. Roberts, “Histotripsy fractionation of prostate tissue: local effects and systemic response in a canine model.,” *J. Urol.*, vol. 185, no. 4, pp. 1484–9, May 2011.

[73] T. L. Hall, K. Kieran, K. Ives, J. B. Fowlkes, C. A. Cain, and W. W. Roberts, “Histotripsy of rabbit renal tissue in vivo: temporal histologic trends.,” *J. Endourol.*, vol. 21, no. 10, pp. 1159–66, Oct. 2007.

[74] T. Khokhlova, J. Simon, Y.-N. Wang, V. Khokhlova, M. Paun, F. Starr, P. Kaczkowski, L. Crum, J. H. Hwang, and M. Bailey, “In vivo tissue emulsification using millisecond boiling induced by high intensity focused ultrasound,” *J. Acoust. Soc. Am.*, vol. 129, p. 2477, 2011.

[75] Unos.org, “Organ allocation,” *United network for organ sharing*, 2013. [Online]. Available: http://www.unos.org/donation/.

[76] T. Kaboyashi, R. Sumimoto, H. Shimada, N. Kamada, and G. Nakagawara, “Effect of Sugars in the Preservation Liver Storage in Rats,” *Cryobiology*, vol. 28, pp. 428–435, 1991.

[77] J. H. Southard, “The Right Solution for Organ Preservation,” *Bus. Brief. Glob. Surg.*, vol. 16, pp. 79–84, 2004.

[78] R. G. Boutilier, “Mechanisms of cell survival in hypoxia and hypothermia,” *J. Exp. Bio.*, vol. 204, pp. 3171–3181, Sep. 2001.

[79] N. Ahmad, H. Kashi, H. Helmy, J. Hadingham, and D. J. Potts, “Renal Preservation With Phosphate Buffered Sucrose :,” vol. 1345, no. 96, pp. 355–356, 1997.

[80] F. T. Lam, A. I. D. Mavor, D. J. Potts, and G. R. Giles, “Improved 72-hour renal preservation with phosphate-buffered sucrose,” *Transplation*, vol. 47, no. 5, pp. 767–771, 1989.

[81] K. G. M. Brockbank and M. J. Taylor, “Tissue Preservation,” in in *Advances in biopreservation*, Ebook., 2006, pp. 157–196.

[82] C. Lafon, V. Zderic, M. L. Noble, J. C. Yuen, P. J. Kaczkowski, O. A. Sapozhnikov, F. Chavrier, L. A. Crum, and S. Vaezy, “Gel phantom for use in high-intensity focused ultrasound dosimetry.,” *Ultrasound Med. Biol.*, vol. 31, no. 10, pp. 1383–9, Oct. 2005.

[83] K. Koch, S. Lakshmanan, K. Raum, M. Wicke, D. Morlein, and S. Brand, “Sound velocity and attenuation of porcine loin muscle, backfat and skin,” *World Congr. Med. Phys. Biomed. Eng. Munich, Ger.*, vol. 25, no. 13, pp. 96–99, 2010.

[84] G. Uzer, A. Ho, R. A. F. Clark, and F. Chiank, “Mechanical Properties of Pig Skin,” in *Proceedings of the Society for Experimental Mechanics Annual Conference*, 2009.

[85] J. D. B. MacDougall and M. McCabe, “Diffusion Coefficient of Oxygen through Tissues,” *Nature*, vol. 215, no. September 9, 1967, pp. 1173–1174, 1967.

[86] S. H. Bloch, M. R. Bailey, L. A. Crum, P. J. Kaczkowski, P. D. Mourad, and G. W. Keilman, “Measurements of sound speed in excised tissue over temperatures expected under high-intensity focused ultrasound conditions,” *J. Acoust. Soc. Am.*, vol. 103, p. 2868, 1998.

[87] E. L. Madsen, F. Dong, G. R. Frank, B. S. Garra, K. A. Wear, T. Wilson, J. A. Zagzebski, H. L. Miller, K. K. Shung, S. H. Wang, E. J. Feleppa, T. Liu, W. D. O. Brien, K. A. Topp, N. T. Sanghvi, A. V Zaitsev, T. J. Hall, J. B. Fowlkes, O. D. Kripfgans, and J. G. Miller, “Interlaboratory Comparison of Ultrasonic Backscatter, Attenuation, and Speed Measurements,” *J. Ultrasound Med.*, vol. 18, pp. 615–631, 1999.

[88] A. Anand and P. J. Kaczkowski, “Noninvasive determination of in situ heating rate using kHz acoustic emissions and focused ultrasound.,” *Ultrasound Med. Biol.*, vol. 35, no. 10, pp. 1662–1671, Oct. 2009.

[89] F. A. Duck, *Physical Properties of Tissue: A Comprehensive Reference Book*, E-book. San Diego: Academic Press Inc., 1990, pp. 76–84; 98; 138–140.

[90] X.-L. Ren, X.-D. Zhou, J. Zhang, G.-B. He, Z.-H. Han, M.-J. Zheng, L. Li, M. Yu, and L. Wang, “Extracorporeal ablation of uterine fibroids with high-intensity focused ultrasound,” *J. Ultrasound Med.*, vol. 26, pp. 201–212, May 2007.

[91] B. I. Il’in and O. K. Eknadiosyants, “Nature of the atomization of liquids in an ultrasonic fountain,” *Sov. Phys. - Acoust.*, vol. 12, no. 3, pp. 269–275, 1967.

[92] B. I. Il’in and O. K. Eknadiosyants, “Influence of static pressure on the ultrasonic fountain effect in a liquid,” *Sov. Phys. - Acoust.*, vol. 14, no. 4, pp. 452–455, 1969.

[93] A. D. Maxwell, C. C. Cain, T. L. Hall, J. B. Fowlkes, and Z. Xu, “Probability of cavitation for single ultrasound pulses applied to tissues and tissue-mimicking materials,” *Ultrasound Med. Biol.*, p. in press, 2013.

[94] L. M. Bronskaya, V. S. Vigderman, A. V. Sokol'skaya, and I. E. El'piner, "Influence of the static pressure on utlrasonic chemical and biological effects," *Sov. Phys. - Acoust.*, vol. 13, no. 3, pp. 374–375, 1968.

[95] C. R. Hill, "Ultrasonic exposure thresholds for changes in cells and tissues," *J. Acoust. Soc. Am.*, vol. 51, pp. 667–672, 1971.

[96] M. R. Bailey, L. N. Couret, O. A. Sapozhnikov, V. A. Khokhlova, G. ter Haar, S. Vaezy, X. Shi, R. Martin, and L. A. Crum, "Use of overpressure to assess the role of bubbles in focused ultrasound lesion shape *in vitro*," *Ultrasound Med. Biol.*, vol. 27, no. 5, pp. 695–708, 2001.

[97] V. A. Khokhlova, M. R. Bailey, J. A. Reed, B. W. Cunitz, P. J. Kaczkowski, and L. A. Crum, "Effects of nonlinear propagation, cavitation, and boiling in lesion formation by high intensity focused ultrasound in a gel phantom," *J. Acoust. Soc. Am.*, vol. 119, no. 3, p. 1834, 2006.

[98] Kayelaby.npl.co.uk, "Kaye and Laby: Table of Physical and Chemical Constants," *National Physical Laboratories*, 2013. [Online]. Available: http://www.kayelaby.npl.co.uk/.

[99] EngineeringToolbox.com, "The Engineering Toolbox," 2013. [Online]. Available: engineeringtoolbox.com.

[100] E. Herbert, S. Balibar, and F. Caupin, "Cavitation pressure in water," *Phys. Rev. E*, vol. 74, no. 4, p. 041603, Oct. 2006.

[101] H. Li, Y. Li, and Z. Li, "The heating phenomenon produced by an ultrasonic fountain.," *Ultrason. Sonochem.*, vol. 4, no. 2, pp. 217–8, Apr. 1997.

[102] O. K. Eknadiosyants, "Role of cavitation in the process of liquid atomization in an ultrasonic fountain," *Sov. Phys. - Acoust.*, vol. 14, no. 1, pp. 80–84, 1968.

[103] E. Albaugh, B. Amador, J. Molin, D. Poloney, and A. Savage, "MEDICAL MICROBIOLOGY / SOAP," *Rose-Hulman Institute of Technology*, 2008. [Online]. Available: www.rose-hulman.edu/Catapult2008II/reports/group18.pdf.

[104] E. L. Cussler, *Diffusion: Mass Transfer in Fluid Systems*, 2nd Editio. New York: Cambridge University Press, 1997.

[105] N. Akashi, J. Kushibiki, N. Chubachi, and F. Dunn, "Acoustic properties of selected bovine tissues in the frequency range 20-200 MHz," *J. Acoust. Soc. Am.*, vol. 98, no. 6, pp. 3035–3039, 1995.

[106] T. Glozman and A. Haim, “A Method for Characterization of Tissue Elastic Properties Combining Ultrasonic Computed Tomography with Elastography,” *J. Ultrasound Med.*, vol. 29, pp. 387–398, 2010.

[107] H. Medwin, “Sound speed in water: A simple equatino for realistic parameters,” *1J. Acoust. Soc. Am.*, vol. 58, no. 6, pp. 1318–1319, 1975.

[108] T. L. Szabo, “Diagnostic Ultrasound Imaging: Inside Out,” in in *Diagnostic Ultrasound Imaging: Inside Out*, Elsevier Inc., 2004, p. 492.

[109] D. L. Miller, N. B. Smith, M. R. Bailey, G. J. Czarnota, K. Hynynen, and I. R. S. Makin, “Overview of therapeutic ultrasound applications and safety considerations.,” *J. Ultrasound Med.*, vol. 31, no. 4, pp. 623–34, May 2012.

[110] B. A. Herman and G. A. Harris, “Models and regulatory considerations for transient temperature rise during diatnostic ultrasound pulses,” *Ultrasound Med. Biol.*, vol. 28, no. 9, pp. 1217–1224, 2002.

[111] R. O. Cleveland, M. R. Bailey, N. Fineberg, B. Hartenbaum, M. Lokhandwalla, J. A. McAteer, and B. Sturtevant, “Design and characterization of a research electrohydraulic lithotripter patterned after the Dornier HM3,” *Rev. Sci. Instrum.*, vol. 71, no. 6, p. 2514, 2000.

[112] Kidney.org, “Kidney Stones,” 2013. [Online]. Available: http://www.kidney.org/atoz/content/kidneystones.cfm.

[113] kidney.niddk.nih.gov, “Kidney stones in adults,” *US Dept. of Health and Human Services*, 2007. [Online]. Available: http://kidney.niddk.nih.gov.

[114] V. N. Gupta and P. K. Bhagat, “Ultrasonic characterization of acute renal failure,” *Ultrasound Med. Biol.,* vol. 8, no. 3, pp. 249-261, 1982.

[115] F. Cornelis, N. Grenier, C. T. Moonen, and B. Quesson, “In vivo characterization of tissue thermal properties of the kidney during local hyperthermia induced by MR-guided high-intensity focused ultrasound.,” *NMR Biomed.*, vol. 24, no. 7, pp. 799–806, Aug. 2011.

[116] R. K. Handa, M. R. Bailey, M. Paun, S. Gao, B. A. Connors, L. R. Willis, and A. P. Evan, “Pretreatment with low-energy shock waves induces renal vasoconstriction during standard shock wave lithotripsy (SWL): a treatment protocol known to reduce SWL-induced renal injury.,” *BJU Int.*, vol. 103, no. 9, pp. 1270–4, May 2009.

[117] A. P. Evan, J. A. McAteer, B. A. Connors, P. M. Blomgren, and J. E. Lingeman, “Renal injury during shock wave lithotripsy is significantly reduced by slowing the

rate of shock wave delivery.," *BJU Int.*, vol. 100, no. 3, pp. 624–7; discussion 627–8, Sep. 2007.

[118] S. Giraud, F. Favreau, N. Chatauret, R. Thuillier, S. Maiga, and T. Hauet, "Contribution of large pig for renal ischemia-reperfusion and transplantation studies: the preclinical model.," *J. Biomed. Biotechnol.*, vol. 2011, p. 532127, Jan. 2011.

[119] P. M. Blomgren, B. A. Connors, J. E. Lingeman, L. R. Willis, and A. P. Evan, "Quantitation of shock wave lithotripsy-induced lesion in small and large pig kidneys.," *Anat. Rec.*, vol. 249, no. 3, pp. 341–8, Dec. 1997.

[120] N. S. Mandel, J. D. Henderson, L. Y. Hung, D. F. Wille, and J. H. Wiessner, "A porcine model of calcium oxalate kidney stone disease.," *J. Urol.*, vol. 171, no. 3, pp. 1301–3, Mar. 2004.

[121] D. U. Silverthorn, *Human Physiology: An Integrated Approach*, 3rd ed. San Francisco: Pearson Education Inc., 2004, p. 602.

[122] H. J. S. Bagetti Filho, M. a Pereira-Sampaio, L. a Favorito, and F. J. B. Sampaio, "Pig kidney: anatomical relationships between the renal venous arrangement and the kidney collecting system.," *J. Urol.*, vol. 179, no. 4, pp. 1627–30, Apr. 2008.

[123] kidney.niddk.nih.gov, "Cystoscopy and Ureteroscopy," *US Dept. of Health and Human Services*, 2012. [Online]. Available: http://kidney.niddk.nih.gov.

[124] T. G. Leighton, "Acoustic Cavitation: Effects on the Local Environment," in in *The Acoustic Bubble*, 1st edition, San Diego: Academic Press Inc., 1994, pp. 531–566.

APPENDIX A

List of Urine and Blood Clinical Pathology Analysis

A.1. Serum Chemistry

Blood was collected in a serum separator tube and the following parameters were evaluated:

Sodium	Potassium	Chloride
Total bilirubin	Alkaline phosphatase (ALP)	Lactate dehydrogenase (LDH)
Aspartate aminotransferase (AST)	Alanine aminotransferase (ALT)	Gamma-glutamyltranserase (GGT)
Creatine phosphokinase (CK)	Creatinine	Calcium
Inorganic phosphorus	Glucose	Urea nitrogen (BUN)
Total protein	Albumin	Globulin
Albumin/globulin ratio	Cholesterol	Triglycerides

A.2. Hematology

Blood was collected in EDTA-containing tubes and the whole blood sample was analyzed for:

Red blood cells (RBCs)	White blood cells (WBCs)	Hemaglobin concentration
Hematocrit	Reticulocyte counts	Platelet counts
Mean corpuscular hemoglobin (MCH)	Mean corpuscular hemaglobin concentration (MCHC)	Mean corpuscular volume (MCV)

A.3. Coagulation

Blood was collected in sodium citrate containing tubes, centrifuged to obtain plasma, and used for the determination of prothrombin time (PT)

A.4. Urinalysis

Urine was collected via a transcutaneous bladder puncture for the survival studies or directly from the kidneys via ureteral balloon catheterization.

Color	Clarity	pH
Ketones	Bilirubin	Specific gravity
Glucose	Occult blood	Nitrite
Protein	Urobilinogen	Leukocytes

A.5. List of Tissues Collected from Necropsies

Below is a list of samples (when present) that were collected from the necropsies after the survival studies:

Cardiovascular	Urogenital
Aorta	Kidneys
Heart	Ureters
Right AV Valve	Urinary Bladder
Left Ventrical	Testes
Digestive	Epididymides
Tongue	Penile Shaft
Esophagus	Ovaries
Stomach	Uterus
Small Intestine	Vagina
Duodenum	Respiratory
Jejunum	Trachea
Ileum	Lung
Large Intestine	Vocal Cords
Cecum	Lymphoid/Hematopoietic
Colon	Bone Marrow (Rib)
Pancreas	Thymus
Liver	Spleen
Left Lobe	Lymph Nodes
Right Medial Lobe	Nervous/Special Sense
Right Lateral Lobe	Brain
Caudate Lobe	Cerebrum
Gall Bladder	Cerebellum/Brain Stem
Endocrine	Spinal Cord (Lumbar)
Adrenals	Other
Thyroid/Parathyroid	Gross Lesions
Skin/Musculoskeletal	
Skin/Mammary Gland	
Bone (Rib)	
Skeletal Muscle *(Biceps Femoris)*	

Curriculum Vitae

Julianna Simon

Education

2013	Ph. D.	Department of Bioengineering, University of Washington
2009	B.S.	Bioengineering, Washington State University

Peer-Reviewed Publications

Simon J, Sapozhnikov O, Khokhlova V, Wang Y-N, Crum L, and Bailey M (2012). "Ultrasonic atomization of tissue and its role in tissue fractionation by high intensity focused ultrasound," Phys. Med. Biol. 57, 8061-8078.

Wang Y-N, **Simon JC,** Cunitz BW, Starr F, Paun M, Liggitt DH, Evan AP, McAteer JA, Liu Z, Dunmire B, and Bailey MR (2013) "Focused ultrasound to displace renal calculi: threshold for tissue injury." J. Therapeutic Ultrasound. Submitted April 11, 2013.

Khokhlova T, Wang Y-N, **Simon J,** Cunitz B, Starr F, Paun M, Crum L, Bailey M, and Khokhlova V (2013). "Ultrasound-guided tissue fractionation by high intensity focused ultrasound in an in vivo porcine liver model," PNAS. Submitted September 27, 2013.

Poliachik SL, Khokhlova TD, Wang Y-N, **Simon JC,** and Bailey MR (2013). "Pulsed focused ultrasound treatment of muscle mitigates paralysis-induced bone loss in the adjacent bone: A study in a mouse model." Ultrasound Med. Biol. Submitted July 24, 2013.

Connors BA, Evan AP, Blomgren PM, Hsi RS, Harper JD, Sorensen MD, Wang Y-N, **Simon JC,** Paun M, Starr F, Cunitz BW, Bailey MR, and Lingeman JE (2014). "Comparison of tissue injury from focused ultrasonic propulsion of kidney stones versus extracorporeal shock wave lithotripsy," J. Urol. S0022-5347(13)05053-2.

Sorensen MD, Bailey MR, Hsi RS, Cunitz BW, **Simon JC,** Wang Y-N, Dunmire BL, Paun M, Starr F, Lu W, Evan AP, and Harper JD (2013). "Focused ultrasonic propulsion of kidney stones: Review and update of preclinical technology," J. Endourology 27(10), 1183-1186.

Harper JD, Sorensen MD, Cunitz BW, Wang Y-N, **Simon JC,** Starr F, Paun M, Dunmire B, Liggitt HD, Evan AP, McAteer JA, Hsi RS, and Bailey MR (2013). "Focused ultrasound

to expel calculi from the kidney: safety and efficacy of a clinical prototype device," J. Urol. In press.

Shah A, Harper JD, Cunitz BW, Wang Y-N, Paun M, **Simon JC**, Lu W, Kaczkowski PJ, and Bailey MR (2012). "Focused ultrasound to expel calculi from the kidney." J. Urol. 187(2).

Hicks DG, Pitts MJ, Bagley RS, Vasavada A, Chen AV, Wininger FA, **Simon JC**. (2009) "In vitro biomechanical evaluations of screw-bar–polymethylmethacrylate and pin-polymethylmeth-acrylate internal fixation implants used to stabilize the vertebral motion unit of the fourth and fifth cervical vertebrae in vertebral column specimens from dogs." Am. J. of Vet. Research. 70(6), 719-726.

Patents

Sapozhnikov OA, Bailey MR, Crum LA, Khokhlova TA, Khokhlova VA, **Simon JC,** Wang Y-N. "Methods of soft tissue emulsification using a mechanism of ultrasonic atomization inside gas or vapor cavities and associated systems and devices." Filed April 11, 2012 with US Patent Office.

Bailey MR, Hsi R, Cunitz BW, Dunmire BL, Harper JD, Sorensen MD, **Simon JC,** Khokhlova VA, Sapozhnikov OA, Kreider W, Wang Y-N. "Producing propulsion signals and receiving feedback signals to adjust a position of an object," Filed May 17, 2013 with US Patent Office.

Academic Awards

2013 Recipient of the National Space Biomedical Research Institute (NSBRI) First Award Postdoctoral Fellowship

2013 Nominated for a poster presentation at the Bioengineering Sponsored Rushmer Lecture

2013 Best Paper Award Co-Author for the American Urological Association Conference, San Diego, CA

2012 Recipient of the University of Washington Dean of Engineering Fellowship

2012 Student travel grant recipient for the IEEE International Ultrasonics Symposium in Dresden, Germany

2012 Winner of "UW INVENTS" award sponsored by the Center for Commercialization and College of Engineering at the University of Washington

2012 Best Paper Award Co-Author for the Engineering and Urology Society Conference in Atlanta, GA, USA

2012 Awarded 1st Runner Up in the Science and Technology Showcase sponsored by the Foster School of Business at the University of Washington

2012 Featured in video produced by the Applied Physics Lab to promote our work in repositioning kidney stones with ultrasonic propulsion. Video was also used by NASA for advertising purposes.

2011 Received the University of Washington College of Engineering Donald W. and Joan P. Baker Endowed Scholarship.

2009 Member of 2nd Place team in the Business Plan Competition sponsored by the Center for Entrepreneurial Study and College of Business International Competition at Washington State University

2008 Received Outstanding Student Mentor Award for the NASA Lewis Educational and Research Collaborative Internship Program (LERCIP) for high school students

2008 Received Outstanding Team Award for the NASA LERCIP Undergraduate Program

Conference Proceedings Publications

Simon JC, Sapozhnikov OA, Khokhlova VA, Wang Y-N, Crum LA, Bailey MR (2013). "Ultrasonic atomization: a method of tissue fractionation." J. Acoust. Soc. Am. Montreal, Canada, June 2-7.

Wang Y-N, **Simon JC,** Cunitz BW, Starr F, Paun M, Liggitt D, Evan AP, McAteer JA, Williams Jr. JC, Liu Z, Kaczkowski PJ, Hsi RS, Shah A, Sorensen MD, Harper JD, Bailey MR (2013). "Determination of tissue injury thresholds from ultrasound in a porcine kidney model," J. Acoust. Soc. Am. Montreal, Canada, June 2-7.

Bailey MR, Wang Y-N, **Simon JC,** Cunitz BW, Harper JD, Sorensen MD, Hsi RS, Starr F, Paun M, Dunmire B, Sapozhnikov OA, Crum LA (2013). "Acoustic radiation force to resposition kidney stones," J. Acoust. Soc. Am. Montreal, Canada, June 2-7.

Kreider W, Maxwell AD, Khokhlova TD, **Simon JC,** Khokhlova VA, Sapozhnikov OA, Bailey MR (2013). "Rectified growth of histotripsy bubbles." J. Acoust. Soc. Am. Montreal, Canada, June 2-7.

Simon JC, Sapozhnikov OA, Khokhlova VA, Wang Y-N, Crum LA, Bailey MR (2012). "Tissue atomization by high intensity focused ultrasound." IEEE International Ultrasonics Symposium Proceedings, Dresden, Germany October 7-10, pp. 1003-1006.

Conference Abstracts

Simon JC, Sapozhnikov OA, Khokhlova VA, Wang Y-N, Crum LA, and Bailey MR (2014). "Ultrasonic Atomization of Tissue: A Mechanism for Ultrasound-Based Surgery," NASA Human Research Program Investigators' Workshop (HRP 2014) Galveston, TX February 13-14, 2014.

Dunmire BL, Harper JD, Sorensen MD, Wessells HB, Lingeman JE, Coburn M, Cunitz BW, Wang Y-N, **Simon JC,** Maxwell AD, Kreider W, Paun M, Crum LA, Khokhlova VA, Sapozhnikov OA, and Bailey MR (2014). "Prevention of Renal Stone Complications in Space Exploration," NASA Human Research Program Investigators' Workshop (HRP 2014) Galveston, TX February 13-14, 2014.

Poliachik SL, Khokhlova TD, Wang Y-N, Simon JC, Gross TS, and Bailey MR (2013). "Pulsed focused ultrasound treatment of muscle mitigates paralysis-induced bone loss in the adjacent bone: a study in a murine model," J. Acoust. Soc. Am. 134(5), 4181.

Crum L, Cunitz B, Dunmire B, Harper J, Kaczkowski P, Kucewicz J, Lu W, Paun M, Sapozhnikov O, **Simon J**, Sorensen MD, Starr F, Wang Y-N, and Bailey MR (2013). "Recent developments in therapeutic ultrasound: Kidney stone imaging and repositioning by ultrasound," International Congress on Ultrasonics Opening Plenary Paper May 2-5 Singapore, China.

Khokholva VA, **Simon JC,** Khokhlova TD, Wang Y-N, Paun M, Starr FL, Sapozhnikov OA, Crum LA, Bailey MR (2013). "In vivo tissue emulsification using boiling histotripsy HIFU exposures," International Symposium on Therapeutic Ultrasound (ISTU) May 12-15 Shanghai, China.

Connors B, Evan A, Blomgren P, Hsi R, Harper J, Sorensen M, Wang Y-N, **Simon J,** Paun M, Starr F, Cunitz B, Bailey M (2013). "Comparison of tissue injury from a novel technique of focused ultrasonic propulsion of kidney stones versus extracorporeal shock wave lithotripsy," Am. Urological Assoc. San Diego, CA May 4-8, 2013.

Wang Y-N, **Simon J,** Hsi RS, Harper JD, Sorensen MD, Starr F, Paun M, Cunitz B, Liggitt HD, Evan AP, McAteer JA, Bailey MR (2013). "Determination of tissue injury threshold from focused therapeutic ultrasound," Am. Urological Assoc. San Diego, CA May 4-8, 2013.

Crum LA, **Simon JC,** Khokhlova TD, Wang Y-N, Hwang J-H, Khokhlova VA, Bailey MR (2012). "Boiling histotripsy: a method of tissue emulsification using millisecond-long pulses of high intensity focused ultrasound," 3rd International Symp. On MR-guided Focused Ultrasound, Oct. 2012, Bethesda, MD, USA.

Bailey M, Cunitz B, Dunmire B, Wang Y-N, **Simon J,** Paun M, Starr F, Lu W, Harper J, Sorensen M (2012). "Preclinical testing of ultrasonic propulsion of kidney stones," IEEE UFFC Oct. 2012, Dresden, GER.

Crum LA, **Simon JC,** Khokhlova TA, Wang Y-N, Hwang J-H, Khokhlova VA, Bailey MR (2012). "Boiling histotripsy: A method of tissue emulsification using millisecond-long pulses of high intensity focused ultrasound," 3rd Int. Symp. On Focused Ultrasound. Oct. 14-17, 2012, Washington DC, USA.

Sorensen M, Harper J, Hsi R, Cunitz B, **Simon J**, Wang Y-N, Paun M, Starr F, Lu W, Evan A, Bailey M (2012). "Preclinical efficacy and safety of ultrasonic propulsion of kidney stones," World Cong. On Eng. July 2012, London, UK.

Sapozhnikov O, **Simon J,** Khokhlova V, Khokhlova T, Kreider W, and Bailey M (2012). "Comparison of Ultrasonic Atomization of Tissue and Liquids," Intern. Symp. Of Therapeutic Ultrasound, June 10-13, 2012, Heidelberg, Germany.

Sorensen M, Harper J, Hsi R, Cunitz B, **Simon J**, Wang Y-N, Paun M, Starr F, Lu W, Evan A, Bailey M (2012). "Preclinical safety and efficacy of ultrasonic propulsion of kidney stones," Eng. Urol. Soc, May 19, 2012, Atlanta, GA, USA.

Crum LA, Bailey MR, Khokhlova TA, Khokhlova VA, Kreider W, **Simon JC,** Wang Y-N, Sapozhnikov OA (2012). "Therapeutic ultrasound: Recent advances and future perspectives," 9th Int. Symp. On Modern Acoustics, May 2012, Nanjing, China.

Crum L, Bailey M, Khokhlova T, Khokhlova V, Sapozhnikov O, and **Simon J** (2012). "Boiling histotripsy: A promising approach to tumor ablation," Intern. Symp. On Modern Acoustics, May 20-22 2012, Nanjing, China.

Crum L, Bailey M, Khokhlova T, Khokhlova V, **Simon J,** and Sapozhnikov O (2012). "Therapeutic Ultrasound: A potential Revolution in Health Care," Acoustic Waves for the Control of Microfluidics Flows, April 23-27, 2012, Leiden, Netherlands.

Simon JC, Sapozhnikov OA, Khokhlova VK, Wang Y-N, Khokhlova TD, Crum LA, and Bailey MR (2011). "A mechanism of tissue emulsification by high intensity focused ultrasound," J Acoust Soc Am 130.

Simon JC, Wang Y-N, Evan AP, Paun M, Starr FL, Crum LA, and Bailey MR (2011). "Determination of thresholds for renal injury in a porcine model by focused ultrasound," J Acoust Soc Am 130.

Crum LA, Canney M, Bailey M, Khokhlova T, Khokhlova V, Sapozhnikov O, Kreider W, and **Simon J** (2011). "Histotripsy without cavitation." Medical Physics. 38(6), 3811-3812.

Crum LA, Bailey MR, Canney M, Khokhlova TD, Khokhlova VK, Sapozhnikov OA, and **Simon JC** (2011). "The use of high intensity focused ultrasound to induce tissue ablation." Invited Plenary Lecture at 2011 International Congress on Ultrasonics, Gdansk, Poland.

Simon JC, Sapozhnikov OA, Khokhlova VK, Khokhlova TD, Bailey MR, and Crum LA (2011). "Miniature acoustic fountain mechanism for tissue emulsification during millisecond boiling in high intensity focused ultrasound fields," J Acoust Soc Am 129.

Simon JC, Crum LA, Shah A, Cunitz BW, Wang Y-N, Kaczkowski PJ, and Bailey MR. (2011). "Preventative ultrasonic detection and expulsion of kidney stones," 18th IAA Humans in Space Symp., April 11-15, 2011, Houston, TX.

Sapozhnikov OA, **Simon JC,** Khokhlova VA, Khokhlova TD, and Bailey MR (2011). "Tissue emulsification through ultrasonic atomization," Intern. Symp. Of Therapeutic Ultrasound, April 11-13, 2011, New York, NY.

Khokhlova TD, **Simon JC**, Wang Y-N, Khokhlova VA, Paun M, Starr FL, Kaczkowski PJ, Crum LA, Hwang J-H, and Bailey MR (2011). "In vivo tissue emulsification using millisecond boiling induced by high intensity focused ultrasound," Acoust Soc Am 129.

Bailey MR, Cunitz BW, Kucewicz JC, Wang Y-N, **Simon JC**, Lu W, Kaczkowski PJ, and Sapozhnikov OA (2011)."Prototype for expulsion of kidney stones with focused ultrasound," Intern. Symp. of Therapeutic Ultrasound, April 11-13, 2011, New York, NY.

Shah A., Harper JD, Cunitz BW, Kucewicz JC, Wang Y-N, **Simon JC**, Lu W, Kaczkowski PJ, Bailey MR (2011). "Prototype for Expulsion of Kidney Stones with focused ultrasound," J Acoust Soc Am 129.

Khokhlova VA, Canney MS, Bailey MR, Hwang JH, Khokhlova TD, Kreider W, Wang Y-N, **Simon JC**, Zhou Y, Sapozhnikov OA, Crum LA, (2011), "A method of mechanical emulsification in a bulk tissue using shock wave heating and millisecond boiling" J Acoust Soc Am 129.

Crum L, Canney M, Bailey M, Hwang J, Khokhlova T, **Simon J**, and Khokhlova V (2010). "Boiling and cavitation during HIFU exposures." Current and Future Applications of MR-guided Focused Ultrasound 2nd Intern. Symp., October 17-20, 2010, Washington DC.

Cuntiz B, Shah A, **Simon JC**, Lu W, Paun M, Crum LA, Bailey MR. (2009) "Ultrasound to detect and accelerate passage of kidney stones." Aviation, Space, and Environmental Medicine. 81(3), 83.